THESIS

Presented to obtain a grade of:

INTERNATIONAL DOCTOR OF PHILOSOPHY

UNIVERSITY OF SALAMANCA

by

Sophia MALKO

Laser-driven charged particle transport in warm dense matter and plasma

Director of thesis :	M. Luca VOLPE	Professor, University of Salamanca (*Spain*)
Co-director of thesis :	M. Robert FEDOSEJEVS	Professor, University of Alberta (*Canada*)

Committee composed by:

President:	Javier HONRUBIA	Professor, Universidad Politécnica de Madrid (*Spain*)
Vocal:	Markus ROTH	Director, Technische Universitat Darmstadt (*Germany*)
Secretary:	Sebastien LE PAPE	Deputy director, LULI, École Polytechnique (*France*)
Reporters:	Johan FRENJE	Research scientist, PSFC, MIT (*USA*)
	Robbie SCOTT	Research scientist, Central Laser Facility (*UK*)

19 March 2020

I would like to dedicate this thesis to my dear mother ... ...

Declaration

I hereby declare that except where specific reference is made to the work of others, the contents of this dissertation are original and have not been submitted in whole or in part for consideration for any other degree or qualification in this, or any other university. This dissertation is my own work and contains nothing which is the outcome of work done in collaboration with others, except as specified in the text and Acknowledgements.

Sophia Malko
February 2020

Acknowledgements

I would like to acknowledge the people without whose support and help, I would be not preparing my thesis defence right now. The results achieved in this PhD thesis would not be possible without the collaboration of many research institutions all over the world united together towards understanding laser - driven plasma physics. I would like to thank all the people who contributed to the theoretical modelling, experimental designs, precious scientific discussions and who were just around, providing strong personal support during my PhD studies at the University of Salamanca and at the Centro de Laseres Pulsados (CLPU) in Spain. With many of them, we became good friends and I hope this friendship will remain throughout the years. And I would like to express my sincere gratitude to the scientists who introduced me to the world of experimental physics and showed it to me in new colours, and who contributed the most to my professional and personal growth.

First of all, I would to thank my PhD supervisors, Luca Volpe and Robert Fedosejevs, who supported and guided my research during these four years, taught me physics and gave me many opportunities to realize my ideas. Special thanks for their tremendous kindness and patience with me.

Secondly, I would like also to thank my professors Igor Girka, Konstantin Sereda, Sergiy Kononenko and Igor Grakusha from my the faculty of Physics and Technology of V.N. Kharkiv Karazin University, as well as my supervisor Segrey Pavlov for undergraduate projects, who gave me a strong plasma physics background and motivated me to continue research in this field.

A special acknowledgement is dedicated to my close friend Joao Santos, without whom I would not even have started my PhD adventure in Salamanca. Besides that, special thanks for his support in difficult moments and trust in my success during all these years. It is insane to think, how one accidental meeting with him at the Kudowa Summer School back to 2014 could change my so life drastically.

My sincerest gratitude I would like to express to a key figure in my PhD study and one of my best friends, Xavier Vaisseau, who showed me an example of the high level of experimental scientist I would like to become. Thanks for being such a generous and amazing person.

And of course, I would like thank Jon Apiñaniz, my colleague at work and my friend, who become like a brother for me in the last years. Special thanks for his dedication to our common work, patience and for understanding me so well.

Furthermore, I would like to thank Dimitri Batani, who was my supervisor during my internship at CELIA, and provided tremendous help for my research in fast electron transport and shock ignition experiments. I also want to thank Witold Cayzac for his huge contribution in the understanding proton stopping power physics presented in this thesis, Javier Honrubia for the help with the fast electron transport modelling, as well as for the support of this research line, and Frederic Perez for the help in the experimental campaign at LULI-ELFIE facility and for PIC simulations of the fast electron source. I also would like to acknowledge Anna Tauschwitz for performing the RALEF2D simulations.

My special thanks are for Micha Ehret, who besides being an awesome friend, with whom you can go to the end of the world, is also a great scientist, who helped me a lot in the LULI - ELFIE experimental campaign.

I would like to acknowledge my "proton stopping power rangers" team - Jon Apiñaniz , Witold Cayzac, Xavier Vaisseau, Micha Ehret, Valeria Ospina, Chris Mcguffey, Krish Bhutwala, Mathieu Bailly - Grandvaux, Luca Volpe, Robert Fedosejevs, Diego de Luis and Jose Antonio Perez, people who used their experimental and theoretical "super powers" in order measure ion stopping power in warm dense matter.

Particularly, special thanks I would like to address to Diego de Luis for his extraordinary engineering skills in building the energy selector magnet.

Indeed, my largest gratitude is addressed to all my colleagues in the scientific area of CLPU, who became my friends, particularly to Ghassan Zeraouli, Carlos Salgado and Valeria Ospina with whom we shared many amazing and not so amazing moments of the PhD life. Thanks for bringing a lot of positive vibes and good mood to the situations where one would cry instead. We started this adventure together, and we are almost finishing it, also together. Special thanks to all the stuff of CLPU and to my chief, Giancarlo, for leading the CLPU to the next level of user laser facility.

I am also expressing my greatest gratitudes to my mother Natalia, my brothers, Dima and Andrew (who will also become Doctor of Philosophy very soon), as well as to my dear friends Katya, Anastasia, Chess, Lena, Polina, Joe, Andrew, Duc, and Fernando who supported me through all my PhD studies and didn’t let me give up.

The last, but not least, I thank Prav, who helped me to believe in myself, showed me a light in the dark times, and motivated me to finish these PhD studies.

In the end I can say, that this manuscript is a result of the friendship and deep connection between all these people together.

Abstract

This thesis focuses on the physics of intense laser-generated charged particle beam transport. The two important applications related to inertial confinement fusion and particle acceleration: (i) the transport and collimation of fast electrons created in high intensity laser-matter interactions, and (ii) ion stopping power close to the Bragg peak in extreme states of matter. Both topics have been investigated in an integrated approach that combines experimental campaigns with detailed theoretical and numerical studies used to support the experiments both in the design prior to the experiments being carried out, and in the analysis of the experimental results afterwards. The experiments presented here are are the result of a long and extended collaboration with research institutions across the EU and abroad—without whom this work would not been possible. The most important results achieved in this work can be stated as following:

- A first detailed parametric investigation of relativistic electron beam collimation as a controllable and reproducible technique by using the double pulse technique for fast Ignition and laser-particle and radiation sources acceleration.
- The establishment of a dedicated workstation for laser-driven ion sources implementation for applications including generation, selection and transport of proton beams.
- A first experimental measurement of proton stopping power close to the Bragg peak region in Warm Dense Matter for laser Inertial Confinement Fusion and proton particle applications using laser-driven ion sources.

Table of contents

Chapter 1

Introduction

High power pulsed lasers are becoming a well established technology in the European Union (EU) and internationally, supporting numerous lines of basic research in plasma physics, fusion, particle acceleration, astrophysics, and many other scientific and technological applications. The performance of a laser system depends on several key parameters including the laser energy, peak power, pulse duration and central wavelength. One can broadly define two main classes of laser systems: (i) multi-beam high energy systems such as the 192-beam 1.8 MJ National Ignition Facility (NIF) in the US, the 176-beam 1.3 MJ Laser Mégajoule (LMJ) in France, the 60-beam 30 kJ OMEGA laser in the US, the 12-beam 10 kJ Gekko XII laser in Japan, and (ii) high power systems such as the Apollon 10 PW laser facility in France and the Extreme Light Infrastructure (ELI) facilities in Europe. The first are characterised by long pulse durations of hundreds of picoseconds to nanoseconds, while the second by extremely short pulses of femtosecond to sub-picosecond time durations. PW class laser system are already in operation in EU and among which the laser system VEGA laser at the Centro de Laseres Pulsados (CLPU) in Spain is the one where most of the described experimental results have been obtained. Historically, the primary interest in developing high energy nanosecond-pulsed lasers was, and continues to be, for the study of laser-driven fusion. However, with the advent of chirped pulse amplification (CPA) technology in the 1980s it became possible to reduce pulse durations by several orders of magnitude to the sub-picosecond regime and obtain a correspondingly great increase in the laser peak power and intensity. This opened the door for major new avenues of research including the ability to heat matter to extreme states within very short times on the order of the hydrodynamic time scale. This also implied an enormous increase in the net electron current driven and the related induced quasi-static electric field of the order of $10^{10} - 10^{12}$ V/m able than to accelerate particles up to several MeV for ions and a few GeV for electrons—far into the relativistic regime. Such laser-generated charged particle beams are characterised by high

brilliance, small divergence, and short duration, and are candidates to be complementary sources to the particle beams usually produced in large conventional accelerators. Laser acceleration mechanisms rely first on the primary interaction of laser light with the lightest particles, i.e., electrons. The electrons accelerated by the laser then transfer energy as they propagate through the matter. The detailed characteristics of the electron source are therefore important in many applications, including, for instance, ion acceleration mechanisms and X-ray sources generation. This thesis focuses on the physics of intense laser-generated charged particle beams transport. Two important applications related to inertial confinement fusion and particle acceleration are studied: (i) the transport and collimation of fast electrons created in high intensity laser-matter interactions, and (ii) ion stopping power close to the Bragg peak in extreme states of matter. Both topics have been investigated in an integrated approach that combines experimental campaigns with detailed theoretical and numerical studies used to support the experiments both in the design prior to the experiments being carried out, and in the analysis of the experimental results afterwards. The experiments presented here are the result of a long and extended collaboration with research institutions across the EU and abroad—without whom this work would not have been possible. The most important results achieved in this work can be stated as following:

- A first detailed parametric investigation of relativistic electron beam collimation as a controllable and reproducible technique by using the double pulse technique for fast Ignition and laser-particle and radiation sources acceleration.
- The establishment of a dedicated workstation for laser-driven ion sources implementation for applications including generation, selection and transport of proton beams.
- A novel proposal for experimental measurement of proton stopping power close to the Bragg peak region in Warm Dense Matter for laser Inertial Confinement Fusion and proton particle applications using laser-driven ion sources.

1.1 Laser driven plasma

More than 99% of the visible matter in the universe exists in the plasma state. Stellar interiors and atmospheres, gaseous nebulae, and much of the interstellar hydrogen are plasmas. On Earth, plasmas are present for example in the flash of a lightning bolt, the soft glow of an Aurora Borealis, and as the conducting gas inside a fluorescent tube or neon sign. Figure 1.1 shows a chart of temperature and density, where one can see that the plasma state is a quite diverse definition of the matter is between relatively cold states close to solid density and very high temperature, low density states. Laser-matter interactions are a common tool to

reach high density and temperature plasmas, that can be comparable with stellar interiors or coronas.

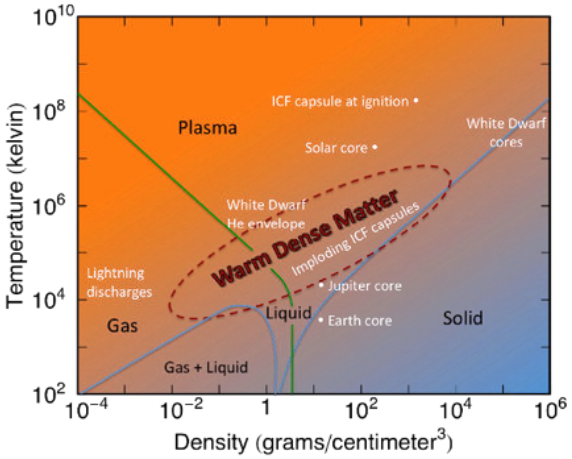

Fig. 1.1 Chart of density and temperature of plasma in the universe. Graph taken from [2].

Laser-driven plasmas have been extensively studied in the context of nanosecond and picosecond time domains, as permitted by the available laser technology. They can be produced with laser intensities above $10^{12}\mathrm{W/cm^2}$. The advent of high energy Chirped Pulse Amplification (CPA) Ti:Sapphire laser technology has pushed laser pulse durations into the range of femtoseconds giving the possibility to reach comparable or greater laser intensities than obtained by preceding laser systems [202]. Plasma formation in the fs regime is expected to behave differently due to the fact that the laser pulse duration is of the order of the electronic motion timescale and shorter then the ionic motion time scale which is comparable to previous ns- and sub-ns laser systems. Indeed, femtosecond laser pulses deposit energy into the matter before any ionic motion can start to be relevant providing an efficient way to generate plasmas with negligible expansion (so-called isochorically heated plasmas). In the last decades the physical mechanisms governing the transition between solid and plasma states by laser interaction have been investigated more in detail to better understand such "fast" ionisation processes and theoretical models still need to be validated in this regime. The crucial role in laser-plasma interactions is played by the electron population in transporting and distributing energy into the target and so driving the ionization processes that will transform solid matter into a plasma state. Laser-plasma interactions can generate several instabilities which grow up supported by the mutual interaction between laser and plasma (electronic or ionic) waves [123] and are on the basis of the so-called ponderomotive force. In addition, by increasing the laser intensity the magnetic component of the laser wave

starts to become important and contributes to the acceleration mechanism via the so called $\mathbf{j} \times \mathbf{B}$ force.

Laser-driven electron beam energy deposition into the matter is given by both collisional and resistive stopping power. Indeed whenever the electron beam is travelling in dielectric medium the local charge neutrality is broken, and so needs to be re-established by providing an additional electron current that is responsible for the resistive stopping power [16, 215]. The neutralization time depends on the target conductivity whose value changes during the laser irradiation as it depends on the target temperature and density. The target temperature variation leads to a drastic change of the electric resistivity of the matter [44]. The knowledge of it, is crucial especially in the warm dense matter regime where both quantum (plasma temperature of the order of the Fermi temperature T_F) and collision (plasma density is such that collisions are not negligible) effects are relevant. This warm dense matter state still is not well understood even though it is frequently present in the universe (interior of planets) and in many field of research such as fusion and laboratory astrophysics [59]. From a theoretical point of view low density and high temperature plasmas can be described by the Vlasov equation, while for higher densities the full Vlasov-Focker-Planck equation is necessary. Low temperature (close to T_F) and low density represent the Fermi gas. Both these states are well described by both classical or quantum descriptions, but when the temperature is close to T_F for a dense plasma, a full quantum multi-body [12] theoretical description is required. A complete understanding of such different states of matter can be achieved only by considering both theoretical and experimental approaches at the same level in a mutual interaction. This can allow the consequent studies of fast electron transport in the matter, solid and dense plasmas in short-pulse high-intensity laser interactions, which are important for a large range of applications such as proton acceleration and inertial confinement fusion (ICF). In this thesis two different plasma regimes are studied: relatively hot plasma states with $T_e \approx 200$ eV, and warm dense plasma states with densities close to solid $\rho \approx 1$ g/cm^3 and relatively low temperatures $T_e \approx 1$ - 100 eV.

1.2 Applications

1.2.1 Laser - driven particle sources

As was mentioned before the laser technology has advanced to the point where hitherto unobtainable intensities are now routinely achievable, and rapid progress is being made to increase intensities further [202]. One of the most important applications of high power lasers is the generation of compact, high brightness particle and radiation sources based

on increased the efficiency and repetition rate of the lasers. A result of this technological development can be seen in the new generation of ultrafast high power laser systems working at High Repetition Rate (HRR) which have been built across Europe [47]. One can define two main interaction regimes for the particle generation such as under-dense laser-matter interaction where short pulsed high intensity lasers ($I > 10^{18}$ W/cm^2) are focused onto a low density gas-jet generating via wake field mechanism [203, 140, 68, 82, 139] electron beams with energy $\approx$ GeV and an X-ray betatron source with 10 - 20 keV characteristic critical energy [5, 114, 145, 6]. And second one - over critical density laser-matter interaction where short pulsed high intensity laser is focused onto a solid target generating relativistic electron beams > MeV [221, 19]. Same regime corresponds to the generating via Target Normal Sheath Acceleration (TNSA) mechanism [222, 138, 198] of a proton beam by focusing ultra intense lasers ($I > 10^{19}$ W/cm^2) onto thin solid targets. The generation and transport of **relativistic electron beam** has been studied in the framework of this thesis. Particularly, the electron beam collimation scheme using two consecutive laser pulses has been investigated numerically and experimentally at ELFIE LULI laser facility. It features well controlled efficiency of the collimation of the electron beam in solid target, that induces an artificial reduction (similar to the one obtained via mass-limited target technique) the transversal area and then increase the total electron current density. This effect increase proton acceleration and X ray generation in laser solid interaction schemes. Therefore, one can implement the scheme for the high brilliance x-ray sources and enhancement of the laser-driven proton generation. The use of the laser - driven ion sources is mostly motivated by its maximum energy deposition at the end of the ion range directly related to the initial ion energy (Bragg peak); this can be used for applications which interest is a control of the well - characterised energy deposition into material. However, the typical laser-driven proton energy spectrum is naturally very broad. Then the generation of **proton beam** via laser-matter interaction need to be complemented with a secondary system for the energy selection and transport of such proton sources. This is fundamental for the use of such sources for applications. A first step in this direction has been done at CLPU in Salamanca where a first experimental station has been established to select short proton beams (tens of ps) with energies bandwidth within 10-20 KeV. The capability to generate and transport such special ion sources pave the way to the experimental investigation related to several civil applications such us:

- Stopping power measurements
- Ion -induced isochoring heating of matter
- Proton Induce X-ray Emission PIXE for cultural heritage studies
- Medical and Biological applications with short ion sources

- Material science applications

1.2.2 Inertial Confinement Fusion

Fast ignition Achieving fusion ignition requires assembling a given mass of deuterium-tritium (DT) fuel to simultaneously very high densities and temperatures. In the conventional central hot-spot ignition approach being pursued on the NIF and LMJ MJ-class laser facilities a spherical implosion is used to produce a high temperature (> 5 keV) DT hotspot surrounded by a dense shell of cold DT fuel ($\sim$ 1000 g/cm^3). If the hotspot can be ignited it would launch a burn-wave into the dense fuel significantly increasing the total fusion output and gain. A key challenge for this scheme is that achieving the conditions needed for ignition requires an implosion with high velocity and high convergence, which will then be highly susceptible to hydro instabilities. M. Tabak *et al.* [204] developed an alternative approach which separated the compression and heating stages. A relatively lower velocity, lower convergence implosion assembles DT fuel to a moderate density ($\sim$ 300 g/cm^3).

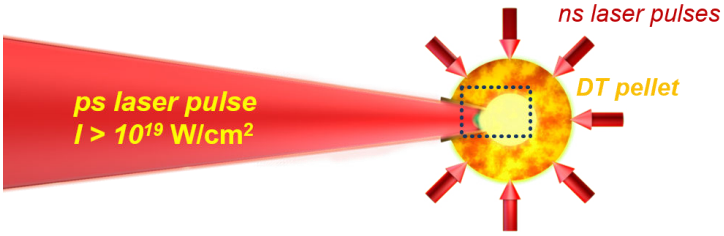

Fig. 1.2 Scheme of the fast ignition approach to inertial confinement fusion

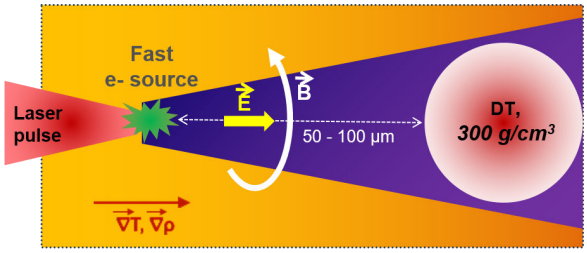

Fig. 1.3 The scheme of the fast electron transport through the dense plasma to the DT core.

A small volume of this DT fuel ($\sim$ 40 μm diameter) is then heated isochorically to ignition temperatures using a **fast electron beam** of MeV energies generated by a short-pulse high power laser as shown in the Figure 1.2. The principal challenge for this fast ignition approach is if a heating beam with the necessary characteristics can be produced and transported to the DT core (Fig.1.3). By nature electrons are divergent and the development

of the electron collimation scheme is a task of a high importance. The alternative scheme of using of **ion beam** as a secondary driver for ignition in ICF instead of electrons has been proposed by M. Roth *et al.* [181] and called proton fast ignition. Indeed, knowing the ion energy deposition and its stopping power in high energy density plasma is obligatory for the success of the scheme.

Alpha particle heating Knowing Ions stopping power in extreme states of matter is also relevant for the alpha particle transport that is important for the propagation of fusion process from the hot dense DT fuel to the rest of the target. The alpha particles of ${}^4_2He$ are generated from the fusion reaction ${}^1_2He + {}^1_3He - > {}^4_2He(3.5\text{MeV} + n(14.1\text{MeV}))$. Proton stopping power measurement is the first step to go for alpha particle measurements. Indeed alpha particle stopping power measurement require similar experimental conditions with an additional difficulty to generate a collimate beam of alpha particle with laser.

1.3 Goal of the thesis

This thesis focuses on the physics of intense laser-generated charged particle beam transport investigating two specific topics. The first relates to the transport of MeV electrons produced in intense laser-solid interactions. In particular, the problem of controlling the fast electron divergence or collimation. Controlling electron divergence is critical for electron fast ignition because of the need to heat a small < 40 μm volume of DT fuel to keV temperatures. Indeed, this is perhaps the biggest single challenge for the electron fast ignition scheme. Several methods have been suggested and investigated (external B-fields, multiple resistivity materials, etc.). The related work is focused on a “double-pulse” method which would be valuable because of its simplicity if it can be made to work (it doesn’t require complex targets or external fields). The second topic is ion stopping in WDM. This is important because nearly all laser-produce plasmas go through the WDM state and measurements there can help constrain WDM models which are highly uncertain. A novel method to produce a laser-generated short-pulse quasi-monoenergetic proton beam is described together with its application of proton stopping power measurements in WDM The thesis is organized as follows: the theoretical aspects of laser driven plasma, fast electron generation and transport as well as proton source generating and stopping power are described in the second chapter. The third chapter presents numerical and experimental study of fast electron transport performed on the ELFIE laser facility. And the forth chapter presents the proton stopping power modelling in WDM and detailed design and preliminary results of the experimental campaign performed on the VEGA laser system at the Centro de Laseres Pulsados (CLPU)

in Salamanca Spain which has been focused on ion stopping power measurements in WDM based on the developed proton energy selector system developed in the framework of this thesis.

Chapter 2

Theoretical aspects

In this chapter, the theoretical aspects that are important in this thesis are presented. Its goal is to provide an introduction about laser - plasma interaction and to provide a detailed theoretical description of the laser - driven charge particle generation and transport, in particular, relativistic electron beam (REB) and ion beam projectiles, necessary for understanding the experimental and numerical studies presented later. The introduction consists of three main parts. The first part of the introduction is focused on the description of a plasma, its important parameters and on the different approaches to model it. The second part presents the state of art and the overview of the theory of relativistic electron beam generation and transport in plasma. The third part presents the overview of the laser driven ion acceleration and ion stopping power in extreme states of matter.

2.1 Laser - plasma interaction

2.1.1 Plasma as a medium

A quasi neutral gas of charged and neutral particle which exhibit collective behaviour. One of the biggest complexities of plasma definition comes from the fact that there is no clear phase transition as for other three states of matter. The plasma transition is related to its partial ionization. From another hand, a plasma can be seen as electrically neutral because of the mutual screening of the electric potentials of the ions and of the free electrons. But locally the generated electric fields between the species can lead to spatially limited charge fluctuations. Therefore, a plasma cannot be considered as neutral locally. Then one can use the term of quasi-neutrality $n_e = Z^* n_i$, where n_e and n_i are the electron and ion densities, respectively, and Z^* is an ion charge.

We can say that a plasma is quasi-neutral at macroscopic scales and that the overall interaction energy does not diverge. The quasi-neutrality is nonetheless not presented locally and, as charges move around, they can generate local concentrations of positive or negative charges, which give rise to electric fields. The motion of charges also generates currents and consequently magnetic fields. These fields affect the motion of other distant charges particles. It is this long-ranged Coulomb forces that make a plasma "collective" as motions not only depend on local conditions but also on properties of the plasma in remote regions.

In the following plasma description - the fluid model , when the plasma is simplified as a medium composed of two component fluids and characterized by macroscopic physical quantities for electron and ion density - n_e, n_i, mean velocities - $\mathbf{v_e}$,$\mathbf{v_i}$, temperature - T_e, T_i, as well as the mean ionization degree Z_T.

Before introducing plasma parameter and its description it is important to note the basics of plasma statistics. Let's define the Fermi energy for a given electron system:

$$E_F = \frac{m_e v_F^2}{2} = \frac{\hbar^2}{2m_e}(3\pi^2 n_e)^{2/3} \tag{2.1}$$

where v_F is the Fermi velocity, $\hbar$ is a reduced Plank constant and m_e is the electron mass.

In order to understand which energy distribution can be used for a given plasma one should have a look at the ratio between electron temperature T_e and Fermi temperature $T_F = E_F/k_B$ or between electron kinetic energy E_K and Fermi energy E_F:

1. $T_e \gg T_F$: Maxwell-Boltzmann statistics. In this case, the mean kinetic energy of the nondegenerate free electrons can be written as:

$$E_k = \frac{3}{2}k_B T_e = m_e v_{th}^2 \tag{2.2}$$

   where k_B is the Boltzmann's coefficient and the electron thermal velocity v_{th} is defined as:

$$v_{th} = \sqrt{\frac{k_B T_e}{m_e}} \tag{2.3}$$

2. $T_e \approx T_F$: Fermi-Dirac statistics.

In the experiments described in this thesis the Fermi temperature is estimated as $T_F \approx 0.3 - 0.4$ eV and the electron temperature 20 eV $< T_e <$ 200 eV. Therefore the Maxwell - Boltzmann statistics is applied.

2.1.2 Plasma characteristic lengths

A few characteristic lengths can be defined in a plasma. They play an important role in the characterization of plasma interactions or of the interaction between an external beam and a plasma. Indeed, due to the nature of a plasma and especially because of the property of quasi-neutrality, different types of particle interactions can take place depending on the considered length scale. Locally, particle collisions (Coulomb scattering) are the relevant process, while on a larger spatial scale, collective plasma effects can arise. The hierarchy of the characteristic lengths also allows, in addition to describe the collisional and collective aspects of the plasma interactions, to estimate the strength of the interaction between two particles in the plasma.

De Broglie wavelength

Let's define the system of two plasma particles α and β. Then the relative velocity is $v_r = |v_\alpha - v_\beta|$ and $\mu = m_\alpha m_\beta/(m_\alpha + m_\beta)$ is the reduced mass of the interacting system. The De Broglie wavelength $\lambda\!\!\!^{-}_{Broglie}$ is the distance under which quantum diffraction effects start appearing in the interaction between particles α and β and can be written as:

$$\lambda\!\!\!^{-}_{Broglie} = \frac{\hbar}{\mu v_r} \tag{2.4}$$

where $\hbar$ is the reduced Plank's constant. A De Broglie wavelength can in particular be defined for the plasma electrons, called thermal plasma wavelength and expressed by:

$$\lambda\!\!\!^{-}_{e} = \frac{\hbar}{m_e v_{th}} \tag{2.5}$$

Wigner-Seitz radius

The parameter to define the mean distance a between two plasma electrons is called Wigner-Seitz radius and depends on the electron density:

$$a = \left(\frac{4\pi n_e}{3}\right)^{-1/3} \tag{2.6}$$

Landau length

The minimum distance between two plasma electrons is called the Landau length r_0 and it is defined at a distance which the electron kinetic and potential energies are equal:

$$\frac{mev_e^2}{2} = \frac{e^2}{4\pi\varepsilon_0 r_0} \tag{2.7}$$

where ε_0 is a vacuum permittivity. Then Landau length r_0 is equal to:

$$r_0 = \frac{e^2}{4\pi\varepsilon_0 k_B T_e} \tag{2.8}$$

The generalized Landau length for the interaction between two particles α and β in a plasma with respective charges Z_α and Z_β can be also defined using the same classical approach. Then the generalized Landau length $r_{\alpha\beta}$ is given by:

$$r_{\alpha\beta} = \frac{Z_\alpha Z_\beta e^2}{4\pi\varepsilon_0 \mu v_r^2} \tag{2.9}$$

Debye length

One of the challenges in the theoretical description of plasma is the existence of collective effects arising from the property of quasi-neutrality of the plasma. This fundamental plasma property is a screening of a charge in an ionized medium discovered by Peter Debye and Erich Huckel in 1923. It means that while the electric potential of a charge in a plasma can have a strong local influence, the range stays limited to a plasma region defined by the screening sphere. The radius of this sphere - screening length λ_D characterizes the range of an electric potential in a plasma before it is screened by the surrounding particles. Or in other words its a length beyond which neutrality becomes valid. The screening length is also often referred as the Debye length and it can be obtained for the case of a distribution of electrons by solving the Boltzmann-Poisson equation with suitable boundary conditions:

$$\lambda_D = \sqrt{\frac{\varepsilon_0 k_B T_e}{4\pi e^2 n_e}} \tag{2.10}$$

Evaluating all the constants it can be also rewritten as:

$$\lambda_D[cm] = 743\sqrt{\frac{T_e[\mathrm{eV}]}{n_e[\mathrm{cm}^{-3}]}} \tag{2.11}$$

The number of electrons in the screening sphere is defined as:

$$N_D = \frac{4}{3}\pi n_e \lambda_D^3 \tag{2.12}$$

The screening effect can only be defined if there are enough electrons in the screening sphere $N_D \gg 1$.

2.1.3 Plasma characteristic time lengths

Plasma frequency

The tendency of a plasma to be quasi-neutral can be explored through the study of the electronic response of an electric perturbation inside the plasma : rapid processes would be able to break the neutrality and induce a charge separation and slow processes would let the plasma reorganize itself and suppress the perturbation. This collective effect leads to oscillations of the free electrons similarly to a harmonic oscillator, with a characteristic frequency ω_{pe}:

$$\omega_{pe} = \sqrt{\frac{n_e e^2}{m_e \varepsilon_0}} \tag{2.13}$$

The rapid oscillations of the plasma density characterized by ω_{pe} are called Langmuir waves and correspond to the propagation of plasmons.

Electron - ion collision frequency

The thermal equilibrium in plasma is achieved through collisional energy exchange between the plasma particles. At first, electrons reach their equilibrium temperature T_e , in a second time, ions reach their equilibrium temperature T_i. Then the electron-ion relaxation process starts by means of electron-ion collisions until the thermal electron - ion equilibrium $T_e = T_i$. It is characterized by a collision frequency $\nu_{e,i}$:

$$\nu_{e,i} = \frac{\sqrt{2\pi} Z^2 e^4 n_i \ln\Lambda}{12\pi^2 \varepsilon_0^2 \sqrt{m_e} (k_B T_e)^{3/2}} \propto \frac{n_i}{T_e^{3/2}} \ln(\Lambda) \tag{2.14}$$

This expression works for a classical plasma dominated by weak collisions ($\Gamma_{e,i} \gg 1$) and corresponds to Landau - Spitzer model [[199]]. The collision frequency of electrons with phonons $\nu_{e,ph}$ or electrons $\nu_{e,e}$ can be estimated in a similar manner. The electron collision frequency is an important parameter for the plasma resistivity evaluation explained in the section 2.3.5.

The collision frequency can be used for defining the distance that a particle can travel in the plasma between two successive collisions. This distance is called the mean free path of the particle and it can be expressed as follows for an ion undergoing electron collisions in the plasma:

$$l_{e,i} = \frac{v_{th}}{\nu_{e,i}} \tag{2.15}$$

Coulomb logarithm

From another side interaction processes occurring over distances below the screening length are direct particle interactions, i.e particle collisions or Coulomb scattering. The parameter that defines which kind of effect is dominant is called the impact parameter of interaction b and it roughly the distance between two interacting particles. Let's introduce the parameter that can quantify the importance of small-angle collisions over large-angle collisions, so called "soft" (distant) and "hard" (close) collisions. The aforementioned impact parameter b plays an important role in defining of nature of collisions. For a strongly coupled plasma one finds $b < a$. The minimum value of b - b_{min} is equal to the Landau length $r_{\alpha\beta}$ of the two colliding particles at an angle deflection of 90°. It is a classical distance of minimum approach b_0. Or if quantum effects are important b has a maximum value of b_{max} that is equal to the De Broglie wavelength of the two-particle interaction. One can consequently define the type of collisions by:

1. $b \approx b_{max}$: soft collisions or small-angle scattering.
2. $b \approx b_{min}$: hard collisions or large-angle scattering.

The ratio quantifying the relative importance of small-angle to large-angle scattering is the Coulomb logarithm $\ln\Lambda$:

$$\ln\Lambda = \ln\left(\frac{b_{max}}{b_{min}}\right) = \max\left(\ln\left(\frac{\max(\lambda_D, a)}{\max(b_0, \lambda_{Broglie})}\right), 2\right) \tag{2.16}$$

This parameter defines the dominant collision phenomena in plasma. Its minimum value is often taken as 2 in the literature in order to ensure its positivity.

2.1.4 Plasma parameters

Relation between scale-length define th3 status of plasma. At first approximation two parameters can be defined to describe plasma state: For this purpose, several new parameters are defined: the plasma coupling parameter Γ related to the density effects, the degeneracy parameter Θ related to statistics. The plasma interaction processes can be defined as collisional and collective effects depending on the scale length. For example processes occurring in a scale length larger than the screening length λ_D are referred as collective effects such as the excitation of plasmons or dynamic screening. Simultaneously for the case of a strongly

non-ideal plasma where the screening length is very small (the electric potential of a particle is almost immediately screened), with $\lambda_D < a$, collective effects are defined for interaction distances larger than a.

Plasma coupling parameter

The plasma coupling parameter is defined by the ratio between the density of electrostatic potential energy $< E_p >= e^2/4\pi\varepsilon_0 a$ and the mean density of kinetic energy $< E_k >= k_B T_e$. It measures the strength of electron-electron correlations or of the electron-electron coupling in plasma:

$$\Gamma = \frac{< E_p >}{< E_K >} = \frac{e^2}{4\pi\varepsilon_0 k_B T_e} \sqrt[3]{\frac{4\pi n_e}{3}} \tag{2.17}$$

This parameter allows to distinguish:

1. $\Gamma \ll 1$: Weakly coupled plasmas, for which the kinetic energy of the electrons dominates over their potential energy, which means that the plasma is ideal, collisionless and dominated by long-range collective plasma effects.

2. $\Gamma \gg 1$: Strongly coupled plasmas referred as non-ideal, dominated by interactions between the electrons.

The given expression for Γ is valid as long as the considered plasma is nondegenerate. It is worth to note that the Eq. 2.17 characterizes the the strength of the correlations between electrons - Γ_{ee}. At the same time, in order to define the similar parameter for the correlations between ions Γ_{ii} one should take into account the ionization state $Z\,\Gamma_{ee} = Z^{1/3}\Gamma_{ii}$.

Plasma degeneracy parameter

The plasma degeneracy degree measures the influence of the Pauli exclusion rule on the target electrons and is quantified by the parameter:

$$\Theta = \frac{k_B T_e}{E_F} \tag{2.18}$$

where E_F is the Fermi energy. Θ is the ratio between the kinetic energy of the plasma electrons and their Fermi energy. By using this parameter one can distinguish:

1. $\Theta \gg 1$: Non degenerate plasmas for which the kinetic energy of the electrons dominates over their Fermi energy, obeying classical Maxwell-Boltzmann statistics.

2. $\Theta \leq 1$: Degenerate plasmas, obeying Fermi-Dirac statistics (the effect of Pauli exclusion cannot be ignored). The electron kinetic energy is then expressed as $E_k = k_B T_e + E_F$.

In the case of degenerate plasmas one should re - write the expression for the plasma coupling parameter:

$$\Gamma = \frac{e^2}{a(k_B T_e + E_F)} \tag{2.19}$$

2.1.5 Laser - plasma modelling

In this thesis three different approaches of plasma descriptions are used : hydrodynamic, kinetic and particle in cell (PIC).

Hydrodynamic plasma description

In the hydrodynamic model, the plasma is considered as neutral, made of two different fluids of two species - the electrons and the ions. Each fluid can be described by four hydrodynamic variables: the mass density $\rho_{e,i}$, the average velocity $\mathbf{u_{e,i}}$, the average energy ε, and the pressure P. For both the electron and the ion fluid, the equations of conservation of mass, momentum and energy are written as:

$$\frac{\partial \rho_{e,i}}{\partial t} + \nabla \rho_{e,i} \mathbf{u_{e,i}} = 0 \tag{2.20}$$

$$\rho_{e,i} \frac{\partial \mathbf{u_{e,i}}}{\partial t} + \rho_{e,i} (\mathbf{u_{e,i}} \nabla) \mathbf{u_{e,i}} + \nabla P = \mathbf{F_{ext}} \tag{2.21}$$

$$\begin{aligned} \frac{\partial}{\partial t} \left[\rho_{e,i} \left(\varepsilon + \frac{1}{2} u_{e,i}^2 \right) \right] + \nabla \left[\rho_{e,i} \mathbf{u_{e,i}} \left(\varepsilon + \frac{1}{2} u_{e,i}^2 \right) + P \mathbf{u_{e,i}} \right] = \\ w_V + w_S + q_H + q_{ext} + q_{exhange} + q_{rad} \end{aligned} \tag{2.22}$$

The terms in the right side of the equations 2.21 and 2.22 are the external forces $\mathbf{F_{ext}}$, the volumetric work w_V, the surface work w_s, the heat transport q_H , the external heat q_{ext}, the heat exchanged between the two fluids $q_{exhange}$ and the radiative contribution q_{rad}. In order to find the unknown variables - the plasma physical quantities $\rho_{e,i}$, $\mathbf{u_{e,i}}$, ε, P a forth equation is required. The latter gives a relation between these hydrodynamic variables. Such equation is called Equation of State (EOS) and is usually presented as:

$$\varepsilon = \varepsilon(P, \rho) \tag{2.23}$$

The resolution of the system by means of the EOS requires that the local thermal equilibrium (LTE) condition is achieved, when the collision processes are dominant over excitation and de-excitation processes caused by plasma radiation. In this thesis, LTE regime for the plasma description is assumed. It is based on the following :

1. collision frequency $\nu_{e,i} \gg 1/\tau_H$, where τ_H is a characteristic time of hydrodynamic motion (on ns- scale)

2. $l_{e,i} \ll L_H$, where L_H is a characteristic hydrodynamic length.

For a complete resolution, the heat transport coefficients of the system also have to be determined, and furthermore the hydrodynamic equations have to be coupled to the Maxwell equations, as the external force $\mathbf{F_{ext}}$ and the pressure P may depend on the electromagnetic fields. The plasma hydrodynamic codes are usually based on the solving of the hydrodynamic equations coupled with Maxwell equations in order to predict the evolution of the plasma variables over space and time.

MULTI - 2D and MULTI - fs [172] codes were used to model the plasma expansion in fs and ps time scale.

Kinetic plasma description

The kinetic approach does not require LTE condition and describe a macroscopic plasma system applying statistics. Therefore it is the most complete and precise method of plasma description in a 6-dimensional space. The plasma species j are described by an average distribution function $f_j(\mathbf{r}, \mathbf{v}, t)$ and the temporal evolution of this distribution function is ruled by a kinetic equation for this species. In this approach the Vlasov - Poisson equation system is to be solved. It consist in a set of kinetic equations for the distribution functions of the plasma species combined with the Maxwell equations, or with the Poisson equation (if the magnetic fields are neglected). The kinetic description totally depends on the level of approximation of the plasma interactions. To describe the temporal evolution of a collisionless plasma the kinetic Vlasov equation is employed:

$$\frac{\partial f_j}{\partial t} + \mathbf{v}\frac{\partial f_j}{\partial \mathbf{r}} + \frac{q_j}{m_j}\left(\mathbf{E} + \frac{\mathbf{v}\times\mathbf{B}}{c}\right)\frac{\partial f_j}{\partial \mathbf{v}} = 0 \tag{2.24}$$

where q_j and m_j are the charge and the mass of jth plasma specie and $\mathbf{E}$ and $\mathbf{B}$ are associated with the collective behaviour. From the equation, $f_j(\mathbf{r}, \mathbf{v}, t)$ remains constant while following

a dynamical trajectory. The Vlasov equation combined with Maxwell equation is fully describing the collisionless plasma behaviour. However in order to describe a collisional plasma, a collision integral $(\partial f_j/\partial t)_c$ has to be added to the right side of Vlasov equation. To derive this term one should take into account the considered impact-parameter domain (small-angle or large-angle Coulomb scattering) to choose the right approximation. For soft to moderate collisions, a Landau or Lenard-Balescu collision integral is employed and for the case of moderate to close collisions the Boltzmann collision integral should be used.

Particle in Cell (PIC)

In comparison with the kinetic approach the particle in cell method solves numerically the Newton - Maxwell set of equation by considering the plasma as composed of macro particles. The PIC approach only describes the collective plasma phenomena and not collisional. The PIC evaluates the displacement of particles according to the equations of motion, and the modification of the fields according to the Maxwell equations:

$$\frac{d\mathbf{r_j}}{dt} = \mathbf{v_j} \tag{2.25}$$

$$\frac{d\mathbf{v_j}}{dt} = \frac{q_j}{m_j}\left(\mathbf{E} + \frac{\mathbf{v}\times\mathbf{B}}{c}\right) \tag{2.26}$$

$$\frac{d\mathbf{B}}{dt} = -\nabla\times\mathbf{E} \tag{2.27}$$

$$\frac{d\mathbf{E}}{dt} = \nabla\times\mathbf{B} - \mu_0\mathbf{j} \tag{2.28}$$

where q_j, m_j v_j are the charge, the mass and the velocity of a macro particle, respectively, **E** and **B** are the electric and magnetic fields. The basic scheme of the PIC code can be explained as following: each time step is split into two parts n and $n+1/2$. The part n corresponds to the calculation of the positions and the electric field **E**, and the $n+1/2$ part to the calculations of the velocity and the magnetic field **B**. Then, the position of each particle is modified according to the value of its velocity. Simultaneously this velocity is governed by the equations of motion involving both electromagnetic fields. The variation of the field **B** is obtained from **E** by the equation of Maxwell-Faraday. The variation of the field **E** is derived from the current and the field **B** from the Maxwell-Ampere equation Eq. 2.27, 2.28. This two-stage structure is called leapfrog to show that each magnitude is changed successively instead of modifying them all at once. This is the simplest of methods but it can pose stability problems and requires a fairly short time step to overcome them.

The PIC code Smilei [55] was used to completely evaluate the generation of fast electron beam, simulating the laser - produced electrons acceleration and propagation into the target. The PIC code describes the electron beam generation by the interaction of the laser with the different particles composing the plasma. The output of the PIC code such as the fast electron source energy spectrum and angular distribution can be explicitly injected into a plasma considered fluid in order to perform hybrid simulations.

Hybrid method

The hybrid method is based on using a particle model for fast electrons while treating the rest of plasma with a fluid model. As in PIC code it is necessary to discretize the time according to a step δt and to treat a large number electrons. At the same time, it is necessary to replace the notion of particle by that of macro-particle. The rest of the plasma is not in the form of particles, but simply of current densities and energy. Each spatial mesh has three vectors of current $\mathbf{j}$, electric field $\mathbf{E}$ and magnetic field $\mathbf{B}$. We see that it is possible to easily process the return current, without knowing precisely its microscopic structure. The total current is written $\mathbf{j} = \mathbf{j_b} + \mathbf{j_p}$ where $\mathbf{j_b}$ is the current of the fast electron beam and $\mathbf{j_p}$ is the current of the rest of the plasma. This model was initially proposed by Bell et. *al.* [21] and Davies et *al.* [52] and then improved successively by different authors [126, 49, 102].

Particles and fields change each other. Fields create shifting forces on the particles via the motion equations. Particles generate currents that induce the fields via Maxwell's equations. The fields are generating a Lorentz force that is calculated for each particle, then each particle is moved and diverted accordingly and the current is calculated in each mesh. In the end Maxwell's equations give the new value of the fields:

$$\frac{d\mathbf{B}}{dt} = -\nabla \times \mathbf{E} \tag{2.29}$$

$$\nabla \times \mathbf{B} = -\mu_0 \mathbf{j} \tag{2.30}$$

It's worth to note that the Maxwell-Ampere equation does not contain a time derivative of $\mathbf{E}$ due to the neglect of the transient phase where current neutralization occurs. By repeating this process for each time step, we can simulate the evolution of a large number of particles over time. Meanwhile the rest of the plasma is described by a fluid. The fluid model assumes that no macroscopic material movement has time to occur. The density of the plasma is therefore assumed to be constant. The varying quantities are the atomic number Z, the temperature T_e, the resistivity η and the current $\mathbf{j_p}$. Then we can complete Maxwell's equations presented above by using Ohm's law $\mathbf{E} = \eta \mathbf{j_p}$:

$$\frac{d\mathbf{B}}{dt} = \nabla \times (\eta \mathbf{j_p}) - \nabla \times (\eta \nabla \times \mathbf{B}) \tag{2.31}$$

$$\mathbf{E} = \eta(\nabla \times \mathbf{B} - \mathbf{j_p}) \tag{2.32}$$

The only current remaining in these formulas is that of fast electrons. There is consequently no need to perform a complete treatment of the return current. The latter is automatically eliminated in the equations and it can be found via the field **E**. At each time step the position of each particle is modified according to its velocity, that is governed by the motion equations involving the two electromagnetic fields. The variation of the field **B** is obtained from Maxwell-Faraday equation by means of $\mathbf{j_p}$. The value of the **E** field is derived from **B** and $\mathbf{j_p}$ by the Maxwell-Ampere equation.

In this thesis the Hybrid - PIC code developed by Javier Honrubia [102, 104] is used to simulate the propagation of the fast electron beam with initialized energy distribution function obtained from Smilei PIC simulations.

2.2 Generation and acceleration mechanisms of relativistic electrons in solid target

This section is dedicated to describe the mechanism of laser-driven electron acceleration. During the laser - solid interaction, relativistic electrons are generated through several mechanisms. Electrons whose energy is of the order of the cycle-average oscillation energy in the electric field of the laser in vacuum are called relativistic. To understand the process of electron one e can introduce the different possible laser absorption mechanisms classified as by dominance of the interaction regimes following:

1. $I\lambda^2 \leq 10^{18}$ W/cm$^2\mu$m^2: Non - relativistic interaction regime - collisional or inverse bremsstrahlung absorption mechanisms are dominant.

2. $I\lambda^2 \geq 10^{18}$ W/cm^2 Relativistic interaction regime - hole boring and relativistic $j \times B$ heating absorption mechanisms dominate.

The first regime is taking place in the long pulse (ns) laser solid experiments, meanwhile the relativistic regime takes place in the intense laser-interaction (picosecond and sub-picosecond laser pulses). It's worth to note that this regime started to be accessible after the advent of chirped pulse amplification (CPA) technique developed by Donna Strickland and Gérard Mourou [202]. As far as this thesis is focused on the high intensity laser interactions

with intensities $I \geq 10^{18}\mathrm{W/cm^2}$, we would like to give a fast overview of the existing laser absorption mechanisms paying more attention to the ones that are relevant to this intensity domain.

2.2.1 Laser absorption mechanisms

When an intense laser beam irradiates the surface of a solid target, the ionization process starts. The photons of the laser beam interact with the free electrons that are always present on the surface of a solid due to thermal energy, or to the presence of defects or impurities in the crystal structure. These electrons are accelerated by the electric field of the laser and can therefore ionize atoms on the target surface, whose freed electrons can in turn be accelerated and cause further ionization processes. A thin layer of ionized matter is created on the target surface, that is further heated by the laser light over the whole duration of the laser pulse. However the laser light cannot just penetrate far into the generated plasma in the direction of propagation. Indeed, as as soon as an incoming laser radiation reaches a density n_c for which the plasma frequency ω_{pe} is equal to the (circular) frequency of the laser light ω_L, the latter can not propagate further and is rejected. Then plasma is considered overdense when $\omega_L < \omega_{pe}$, which can also be explained in terms of electron density - $n_e > n_c$. It is expressed by equalling $\omega_L = \omega_{pe}$:

$$\omega_L = \sqrt{\frac{n_c e^2}{\varepsilon_0 m_e}} \tag{2.33}$$

$$n_c = \frac{m_e \varepsilon_0 \omega_L}{e^2} \tag{2.34}$$

$$n_c[\mathrm{cm^{-3}}] = 1.1 \times 10^{21} \left(\frac{1\mu\mathrm{m}}{\lambda_L[\mu\mathrm{m}]} \right)^2 \tag{2.35}$$

where λ_L is the laser wavelength in μm.

We can define the following laser - plasma interaction behaviour:

1. $\omega_L < \omega_{pe}$ or $n_e > n_c$: Laser light is dumped and reflected. No laser can propagate in overdense plasmas. We can also define the plasma skin depth, in which the laser wave is evanescent because of the imaginary values of refraction index $R = \sqrt{1 - n_e/n_c}$. It is also can be explained as a depth where the light is dumped:

$$\delta_s = \frac{c}{\sqrt{\omega_{pe}^2 - \omega_L^2}} \approx \frac{c}{\omega_{pe}} \tag{2.36}$$

2. $\omega_L \geq \omega_{pe}$ or $n_e \leq n_c$: Laser light can propagate and the interaction between the laser field and target particles will occur in the undersense region. This zone, in which the laser can propagate up to the critical layer (surface corresponding to the critical density n_c) is called the plasma corona.

In the relativistic regime, the relativistic effects have to be taken to account in the refractive index $R^{'} = \sqrt{1 - n_e/\gamma n_c}$, where γ is the Lorentz factor. The laser can propagate till the relativistically modified critical density, and this effect is known as self-induced relativistic transparency. The relativistic transparency occurs, when the local laser beam intensity is larger than $10^{18}\mathrm{W/cm^2}$ in the region where $n_c < n_e < \gamma n_c$, a region that is also affected by ponderomotive effects, that will be discussed in the relativistic regime section. Another important parameter can be introduced, the normalized vector potential of the laser pulse a_0:

$$a_0 = \frac{eE}{m_e \omega_L c} \rightarrow a_0 \approx 0.85\sqrt{\frac{I\lambda_L^2[\mu\mathrm{m}^2]}{10^{18}[\mathrm{W/cm^2}]}} \tag{2.37}$$

where E is the laser electric field and I is the intensity of the laser beam $I = \varepsilon_0 c < E^2 > /2$. Then one can write the average Lorentz factor as a function of the normalized vector potential of the laser pulse a_0, $\gamma = \sqrt{1 + a_0^2/2}$ for a linearly polarized laser field and $\gamma = \sqrt{1 + a_0^2}$ for a circular polarization.

Non - relativistic regime

Collisional absorption Collisional absorption, in which a photon is absorbed by an electron while being scattered on a plasma ion is the dominant absorption for laser intensities $\sim 10^{11} - 10^{12}\mathrm{W/cm^2}$. It is also called inverse bremsstrahlung, since it is the opposite process of the electron bremsstrahlung emission. The inverse bremsstrahlung theory can be derived from the Vlasov equation taking into account the distribution function of the electrons and the positions of the ions. One can write the spatial damping rate of the laser beam by inverse bremsstrahlung k_{IB}, that can be derived from the dispersion relation for transversal waves in plasma, obtained by combining the equation of motion and the Maxwell equations for a free charge in vacuum:

$$k_{IB} = \left(\frac{\nu_{e,i}}{c}\right)\left(\frac{\omega_{pe}^2}{\omega_L^2}\right)\left(1 - \frac{\omega_{pe}^2}{\omega_L^2}\right)^{-1/2} \propto \frac{Z^* n_e^2}{T_e^{3/2}}\left(1 - \frac{n_e^2}{n_c^2}\right)^{-1/2} \tag{2.38}$$

where Z^* is the number of free electrons per atom and $\nu_{e,i}$ is the electron-ion collision frequency written in the Spitzer regime of high temperatures by Eq. 2.14.

In order to evaluate the absorption coefficient of this mechanism, we need to consider a laser beam of intensity I passing through a slab of plasma in the z direction. Its attenuation can be estimated as follows:

$$\frac{dI}{dz} = -k_{IB} I \tag{2.39}$$

Then the absorption coefficient α_{IB} for a slab of plasma with a length L is given by:

$$\alpha_{IB} = 1 - \exp\left(-\int_0^L k_{IB} dz\right) \tag{2.40}$$

We can see that there is a strong connection between the plasma parameters n_e , T_e , $\ln\Lambda$ and the absorption coefficient α_{IB}. Therefore the solution of the Eq. 2.39 will depend on the plasma profile . In the case of exponential plasma density profile $n_e = n_c \exp(z/L)$ the absorption coefficient derived in the book of William Kruer [122]:

$$\alpha_{IB} = 1 - \exp\left(-\frac{8}{3}\frac{\nu_{e,i}(n_c L)}{c}\right) \tag{2.41}$$

The inverse bremsstrahlung absorption coefficient has also been derived for the different plasma profiles [147] and laser incidence and polarization.

Resonant absorption This absorption mechanism is effective for pre-plasmas characterized by a long length: $L \gg \lambda_L$ or for larger angles of incidence. In this case the absorption of the laser field consequently becomes non-local, the energy being transported deeper into the plasma. The laser pulse, in oblique incidence and p polarized, propagates up to the electron density $n_e = n_c \cos^2\theta_0$. The longitudinal electric field induced by the interference of the incident and reflected waves will excite an electronic pulsation plasma wave ω_L in the direction of the normal which, at the critical surface, where $n_e = n_c$ becomes resonant ($\omega_L = \omega_{pe}$). For a linear density profile and a p-polarized laser, the absorption coefficient has been calculated :

$$\alpha_{RA} = 36\tau^2 \frac{|Ai(\tau)|^3}{|Ai'(\tau)|} \tag{2.42}$$

where Ai and Ai' are respectively the Airy function and its derivative and τ is expressed as a function of the laser wavelength λ_L and laser incidence θ_0 angle [63, 165]:

$$\tau = \left(\frac{2\pi L}{\lambda_L}\right)^{2/3} sin^2\theta_0 \tag{2.43}$$

In the case of a laser pulse arriving at normal incidence on the target surface $\theta_0 = 0°$, resonant absorption can still be significant if the plasma is weakly magnetized or if the critical density surface is rippled [48]. It is especially the case for long-pulse irradiation where density instabilities of the critical surface have time to develop. It is worth to mention that this mechanism is the predominant mechanism for intense long-pulse lasers.

Apart from inverse bremsstrahlung and resonant absorption, other absorption mechanisms exist. They arise through parametric instabilities and consist in the coupling of the laser light with various plasma waves. Unlike the resonant absorption, they can also take place in a homogeneous plasma, i.e without density gradient. These are (i) stimulated Raman scattering (SRS), in which the laser beam couples with a Langmuir wave, (ii) stimulated Brillouin scattering (SBS), in which it couples with an ion acoustic wave, (iii) parametric decay where a laser photon is converted into a plasmon and an ion acoustic wave, and (iv) two-plasmon-decay for which a photon decays into two Langmuir waves.

Relativistic regime

Pondemorotive force Let us introduce the ponderomotive force that describes the motion of the guiding center of a charged particle in a non-uniform, alternating electric field, over a timescale longer than the oscillation period. Such a force is nonlinear and rises as a function of the spatial and temporal profile of laser intensity [153]. The vector potential envelope is assumed to be sufficiently smooth in space and time. By considering the problem of a single electron oscillation in a quasi-monochromatic electromagnetic field (field of a a linear polarized laser) we can write its relativistic kinetic energy averaged over an oscillation period:

$$E_K = m_e c^2(\gamma - 1) = m_e c^2 \left(\sqrt{1 + \frac{a_0^2}{2}} - 1 \right) \tag{2.44}$$

The pondemorotive force can be written as:

$$\mathbf{F_p} = -\nabla E_k = -m_e c^2 \nabla \left(\sqrt{1 + \frac{a_0^2}{2}} - 1 \right) \tag{2.45}$$

This force is responsible for the generation of a very steep density gradients and charge separation that lead to the creation of the electrostatic field on the back surface of a target that can accelerate ions by so called Target Normal Sheath Acceleration (TNSA) [135]. Because of the ion movement, the ponderomotive effect is also directly involved in the hole boring mechanism where the laser pulse is responsible for the inward movement of

the target surface [221]. In the relativistic regime, electrons are not only radially ejected from the laser propagation axis, but they also acquire a longitudinal momentum due to the magnetic contribution of the Lorentz force. In underdense plasmas, where the laser pulse can propagate, the ponderomotive force created by charge displacements triggers longitudinal electrostatic waves that can be used to trap and accelerate electrons up to GeV energies [128]. The amplitude of oscillations of electrons in the laser field is v_{quiv}/ω_L, where the quiver velocity of electrons in the electromagnetic field of the laser is given as:

$$v_{quiv} = \frac{eE_L}{\gamma m_e \omega_L} \tag{2.46}$$

Vacuum heating The vacuum heating mechanism was proposed by Brunel [34]. Vacuum heating is responsible for the acceleration of electrons up to energies close to the ponderomotive potential from Eq. 2.45. Let's consider the interaction of a linearly polarized (p-polarized) laser pulse focused at very high intensities with a steep density gradient at an oblique incidence with the angle θ_0. Due to the steep gradient and the increase of laser intensities, the laser electric field is sufficiently intense to drag out into vacuum a fraction of electrons initially heated in the target skin depth, beyond the Debye screening length, during a half-period of the pulse. Unlike resonant absorption, the laser field does not drive any plasma wave. During the second half-period of the pulse, the electrons are redirected back to the target accelerated by the electric force created by charge separation. Then the adiabaticity of electron motion is broken at the moment when they cross the plasma skin layer and they acquire the kinetic energy gained from the electric force. In this model the capacitor model was use for the electric field expression. The laser energy absorption for this mechanism can be estimated by considering that the accelerated electron mean kinetic energy is given by the ponderomotive potential and that all electrons propagate into the depth of the solid target after being re-injected [85]:

$$\alpha_{VH} = \frac{1}{\pi a_0}\beta\left(\sqrt{1+(\beta a_0 \sin\theta_0)^2}-1\right)\frac{\sin\theta_0}{\cos\theta_0} \tag{2.47}$$

where $\beta = 1+\sqrt{1-(4a_0\sin^3\theta_0/\pi\cos\theta_0)}$. The fast electron temperature has been assumed as:

$$T_h \approx \left(\sqrt{1+\frac{v_e^2}{c}}-1\right)m_e c^2 \approx \left(\sqrt{1+4a_0^2}-1\right)m_e c^2 \tag{2.48}$$

Gibbon et al. [86] performed the numerical simulation to study the nature of vacuum heating mechanism as a transition from the resonant absorption mechanism. It was found

that the maximum absorption takes place at the laser incidence angle of $\Theta_0 \approx 45^\circ$ as shown in Fig. 2.1

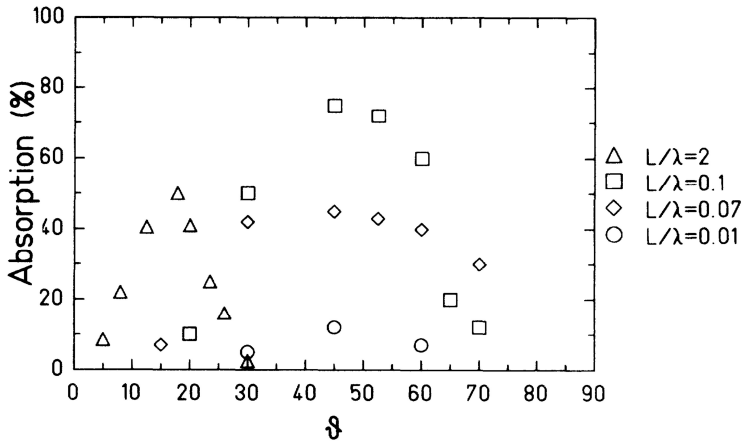

Fig. 2.1 Absorption vs obliquity for p-polarized light for the density profiles (simple linear ramps) shown are $L/\lambda_L = 2$ (triangles), $L/\lambda_L = 0.1$ (squares), $L/\lambda_L = 0.07$ (diamonds), and $L/\lambda_L = 0.01$(circles). Parameters common to each case were $I\lambda_L^2 = 10^{16}\mathrm{W/cm^2}\mu\mathrm{m}^2$, $n_e/n_c = 2$, $T_e = 1$ keV. Graph and legend are taken from [86].

Indeed, the use of the capacitor model means that the magnetic fields are neglected, that makes this absorption mechanism not valid for the high intensity laser fields $I > 10^{18}\mathrm{W/cm^2}$, where the generated magnetic fields deflect electron orbits by the $\mathbf{v} \times \mathbf{B}$ component of the Lorentz force.

Relativistic j × B heating The so-called $\mathbf{j} \times \mathbf{B}$ heating was introduced by W. Kruer *et al.* [124]. In contrast to vacuum heating it takes to account the magnetic fields and become the main absorption mechanism at laser intensities $I\lambda_L^2 \geq 10^{18}\ \mathrm{W/cm^2}\mu\mathrm{m}^2$. First, by considering an incident laser pulse on a solid target, all charged particles, independently of their charge, are pushed away from the high intensity laser regions, both radially and inside the target. However, as seen before, the ponderomotive force is proportional to the inverse of the mass of the particle and the resulting effect is small on ions. Consequently, a charge separation occurs and an electric field drives ions at higher time scales, of the order of several ps. This effect is directly involved in the so-called hole boring process that has been demonstrated experimentally at laser intensity of $10^{18}\mathrm{W/cm^2}$ [108] and causes the inward movement of the target surface [221]. This is due to the light pressure in the plasma which is higher than the thermal pressure and thus pushes the critical density surface.

In this regime, the $\mathbf{v} \times \mathbf{B}$ component of the Lorentz force creates an oscillating component of the ponderomotive force in Eq. 2.45 for a p-polarized laser pulse that can lead to laser energy absorption: during a quarter of the laser optical cycle, electrons from the plasma surface are ejected into vacuum by this force, then a strong electrostatic field is generated due to the induced charge separation ; during the following quarter of the laser cycle, electrons are recalled back to the surface being accelerated by the electrostatic field. Bunches of electrons accelerated up to several MeV are then re-injected into the target at each half laser period. This effect is more efficient at normal incidence angle of the laser pulse, and with increasing laser intensity. The numerical simulations performed by S. Wilks *et al.* [221] have shown that the temperature of accelerated electrons is close to the ponderomotive potential Eq. 2.44:

$$T_{\mathbf{j}\times\mathbf{B}} \simeq m_e c^2 \left(\sqrt{1 + \frac{a_0^2}{2}} - 1 \right) = m_e c^2 (\sqrt{1 + 0.73 I_{18} \lambda_L^2 [\mu\mathrm{m}]} - 1) \tag{2.49}$$

where laser intensity I is expressed in the 10^{18} W/cm^2.

2.2.2 State of the art of relativistic laser driven electron acceleration

Laser to electron conversion efficiency

For the last decade numerous experiments were carried out on to measure the radiation emitted by electrons when interacting with matter allowing to estimate the conversion efficiency from laser absorbed energy to electrons. The measured efficiency at a laser intensity of 3×10^{19} W/cm^2 using K_α emission, was evaluated to 25 % [158, 219]. The Bremsstrahlung emission measurement coupled to numerical simulations have shown that the conversion can reach values of the order of 40-50 % at a higher laser intensity of 3×10^{20} W/cm^2 [95]. The experimental measurements of the conversion efficiency were performed varying laser intensities from 10^{18} W/cm^2 to 3×10^{20} W/cm^2 and seem to follow the scaling with the intensity. The conversion efficiency was seen to increase from 10 to 50 % [et al.]. However, these works did not consider the fast electron refluxing at the target rear-side which amplifies the emission caused by electrons and consequently artificially increases the conversion efficiency. Recent experiments with laser intensities $> 10^{19}$ W/cm^2 evaluated the conversion efficiency to 30-40 % [79, 157, 42]. The experimental studies pointed out that the conversion efficiency is depends on:

- Laser intensity
- Hydrodynamic state of the plasma

- Laser contrast [187]
- Laser beam incidence angle [51]

The published data of absorption values as a function of $I\lambda_L^2$ are shown in Figure 2.2. Here the solid black symbols are experimental and numerical results from [167]: normal or near normal incidence of 6°(circles), oblique incidence of 30° or 45° (squares) and vertical lines join numerical results with the lower values for short pre-plasma and the upper values for long pre-plasma. The solid black (upper) curve is a fit to the experimental results [86]. The hollow blue symbols are results from other numerical modelling following the same convention. The solid red crosses and boxes are results for fast electron absorption from the Nova laser, boxes delimiting a group of points [207]. The solid red (lower) curve is a fit to the Nova results [84]. Dashed black crosses and boxes are results for fast electron absorption from other experiments.

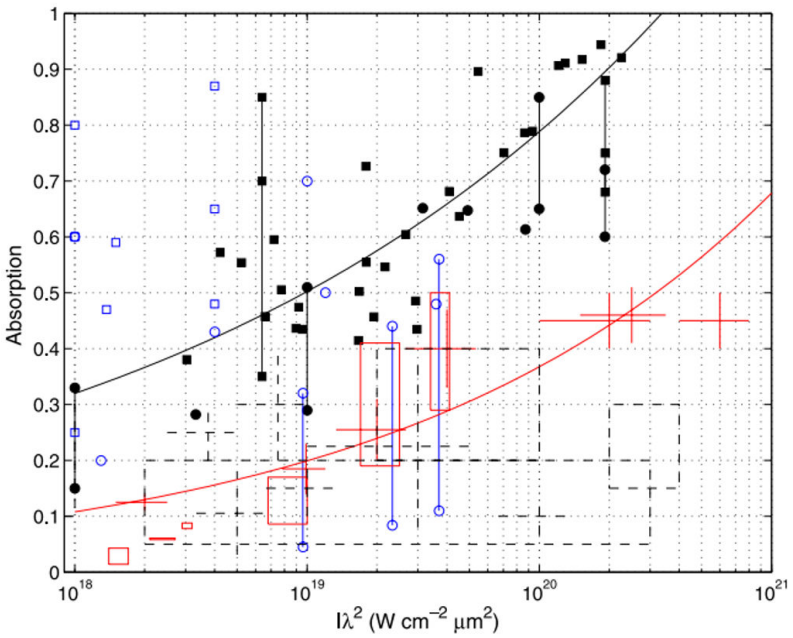

Fig. 2.2 Experimental and numerical absorption as a function of $I\lambda_L^2$ [52]. Explanations about the meaning of the different symbols can be found in the text.

Two experimental fits were done by J. Davies [51] following the experimental results shown on the Figure 2.2. The increase in absorption with $I\lambda_L^2$ can be shown by finding the coefficients A and p for the function $(I\lambda_L^2/A)^p$. The best fit for the results of [167] was found as:

$$f_{abs}^{(a)} = \left(\frac{I\lambda_L^2}{3.37 \times 10^{20} \mathrm{W/cm^2 \mu m^2}} \right)^{0.1958} \tag{2.50}$$

For second group of results of [207] we have:

$$f_{abs}^{(b)} = \left(\frac{I\lambda_L^2}{4.3 \times 10^{21} \mathrm{W/cm^2 \mu m^2}} \right)^{0.2661} \tag{2.51}$$

The fits are valid for $I\lambda_L^2$ in the range from $2-3\times10^{18}$ to $2-3\times10^{20}$ $\mathrm{W/cm^2 \mu m^2}$. The absorption coefficient given in Eq. 2.50 is more appropriate for high laser contrast conditions ($10^{-6}-10^{-8}$) and the second one given in Eq. 2.51 works better for a lower laser contrast ($10^{-3}-10^{-4}$). Both fits are shown in the Figure 2.2 as black curve and red curve for the $f_{abs}^{(a)}$ and $f_{abs}^{(b)}$ respectively. A more general conversion efficiency from laser energy to fast electrons following the results of [111] is given by:

$$\eta_L = 1.2 \times 10^{-15} \left(I[\mathrm{W/cm^2}] \right)^{0.74} \tag{2.52}$$

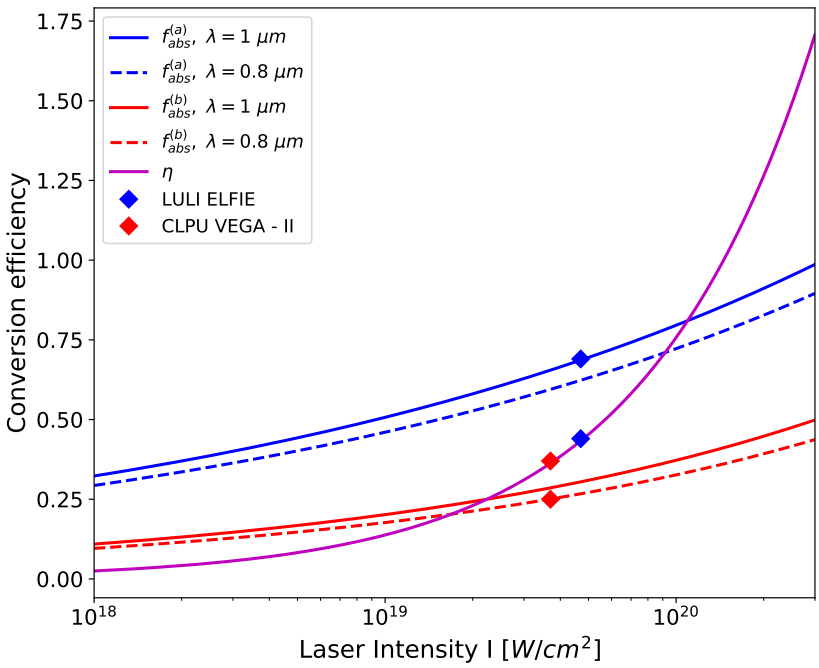

Fig. 2.3 Conversion efficiency as a function of the laser intensity calculated with $f_{abs}^{(a)}$ for a laser wavelength $\lambda_L = 1.024$ μm (blue solid line), $\lambda_L = 0.8$ μm (blue dashed line) and $f_{abs}^{(b)}$ (red solid and dashed lines) respectively. The violet line corresponds to the generalized conversion efficiency η_L.

Figure 2.3 represents the evaluated conversion efficiency for two laser wavelengths corresponding to the experiments carried on for this thesis at the LULI ELFIE ($\lambda_L = 1.024\ \mu$m) and CLPU VEGA - II ($\lambda_L = 0.8\mu$ m) laser facilities using three experimental fits. Taking into account the laser contrast condition we can choose the fit that works better for each case. Particularly the ELFIE laser system has a moderate laser contrast and $f_{abs}^{(a)}$ is chosen (blue solid line) while CLPU VEGA - II has lower laser contrast that corresponds to the fit of $f_{abs}^{(b)}$ (red dashed line). The typical laser intensities for both experiments are marked as blue diamonds for LULI ELFIE and red diamonds for CLPU VEGA-II. It is easy to see that the fits $f_{abs}^{(a)}$ and η_L are giving a discrepancy of ~ 25 % for the LULI ELFIE laser intensity. For the case of VEGA-II laser intensity the difference is not so drastic ~ 12 %. Clearly, there will be always an error of the conversion efficiency estimation depending which expression is chosen.

As mentioned before the conversion efficiency depends on several effects and therefore is strongly dependent on the absorption mechanism . It is very complex and still remains an open question for the laser - plasma interaction community. The best fits are found for specific cases of the experimental measurements performed at different laser system and various laser - plasma interaction conditions in order to estimate the conversion efficiency. We can also deduce the total number of electrons using the following formula:

$$N_0 = \frac{\eta_L E_L}{c\tau_L \pi R_0^2 k_B T_{hot}} \tag{2.53}$$

where η_L is the laser to electron conversion efficiency, E_L and τ_L are the laser pulse energy and duration, respectively, R_0 the electron beam radius and T_{hot} the electron temperature discussed in the following subsection.

Hot electron temperature

One the most important and still open issues in laser-driven electron acceleration is the determination of the hot electron temperature and number of particles. This can be done by deducing the scaling of hot electron temperature from laser intensity. Yet there is no consistent analytical model that can accurately predict the scalings seen in experiments and simulations for both non relativistic and relativistic intensities This is partly due to the fact the temperature depends on the pre-plasma scale length, intensity and polarization of the laser pulse, and on the aforementioned absorption mechanisms of laser energy by electrons, such as resonance absorption, skin layer heating, Brunel heating, and $v \times B$ heating. However early experiments and simulations confirmed that the fast electron energy was consistent with the pondemorotive scaling firstly proposed by [221]. A useful metric to quantify the

hot electrons consists in using the slope of the hot electron energy distribution, hereafter referred to as the effective electron temperature, T_{hot}. Assuming that the slope of measurable electron energy is similar to that which extends to lower energies inside the target, one can infer the T_{hot} of the electrons generated from the laser target interaction. Then the measured electron spectra is commonly fitted with the relativistic Maxwellian distribution with the electron temperature T_{hot} that has several forms. One of the forms presented below is in a good agreement with experimentally measured spectra [223]:

$$f(E) = N_0 E^2 \exp\left(-\frac{E}{T_{hot}}\right) \tag{2.54}$$

where N_0 is number of electrons, E the electron energy. In the literature, different distribution forms could be found due to the different acceleration mechanisms of the fast electron population. For example, the two temperature distribution corresponds to the weighted sum of a colder part at moderate energies ($\geq$ 10 keV) and hotter part at higher energies ($\geq$ 100 keV). Recent experiments showed that the colder part of the electron distribution is better fitted with a power law instead of an exponential law [174, 144, 212]. The total fast electron distribution can be presented as:

$$\begin{cases} f(E) = \left(\dfrac{E_0}{E}\right)^{\alpha}, \ 0.01 < E < 5 \text{ MeV} \\ f(E) = N_0 \exp\left(-\dfrac{E}{T_{hot}}\right), \ 5 \leq E \leq 20 \text{ MeV} \end{cases} \tag{2.55}$$

The ponderomotive scaling proposes the scaling of the fast electron temperature with laser intensity as [221] also called Wilks's law:

$$T_{hot}^{Wilks}[\text{keV}] = 511 \left(\sqrt{1 + \frac{I_{18}\lambda_{\mu m}^2}{1.37}} - 1\right) \tag{2.56}$$

where I_{18} is the laser intensity in the units of 10^{18}W/cm^2 and the wavelength $\lambda_{\mu\text{m}}$ is in μm.

This scaling was proposed to be valid when the laser plasma interaction density was close to the critical density. Depending on laser prepulse conditions, spot size, energy, and pulse length this constraint may be satisfied for a wide range of intensities. Another empirical scaling was proposed by F. Beg *et al.* [19] based on an experimental study with a wide range of laser intensities, using the measured Bremsstrahlung emission:

$$T_{hot}^{Beg}[\text{keV}] = 215 \left(I_{18}\lambda_{\mu m}^2\right)^{1/3} \tag{2.57}$$

This law is however valid for the laser intensities up to 5×10^{18} W/cm$^2\mu$m^2. For laser intensities $I\lambda_L^2 = 1 \times 10^{19} - 1 \times 10^{20}$ W/cm$^2\mu$m^2 the ponderomotive scaling given in Eq. 2.56 is more consistent with the experimental results. Recent experiments performed at different laser facilities in the period of the rise of interest to the fast ignition approach to ICF reported more reasonable scaling laws fitting experimental measurements under various laser and target conditions. Besides the laser intensity, quantities such as the laser incidence angle on target, the laser pulse duration and the pre - plasma conditions were carefully studied. H. Chen *et al.* [43] reported some discrepancy between measured electron spectra in the range between $0.1 - 4$ MeV and pondemorotive potential energies , especially at higher intensities. The experimental measurements were performed at two laser facilities (RAL VULCAN PW and LLNL Calisto) using p - polarized laser pulse varied in a wide range of intensities and irradiating different target materials. A fit to the experimental data at high intensities up to 8×10^{20} W/cm^2 revealed that the scaling of hot electron temperature is proportional to the 0.34 power of the laser intensity:

$$T_{hot}^{Chen}[\text{keV}] \approx \left(I\lambda_{\mu m}^2\right)^{0.34\pm0.04} \tag{2.58}$$

It was also observed that for the same intensity the electron distribution does not vary with the change of target material.

The experimental measurements at RAL VULCAN PW and GEKKO GXII PW made by Tanimoto *et al.* [Tanimoto et al.] performed in the intensity range of $10^{18} - 10^{21}$ W/cm^2 also confirmed the clear departure from the pondemorotive scaling as well as a good consistency with Chen's fit (Eq.2.58). A least square fit to the experimental data shows that the fast electron temperature scales as:

$$T_{hot}^{Tanimoto}[\text{keV}] = 400\left(I_{18}\lambda_{\mu m}^2\right)^{1/3} \tag{2.59}$$

As was mentioned before the effect of the preplasma tends to increase the mean kinetic energy of accelerated electrons [159]. A recent scaling law obtained by Kluge *et al.* [113] took into account the preplasma. This scaling required a special Lorentzian scalar steady state distribution function. It is written in terms of laser strength parameter $a_0 = \left[2I/(n_c m_e c^3)\right]^{1/2}$ where $n_c = m_e\varepsilon_0\omega_0^2 e^{-2}$ is a critical density of the cold plasma :

$$T_{hot}^{Kluge}[\text{keV}] = 1000 \times 2\pi\left[\int_0^{2\pi}(1 + a_0^2\sin^2\omega_0 t)^{-1/2}dt\right]^{-1} - 1 \tag{2.60}$$

This law is in good agreement with the ponderomotive scaling for moderate intensities $I < 10^{19}$ W/cm^2 while correcting the overestimation of the ponderomotive scaling for higher intensities.

Another formulation of the scaling law can be given by taking to account the aforementioned fast electron distribution composition of a colder and hotter parts. It can be used for a wide intensities range:

$$T_{hot}[\mathrm{keV}] \approx max\left[T_{hot}^{Wilks}, T_{hot}^{Beg}\right] \tag{2.61}$$

As was mentioned before the reported scaling laws are in good consistency with experimental data for the sub-picosecond short laser pulses. However these scallings are no longer applicable to multi-picosecond (multi-ps) laser experiments. Here, the production of relativistic electrons (RE) was experimentally investigated via multi-ps relativistic laser–plasma-interaction (LPI). The recent experiment of S. Kojima *et al.* [119] reported that the lower slope temperature shows little dependence on the pulse duration and is close to the ponderomotive scaling value, while the higher slope temperature appears to be affected by the pulse duration. The higher slope temperature is far beyond the ponderomotive scaling value, which indicates super-ponderomotive REs (SP-REs). SP-RE acceleration is started when the plasma thermal pressure exceeds the laser ponderomotive pressure. The quasi-static magnetic field generated at the critical density surface starts to re-inject electrons into the region where the laser field and quasi-static electric fields coexist. The RE acceleration mechanism with re-injection has been investigated as loopinjected direct acceleration (LIDA). In particular, Krygier et al [125] predicted that the super-ponderomotive REs (SP-REs) can be accelerated by multi-ps LPI via the LIDA mechanism.

Fast electron divergence

Fast electron beam divergence is one of the major issues encountered in fast ignition. The divergence of the electron beam is mainly attributed to the development of the Weibel instability at the target surface. It is however fairly complicated to theoretically calculate the fast electron divergence. Several experiments were performed to characterize the divergence of the electrons accelerated into the target. Green *et al.* [88] reported the increase of divergence with $I\lambda_L$ and a clear independence of the laser pulse duration. The divergence angle was estimated from the slope of the plotted K_α spot FWHM as a function of the target depth as $2 \times \arctan(s)$, where s is the slope (Figure 2.5).

It was determined from spatially resolved measurements of x-ray K_α emission and from transverse probing of the plasma formed at the rear side of the targets. The least squares fit

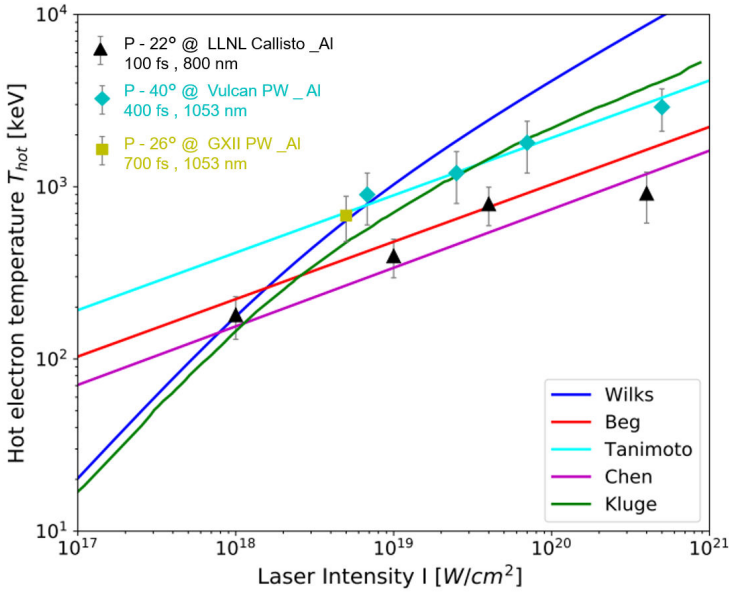

Fig. 2.4 Fast electron temperature T_{hot} scaling law obtained from 2.56 (blue), 2.57 (red), 2.60 (green), 2.59 (cyan) and 2.58 (magenta). Experimental results obtained using three different laser systems are shown: LLNL Jupiter Laser Facility Callisto Laser (black triangles) [43], RAL VULCAN PW (green diamonds) and GEKKO XII LFEX Petawatt (yellow squares).

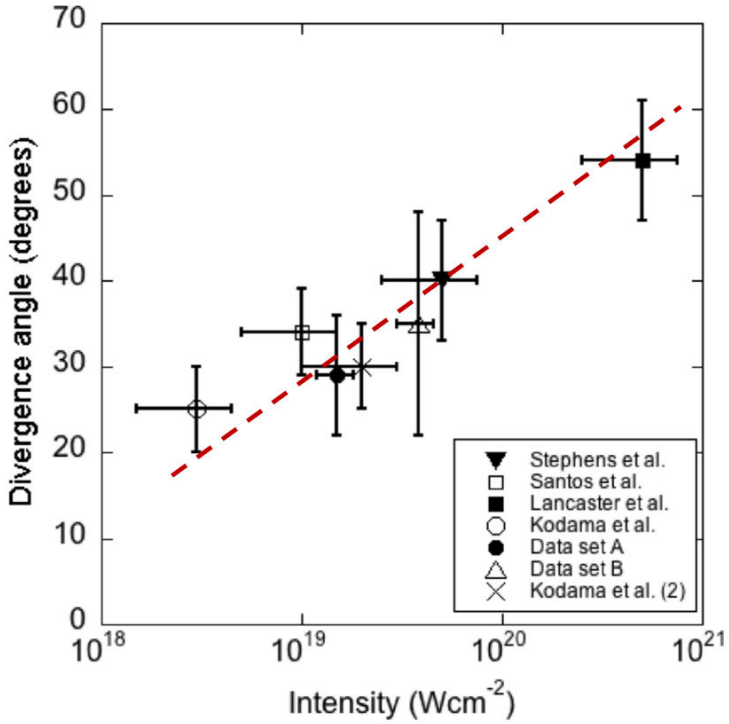

Fig. 2.5 Electron beam divergence as a function of the laser intensity on target [88], along with other data published in the literature [[127, 186, 117, 118]. It is assumed that the error bars in the other published work are similar, as the techniques employed are comparable.

of the experimental results summarized by Green *et al.* gives us the following empirical law to estimate the electron beam divergence as a function of the laser intensity:

$$\theta_{1/2} \approx (17 \pm 3.8)^{\text{deg}} + (13 \pm 2.5)^{\text{deg}} \log\left(\frac{I}{10^{18}\text{W/cm}^2}\right) \tag{2.62}$$

where $\theta_{1/2}$ is the divergence half angle (Figure 2.6).

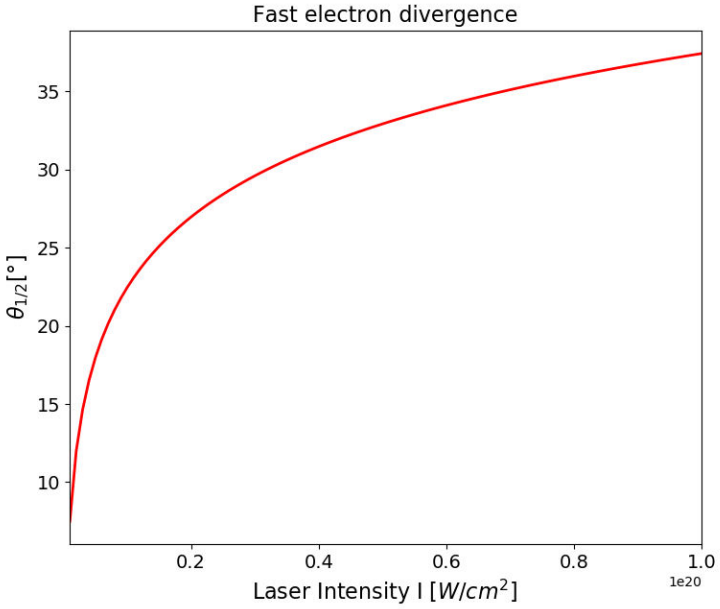

Fig. 2.6 Fast electron divergence half - angle as a function of the laser intensity calculated from a least square fit of the experimental results 2.62.

Recent studies report that the pre-plasma can strongly affect the electron divergence due to the modification of the laser-plasma interaction region. The Figure 2.7 shows the additional parameters of the electron angular distribution introduced by A. Debayle *et al.* [54] such as $\theta_0(r)$ is the mean propagation angle of electrons at the radial distance r and $\Delta\theta_0$ is the mean dispersion angle around the direction defined by $\theta_0(r)$. It seems, that the divergence increases with the radial distance respect to the laser-spot center - that corresponds to the center of the electron source. Then the fast electron angular distribution can be expressed using the following function:

$$f_\theta \approx \exp\left[-\left(\frac{\theta - \theta_0(r)}{\Delta\theta_0}\right)^2\right] \tag{2.63}$$

The mean propagation angle is defined by formula:

$$\theta_0(r) = \arctan[\tan(\xi)r/R_0] \tag{2.64}$$

where R_0 is the initial electron beam radius.

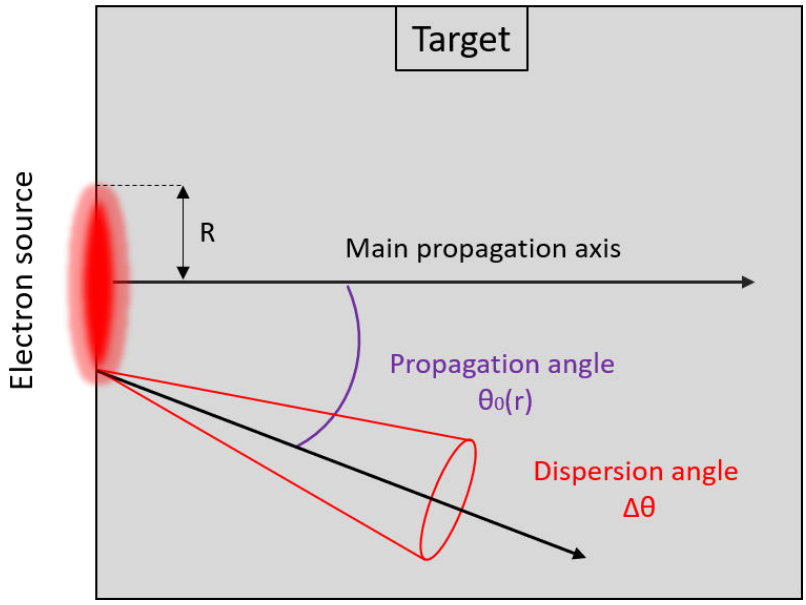

Fig. 2.7 Scheme illustrating the propagation and dispersion angles.

The preplasma also affects the initial radius of the fast electron beam which is evaluated empirically to range between 3-4 times the focal spot radius.

2.3 Fast electron transport

2.3.1 Angular scattering

Fast electron beams propagate into the target at relativistic velocities much greater than background electron or ion velocities suffering the principal effects of collisions: energy losses and angular scattering. Let's consider elastic collisions. It is then important to introduce first a simple description of elastic collision occurring from the interaction between a fast electron and an immobile point-like ion (much heavier the electron with a mass ratio ≈ 1836). As a result of this collision the trajectory of the incident electron changes while its energy remains approximately constant. The electron is angularly scattered from its initial trajectory. In this case the ion gains a small fraction of the incident electron energy. One can introduce the cross section that describes the probability of a single collision. The expression for the relativistic cross section (corrected classical Rutherford cross section) was firstly

obtained by B. Nigam *et al.* [156] by using a quantum approach based on the first Born approximation which considers a small angle deviation and a moderate Z target and given by:

$$\left(\frac{d\sigma}{d\Omega}\right)_i = 4r_e^2 \frac{Z^2}{\beta^4\gamma^2}\left(\frac{1}{4\sin^2(\theta/2)+{\theta_0}^2}\right)^2 \tag{2.65}$$

where $\theta_0 = \alpha Z^{1/3}/(0.885\gamma\beta)$ is a screening angle with $\alpha = e^2(4\pi\varepsilon_0 hc)$ the fine constant and γ is the Lorentz factor. Let's consider the situation for which an entire fast electron beam scatters over a large number of ions while propagating inside the target, that is a case of multiple scattering. Multiple scattering theory [146] had been introduced by G. Moliere *et al.* and completed by H. Bethe [26], which has the advantage of being fully analytic even if restricted to the small angle approximation. The electron diffusion angle is given as:

$$\sqrt{\langle\theta^2\rangle} = \theta_c\sqrt{\ln 2 \ln\left(\frac{{\theta_c}^2}{1.167{\theta_M}^2}\right)} \tag{2.66}$$

The θ_c defines the probability of a single scattering event at angle $> \theta_c$ takes place over the unit of length s:

$$\theta_c = 4\pi n_i s Z(Z+1)\left(\frac{r_e}{\gamma\beta^2}\right)^2 \tag{2.67}$$

with n_i the atomic number of the material and r_e is classical radius of an electron.

The screening angle θ_M is given by:

$${\theta_M}^2 = {\theta_0}^2\left[1.13+3.76\left(\frac{Z\alpha}{\beta}\right)\right]^2 \tag{2.68}$$

However, this theory is only valid when considering the propagation of electrons in a cold non-ionized matter. The work of L. Gremillet [89] reports an estimation of the screening angle taking to account the plasma ionization depending on its temperature, which is the case of the heated target in our experiments. It is worth to note that the mean deviation angle increases with the penetration range s and with the background electron temperature T_e and decreases when the energy of the incident electron increases. The propagation of high energy electrons (> 500 keV) is not so much influenced by elastic collisions. As we are interested in relativistic electrons, it is clear that the dispersion angle is determined mainly by the laser-plasma interaction, and less by elastic electron-ion collisions along their transport into the target depth.

2.3.2 Collisional stopping power

The propagation of the fast electron beam inside the target is basically determined by its collisions with other particles, that would slow it down. As was mentioned before the collisions with background ions is elastic and do not contribute significantly to the electron energy loss. Therefore the main source of the energy loss is collisions with other electrons. The electron collisional stopping power with background electrons can be written as:

$$\frac{dE}{ds} = -Z(\gamma-1)m_e c^2 n_i \int_0^{1/2} \varepsilon \frac{d\sigma}{d\varepsilon} d\varepsilon \tag{2.69}$$

with n_i the density of atoms, $E = (\gamma-1)m_e c^2$ the energy of incident electron, $\varepsilon = \Delta E/E$ the fraction of transferred energy and therefore $\dfrac{d\sigma}{d\varepsilon}$ the energy transfer differential cross section.

To calculate the energy loss contribution due to the collisions of free electrons with bound electrons ($\varepsilon > \varepsilon_c$) and free electrons with screened free electrons ($\varepsilon < \varepsilon_c$) it is necessary to introduce the parameter:

$$\varepsilon_c \approx \left(\frac{b_{e,min}}{b_{e,max}}\right)^2 = \left(\frac{max(r_0, \lambda\!\!\!^{-}_{Broglie})}{D}\right)^2 \tag{2.70}$$

where r_0 is the Landau length, $\lambda\!\!\!^{-}_{Broglie}$ calculated in the center of mass frame $M = \hbar/m_e c\sqrt{2(\gamma-1)}$ and $D = max(\lambda_D, r_e)$ is an effective Debye length.

When the incident electron propagating in cold matter transfers a part of its energy to an atomic bound electron, the collision leads to atomic excitation - the jump of the bound electron from an atomic level to another one. Therefore the energy loss has to be calculated taking to account the binding energies of the bound electrons and all the contributions of the excited quantum states. The Bethe stopping power formula can be written as [25]:

$$\left(\frac{dE}{ds}\right)^{cold}_{bound} = -ZEn_i \int_0^{\varepsilon_c} \varepsilon \frac{d\sigma}{d\varepsilon} d\varepsilon = -En_i Z\sigma_e \left[\ln\left(\frac{2\varepsilon_c(\gamma^2-1)(\gamma-1)}{(I_0/m_e c^2)^2}\right) - \beta^2\right] \tag{2.71}$$

where $\sigma_e = 2\pi r_e^2/\beta^2(\gamma-1)$ is the electron characteristic cross section , $r_e = e^2/4\pi\varepsilon_0 m_e c^2$ is the electron classical radius and the mean ionization potential is:

$$\ln I_0 = \sum_n f_n \ln E_n \tag{2.72}$$

where the excitation energy E_n is weighted by the oscillator strengths f_n. There are several approximations to evaluate the ionization potential. For $Z \geq 13$ the semi - empirical formula

obtained by [200] works in the cold matter case:

$$I_0[\mathrm{eV}] \approx 9.76Z + 58.9Z^{-0.19} \tag{2.73}$$

The stopping power due to the scattering with background free electrons in cold matter can be obtained by integrating Eq. 2.69, where the integration is from ε_c to $1/2$ that considers only binary collisions:

$$\left(\frac{dE}{ds}\right)^{cold}_{free} = -En_i Z\sigma_e \left[\ln\frac{1}{4\varepsilon_c} + 1 - \frac{2\gamma-1}{\gamma^2}\ln 2 + \frac{1}{8}\left(\frac{\gamma-1}{\gamma}\right)^2\right] \tag{2.74}$$

The total stopping power in the cold matter then is given by the sum of 2.71 and 2.74 [178, 195]:

$$\left(\frac{dE}{ds}\right)^{cold}_{total} = -En_i\sigma_e Z \left[\ln\left(\frac{(\gamma^2-1)(\gamma-1)}{2(I_0/m_e c^2)^2}\right) 1 - \beta^2 - \frac{2\gamma-1}{\gamma^2}\ln 2 + \frac{1}{8}\left(\frac{\gamma-1}{\gamma}\right)^2 - \delta\right] \tag{2.75}$$

To account for the polarization electric field which screens the incident electron field at the position of the projectile, an additional parameter δ has been introduced. The so called density effect leads to a decrease of the electron stopping power, especially for high energy electrons propagating at the same speed as the polarization wave $c/\sqrt{\varepsilon_r\varepsilon_0}$, with ε_r the relative dielectric permeability of the medium. It was derived by [70] in the limit of an ultra-relativistic electron projectile:

$$\delta = 2\ln\left(\frac{\gamma\hbar\omega_{pe}}{I_0}\right) - \beta^2 \tag{2.76}$$

An approximate analytic formula for the parameter δ was further derived for a relativistic electron [201] in the case of bound electrons:

$$\delta = \begin{cases} 0 & \text{if } X \leq X_0 \\ 4.606X + C + a(X_1 - X)^m & \text{if } X_0 < X < X_1 \\ 4.606X + C & \text{if } X \geq X_1 \end{cases} \tag{2.77}$$

The parameters X, C and a are given by:

$$\begin{aligned} X &= \log \gamma\beta \\ C &= -2\ln I_0/(h\omega_{pe}) \\ a &= -(C+4.606X_0)/(X_1-X_0)^m \\ m &= 3 \end{aligned} \tag{2.78}$$

The parameters X_0 and X_1 are defined as:

$$X_{0,\ I_0<100\text{ KeV}} = \begin{cases} 0.2 & \text{if } -C < 3.681 \\ -0.326C - 1 & \text{if } -C \geq 3.681 \end{cases} \tag{2.79}$$

$$X_{0,\ I_0>100\text{ KeV}} = \begin{cases} 0.2 & \text{if } -C < 5.215 \\ -0.326C - 1.5 & \text{if } -C \geq 5.215 \end{cases} \tag{2.80}$$

$$X_1 = \begin{cases} 2 & \text{if } I_0 < 100\text{ KeV} \\ 3 & \text{if } I_0 > 100\text{ KeV} \end{cases} \tag{2.81}$$

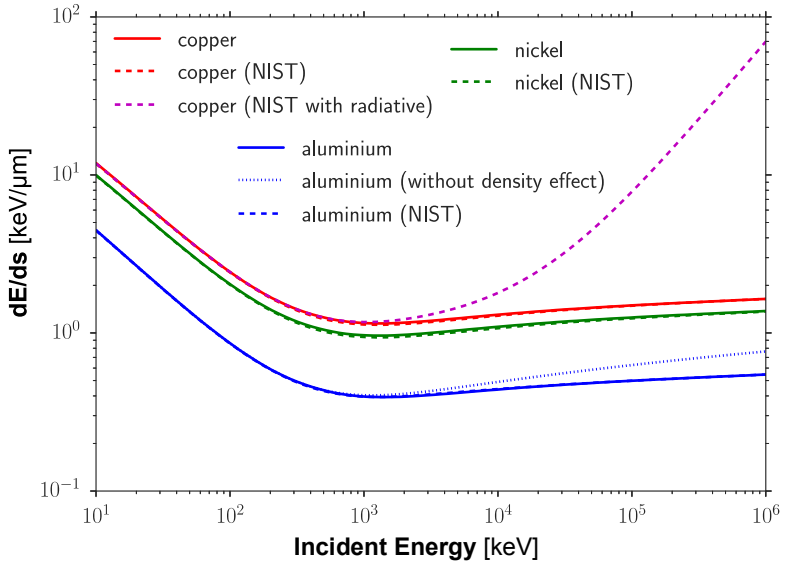

Fig. 2.8 Total stopping power at solid densities for cold copper (red), aluminium (blue) and nickel (green). The results are compared with the NIST-Estar database. The dashed magenta line corresponds to copper from the NIST database, including effects of radiative stopping power. The dotted blue line stands for an aluminium case for which the density effects are not taken into account. The graph and legend is taken from [9].

The stopping power formula must be modified for the case when matter starts to be hot and therefore partially ionized. We have to take to account the collisions with free electrons along with the contribution of bound electrons. Using a Thomas-Fermi model [105] a formula for the ionization potential can be derived for a hot plasma at any charge state:

$$I_0^{hot}[\text{eV}] \approx 10Z\frac{\exp[1.29(Z^*/Z)^{0.72-0.18(Z^*/Z)}]}{\sqrt{1-(Z^*/Z)}} \tag{2.82}$$

Then the formula 2.71 for energy losses due to collisions with bound electrons in ionized matter case is defined as:

$$\left(\frac{dE}{ds}\right)_{bound}^{hot} = -En_i(Z-Z^*)\sigma_e\left[\ln\left(\frac{2\varepsilon_c(\gamma^2-1)(\gamma-1)}{(I_0/m_ec^2)^2}\right)-\beta^2\right] \tag{2.83}$$

where Z^* - the ionization degree, characterizing the number of electrons which actually remain bound to the nucleus.

Energy losses due to collisions with the Z^* free electrons is also very similar to 2.74 with minor modifications:

$$\left(\frac{dE}{ds}\right)_{free}^{hot} = -En_iZ^*\sigma_e\left[\ln\frac{1}{4\varepsilon_c}+1-\frac{2\gamma-1}{\gamma^2}\ln 2+\frac{1}{8}\left(\frac{\gamma-1}{\gamma}\right)^2\right] \tag{2.84}$$

Another contribution to the stopping power of electrons in plasmas is due to the electron driven plasma waves. The corresponding contribution to the stopping power can be written as [166]:

$$\left(\frac{dE}{ds}\right)_{plasmon}^{hot} = -En_iZ^*\sigma_e\ln\left[1+\left(\frac{v_e}{\omega_{pe}\lambda_D\sqrt{3/2}}\right)^2\right] \tag{2.85}$$

with v_e the incident electron speed and ω_{pe} the electron plasma frequency. Then the total collisional stopping power in hot matter finally can be written as a sum of the three contributions:

$$\left(\frac{dE}{ds}\right)_{total}^{hot} = \left(\frac{dE}{ds}\right)_{bound}^{hot} + \left(\frac{dE}{ds}\right)_{free}^{hot} + \left(\frac{dE}{ds}\right)_{plasmon}^{hot} \tag{2.86}$$

Figure 2.9 represents these three contributions and their sum for a copper plasma at $T_e = T_i = 10$ eV (solid lines) and $T_e = T_i = 1000$ eV (dashed lines), at solid density. The contribution of bound electrons is seen to vanish when reaching background temperature in excess of ≈ 1 keV.

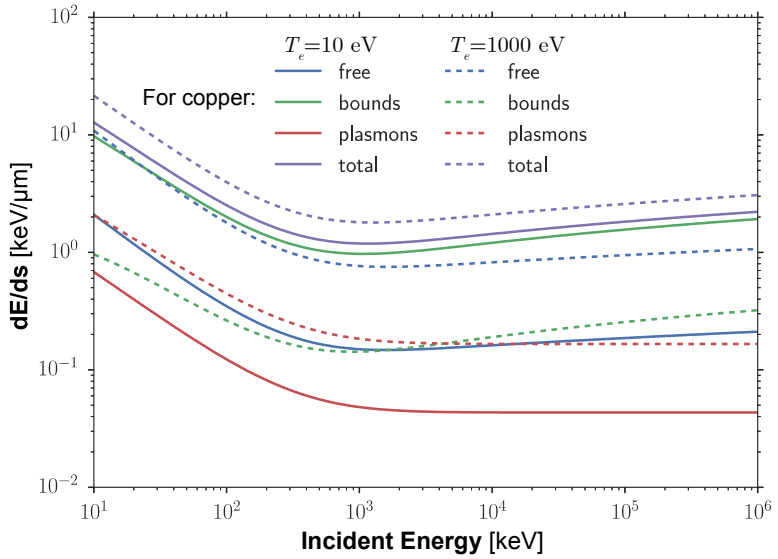

Fig. 2.9 Different contributions of the total stopping power in ionized copper at solid density. The solid lines correspond to$T_e = T_i = 10$ eV while the dashed lines correspond to $T_e = T_i =$ 1000 eV. The graph and legend is taken from [9].

2.3.3 Collective electron transport

The propagation of fast electrons in dense matter cannot be only described as a sum of physical phenomena associated with each particle. In addition to the energy losses of each electron separately the collective processes provide a contribution proportional to the fast electron current.

2.3.4 Neutralization of relativistic electron beam: Alfvén limit and return current

The propagation of a relativistic electron beam in a dense plasma will generate an electric field due to the negative charge accumulation that will expel radially the background thermal electrons out of the beam and generate a return current. The return current $\mathbf{j_e}$ will tend to compensate the beam current density $\mathbf{j_e} \approx -\mathbf{j_b}$. This charge compensation is of a time scale of $\tau_{neut} \sim \max[1/\nu_{ei}, 1/\omega_{pe}]$, with ν_{ei} the electron ion collision frequency and ω_{pe} the plasma frequency. The combined flux of a large number of fast electrons generates an intense current, $I_b \simeq N_b e/\tau_L \approx 1$ MA in the experimental conditions described in this thesis with N_b the number of fast electrons and τ_L the laser pulse duration. This current creates a magnetic field that pinches the electron beam by itself. The generated pinching magnetic field deviates the beam from the initial propagation direction and consequently prevents the

beam propagation into the target [8]. This return current is also referred to the Alfvén limit current [92] and is given by:

$$I_A = \frac{4\pi m_e c}{e\mu_0}\gamma_b\beta_b \approx 17\gamma_b\beta_b[\text{kA}] \tag{2.87}$$

In order to derive this maximum current one should consider a relativistic electron beam of radius R_0 and of uniform density across its propagation direction and characterized by a current I.. The generated electron beam current drives a magnetic field B_I at the edge of a beam given by :

$$B_I = \frac{\mu_0 I}{2\pi R} \tag{2.88}$$

The Larmor radius of a single electron propagating with a momentum $p = \gamma m_e v_e$ into this field is given by:

$$r_L = \frac{\gamma m_e v_e}{eB_I} \tag{2.89}$$

The Alfven limit current can be derived by equalling the Larmor radius to the electron beam radius $r_L = R/2$.

This limit that would prevent the propagation of MeV - energy relativistic electron beam with MA-currents is evaluated without considering the previously already mentioned neutralization current. The net total current density $\mathbf{j} = \mathbf{j_b} + \mathbf{j_e}$ decreases rapidly to lower values due to the beam neutralization. A perfect neutralization of the beam is however never reached completely and its efficiency depends on the ratio between the radius of the beam and the skin depth R_0/λ_e. When this ratio is < 1 the return current is able to counter the beam current within the magnetic field region and the neutralization is efficient. In our experiments, this can be considered as always fulfilled, except for the very beginning of the injection.

The time scale of the neutralization is given by the magnetic diffusion time:

$$\tau_D = \frac{\mu_0 R_0^2}{\eta} \tag{2.90}$$

where η is the resistivity of the background plasma. In the LULI - ELFIE experimental campaign we have $\tau_D \sim 5$ ps and the neutralization is considered efficient.

2.3.5 Resistivity effects

The collective mechanisms acting on fast electron propagation in plasmas directly depend on the plasma electric resistivity. This parameter plays a major role in relativistic electron

energy losses and has a big variation with a change of target temperature. One should consider the electron collision frequency parameter that describes the plasma resistivity and plasma conductivity. Several models have been proposed to infer the collision frequency as a function of the electron temperature. The main attention will be concentrated on the Eidmann-Chimier model [62, 44] that was used in the numerical simulations for this thesis.

Electric resistivity

The Drude model describes the electric resistivity where valence electrons are considered as free to move into the material, colliding with fixed ions. The resistivity can be written as:

$$\eta = \frac{m_e \nu_e}{e^2 n_e} \tag{2.91}$$

with ν_e the background electron relaxation rate or collision frequency. This is an important parameter to be evaluated in order to know the electrical resistivity on a wide range of background electron temperatures. This parameter is determined for two temperature ranges delimited by the Fermi temperature $T_F = E_F/k_B$ with the Fermi Energy $E_F = \hbar^2(3\pi^2 n_e)^{2/3}/(2m_e)$: Then ν_e is dominated by :

- electron - phonon collisions for low temperatures $T_e << T_F$
- electron - electron collisions for moderate temperatures $0.1T_F < T_e < T_F$
- collisions described by the Spitzer model for high temperatures $T_e >> T_F$

Then for the low temperatures $T_e << T_F$ which is the case of cold - solid material the electron - phonon collision frequency was obtained as [224]:

$$\nu_{e,ph} \approx \frac{k_S e^2 k_B T_i}{2\pi\varepsilon_0 \hbar^2 \mathrm{v}_F} \tag{2.92}$$

with T_i the ion temperature, the Fermi velocity $\mathrm{v}_F = \sqrt{2E_F/m_e}$ and k_S is a tabulated constant depending on the considered material and used to adapt the previous expression to measured values of cold metals. For materials used in our experiment we have k_s(aluminium) ≈ 1.25 and k_s(copper)≈ 0.37. Also it is worth to note that this formula is valid only in thermal equilibrium case $T_e = T_i$.

At moderate temperatures $0.1T_F < T_e < T_F$, the material is ionized and the electron-electron collisions become the dominant process:

$$\nu_{e,e} = A_\nu \frac{k_B T_e^2}{\hbar T_F} \tag{2.93}$$

with A_ν a fitting parameter ranging from 1 to 1000. For aluminium and copper one obtains A_ν (aluminium) $= 1$ and A_ν (copper) $= 10$ [44].

At high temperatures, the collision frequency is described by the Spitzer model, considering a Maxwellian background electron distribution [199]:

$$\nu_{sp} = \frac{4}{3}\sqrt{2\pi}k_{sp}\frac{Z^* e^4 m_e n_e}{(4\pi\varepsilon_0)^2(m_e k_B T_e)^{3/2}}\ln\Lambda \tag{2.94}$$

with k_{sp} a a dimensionless parameter equal to $3\pi/32$ and $\ln\Lambda$ the Coulomb logarithm.

The Spitzer collision frequency decreases rapidly with the electron temperature with a power of 3/2. However, the Spitzer model is not valid at low electron temperatures, close to the Fermi temperature, when both the electron degeneracy effects and ion correlations are taking place in material. In order to find the collision frequency in between the regime below the Fermi temperature (scaling as T_e^2) and the Spitzer regime (scaling as $T_e^{-3/2}$) we have to note that the mean free path λ_e of an electron around the maximum value of ν_e can not be smaller than the atomic inter-distance r_i at a characteristic electron velocity chosen as a combination of the Fermi velocity and the electron thermal velocity $\mathrm{v}_{ch} = \sqrt{\mathrm{v}_F^2 + \mathrm{v}_{T_e}^2}$. The maximum collision rate was introduced by K. Eidmann *et al.* [62]:

$$\nu_c = \frac{\mathrm{v}_{ch}}{r_i} \tag{2.95}$$

The interpolation expression for the collision frequency given by Eidmann and modified by Chimier [44] is written as a weighted average of the electron relaxation rate at different temperature regimes:

$$\nu_e^{-2} = (\nu_{e,ph} + \nu_{e,e})^{-2} + \nu_c^{-2} + \nu_{sp}^{-2} \tag{2.96}$$

The resulting collision frequencies for solid copper and aluminium are plotted in the Figure 2.10 as a function of electron temperature.

2.3.6 Resistive heating

The heating of the target by collisions will induce a resistive process which also contributes to the electron energy losses. The already mentioned return current is responsible for the target heating by the collisions of thermal electrons that constitute it. If the electron beam current is high enough ($j_b \geq 10^{10} - 10^{11}\mathrm{A/cm^2}$), the counter return current will be also high enough to heat significantly the target and the resistive losses become non negligible and can even exceed the collisional losses. To describe the collective stopping power one should assume the rigid beam approximation which implies a fixed current density. This strong assumption,

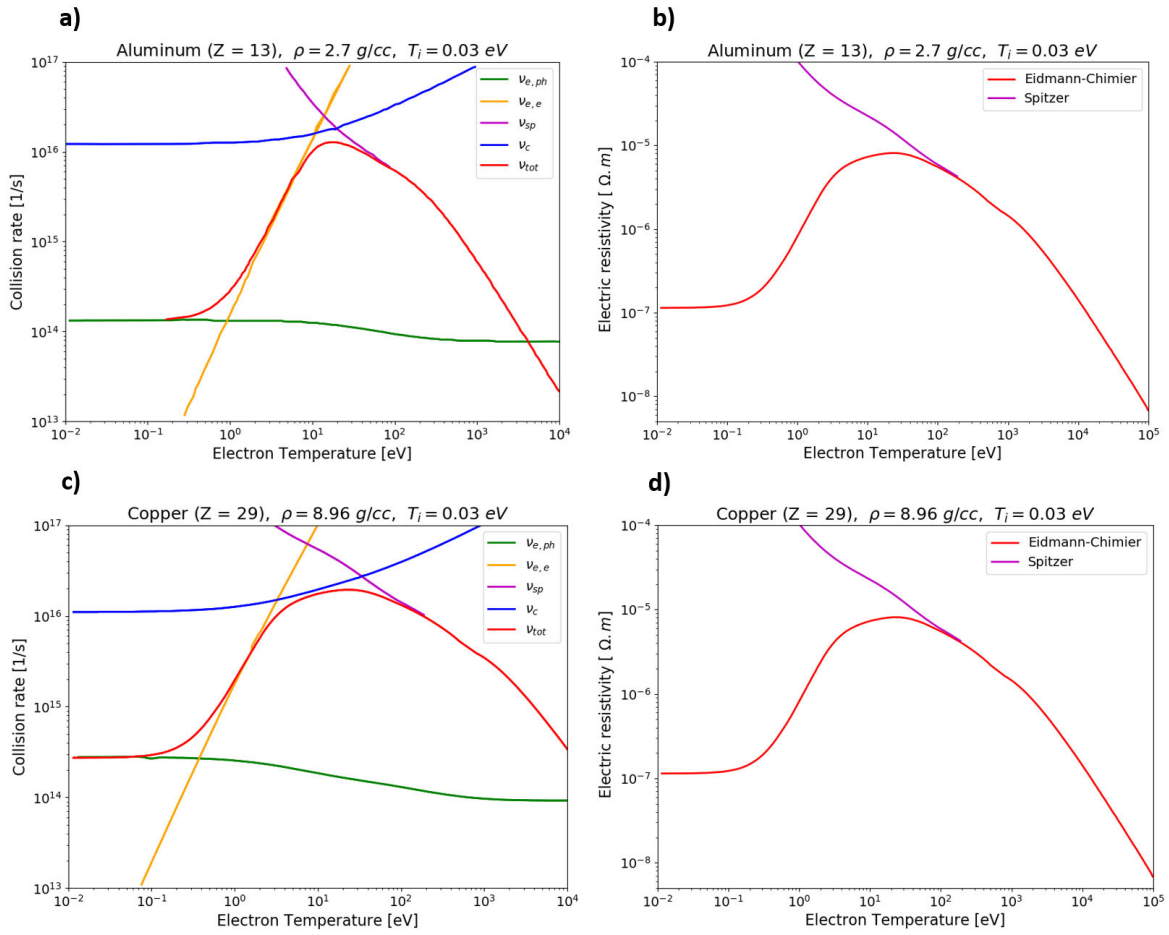

Fig. 2.10 Collision frequency ν_e and its different components (see Eq. 2.96) as a function of the background electron temperature assuming an ion temperature $T_i = 0.03$ eV for aluminium (a) and copper (c). Electric resistivity (see Eq.2.91) obtained by the Eidmann-Chimier model (red curve) and Spitzer model (violet curve) for aluminium (b) and copper (d) respectively.

which does not allow to model the dynamic of fast electron beams, is sufficient to derive rough estimations on fast electron beam energy losses. This model [133] modified by [89] is based on the solution of the energy conservation equation separately for the contribution of the magnetic field of the beam $\mathbf{B}_b$ and of the plasma $\mathbf{B}_p$ linked by $\mathbf{B}_b = -f\mathbf{B}_p$, with f the neutralization rate. The energy conservation equation is given by the Poynting theorem:

$$\frac{\partial E_{b,p}}{\partial s \partial t} = \int \mathbf{j_{b,p}} \mathbf{E} dS \tag{2.97}$$

The rigid beam is assumed to be collimated and its spatial distribution is characterized by a Gaussian shape (in the transverse plan). We also consider a monoenergetic electron beam propagating at the speed $\beta_b c$. After integration over time, the amount of energy per unit of length lost in the electromotive field is given by:

$$\frac{dE_b}{ds}(t) = \frac{I_b^2}{4\pi\varepsilon_0 c^2} \ln\left(1 + 2\frac{t}{\tau_D}\right) \tag{2.98}$$

where $I_b = e\pi r_b^2 n_b \beta_b c$ the fast electron current and τ_D the magnetic diffusion time.

Then the resistive energy transferred to the plasma via the Joule's effect can be written:

$$\frac{dE_p}{ds}(t) = \frac{1}{2}\frac{I_b^2}{4\pi\varepsilon_0 c^2} \ln\left(1 + 4\frac{t}{\tau_D}\right) \tag{2.99}$$

We can also deduce the plasma temperature, by using a model of an ideal electron gas for the electrons of the beam:

$$\frac{dE_p}{ds} = \frac{3}{2} n_p k_B T_e \pi R_0^2 \tag{2.100}$$

The evolution of the temperature as a function of time is then given by:

$$T\,[\mathrm{eV}] \approx 400\beta_b^2 \left(\frac{Z^* n_i}{6\times 10^{22}\mathrm{cm}^{-3}}\right)^{-1} \left(\frac{n_b}{10^{20}\mathrm{cm}^{-3}}\right)^2 \left(\frac{\eta}{10^{-6}\Omega\mathrm{m}}\right) \left(\frac{\Delta t}{500\mathrm{fs}}\right) \tag{2.101}$$

To obtain the resistive heating we can also use an approximation of the current neutralization $\mathbf{j_b} = -\mathbf{j_r}$ and by neglecting both thermal conduction and neutralization [50]. The energy conservation law can be written as :

$$C_e \left(\frac{\partial T_e}{\partial t}\right)_{res} = -n_b v_b \left(\frac{dE}{ds}\right)_{res} = \mathbf{j_r}\mathbf{E_r} = \eta j_b^2 \tag{2.102}$$

with the thermal capacity C_e at a constant volume, v_b and n_b the electron beam velocity and density, respectively.

Let's compare the contribution of resistive heating by the electron beam with collisional energy losses. The energy conservation equation to both collisional and resistive processes yields the total energy deposition:

$$C_e\left(\frac{\partial T_e}{\partial t}\right)_{res} = -n_b \mathrm{v}_b \left(\frac{dE}{ds}\right)_{res} - n_b \mathrm{v}_b \left(\frac{dE}{ds}\right)_{coll} = \eta j_h^2 + \frac{j_b}{e}\left(\frac{dE}{ds}\right)_{coll} \tag{2.103}$$

with $(dE/ds)_{coll}$ is given by Eq. 2.75 in the case of a cold material keeping only the logarithmic term. Then the energy deposition by collisional processes can be written:

$$C_e\left(\frac{\partial T_e}{\partial t}\right)_{coll} = n_b v_b \left(\frac{dE}{ds}\right)_{coll} = \frac{2\pi r_e^2 Z m_e c^2 v_b n_i n_b}{\beta_b^2(\gamma_b - 1)} \ln\left(\frac{(m_e c^2)^2(\gamma_b^2 - 1)(\gamma_b - 1)}{2I_0^2}\right) \tag{2.104}$$

We can see that the collisional heating scales as j_b while resistive heating scale as j_h^2 [Eq. 2.103]. The resistive heating will be the dominant heating term at high current density, for example at the front side of a target. The decrease of j_b as the fast electron beam propagates into the target related to the inherent fast electron energy losses and to the beam divergence inverts this trend, making collisional heating the dominant heating mechanism. The ratio between collisional to resistive losses is given by:

$$R_{coll/res} = \frac{\partial_t T_e|_{coll}}{\partial_t T_e|_{res}} = \frac{2\pi r_e^2 Z m_e c^2 v_b n_i}{\beta_b^2(\gamma_b - 1) e \eta j_b} \ln\left(\frac{(m_e c^2)^2(\gamma_b^2 - 1)(\gamma_b - 1)}{2I_0^2}\right) \tag{2.105}$$

The ratio $R_{coll/res}$ is shown in Figure 2.11 as a function of fast electron current density, for aluminium at solid density and T_i = 0.03 eV. The resistivity is computed using Eidmann-Chimier model [44]: $\eta = 2.3 \times 10^{-6}$ Ωm for T_e = 10 eV (green colour curves) and $\eta = 3.3 \times 10^{-8}$ Ωm for T_e = 100 eV (magenta colour curves). The ratio is calculated for two different fast electron temperatures valid for our experiment T_b = 500 keV (solid curves) and T_b = 1000 keV (dashed curves). Globally the resistive heating become preponderant at current density in excess of 10^{11} - 10^{12}A/cm^2

2.3.7 Self - induced magnetic fields

The propagation of a fast electron beam in dense plasma induces intense electromagnetic fields which can greatly affect the beam propagation itself. The nature of self-generated fields effects over the transport of a fast electron beam is a complex picture to draw as it

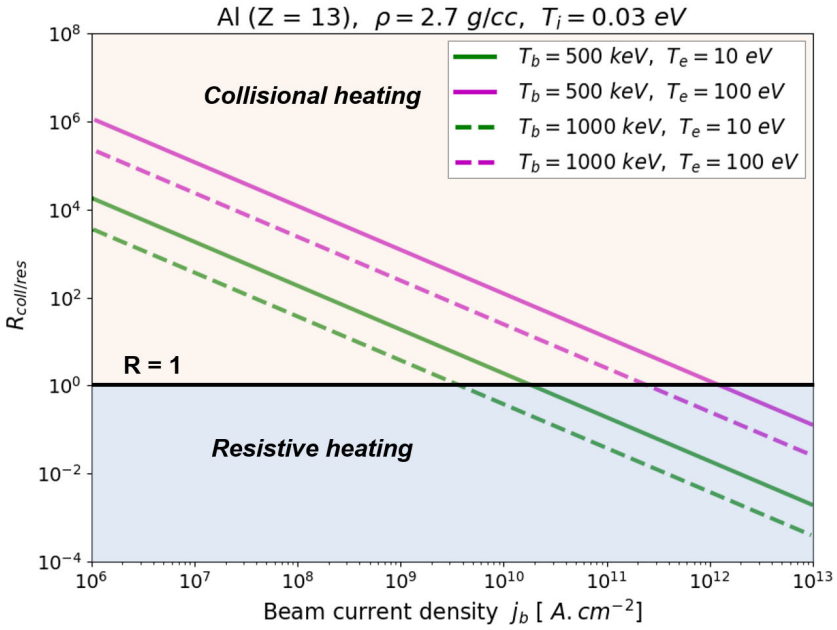

Fig. 2.11 Ratio between collisional and resistive losses as a function of beam current density. The ratio is obtained for two the beam temperatures T_b and background electron temperatures T_e. The resistivity is computed using the Eidmann-Chimier model [44] at $T_i = 0.03$ eV

affects the electron beam both positively (it can compensate the divergence of the beam and self-focalize it) and negatively (divergence or instabilities and filamentation). To describe self generated magnetic fields we firstly need to introduce the generalized Ohm's law and Maxwell-Faradays's law [155]:

$$\mathbf{E} = -\eta \mathbf{j_b} + \frac{\eta}{\mu_0} \nabla \times \mathbf{B} + \frac{1}{e n_e} \nabla (n_e T_e) \tag{2.106}$$

$$\frac{1}{c} \frac{\partial \mathbf{B}}{\partial t} = -\nabla \times \mathbf{E} \tag{2.107}$$

This equation remains valid under the assumption of a fast electron beam duration longer than the charge neutralization time, and shorter than the magnetic diffusion time. By combining two equations we get:

$$\frac{\partial \mathbf{B}}{\partial t} + \frac{\partial}{\partial \mathbf{r}} \times \left[\frac{\eta}{\mu_0} \nabla \times \mathbf{B} \right] = \eta \nabla \times \mathbf{j_b} + \nabla(\eta) \times \mathbf{j_b} + \frac{1}{n_e e} \nabla(n_e) \nabla(T_e) \tag{2.108}$$

The magnetic field formation and evolution is due to three main effects . The first term is a curl of the current that is responsible of self-collimation of the fast electron beam. The second term stands for the generation of magnetic fields by resistivity gradients, which can

be produced due to inhomogeneous compression or specific target designs and/or heating of the medium. This term can also collimate or deflect the electron beam by variation of a sign of the resistivity gradients. The third term is the thermoelectric effect. The first two terms can be used to reduce the intrinsic divergence of fast electron beams. The collimation by self - generated fields is a major topic of this thesis and will be discussed in the next section. The the maximum electric and magnetic field amplitudes can be estimated as a function of the laser intensity I_0, pulse duration τ_L , plasma resistivity η, the fast electron beam radius R_0 and of the laser-to-fast electrons conversion efficiency η_L [52]:

$$E_{max}[\mathrm{V.m^{-1}}] \approx 6\times 10^9 \left(\frac{\eta}{2\times 10^{-6}\Omega\mathrm{m}}\right)\left(\frac{\eta_L}{0.3}\right)\left(\frac{I_L}{10^{17}\mathrm{W.cm^{-2}}}\right)\left(\frac{1\mu\mathrm{m}}{\lambda_L}\right)^{2/3} \tag{2.109}$$

$$B_{max}[\mathrm{T}] \approx 3.83\times 10^{-8} E_{max}[\mathrm{V.m^{-1}}]\left(\frac{2\tau_L}{1\mathrm{ps}}\right)\left(\frac{10\mu\mathrm{m}}{r_b}\right) \tag{2.110}$$

This works only with assumption that the laser pulse has a Gaussian time and space profile. For the experiment performed at the LULI - ELFIE laser facility reported in this thesis the laser intensity does not exceed $I_L = 10^{18} - 10^{19}\mathrm{W/cm^2}$ and therefore the electromagnetic effects are expected to dominate over the collisional effects.

2.3.8 Electron beam collimation schemes

Reducing electron beam divergence as well as optimizing electron beam transport in plasmas is crucial for several important application: i) In proton acceleration induced by laser it has been proven that a transversal confinement of the electron beam increases the maximum energy of the proton beam; ii) In the fast ignition approach to ICF electron beam collimation is crucial for the success of the scheme. Previous investigations have shown that the dynamics of electron beams propagation in plasmas is mainly affected by: i) resistivity effects [215, 214, 212, 188, 210, 189, 168, 17, 16] on the electron stopping power, which become important at relativistic intensities ($I_L \geq 10^{18}\,\mathrm{W.cm^{-2}}$) and reduce the final penetration length of the electron beam; ii) collisionless Weibel instabilities which start to grow and become very important for laser intensities $I_L > 10^{19}\,\mathrm{W.cm^{-2}}$, at the level of the plasma skin depth, generating micro magnetic fields that strongly contribute to increase the initial electron divergence [54]. Different strategies to control REB propagation in solid matter have been proposed. They rely on the use of ∼kT magnetic fields, which can be externally generated by coils [184, 10] or self generated [20], either by artificial resistivity gradients [110, 191, 53, 185, 164] or by exploiting the intrinsically high resistivity of a material [211].

One of the schemes using self-generated magnetic fields was proposed by A. Robinson *et al.* [176, 175], which will be clarified in the next session.

2.4 Double - pulse electron beam collimation scheme

2.4.1 Theoretical background

In this section we will discuss the fast electron beam collimation scheme proposed by A. Robinson *et al.* [176] based on the use of two consecutive laser pulses. In this scheme the electron beam generated by the first laser pulse produces a resistive azimuthal magnetic field which is used to guide a main electron beam produced by the second laser pulse (Fig.2.12).

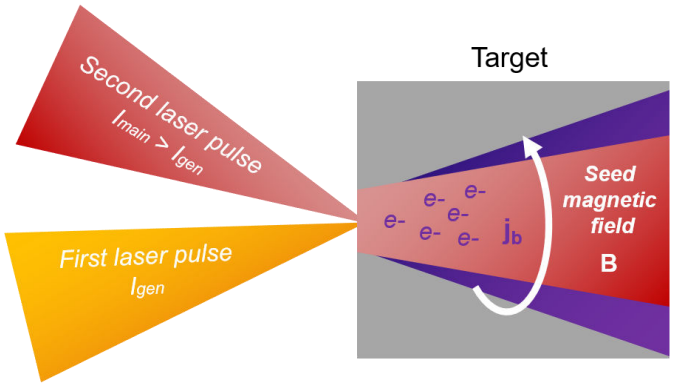

Fig. 2.12 Double laser pulse scheme proposed.

The first laser pulse with intensity I_{gen} and pulse duration τgen is focused onto a solid target within a focal spot ϕ_{gen}. The generated electron beam with initial radial extension of R_{gen} propagates deep into the target with velocity of v_{gen} and fast electron current j_{gen} ,generating self- induced azimuthal magnetic field with flux density B_0 and spatial extent L_x in x - direction (into perpendicular to target surface) and L_y in the y - direction (parallel to target surface). Let's introduce a second electron beam of radial extension R_{main} and velocity of v_{main} generated by second laser pulse with aforementioned parameters I_{main}, τ_{main} and ϕ_{main}. This electron beam has half angle divergence of $\theta_{1/2}$ (in rad). We assume that $R_{gen} \geq R_{main}$. The second electron beam collimation should occur when the angle of deflection of a fast electron during its transit through the pre-generated magnetic field is roughly equal to the divergence half-angle of the beam. By considering the trajectory of a fast electron that enters at the divergence angle one then concludes that following conditions should be satisfied:

$$B_0 L_y > \frac{\gamma v_{main} m_e}{e}(1 - cos(\theta_{1/2})) \tag{2.111}$$

$$B_0 L_x > \frac{\gamma v_{main} m_e}{e} sin(\theta_{1/2}) \tag{2.112}$$

We consider that lateral extension of magnetic field is similar to the radial extension of electron beam $L_y \approx R_{gen}$ and that $L_x > L_y$. Then this guiding imposes a condition on the radial extension R and on the absolute value of the negative magnetic field B_0 generated by the return current of the first electron beam. We can re- write this condition as :

$$R_{gen} \geq r_L \text{ with } r_L = \frac{\gamma v_{main} m_e}{B_0 e}(1 - cos(\theta_{1/2})) \tag{2.113}$$

where r_L - electron Larmour radius.

To estimate the absolute value of magnetic field we can use the approximation of the equation of magnetic field evolution Eq. 2.108:

$$\frac{\partial B_0}{\partial t} \approx \eta \frac{j_{gen}}{R_{gen}} \tag{2.114}$$

where η is an average target resistivity. Then $B_0 \approx \eta j_{gen} t_{gen}/R_{gen}$. Simultaneously, we can replace $\gamma_{main} v_{main}$ in the Eq. 2.111 taking to account the pondemorotive scaling [221] and 2.113:

$$E = (\gamma - 1) m_0 c^2 \text{ with } \gamma = \left(1 + \frac{I \lambda_{\mu m}^2}{1.37 \times 10^{18}}\right)^{1/2} \tag{2.115}$$

Then we can write a primary condition of collimation in terms of laser parameters:

$$\eta j_{gen} t_{gen} > \frac{m_e c}{e} \sqrt{1 + \frac{I_{main} \lambda^2}{1.38 \times 10^{18} W cm^{-2} \mu m^2}} \times (1 - cos(\theta_{1/2})) \tag{2.116}$$

$$j_{gen} \approx \frac{\eta_L I_{gen}}{2 \times 10^5 (I_{gen} \lambda^2 / 10^{18} W cm^{-2} \mu m^2)^{1/3}} \tag{2.117}$$

where η_L is a conversion efficiency that can be estimated by formula Eq. 2.52. We can rewrite this condition in terms of the laser intensity ratio for the wavelength $\lambda_L = 1 \mu$m that is case for the experimental campaign described in this thesis. The expression for fast electron current Eq. 2.117 can be written only in terms of laser intensity by using the formula Eq.2.52 for conversion efficiency:

$$j_{gen} \approx 0.6 \times 10^{-14} (I_{gen})^{1.41} \tag{2.118}$$

Then the collimation condition Eq. 2.116 can be expressed through the intensities of both beams:

$$I_{gen}^{1.41} > \frac{2m_e c}{0.6 \times 10^{-14} e \eta t_{gen}} (I_{main})^{0.5} \times (1 - cos(\theta_{1/2}) \times 10^{-9} \tag{2.119}$$

By evaluating the constants we can write finally the approximate condition as following:

$$I_{gen} > 45.2 \left(\frac{1 - cos(\theta_{1/2})}{\eta t_{gen}} \right)^{0.7} (I_{main})^{0.35} \tag{2.120}$$

Therefore one expects the pre-generated field to collimate the fast-electron beam produced by the main pulse, for this set of parameters. However, this simple analytic approach cannot encompass all of the relevant physics. Numerical calculations were performed to validate the condition of collimation shown in Eq. (2.120) using two laser pulses of intensities 2.5×10^{18} and $5 \times 10^{19} \mathrm{W/cm^2}$) for the first and second laser pulses respectively injected simultaneously to the target. The first exploration of this scheme was performed at RAL Vulcan facility.

2.4.2 First experimental validation

The first validation of the proposed scheme was performed at the Vulcan petawatt laser at the Central Laser Facility, Rutherford Appleton Laboratory in United Kingdom by R. Scott et al. [194]. This laser system delivers a 1054 nm laser pulse of 186 ± 11 J energy and pulse duration of $\tau_L = 1.4 \pm 0.3$ ps yielding a peak intensity $I = 1 \times 10^{20} \mathrm{W/\ cm^2}$. Two laser pulses were created by passing the incident beam through a half wave plate and then a polarizing beam cube. To control the intensity ratio the wave plate angle was tuned to adjust the relative pulse levels $R = I_2/I_1 = 10$ where I_1 and I_2 is the intensity of the first and second pulse respectively. Both laser pulses were focused by using one OAP parabola onto the Al 75 μm - Cu 10 μm - Al 1 μm layered planar targets (transverse dimensions 5 mm) at 45 p-type polarization. The aforementioned condition for collimation suggested by Robinson *et al.* [176] (by assuming the Larmor radius of the second beam smaller than the radial extension of the seed magnetic field) written in terms of the laser focal spots ratio $\varphi_1 > \varphi_2$ was satisfied Eq. 2.113.

The temporal delay between pulses Δt was altered by the translation one of the prisms in the optical path accessing the delay 0 to 10 ps. The fast-electron spatial distribution was measured in a 10 μm Cu fluor layer, 1 μm beneath the target rear surface using the K_α imaging technique described in the X-ray diagnostics section. The spherically bent quartz 2131 Bragg crystal was used to image the Cu - K_α emission onto a FUJI BAS image plate.

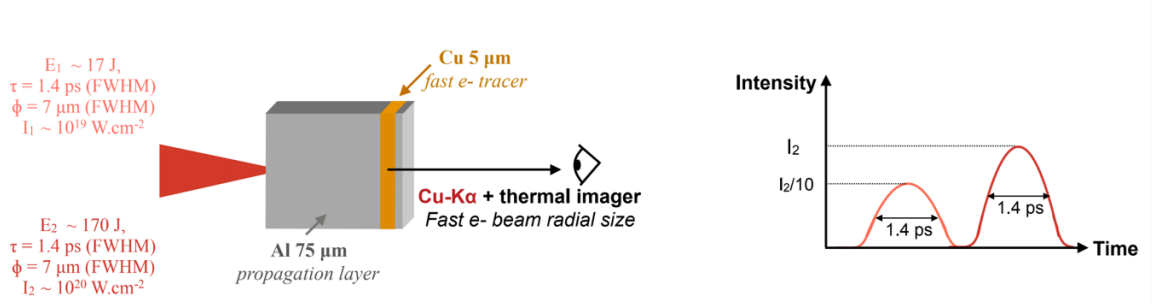

Fig. 2.13 Experimental setup of the double pulse experiment at RAL.

Figure 2.13 presents the experimental setup. To estimate the effect of collimation the Cu - K_α spot sizes were compare. The Figure 2.14 shows experimental half-width-at-half-maximum (HWHM) of the Cu - K_α spot sizes as a function of delay time between pulses Δt (red diamonds). The simulations were performed using the 2D radiation hydrodynamics code CHIC, using MHD and fast electron transport modules. The experimental results had shown that under the optimal conditions, the beam divergence is reduced by a factor of 2.7 with the fast electrons generated by the main laser pulse being guided over a distance of 80 μm. For the intensity ratio of 10 the optimum delay time between pulses when the collimation had occurred was found between 4 to 6 ps. The existence of this optimum can be explained by considering the growth rate and then the dynamics of the spatial diffusion of the seed magnetic field, relative to the arrival time of the main electron beam.

It is worth to note that these results are quite promising for the fast-ignition inertial-confinement fusion and many other applications of intense laser-solid interactions, where the fast-electron beam parameters are critical.

However the reported study is focused only on the influence of the delay time between the laser pulses while other relevant parameters, namely laser intensity and laser focal spot size ratio, were kept constant.

2.4.3 Motivation for the new double pulse experiment

Numerical investigations have been performed to better understand the mechanism [217]. From this study a more clear picture of the physical mechanism is obtained suggesting the relevant role of the ratio between the REB sizes. Following such interpretation we have performed an experimental campaign in which we used two independent focusing parabolic mirrors, allowing one to vary the ratio ϕ_{gen}/ϕ_{main} between the two laser focal spots, therefore controlling the ratio between the radius of the azimuthal magnetic field created by the first beam R_1 and the radius of second electron beam R_2. In addition to the Cu - K_α emission diagnostic used in previous experiment is mainly sensitive to the more numerous electrons in

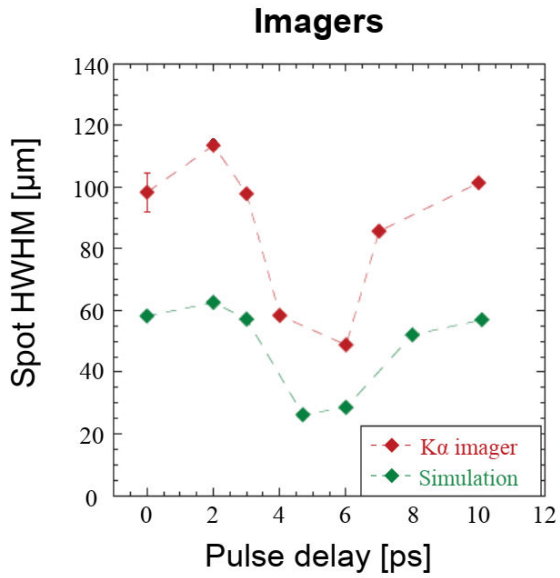

Fig. 2.14 Dependence of the HWHM of the Cu - K_α (red diamonds). The lower curve (green diamonds) shows the results of numerical simulations, this reproduces the delay required for optimal collimation from simulations. Graph taken from [194].

the 10 - 100 keV range. In the new experiment we implemented a measurement of coherent transition radiation (CTR) to evaluate the collimation effect on higher energy electrons (> 1 MeV). The performed experimental study with various laser parameters allowed us to make a detailed characterization of the collimation efficiency.

In summary, the new experimental campaign investigated this collimation scheme in terms of following parameters:

- Laser intensity ratio I_1/I_2
- Delay time Δt
- Focal spot ratio ϕ_1/ϕ_2

We also propose a simple analytical explanation of the observed collimation effect together with more sophisticated modelling involving three integrated steps in order to characterize the hydrodynamic target expansion (MULTI - fs), electron beam source (PIC) and the fast-electron transport to confirm the experimental results (Hybrid PIC).

2.5 Laser driven ion - plasma interaction

In previous sections we considered the generation and transport of laser driven fast electron in plasmas. This section will concentrate on laser driven proton acceleration and transport in plasmas, in particular the stopping power in extreme states of matter. Proton stopping power in solids and plasma has been extensively studied through the last decades. However, a lot of questions are still outstanding especially in the warm dense matter regime, where the EOS is not well known and the theoretical models have the largest discrepancies.

2.5.1 Laser driven ion acceleration

Different laser driven ion acceleration mechanisms has been discovered in recent decades [134] such as target normal sheath acceleration (TNSA), radiation pressure acceleration (RPA) and collisionless shock acceleration (CSA), ion acceleration in ultrathin solid targets which become transparent to intense laser pulses (break-out afterburner (BOA)) or using mass-limited targets. In the framework of this thesis, the TNSA mechanism has been used and it is described below.

TNSA

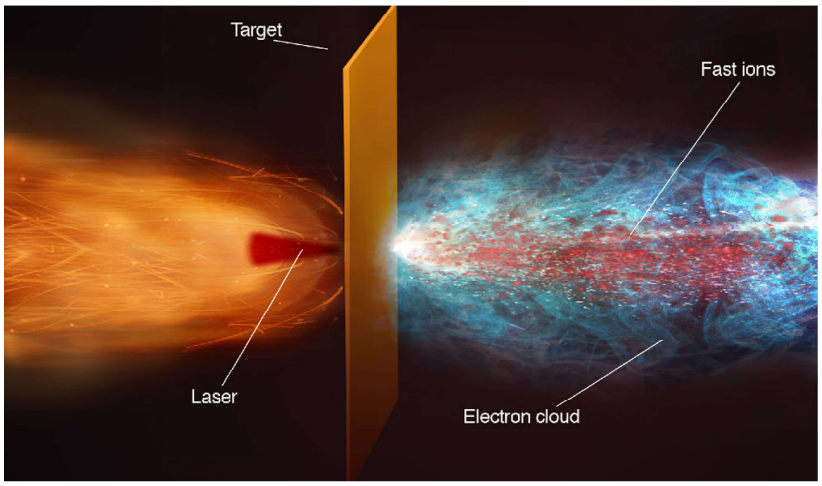

Fig. 2.15 Artistic representation of TNSA mechanism. Taken from [134].

Ion acceleration driven by ultra intense laser pulses has been extensively studied in laser laboratories all over the world. The experimental results, supported by the theoretical

modelling showed the possibility to generate multi - MeV proton and ion beams with high brilliance and ultra short duration and relatively, low emittance. This regime of acceleration has been introduced as target normal sheath acceleration (TNSA) by S. Wilks *et al.* [222]. One can say that TNSA is ion acceleration by a sheath electrostatic field, generated at the rear surface of the target by hot electrons accelerated through the target (2.15). Then the generation of the ion beam mainly depends on the electron driver, which in turn depends on the laser and target - plasma interaction conditions as discussed in the fast electron generation and acceleration section. The first experimental demonstration of proton beam acceleration along the target normal direction at the rear side of the target was performed by Snavely *et al.* [198, 95, 138] by irradiating thin metallic foils with laser pulses of intensities $\geq 10^{19-20}$ $\mathrm{W/cm^2}$. Since then, careful parametric studies have been performed demonstrating the optimization of the proton beam and improving the proton beam quality by adjusting the laser parameters and enhancing the target structure.

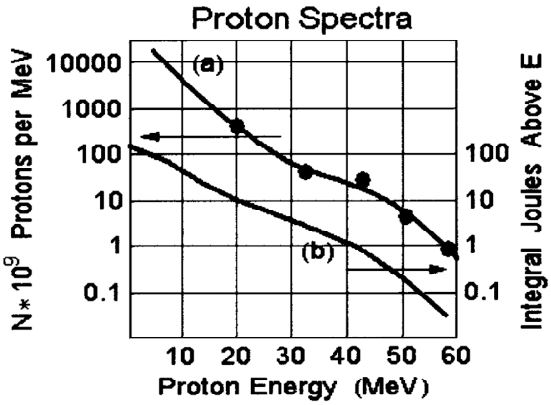

Fig. 2.16 Proton energy spectrum from the rear side of a 100 μ m solid target irradiated by a 423 J, 0.5 ps pulse at normal incidence, corresponding to an intensity of 3×10^{20} $\mathrm{W/cm^2}$. The integrated energy of protons indicates a conversion efficiency of ≈ 10 % for protons above 10 MeV. Taken from [198].

Mechanism In order to estimate the electric field accelerating ions normal to the target rear surface one should find an electric potential Φ in the vacuum region caused by the charge separation from the electrons escaping the target rear surface by solving Poisson equation:

$$\varepsilon_0 \frac{\partial^2 \Phi}{\partial z^2} = e n_e \tag{2.121}$$

An applied ansatz for the solution of this equation is $e\Phi/k_B T_{hot} = -2\ln(\lambda z + 1)$ where $k_B T_{hot}$ is an electron temperature estimated by the pondemorotive scaling Eq.2.56 and λ is a

constant defined in the solution and +1 is necessary to fulfill the boundary condition with the solid matter interface $\Phi(0) = 0$. Then the corresponding electric field is equal to:

$$E(z) = -\Phi = \frac{2k_B T_{hot}}{e} \frac{1}{z + \sqrt{2\lambda_D}} \tag{2.122}$$

where λ_D is the Debaye length defines the distance over which signifiant charge separation occurs [120].

The Debye length defines longitudinal sheath scale length generated by the electrons on target rear side. Meanwhile the scale size of the sheath region extension can be estimated as:

$$r_{sheath} = \phi/2 + d\tan\theta/2 \tag{2.123}$$

where ϕ is a laser focal spot diameter at Full-Width-Half-Maximum, d is a target thickness and $\theta/2$ is electron divergence half angle described in Eq. 2.63. Applying pondemorotive scaling, Eq. 2.56 and the hot electron conversion efficiency Eq. 2.52 one can write the Debye length as :

$$\lambda_D \approx 1.37\mu\text{m} \left(\frac{\phi/2 + d\tan\theta/2}{\phi/2} \right) \frac{\sqrt{1 + 0.73 I_{18} \lambda_{\mu m}^2} - 1}{I_{18}^{7/8}} \tag{2.124}$$

Then the maximum electric field at the vacuum - solid interface $z = 0$ can be also written as:

$$E_{max}(z=0) = \frac{\sqrt{2} k_B T_{hot}}{e\lambda_D} \approx 5.2 \times 10^{11} \text{V/m} \left(\frac{\phi}{\phi/2 + d\tan\theta/2} \right) I_{18}^{7/8} \tag{2.125}$$

By noting the dependence of the electron broadening with target thickness [143] one can find that electric field scales as $E_{max}(z=0) \propto d^{-2}$. This electric field ionizes the target atoms during its evolution in time since it is close to the ionization threshold estimated by the Field Ionization by Barrier Suppression. Almost all of the atoms at the rear side of the target are immediately ionized and as the electric field increases to the maximum strength the ions will also increase to one maximum charge state. Clearly, the stronger the electric field is, and the longer it persists, the more efficient will be the ionization of the target and the acceleration of the ions to high energy.

As an example let's consider the proton acceleration experiments performed at CLPU VEGA II laser with $\tau_L = 30$ fs and laser wavelength of λ_L = 800 nm for two off - axis parabola configurations: short focal length F = 40 cm [216] and long focal length F = 130 cm (described in this thesis). In the first configuration the laser is focused onto a $d = 5\mu$m thick Al foil with ϕ = 7 μm yielding intensity of $I_L = 2 \times 10^{20}$ W/cm^2 and electron divergence

angle then equal to $\theta = 50°$ (Eq. 2.63). The transverse extension of the sheath field sheath radius is $r_{sheath} = 5\ \mu$m leading to a Debye length $\lambda_D = 0.19\ \mu$m at the rear side which results in the formation of the electric field with maximum strength of $E_{max} \approx 3 \times 10^{13}$ V/m. In the second configuration the laser is focused onto a $d = 3\mu$ m thick Al foil with $\phi = 18\ \mu$m yielding an intensity of $I_L = 1 \times 10^{19}$ W/cm^2 and electron divergence angle then equal to $\theta = 40°$ (Eq. 2.63). This corresponds to $r_{sheath} = 10\ \mu$m, $\lambda_D = 0.28\ \mu$m and $E_{max} \approx 3.5 \times 10^{12}$ V/m. Figure 2.17 demonstrates how the Debaye length and maximum electric field scale with the target thickness d. As predicted, a higher laser intensity leads to a shorter Debye length.

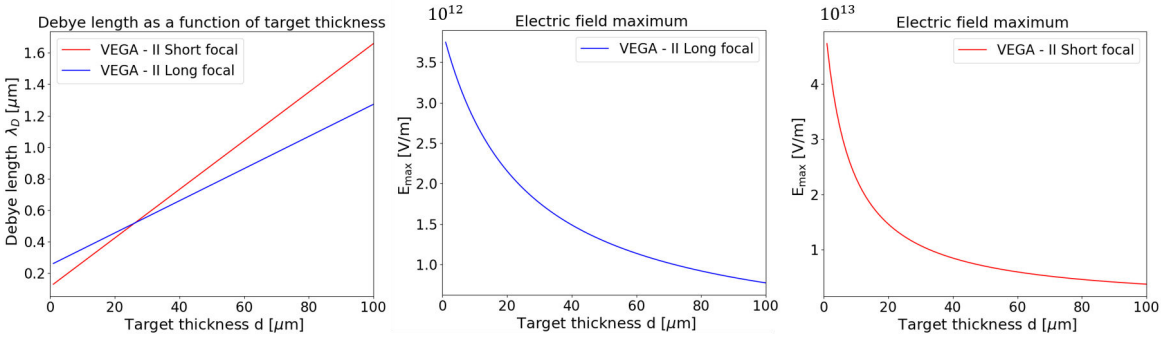

Fig. 2.17 Debaye length λ_D as function of the target thickness for short focal (red solid line) and long focal (blue solid line) configurations at VEGA - II laser facility (right). The corresponding maximum electric field E_{max} at the vacuum - target rear border $z = 0$ for the both configuration respectively(left).

Taking the parameters of the example of the long focal configuration one can demonstrate the behaviour of the electric field as a function of z (Fig. 2.18):

$$\frac{E(z)}{E_{max}} = \frac{\sqrt{2}}{z/\lambda_D + \sqrt{2}} \tag{2.126}$$

The last but not least important parameter for the TNSA is the front side target interaction. As mentioned, the ion acceleration is caused by the electron driver generation and transport which depends on the laser and pre - formed plasma at the target front surface. However, most of the discussions of TNSA are simplified by neglecting the laser interaction with the front target surface and electron transport through the target and instead begin with the fast electron distribution that determines the initial expansion of the rear surface ions [79, 192, 148–150]. Even the simplest models are non linear and the number of analytical solutions are dramatically limited. The TNSA is a very complicated non linear relativistic interaction that includes both kinetic and collective effects and therefore should be considered as a multi - dimensional problem. Analytical techniques mostly employ the 1D plasma expansion model

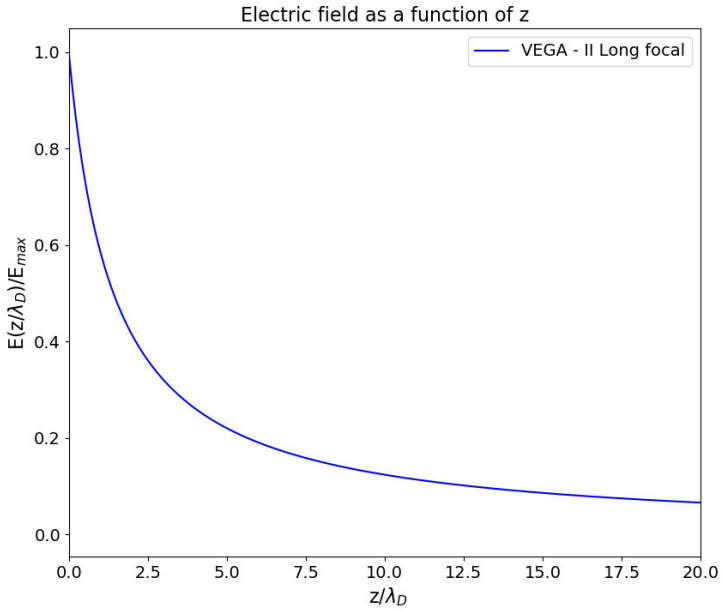

Fig. 2.18 Electric field in the vacuum - target rear interface obtained from formula 2.126 for VEGA II long focal length conditions wit λ_D=0.28 μm.

and one can then use Particle in Cell simulations in two and three dimensions in order to better understand the TNSA mechanism.

Experimental beam optimization The laser driven ion acceleration via the TNSA mechanism has been intensively studied using both theoretical and experimental methods, providing scaling laws with which to extrapolate for future experiments. The investigated ion beam parameters of interest have mainly been:

- **Energy spectrum**. Numerical and experimental results find that the ion energy distribution can be described as an exponential distribution with a cut-off energy $\varepsilon_{cut-off}$. Many studies have been dedicated to the determination of $\varepsilon_{cut-off}$ and parametric studies of its dependence on laser power, laser pulse duration, laser pulse irradiance, pulse energy, and fluence [225, 72, 177, 73]. In one experiment it was observed that the maximum proton energy can be increased from 6.5 to 24 MeV as the target thickness was reduced from 100 to 3 μm [137]. This demonstrates the effect of fast electron beam dynamics on the formation of the sheath electric field. Additionally, it appeared that another crucial parameter for the ion acceleration is the existence of the laser prepulse due to amplified spontaneous emission (ASE), especially in the thin foil target cases [109]. As predicted by models, the pre - plasma generated by the pre - pulse

at the target rear decreased the TNSA cut - off energy, lowering the efficiency of ion acceleration. Therefore the target thickness parameter has to be tuned depending on the existing ASE of the laser pulse in a given experiment. Alternatively, the laser prepulse can be experimentally mitigated by, for example, using plasma mirrors [60, 80]. In proton acceleration experiments at CLPU VEGA - II the typically observed cut off energy is 10 MeV for the short focal parabola configuration [216] and 5 MeV for the long focal parabola configuration (this work). Such relatively low maximum proton energy might be caused by the low contrast of VEGA - II laser system. More detailed study on the laser contrast characterization should be performed.

- **Particle number**. Experimental data reports the detected proton number up to 10^9/ MeV/msrad for the proton energies $\geq$ 0.5 MeV (Figure 2.19. It can be roughly approximated by a quasithermal distribution with a sharp cut-off at a maximum energy that scales with the laser parameters [109].

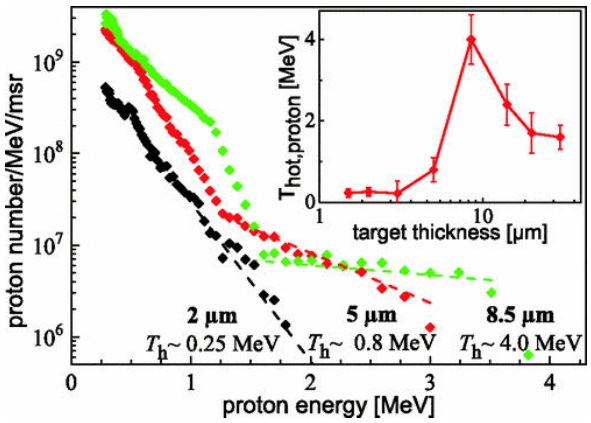

Fig. 2.19 The proton spectra obtained by irradiating foils of different thickness with intensity of $I_L = 3 \times 10^{19}\mathrm{W/cm^2}$. Taken from [109].

- **Divergence**. A divergent cone of protons is emitted from the target rear surface starting from the source size area. Different experimental data reported that the opening angles decrease with increasing proton energy. Typically, the opening half angle is observed to be around 15 - 20°. The opening angle is not exactly the divergence angle. The divergence of the protons decreases slightly with increasing energy while the source size also decreases with proton energy [31, 46]. The half opening angle observed in the proton acceleration experiment here is 21 °.

- **Source size**. Protons with the highest energies are emitted from sources as small as $\leq$ 10 μm diameter. For the protons with lower energies the source size progressively

increases, up to approximately 200 μm [192]. Cowan *et al.* [46] showed that such energy dependence of the source size is related to the electric field strength distribution of the accelerating hot electron distribution in the source assuming an isothermal quasi - neutral plasma expansion. The energy dependence on the source size can be written by fitting experimental data obtained at TRIDENT, LULI - 100TW and Z - Petawatt [143]:

$$E = \exp\left(\frac{-(4\ln(2)\text{source size})^2}{\sigma}\right) \tag{2.127}$$

where 2σ is the FWHM of Gaussian fit of experimental data of E/E_{max} as a function of the source size.

One the biggest challenges is to control these beam parameters in order to get the ion source of the needed brilliance, size, energy, etc. for a given application of TNSA proton beams. As mentioned, by varying the target and laser parameter and profiles one can vary the proton beam characteristics. Additionally, the feature of a ballistic focusing of proton beam was first discovered by Patel *et al.* [161]. This feature allows to focus a proton beam with initial size of several hundred micrometres into few tens of micrometers using ballistic focusing from the rear surface of hemispherical targets. The TNSA proton beam can be also be collimated by use of an external magnetic field generated by with the capacitor coil targets [10]. The ability to collimate the proton beam is highly important for several applications such as proton fast ignition [181] and warm dense matter generation [162].

Applications The discovery of TNSA proton beams launched a new epoch in the fundamental research of proton acceleration and the pursuit of applications featuring multi MeV broad spectrum beams. Many of the applications are based on the use of the proton stopping power property in dense matter at the penetration depth defined by the proton energy and the material characteristics - the so called Bragg Peak discussed more in detail in the following section. Amongst the most successful applications at present are proton radiography [112, 179, 136] used for the target diagnostics and plasma characterization, and isochoric proton heating [161, 162] used for warm dense matter generation and potentially the fast ignition approach to inertial confinement fusion [181, 182]. One of the recent rapidly evolving research lines is in ion beam cancer therapy.

2.5.2 Ion stopping power in matter

General concept of the stopping power

Energy loss Let's consider an incident proton beam or so called ion projectile with energy of E, velocity v_p and charge state Z_p passing through the solid matter sample with the target density ρ. Then the energy loss is given by the integral along the beam trajectory:

$$\Delta E = -\int \frac{\partial E}{\partial(\rho x)} \rho dx \tag{2.128}$$

The stopping power $S(E)$ of an ion in a matter then can be defined as differential energy loss:

$$S(E) = -\frac{\partial E}{\partial x} \tag{2.129}$$

It was experimentally observed that in addition to the energy loss in matter, the projectile may also suffer a change in its charge state due to charge exchange during the interaction that significantly affects the total energy deposition. Such processes occur in ionized matter or plasmas. Then the energy loss and the charge-state evolution of a projectile ion in matter are based on the interaction cross sections of the underlying microscopic Coulomb processes. These can be viewed as collision cross sections, or scattering cross sections in the frame of Coulomb scattering theory. The ion projectile stopping power in matter is a very complicated mechanism that apart of the matter properties also depends on the initial projectile energy. One can distinguish the electronic and nuclear energy loss caused by collisions with the electrons and background ions of the matter, which are referred to as inelastic and elastic collisions, as well as electromagnetic energy loss, and excitation and ionization of the target and projectile itself. Depending on the projectile energy one effect can dominate over another requiring a different proton stopping power description. One can define three regimes of interest, corresponding to low (E $\leq$ 0.1 MeV/u), intermediate (0.1 $\geq$ E $\leq$ 10 MeV/u), and high (E $\geq$ 10 MeV/u) velocity ion projectiles. For instance, in the high velocity projectile domain, besides the losses caused by target electrons excitation and ionization, electromagnetic energy loss from bremsstrahlung or Cherenkov radiation also occurs. The asymptotic Bethe formula that was already mentioned for the electron stopping power works well for this case [23, 24]. Meanwhile for the intermediate regime the ion stopping power description starts to be more complicated as far as the excitation and ionization of the target electrons and target electron capture occurs. This regime is particularly interesting because of the existence of the maximum when the projectile velocity is nearly reaching the plasma thermal velocity v_{th} in case of plasma or Bohr electron velocity v_0. In the cold matter, several modification has been implemented to the Bethe formula [29, 160] taking to account shell

correction that includes the movements of the target electrons individually. Its worth to note that it can be used only for the projectile velocities $\leq$ Thomas - Fermi velocity.

For the low velocity projectile regime, the nuclear energy loss becomes significant. A simplified model [132] can be applied referring to case when the stopping power is close to the friction force. The ion stopping power in solids has become well understood during last decades.The theoretical models were benchmarked with numerous experiments, especially around the stopping-power maximum, and reliable data bases with stopping power data are available.

Bragg Peak The region where the projectile reaches its maximum stopping power in matter is called the Bragg - peak [228, 115]. In other words, it is a peak of energy deposition of ion projectile in matter. One can estimate energy deposition by the proton beams of various energies from 1 to 6 MeV into the 250 μm thick Aluminium foil using databases of NIST PSTAR [Pst], SRIM [228] or by available Monte - Carlo codes such as FLUKA [71, 28], GEANT4 and MCPX. Figure 2.20 demonstrates the simulated deposited energy by means of the FLUKA code. As far as this property makes protons and ions very suitable for highly

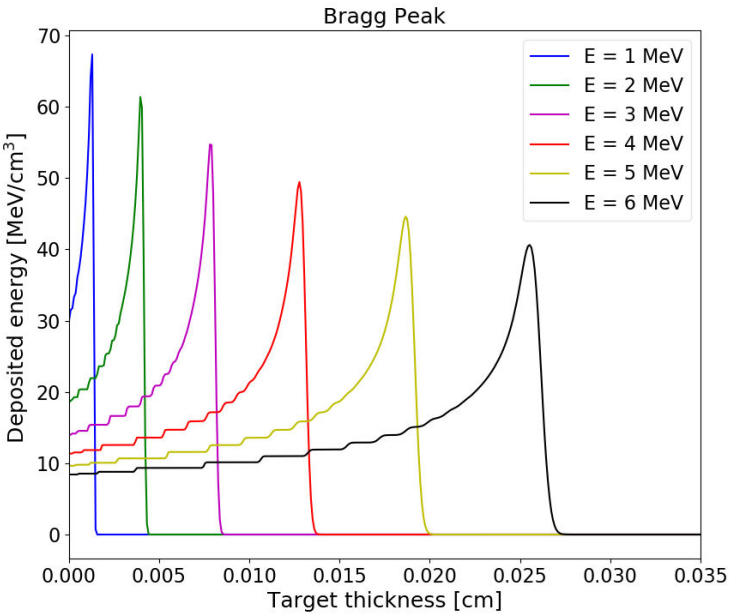

Fig. 2.20 The deposited energy as a function of target thickness for different incident energies of proton beam 1 - 6 MeV on 250μm thick aluminium foil. The simulation is performed with Monte - Carlo code FLUKA with 100000 incident particles.

localized energy deposition, the maximum stopping power region - near the Bragg Peak in

solids is relatively well understood. Still this regime in plasma condition it is not yet well investigated.

Projectile charge state Let's introduce another important parameter of the ion projectile for the stopping power description - the charge state. The Bethe - Bloch model shows that the stopping power depends quadratically on the charge-state value. As mentioned, a projectile experiences the excitation of a projectile electron to an upper energy level, the direct ionization of the projectile in case of cold matter. When the matter starts to be partially ionized one can find recombination by capture of bound target electrons, due to its relatively high cross section as a dominant mechanism. It is based on the presence of the corresponding target atom as a third collision particle for momentum transfer. However, it is not the case for collisions with free electrons, where there is no third partner available. Another recombination process that mainly plays a role in ionized matter is recombination by radiative electron capture. In this mechanism, a free electron is generated by ionization of a target atom and is subsequently captured by the projectile. In order to ensure the conservation of energy and momentum, a photon is emitted, hence the designation "radiative electron capture". This mechanism can be viewed as the inverse process of photo-ionization. In "cold matter", it is only significant if the projectile energy is sufficiently high (several MeV/u) in order to ionize target atoms and thus to create free electrons that can then be captured by the projectile. It becomes dominant in a fully ionized plasma but only at low densities and moderate temperatures. In the following, the capture of bound electrons is designated as NREC (non-radiative electron capture), in contrast to REC (radiative electron capture). The equilibrium mean of charge state validated experimentally in a wide range of beam-target configurations is given by [27]:

$$Q_{eq} = Z\left(1 - a\exp\left(-\frac{v_p}{v_0 Z^f}\right)\right) \tag{2.130}$$

where Z is the atomic number of the projectile , v_0 - Bohr velocity, a and f - fit parameters. This formula does not take to account the medium properties such as charge, density and temperature.

If it is assumed that the projectile is a point charge with charge-state value Z_p, the stopping power depends quadratically on Z_p, at least at high projectile velocity, where the projectile plasma coupling is linear. In the low velocity projectile regime, the bound electrons have to be taken to account. At the same time the effective charge Z_{eff} can be used in the proton stopping power formulas instead and already includes the Coulomb screening by bound electrons. However for the full stopping power description one should consider a

full microscopic description including an impact-parameter dependence to account for the presence of bound electrons around the projectile.

Velocity projectile ratio The velocity projectile ratio is a ratio between projectile velocity v_p and thermal velocity of the free plasma electrons v_{th}. It is widely used in understanding of ion beam - plasma interaction regimes. For example, the interaction between ions and plasma is now pretty well understood for a high projectile ion velocity v_p. This velocity is most adequately measured in units of the thermal velocity of the free plasma electrons v_{th}. Hence, for $v_p/v_{th} \gg 1$, the energy deposition of the ions in plasma can be described by a simple Bethe formula. But when reducing the projectile velocity, effects like close collisions and plasma polarization start gaining importance in the stopping process, and correction terms are needed. When the projectile ion velocity reaches the parameter region $v_p/v_{th} \sim 1$, the theoretical description of the ion stopping power becomes very difficult because of the various phenomena involved.

2.5.3 Ion stopping power in solid

As for the case of electron beam interaction with solid matter described in the section Sec. 2.3.2, the classical approach is also used to obtain collisional proton stopping power [30] with additional corrections due to the quantum mechanical effects [23, 24]. For both electrons and ions, it is caused by the collisions with bound background electrons. As mentioned, this approach is valid for the high ion velocity projectile. And it is considered here as a simple model in order to understand better the nature of ion stopping in solid. Let's define E as an incident ion projectile energy, ΔE as the transferred energy from the projectile to target particles giving $\varepsilon = \Delta E/E$ as a fraction of the transferred energy. The ion projectile is characterized by its mass m_i, charge Z_p and velocity v_p. From another side the impact parameter b indicates its interaction with target electrons. Then the exchanged energy can be written as:

$$\Delta E(b) = \frac{(\Delta p)^2}{2m_e} = 2\frac{Z_p^2 e^2}{b^2 v_p^2} \tag{2.131}$$

Then the stopping power of ion projectile in propagating over a matter with thickness δx:

$$\frac{\partial E}{\partial x} = -\frac{4\pi Z_p^2 e^4 n_e}{m_e v_p^2} \int \frac{db}{b} \tag{2.132}$$

The projectile interacts with the $2\pi n_e b db \delta x$ at the impact parameter b. Then one can note that interaction is limited in distance range by the minimum and maximum impact parameters

$b_{min} = r_0 = Z_p e^2/m_e v_p^2$ and $b_{max} = v_p/\omega_e$ respectively. The Bethe stopping power formula for the projectile then can be written as:

$$\left(\frac{\partial E}{\partial x}\right)^{cold}_{bound} = -\frac{4\pi Z_p^2 e^4 n_e}{m_e v_p^2} \ln\left(\frac{2m_e v_p^2}{I}\right) \tag{2.133}$$

where I is the ionization potential for bound target electrons. It is important to note that the logarithm in the stopping power expression is a Coulomb logarithm that defines the projectile - target interaction.

2.5.4 Ion stopping power in plasmas

Classic stopping power models

In the case of ionized matter, the additional component of stopping power due to collision with free electrons has to be taken to account in the stopping power description. In comparison with the cold matter case, the increase in the Coulomb logarithm due to different ionization potential of the electrons, and the increase in the projectile charge state due to different cross sections of the charge-transfer processes are observed. Ionization by Columb collisions remains the dominant ionization mechanism for the projectile. However, new mechanisms also appearing in the plasma such as ionization by free electrons, dielectronic recombination and three-body recombination.

Bethe - Bloch model The ionization potential is given by Eq. 2.72 with free electron oscillation frequency of plasma frequency ω_{pe}. Then one can write Bethe stopping formula by free electrons in the partially ionized matter:

$$\left(\frac{\partial E}{\partial x}\right)^{hot}_{free} = -\frac{Z_p^2 e^2 \omega_{pe}^2}{v_p^2} \ln\left(\frac{2m_e v_p^2}{\hbar\omega_{pe}}\right) \tag{2.134}$$

This formula is able to describe the stopping power due to the collisions with large impact parameter $b \geq \lambda_0$ taking to account quantum perturbations, where λ_0 is that the dynamic screening length of a projectile ion in plasma.

The Bohr formula describes collisions in range $b_0 < b < \lambda_0$ and is expressed as follows:

$$\left(\frac{\partial E}{\partial x}\right)^{hot}_{free} = -\frac{Z_p^2 e^2 \omega_{pe}^2}{v_p^2} \ln\left(\frac{m_e v_p^3}{Z_p e^2 \omega_{pe}}\right) \tag{2.135}$$

with the upper limit - maximum impact parameter $b_{bax} = v_p/\omega_{pe}$

Then the total stopping power of an ion projectile in plasma is given by:

$$\left(\frac{\partial E}{\partial x}\right)_{total}^{hot} = \left(\frac{\partial E}{\partial x}\right)_{bound}^{hot} + \left(\frac{\partial E}{\partial x}\right)_{free}^{hot} \tag{2.136}$$

The classic approach is in pretty good agreement with the experimental data performed for ion stopping power measurements at high velocities. However it can be also adjusted for the application in the intermediate velocity regime.

Standard Stopping Power Model In order to extend the impact parameter domain of the Bethe formula, the correction adding the closer collisions described in the Bohr stopping power. The required additional correction factor joins together the quantum - mechanical approach for large impact parameter domain and classical approach for smaller impact parameters [29] and is introduced as:

$$L_{Bloch} = \psi(1) - \Re[\psi(1+i\upsilon)] \tag{2.137}$$

where $\upsilon = Z_p e^2/4\pi\varepsilon_0\hbar c$, $\psi(1) = -\gamma_E = -0.57721$ in the negative of Euler's constant.
The additional correction is coming from the observed Barkas effect [14] that featured a difference in energy loss between positive and negative pions defining the energy loss that contained odd powers of Z_p. That means that the target polarization effects for short distant collisions would produce a correction to the energy loss:

$$L_{Barkas} = \frac{3\pi e^2 \omega_{pe}}{2m_e v_p^3} \ln\left(\frac{2m_e v_p^2}{\hbar\omega_{pe}}\right) \tag{2.138}$$

From another side, a thermal correction describes the collisions of ion projectiles with velocity $v_p \leq v_{th}$ [41]. This correction is crucial for the description of the low velocity projectile ratio $v_p/v_{th} \sim 1$. By introducing a temperature coupling parameter $G(v_p/v_{th})$ to the Bethe formula the stopping power $\to 0$ when $v_p \to 0$:

$$G(x) = erf(\sqrt{x}) - 2\sqrt{\frac{x}{\pi}}\exp(-x) \tag{2.139}$$

where erf is the error function.

By introducing these corrections to the Bethe formula it can basically describe th ion stopping power covering larger impact parameter domains and all projectile velocities regimes in ionized matter. It is called standard stopping model and can be expressed as:

$$\left(\frac{\partial E}{\partial x}\right)_{SSM}^{hot} = -\frac{Z_p^2 e^2 \omega_{pe}^2}{v_p^2} G\left(\frac{v_p}{v_{th}}\right)\left[\ln\left(\frac{2m_e v_p^2}{\hbar\omega_{pe}}\right) + L_{Bloch} + Z_p L_{Barkas}\right] \tag{2.140}$$

This model indeed is more valid for the intermediate velocity regimes but does not cover the short impact parameter for this velocity regime. Special attention is required the region of the stopping-power maximum (Bragg peak region) where close collisions become more important together with the collective effects in the plasma and where the projectile - plasma coupling can be strong.

Relevant stopping power theoretical models

The many theoretical studies are concentrated on giving more detailed descriptions of the maximum stopping power. A short summary of the models used in the framework of this thesis is given. Taking to account that the stopping power of the projectile directly depends on its coupling with plasma , one can define the three regime of beam - plasma interaction regimes in terms of the strength of coupling: linear (weak perturbations) , semi - linear (localized perturbations) and non - linear (strong perturbation).

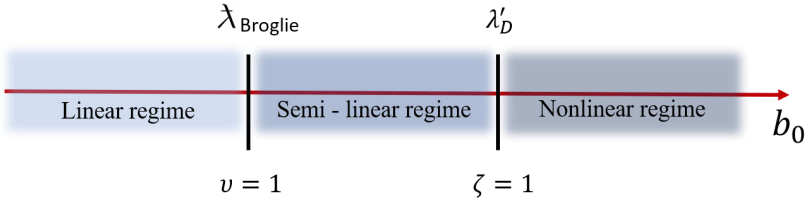

Fig. 2.21 The regimes of the projectile - plasma interaction

In order to define these regimes, let's introduce the characteristic length of projectile plasma interactions. The projectile ion is screened in plasma in a so called dynamic screening length $\lambda_D = \lambda_D^{'}(v_r)$ (collective plasma effect), where v_r is relative velocity between the projectile and plasma electron. The minimal distance between the projectile and target electron in the projectile - electron Coulomb scattering interaction can be determined by the minimum approach value of the impact collision parameter (Sec. 2.1.2) - $b_0 = Z_p e^2/m_e v_r^2$. And from another hand, the De Broglie wavelength determines the distance in the plasma when the quantum effects start to play a dominant role $\lambda\!\!\!^{-}_{Broglie} = \hbar/m_e v_r$. Then the ratio between the minimal approach and screening length defines the nature of the interaction from classical to quantum - mechanical regime. This parameter is called the Coulomb parameter:

$$\upsilon = \frac{b_0}{\lambda\!\!\!^{-}_{Broglie}} = \frac{1}{4\pi\varepsilon_0}\frac{Z_p e^2}{\hbar v_r} \tag{2.141}$$

Coulomb parameter is a local parameter, that estimates the perturbation on a single plasma electron. Based on it, one can define the following regimes of the ion- plasma interaction:

- $\upsilon << 1$. The interaction regime has small perturbations and can be described by a quantum mechanical approach defined as the linear regime of the ion - plasma interaction.

- $\upsilon \geq 1$. The perturbation starts to grow and the interaction has to be described with classical approach that corresponds to the nonlinear regime. In this regime, the plasma coupling parameter Γ has to be taken into account. The characteristic length of the perturbation is then the dynamic plasma screening length and in order to identify the transition between the moderate perturbation to strong perturbation one should introduce the ratio between the minimal approach and the screening length called the non-linearity parameter:

$$\zeta = \frac{b_0}{\lambda_D^{'}} = \frac{1}{4\pi\varepsilon_0}\frac{\sqrt{3}Z_p\Gamma^{3/2}}{(1+(v_p/v_{th})^2)^{3/2}} \tag{2.142}$$

  It defines the border between nonlinear and semi - linear regime: If $\zeta \ll 1$ the perturbation is strong but stays local and can be described as a semi - linear regime. And if $\zeta > 1$ the perturbation length scale is far beyond the screening length and is described as a nonlinear regime.

Figure 2.21 shows the scheme of the beam plasma interaction based on the parameters introduced.

The comparison of the various theoretical models for the different beam - plasma interaction regimes has been performed in by Gericke *et al.* [65, 64, 66]. Figure 2.22 show the stopping power results for beam - plasma interaction conditions. The models seem to be in a good agreement at high projectile velocity but have large discrepancies at lower velocity projectile ratio, reaching 30 50 % around the stopping maximum. Moreover these discrepancies are increasing for the case of strongly coupled plasma 2.22 (right). The featured models are the pertubative models of Bethe, RPA (Lenard-Balescu) and Fokker-Planck (Li and Petrasso model) and models providing an unified stopping power description of T - matrix with $\lambda_D^{'}$ and the combined scheme. These theoretical approaches for stopping power estimation consider the different regimes for various impact parameter domains starting from binary collisions up to long range plasma motions. Indeed the nature of the ion - beam

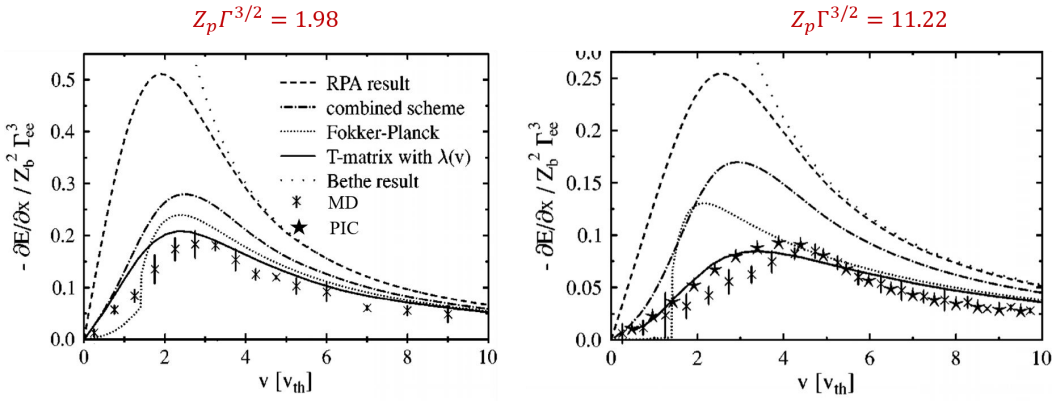

Fig. 2.22 The comparison between stopping power models for the different range of velocity projectile ratio. The beam charge number is $Z_p = 10$. The target is an electron gas with $n_e = 1.25 \times 10^{22}$ cm^{-3}, $T_e = 1.84 \times 10^5$ eV, $Z_p\Gamma^{3/2} = 1.98$ (left) and $n_e = 9.9 \times 10^{22}$ cm^{-3}, $T_e = 1.15 \times 10^5$ eV, $Z_p\Gamma^{3/2} = 11.2$ (right). Taken from [66].

Table 2.1 Classification of proton stopping models

Model	Impact parameter domain	Interaction regime
Bethe	Long range	Linear
SSM	Long range	Linear
RPA	Long and intermediate range	Linear
T-Matrix	Short and intermediate range	Semi-linear and nonlinear
T-Matrix $\lambda_D^{'}$	Short - long range	Semi-linear and nonlinear
Li-Petrasso	Short - long range	Linear
Combined scheme	Short - long range	Nonlinear - linear
BPS	Short - long range	Linear

interaction also depends on the initial ion projectile velocity regimes mentioned before. The models are derived with use of the kinetic theory plasma description approach by adding the different approximations for the collision integral in the right part of Vlasov equation (See Sec. 2.1.5) and a described as follows.

The Random Phase Approximation (RPA) [131] which includes plasma density oscillations using the Lenard - Balescu collision integral [129, 11] estimates the stopping power in the long - range interaction domain which includes the collective effects and moderate collisions ()weak coupled plasma) It is typically evaluated in the first Born approximation [141] in the frame of quantum scattering theory. One can write the simplified case of RPA (Lenard - Balescu) derived from kinetic theory (Vlasov - Poisson equation) as:

$$\frac{\partial E}{\partial x} = -\frac{Z_p^2 e^2 \omega_{pe}^2}{v_p^2} G\left(\frac{v_p}{v_{th}}\right) \ln\left(\frac{\lambda_D}{b_0}\right) + H\left(\frac{v_p}{v_{th}}\right) \ln\left(\frac{v_p}{v_{th}}\right) \tag{2.143}$$

T - Matrix stopping power model describes the short-interaction domain by adding Boltzmann collision integral that includes strong collisions and neglects collective plasma effects [121] (strong coupled plasma) . In this model the scattering cross sections of the Coulomb interaction are calculated by T - Matrix scheme in the Lippmann-Schwinger equation. The analytic expression for the stopping power approximation is given by [151]:

$$\frac{\partial E}{\partial x} = -\frac{m_e^2}{\mu^3}\frac{n_e\lambda_e^3}{4\pi^2\hbar^3}\frac{k_B T_e}{v_p}\int_0^{+\infty} dp p^3 Q_{bc}^T(p)\left[p_- \exp\left(-\frac{m_e v_-^2}{2k_B T_e}\right) - p_+ \exp\left(-\frac{m_e v_+^2}{2k_B T_e}\right)\right] \tag{2.144}$$

where $p_\pm = 1 \pm \mu k_B T_e / m_e p v_p$, $v_\pm = p/\mu v_p$ with projectile momentum p and $Q_{bc}^T(p)$ is transport cross section of the scattering of the projectile ions on target electrons. In the first Born approximation, the collision integral can be re - considered as Laundau collision integral that takes to account Coulumb collisions that can be used for the case of the intermediate interaction range with weak collisions.

The T- Matrix model can also be modified in order to include the collective effects and make it valid in the long range interaction regime. For this case one has to introduce the dynamic screening length in Eq. 2.144 [65]. It is refereed in the literature as **T- Matrix model with $\lambda_D^{'}$**.

Li - Petrasso stopping power model [130] is one of the unified stopping power models that covers all impact parameter domains from short - range to long - range interactions. It is valid for fully ionized plasma, but in the linear regime of the beam - plasma interaction. It was obtained from the Fokker-Plank kinetic equation in the Landau approximation taking into account both, close collision and collective effects:

$$\frac{\partial E}{\partial x} = -\frac{Z_p^2 e^2 \omega_{pe}}{v_p^2} G\left(\frac{v_p^2}{v_{th}^2}\right) \ln\left(\frac{\lambda_D}{b_{min}} + \Xi\left(\frac{v_p^2}{v_{th}^2}\right) \ln\left(1.123\frac{v_p}{v_{th}}\right)\right) \tag{2.145}$$

where Ξ is a step function that takes to account collective effects.

Another proposed kinetic approach to access all the ranges of the interactions based on the combination of the T - Matrix and T-Matrix and RPA in the first Born approximation stopping power models in one and is called the **Combined scheme** [83, 142, 151]:

$$\frac{\partial E}{\partial x} = \left(\frac{\partial E}{\partial x}\right)^{T-Matrix} + \left(\frac{\partial E}{\partial x}\right)^{BornRPA} - \left(\frac{\partial E}{\partial x}\right)^{BornT-Matrix} \tag{2.146}$$

Then, the collective effects are described by Born RPA term for the long range interactions while binary collisions are taken to account by T-Matrix. The third term is needed to subtract the Landau stopping power in intermediate range.

The so called **Brown-Preston-Singleton (BPS) stopping power model** developed by [33] also covers all the ranges and valid for all the velocity projectile velocities for the ideal plasma case. It uses the RPA Lenard - Balescu and Boltzmann equations.

In another approach, one can use numerical simulations to perform stopping power estimation using PIC codes in the long - range interaction regime. However such simulations can only take into account only the collective effects unless the collision modules are included in order to cover intermediate range interactions.

Ion stopping power modelling in WDM One of the most challenging proton stopping power modelling questions is related to the strongly coupled and degenerate plasma conditions known as Warm Dense Matter. Thus far there is no straight - forward technique to estimate beam - WDM interaction due the difficulties of modelling of partially ionized plasma ,where ions stay bound with some of their electrons. In this regime strong many-body coupling and quantum electron degeneracy effects are present that have to be described. Several approaches can be applied to determine the ion stopping power. The ad hoc combination of independent bound- and free-electron components [Hansen et al., 229] can be used to split electronic stopping power into two parts, where one gives the ion stopping power due to the free electrons estimated by the same models as for fully ionized plasma and the other one gives the stopping due to excitation and ionization processes caused by the bound electrons. Recent models of B+F stopping power have been applies for low velocity projectile cases [36, 35, 15]. An example calculation of stopping power in 50 eV aluminium is given in Figure 2.23.

Another approach is based on the first-principles average-atom model self-consistent approach for astrophysical and laboratory plasmas (SCAALP) based on the finite-temperature density-functional theory and the Gibbs–Bogolyubov inequality [69, 81]. More commonly called as AA-LDA Model.

The most recent approach takes into account quantum many body theory [12] and combines it together to estimate the thermal and electric conductivity of WDM for the electronic stopping power estimation [220]. A very recently developed time-dependent orbital-free density functional theory (TD-OF-DFT) method for ab initio calculations developed by Y. Ding *et al.* [58] looks very promising for the charged-particle stopping power with different projectile velocities in warm dense matter. An example calculation of this model compared to 32 eV Be plasma is given in Figure 2.24.

In conclusion, various stopping power models have been outlined in order to describe the ion beam plasma interaction in all domains and for different velocity projectiles. However, large discrepancies between theories is noticed in the region near the Bragg peak in hot

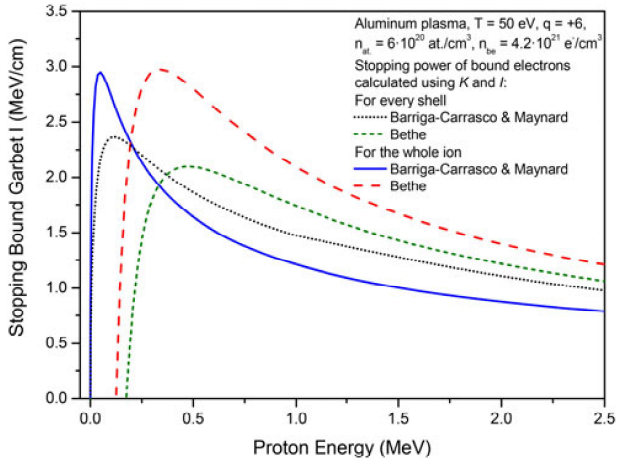

Fig. 2.23 Stopping power of bound electrons as function of proton energy. Two different sets of K and I for the aluminum ion plasma are used in the calculation of stopping power using Bethe-style effective ionization potential and [15] (Barriga-Carrasco & Maynard). The graph and the caption are taken from [35].

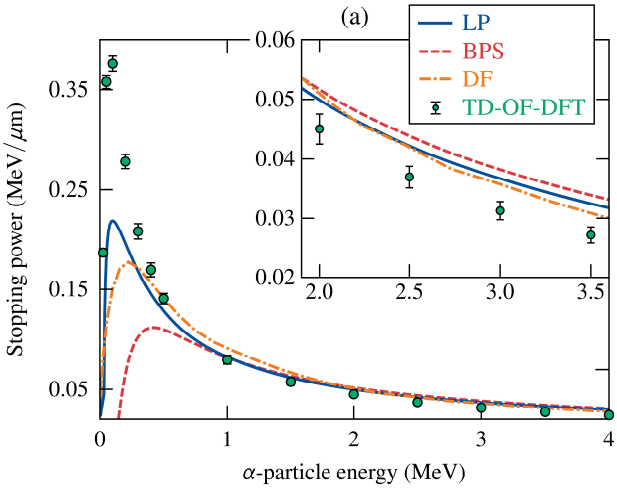

Fig. 2.24 A comparison of TD-OF-DFT calculated proton stopping power by a $k_B T_e$ = 32 eV and ambient-density Be plasma, with (CD) and without (TFW) current dependent dynamic potential, from a single MD snapshot and averaged over initial projectile positions.The graph and the caption are taken from [58].

plasma, likely coming from strong collisions and collective effects as well as nonequilibrium charge - state behaviour. In order to understand better the physics behind these differences, experimental benchmarking is required in different plasma conditions. At present the experimental database is very limited and only a few experiments has been performed, mostly in the high velocity projectile ratio range in extreme states of plasma like hot dense plasma (high energy density plasma) [100, 57, 76, 180, 77, 99, 78] and warm dense matter [231, 76, 39, 40]. The short summary of the state of art of the featured experiments is given below.

2.5.5 Relevant stopping power experiments

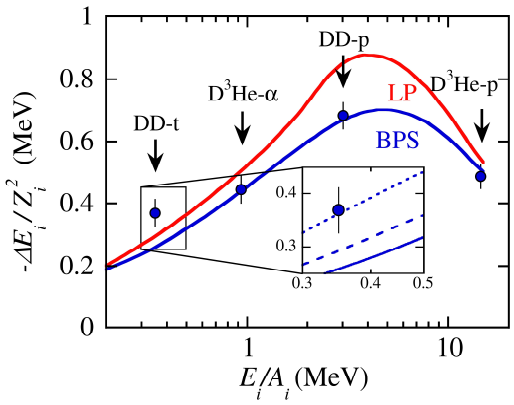

Fig. 2.25 Measured and predicted ion stopping power for different velocity projectile ratios. The blue and red curves represent the BPS and LP predictions, respectively, for the measured $< T_e >$ and $< n_e L >$ values shown in Table2.2. The graph also illustrates the DD-t data point, BPS predictions for tritons interacting only with electrons (solid blue), tritons interacting with electrons and ions (dashed blue), and tritons interacting with electrons and ions where the ion-ion component has been increased to enhance the total ion stopping by 20%. The graph and the caption are taken from [78].

Recently several important experiments have been performed in order to benchmark the stopping power models near the Bragg peak [99, 77, 231, 40, 78]. The experimental conditions are very challenging in terms of the generation of the projectile with certain velocity of interest and plasma conditions with well characterized electron temperature T_e and density n_e. The very first experiments focused on the measurement of ion stopping power covering a wide range of velocity projectiles near the Bragg peak in high energy density plasma were performed by D. Hicks *et al* [99], and the most recent by J. Frenje *et. al* [78] advancing the previous studies [77] at the OMEGA laser facility (USA). In this experiment the 60 laser laser beams deliver 12 KJ in a nanosecond duration pulse to

Table 2.2 Courtesy of experimental conditions from J. Frenje *et al.* [78]

Ion source	E_p [MeV]	$< T_e >$ [keV]	$< n_e >$ [10^{23}cm^{-3}]	v_p/v_{th}
DD - t	1.01	1.5 - 1.6	3.9	0.3
DD - p	3.02	1.5 - 1.6	3.9	1
D^{3}He - α	3.71	1.5 - 1.6	3.9	3
D^{3}He - p	14.63	1.9	3.9	10.5

the deuterium-helium-3 gas-filled capsule to drive a symmetric implosion. It triggers the following nuclear reactions that produces monoenergetic ion sources of different energies:

- D + D $\rightarrow$ t(1.01 MeV) + p (3.02 MeV)
- D + ^{3}He $\rightarrow$ ^{3}He (3.71 MeV) + p (14.63 MeV)

The measured energy loss of these ion projectiles in the hot dense plasma generated by the implosion and the modelled stopping power in the same plasma conditions using the unified stopping power models of Li- Petrasso [130] and BPS [33] are shown in Figure 2.25. A summary of the experimental conditions is given in Table 2.2. It is worth noting, that the presented values of time integrated temperature and density is weighted indicating that energy loss is estimated for the projectile passing from the hot spot to the edge of the imploding shell.

The Fig. 2.25 shows that BPS [33] model is in better agreement with experimental data in comparison with the Li - Petrasso model [130] except for the the lowest projectile ratio of $v_p/vth = 0.3$. One of the possible explanations provided is based on the fact that such significant additional energy loss may be coming from the contribution from the ion-ion nuclear-elastic and Coulomb scattering that are neglected in the stopping power models compared to experimental data.

The experiment performed by W. Cayzac *et al.* [40] at GSI laser facility (Germany) features the ion stopping power measurements at low velocity projectile ratio near the Bragg peak in laser driven plasmas with $T_e \approx 150$ eV and density $n_e \approx 5 \times 10^{20}$cm^{-3} featuring plasma coupling $\Gamma \approx 0.01$ and plasma degeneracy $\Theta \approx 550$. The plasma was generated by focusing laser beams at a Carbon target from both sides to reach quasi-homogeneous plasma conditions. The ion source was generated by an ion bunch of initial energy 3.6 MeV per nucleon degraded through 41 μ m thick Carbon foil resulting in an ion projectile energy of 0.5 MeV per nucleon. The experimental conditions are summarized in Table 2.3. The Figure 2.26 shows the measured energy loss and calculated energy loss for the given

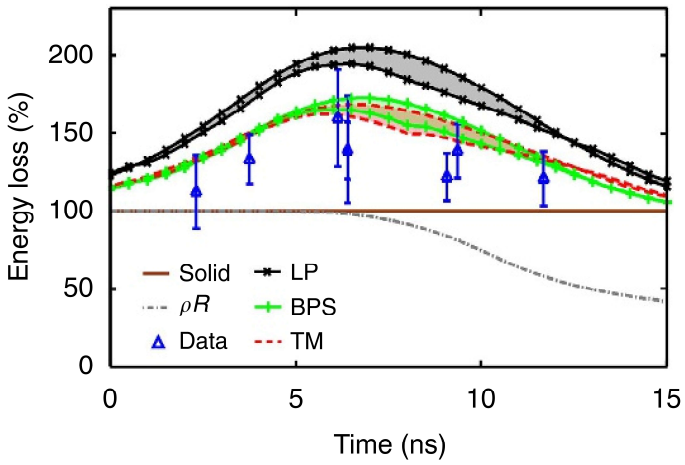

Fig. 2.26 Measured time resolved energy loss compared with the predictions of the LP [130], TM as well as BPS [33] stopping-power models using the Gus'kov projectile charge model [90]. The shaded areas show the differences between calculations considering the 1D (upper lines) or 2D plasma profile (bottom lines) respectively. Time averaging over the 5.5 ns bunch. Graph and legend are taken from [40].

Table 2.3 Courtesy of experimental conditions from W. Cayzac *et al.* [40]

Ion source	E_p [MeV]	T_e [eV]	n_e [10^{20}cm^{-3}]	v_p/v_{th}
Ion bunch	0.586 ± 0.016	150	5	1.2

plasma conditions with the unified stopping models of Li-Petrasso, T-Matrix and BPS. The comparison between the experimental data and models shows that T- matrix and BPS are in quite good agreement with the data while LP model systematically overestimate the energy loss by 20–25%. It seems that the applied models based on perturbation theory are failing to reproduce the experimental data for both described experiments . However approaches with a full description of binary collisions is in better agreement with the data. Therefore for the better stopping power description in the region near Bragg peak the collisions have to be modelled more precisely.

In the context of warm dense matter studies, a recent experiment was performed at the OMEGA laser facility by A. Zylstra *et. al* [231] using monoenergetic protons created from DHe3 exploding pusher targets as projectiles, probing a warm dense beryllium sample isochorically heated by X-rays and featuring $\Gamma = 0.3$ and $\Theta = 2$. In that work, the high-velocity stopping regime was probed using 14.63 MeV protons, with a corresponding velocity ratio $v_p/v_{th} > 10$ for which differences between theoretical stopping power predictions are small. The experimental conditions are summarized in the Table 2.4. The plasma parameters

Table 2.4 Courtesy of experimental conditions from A. Zylstra *et al.* [231]

Ion source	E_p [MeV]	T_e [eV]	n_e [10^{23}cm^{-3}]	v_p/v_{th}
D^3He - p	14.63	32	2.91	10

could not be directly measured and were instead deduced from previous similar experiments. The results are shown in the Figure 2.27 (left) in cold and warm dense matter and compared to the models that allow to treat partially ionized matter such as an ad hoc combination of independent bound and free components [229, Hansen et al.], using the AA-LDA model [69] , or by using a Bethe-style mean ionization potential. The first two models show quite good agreement with the experimental points mostly because they provide better description of the electronic structure of Warm Dense Matter. From another side Figure 2.27(right) the additional theoretical model based on time-dependent orbital-free density-functional-theory formulation (TD-OF-DFT) is compared to the result showing even better agreement with data.

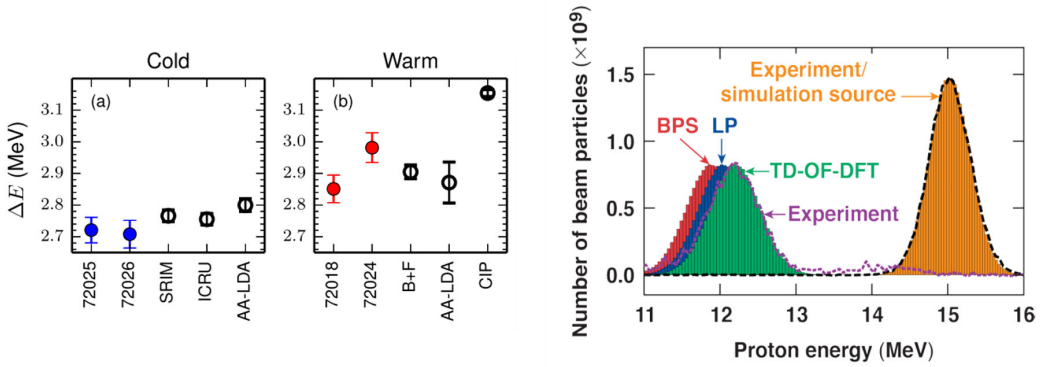

Fig. 2.27 Downshifted (ΔE) for cold (a) and warm (b) shots compared to theory indicated as "B+F" is an ad hoc bound + free model [229], "AA-LDA" [69] and "CIP" refers to BPS model for nondegenerate plasma [33]. The solid points are data (denoted by shot number), and theories are hollow points. The uncertainties in theoretical calculations are due to uncertainties in ρL and plasma conditions. Graph and legend are taken from [231] (left). The calculated downshifted spectra of α particles passing through the 50- μm DT slab at the same warm dense condition from both TD-OF-DFT simulations (green) and the two stopping-power models (red and blue). Graph taken from [58].

2.5.6 Conclusion

Ion stopping in dense plasmas is an important topic in various fields of modern physics that is still far from being completely understood. It plays a central role in Inertial Confinement

Fusion (ICF) for the target self-heating by alpha-particles that triggers ignition and thermonuclear gain [106], and it is even more crucial for target heating schemes using ion beams as main drivers like heavy-ion fusion or ion-driven fast ignition. Ion stopping in plasmas is also essential in high-energy-density physics for the generation and the characterization of Warm Dense Matter (WDM) [220], in astrophysics as well as for plasma diagnostics using ion beams [87, 136, 218, 183]. Moreover, a detailed understanding of the ion-stopping processes is relevant for related transport properties in plasma, like electrical and thermal conductivity or temperature equilibration [65, 97]. Here, we focus on the stopping power due to the target electrons, which is always dominant except in very hot burning ICF plasmas. The experimental database is essentially limited to large projectile velocities, significantly above the thermal velocity of plasma electrons $v_p \gg v_{th}$ [100, 57, 76, 231], validating the perturbative stopping-power models in that range. The parameter region for $v_p \sim v_{th}$(Bragg peak) is theoretically and experimentally more challenging. The beam-plasma coupling is important and both close binary collisions and collective plasma excitations need to be taken into account, which leads to large discrepancies between the predictions of different stopping-power models [39, 66, 61]. Moreover, as the stopping power strongly depends on temperature and density, a precise characterization of the target conditions is required in experiments. Very few measurements are available, done in classical, ideal plasmas [77, 40]. Furthermore, when the plasma target is nonideal (moderate electron coupling, for $\Gamma > 0.1$) and degenerate ($\Theta < 10$), which occurs in WDM conditions, the ion collisions with the plasma electrons are modified and important additional effects are thus expected on the stopping power. The understanding of ion transport properties in coupled and degenerate targets is especially required for guiding and interpreting experiments involving WDM targets generated by ion beams, for example for equation of state investigations, and for better understanding the mechanisms leading to ignition in ICF targets. More generally, it has fundamental implications for non-equilibrium statistical mechanics and the underlying atomic processes. However, until today, ion stopping in WDM conditions remains largely unknown and has only been investigated at high projectile velocity [231]. In this experiment performed at the OMEGA laser facility, monoenergetic protons created from DHe_3 exploding pusher targets were used to probe a warm dense beryllium sample isochorically heated by X-rays and featuring $\Gamma = 0.3$ and $\Theta = 2$. The proton energy was 14.63 MeV, corresponding to a velocity ratio $v_p/v_{th} > 10$. The results were in agreement with well established high-velocity stopping formalisms and did not allow to discriminate between classical and quantum stopping power models. Meanwhile, the velocity region close to the Bragg peak in WDM, where the largest uncertainties on the stopping power are reported [230, 64, 56, 98, 61], has never been experimentally investigated until now. The goal of our

experiment is to provide measurements in this relevant "terra incognita" parameter region. We want to generate WDM conditions comparable to those of [231] and to probe them at a lower velocity ratio $v_p/v_{th} \sim 2-3$ in order to approach the Bragg peak. The experimental requirements are summarized as follows:

1. A well-defined ion source (energy and charge-state): we use a laser-generated proton source, with energy selection to obtain a quasi-monoenergetic beam. As no beam charge state consideration is necessary, theoretical predictions can be directly compared with measurements;

2. A well-defined WDM target (density, temperature, ionization degree) generated by a femtosecond laser pulse, which avoids early hydrodynamic motion and provides a dense and relatively uniform sample;

3. A sufficiently high ionization degree to minimize stopping-power uncertainties due to target bound electrons;

4. A significant degree of electron coupling and degeneracy of the target ($\Gamma > 0.1$ and $\Theta < 10$);

5. A sufficiently low projectile velocity and high temperature for having v_p/v_{th} approaching unity

2.5.7 Motivation for ion stopping power experiment

The large discrepancies between the theories and the fact that only a few experiments have been performed motivates the need for a more comprehensive experimental database for the benchmarking of models and for a better understanding of the nature of the stopping power in the region close to Bragg region under conditions of high energy density plasmas, moderate plasmas and warm dense matter. Special attention is required for the low velocity projectile stopping power in the warm dense matter conditions, where the most uncertainties appear due to the absence a good description of the Equation of State of the partially ionized matter. Many novel models start to appear describing the beam - WDM interaction using various approaches. However, to our knowledge no experiment has been performed yet under conditions featuring a low velocity projectile ratio and warm dense matter state of matter. The main objective of this work is to design an experiment that would allow us to reach such experimental conditions and make measurements with good statistics required for the precise benchmarking and testing of the models. In particular, we consider the ion projectile of 0.5 MeV and WDM with electron temperatures $T_e = 5-20$ eV and density $n_e \approx 1 \times 10^{23}\text{cm}^{-3}$

that gives the velocity projectile ratio of $v_p/v_{th} \approx 2.5$. As far as the ion projectiles generated from nuclear reactions have been quite limited in projectile energy based on limited fusion reactions, we propose to use a laser driven ion source generated by the TNSA mechanism. The generated beam is then selected with a magnet based energy selection system to obtain a minimum energy bandwidth as close as possible to a mono-energetic beam condition. This system allows a very wide range starting from 0.3 MeV up to 2 MeV featuring minimum bandwidth of 3.8 KeV. In addition, the WDM will be generated by use of spatially smoothed fs - laser beam focused on the thin low Z foil providing electron temperatures $T_e = 5 - 20$ eV at near solid density.

Chapter 3

Experimental study of fast electron transport

3.1 Relativistic electron beam diagnostics

Fast electron transport diagnostics are mainly based on the collection of the electromagnetic emission in the keV - MeV energy range produced by the propagation of the fast electrons into the target. Such diagnostics are helping to characterize fast electron sources created by the intense laser pulse interaction. In this section we are focused on the of the X - ray emission and optical emission diagnostics used during the LULI-ELFIE experimental campaign. The collection of the X-ray emission such as X-ray spectroscopy and X-ray imaging methods provide providing information about electron beams in the keV - MeV energy range are discussed. As for optical emission diagnostics the Coherent Transition Radiation (CTR) is described as a tool to access the high energy part of the electron beam ($\geq$ MeV).

3.1.1 X-ray diagnostics

K_α emission

The fast electrons accelerated by a picosecond laser have an extended energy spectrum, from thermal agitation energy (of the order of the eV) to relativistic energies $\sim$ 10 MeV). We are particularly interested in the high-energy portion of this spectrum because only the fastest electrons can cross several tens of microns of matter. We must therefore distinguish the relativistic electrons from the thermal electrons. For this we know that an electron will be able to excite an atomic line only if the kinetic energy E that it possesses is greater than the energy of a corresponding atomic transition E_{ij}. By choosing E_{ij} as high as possible, we can

make sure that only the fastest electrons will be taken into account. In a given atom, the most energetic transition corresponds to a K-level electron (also named 1s orbital, characterized by the quantum number n = 1, the closest to the nucleus) snatched from the atom. It is therefore a bound-free transition. This ionization can only take place if the incident electron has an energy higher than the binding energy of this K-shell B_K, given as a function of the atomic number Z < 92, with a 4 percent of maximum error, by [37]:

$$\frac{B_K}{R_y} = 0.424Z^{2.1822},\ R_y = \frac{m_e e^3}{8\varepsilon_0^2 h^2} \sim 13.606\ [\text{eV}] \tag{3.1}$$

where R_y is the Rydberg energy. When such an ionization process occurs, the ion can decay down to a more stable state by filling in the inner shell gap with an electron coming from an outer shell (L or M shells).

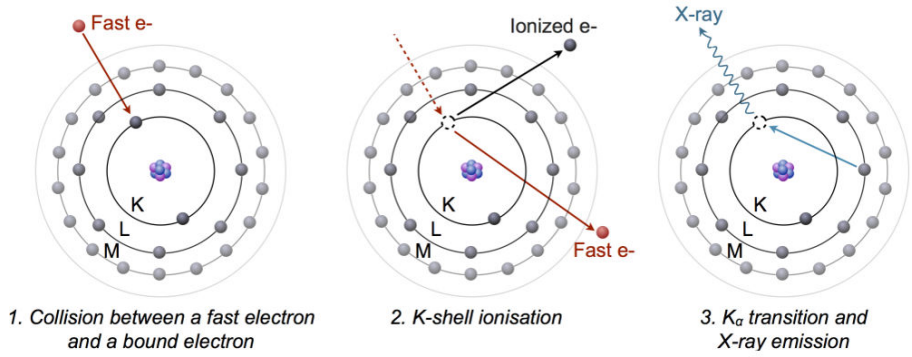

Fig. 3.1 Process of K_α emission caused by fast electron
.Image taken from [209].

For example, for copper, a material commonly used in our experiments, E_{K_α} = 8002 eV. Only electrons whose kinetic energy is higher than B_K = 8996 eV are likely to cause this ionization. The gap thus produced in the layer K is rapidly filled by the electrons of the layer with a higher quantum number. In particular, an electron of the L layer (that is to say $2p_{1/2}$ or $2p_{3/2}$) can fill this gap and emit a photon whose energy is equal to the difference between the starting level E_L and the final level of arrival E_K. To summarize, Figure 3.1 explains that an incident electron with an energy kinetic E can expel a K shell electron by providing it with at least the ionization energy I_K. The gap is then filled by a transition from L to K emitting a photon of energy E_K - E_L. This latter X-ray fluorescence is called K_α emission in the case of a 2p to 1s transition (L-shell to K-shell). This emission is isotropic.
In fact K_α transitions are split into two possible transitions called K_{α_1} and K_{α_2} and corresponding to $2p_{1/2} \rightarrow 1s$ and $2p_{3/2} \rightarrow 1s$ transitions, respectively. However we have to take into account the quantum selection rules allowing atomic transitions between two energy

levels only if $\Delta l = \pm 1$ and $\Delta j = 0, \pm 1$, with l the orbital quantum number and j the total angular quantum number. . As a consequence the $2s_{1/2} \rightarrow$ 1s transition is forbidden. K_β emission corresponding to a 3p $\rightarrow$ 1s transition (M-shell to K-shell) can also occur, even if it is less probable than the K_β emission. Besides, because of the successive ionization of the outer shells for increasing temperature, the probability of K_α emission decreases with the temperature. All these radiative transitions are summarized in 3.2, for the case of copper atoms.

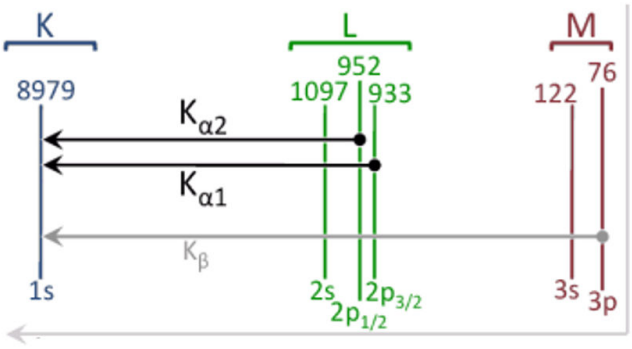

Fig. 3.2 Radiative Transitions in Cu atoms.

The K_α energy transitions can be estimated with the Moseley empirical law as a function of the atomic number Z for 3 < Z < 60. Moseley's model assumes that there is no distinction between K_{α_1} and K_{α_2} emissions and provides an estimation with a 5 % error [152] given by:

$$E_{K_\alpha}[\text{eV}] = 10.206(Z-1)^2 \tag{3.2}$$

Ionization energy

The ionization energy I_K is tabulated according to the atomic number Z with 1 percent accuracy for materials of Z $\geq$ 10. It is given by:

$$I_K[\text{eV}] = Z^{2.16} \times (-3.46 + 8.535 \ln Z - 2.594(\ln Z)^2 + 0.256(\ln Z)^3). \tag{3.3}$$

Cross section

The effective cross-section for K-ionization by electronic impact is given by the semi-empirical formula: [101]:

$$\sigma_K = 2\pi r_0 D \left(\frac{R_y}{I_K}\right)^C D \tag{3.4}$$

where $r_0$is the Bohr radius , R_y is the Rydberg energy, C and D are two quantities without units depending of the incident electron energy ε and I_K. They can be expressed more easily using two dimensionless parameters $U = \varepsilon/I_K$ so called overpotential and $J = m_e c^2/I_K$ [101]:

$$\begin{aligned} D = &\left(\frac{1+2J}{U+2J}\right)\left(\frac{U+J}{1+J}\right)^2\left(\frac{(1+U)(U+2J)(1+J)^2}{J^2(1+2J)+U(U+2J)(1+J^2)}\right)^{3/2}\times \\ &\times\left(3.125-\frac{4.172}{U}+\frac{1.877}{U^2}\right)\frac{\ln U}{U} \end{aligned} \tag{3.5}$$

$$C = 2.0305 - \frac{0.3160}{U} + \frac{0.1545}{U^2} \tag{3.6}$$

The Figure 3.3 presents the cross section σ_K as a function of electron energy for the common materials widely used in experiments demonstrating the efficiency of the K - shell ionization. It is worth to note that the cross section is obviously zero below I_K, and relatively constant above $2I_K$ for energies that interest us.

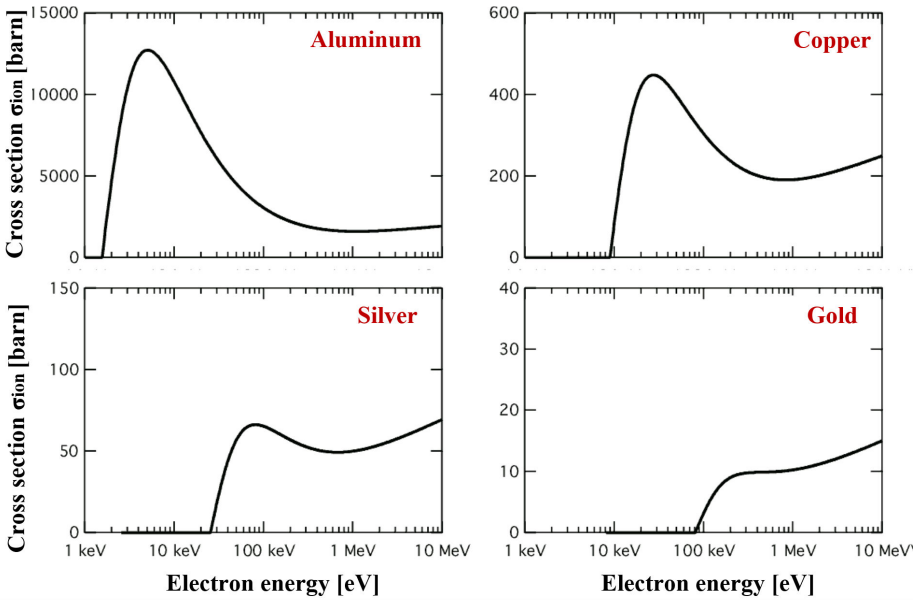

Fig. 3.3 K-shell ionization cross sections as a function of the incident electron energy for the aluminium (top left), copper (top right), silver (bottom left) and gold (bottom right).

K_α fluorescence

Some ionized K-shell atoms do not emit an observable photon. The K_α photon emitted can be directly reabsorbed by another electron from the electronic orbits. This Auger electron is ejected and carries with it the energy of the photon. The probability that the K_α photon is emitted depends on the atomic number Z. A semi-empirical formula allows to easily calculate this yield [13]:

$$W_K(Z) = \frac{\left(\sum_{i=0}^{3} C_i Z^i\right)^4}{1+\left(\sum_{i=0}^{3} C_i Z^i\right)^4}, \tag{3.7}$$

where $C_0 = 0.037$, $C_0 = 0.031$, $C_2 = 5.44 \times 10^{-5}$, $C_3 = -1.25 \times 10^{-6}$.

This yield can also be estimated by an empirical formula proposed by A. Kahoul *et al.* [107], based on experimental results in the $6 \leq Z \geq 99$ range:

$$f_K = 0.985 \frac{(Z/30.896)^{3.847}}{1+(Z/30.896)^{3.847}} \tag{3.8}$$

Figure 3.4 shows the fluorescence yield as a function of the atomic number Z both for experimental results and the fit given by Eq. 3.8. Experimental values are provided by [107].

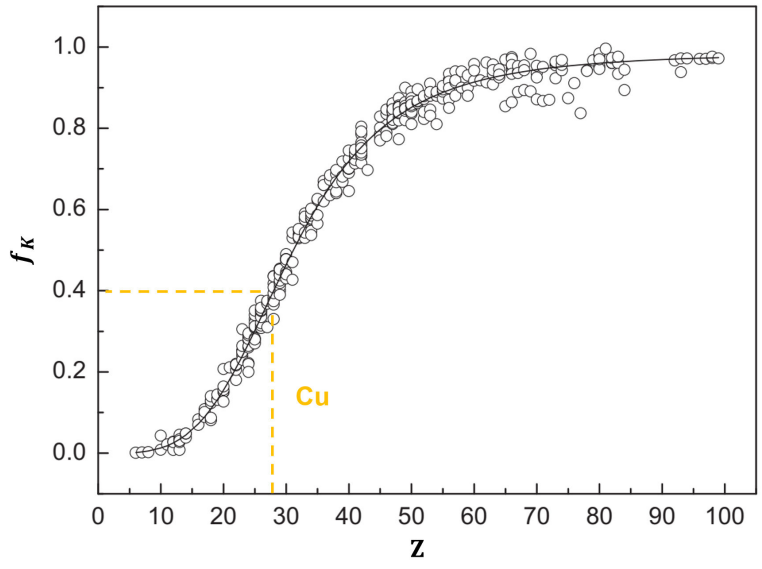

Fig. 3.4 Distribution of experimental K-shell fluorescence yields as a function of atomic number. The curve is the fit according to Eq. 3.8. The highlighted value is for copper (orange) that was used in LULI-ELFIE experiment.Graph taken from [163].

K_α photon number

We can approach to estimate photon number by using the fluorescence formulas Eg. 3.7 or 3.8.

For example using the Eq. 3.7 we can estimate the number of photons emitted per unit of time:

$$\frac{d/N_{photons}}{dt} = W_K n_i \int v\sigma_K(v) f(v) dv \tag{3.9}$$

where $f(v)$ is the velocity distribution of the electron beam that propagates in a medium with an ion density n_i. In our experiment the medium of fast electron beam propagation is a copper tracer with thickness of $\sim 5\mu$m buried into the target rear. And therefore the number of photons emitted per unit of length:

$$\frac{d/N_{photons}}{ds} = W_K n_i \int \sigma_K(v) f(v) ds \tag{3.10}$$

It is easy to see that the amount produced K_α radiation is not so sensitive to injected electron average velocity.

K_α spectrum

The transition K_α with two main lines K_{α_1} and K_{α_2} given for copper atoms is shown on Fig. 3.2. By calculating the energy difference between the levels of departure and arrival, we see that the two lines K_α correspond to an energy of the photon emitted from 8046 and 8027 eV respectively. Corrections including the density of the solid material lead to 8048 and 8028 eV.

We will consider the use of the K_α line spectrum comparing to experimental results of K_α spectroscopy diagnostics used in LULI-ELFIE experiment. Firstly, we can describe some some general behaviour. For this we can simulate it with the atomic code FLYCHK [45] which allows to estimate the spectrum obtained when a fast electron beam passes through a material. The example of copper is given on the Fig. 3.5. An electron beam of 300 keV average energy, with a density 1000 times less than the rest of the electrons, is injected into a plasma of different electronic temperatures. We get two emission lines. The $K_{\alpha 2}$ line is twice as weak as the transition probability is also twice as small. In cold copper, the two lines are well separated, but one observes that they begin to widen towards 40 eV. This enlargement is due to the separation of the levels by the Stark effect, coming from microscopic electric fields all the more important that the ionization is strong [7]. At higher temperatures (100

eV), the lines become even more wide and also start to move towards higher energies. This comes from the change of screening fields when ionization increases [197].

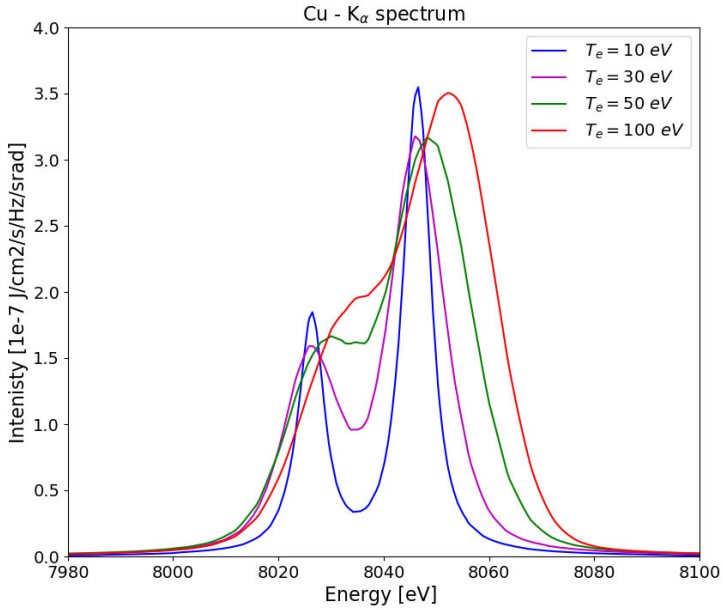

Fig. 3.5 K_α spectrum of copper when it is crossed by fast electron beam with mean energy of 300 keV simulated with the FLYCHK code for different plasma temperatures.

However making the calculations we have to remember that : First, the model used in FLYCHK depends on sometimes poorly known parameters, and the value of absolute temperature, that experimentally can have some inaccuracy in measurement. We can observe therefore temperature differences more accurately than the absolute temperatures. Next, the simulation assumes a uniform temperature and electron beam, and corrections must be made to take into account possible inhomogeneities. Finally, there may also be a significant absorption of K_α lines due to a number L-shell holes. This is not fully taken into account by FLYCHK: opacity codes may be required to determine this effect.

To conclude , the shape of the K_α lines (position and width) is related to the electronic temperature of the plasma. The profile of the spectral lines thus makes it possible to estimate this temperature.

K_β spectrum

The K_β emission corresponding, to a M-shell to K-shell transition, is less intense than Kα emission, by a factor 10 at a low temperature. The Kβ emission, also subject to emission line

broadening. It is more affected by the increase of the electron temperature and the resulting ionization of the M-shell. The plasma temperature can be directly estimated from the K_β emission line, or, in a more common way, by the ratio between the K_α and the K_β emissions as shown in the Figure 3.6 [154, 157].

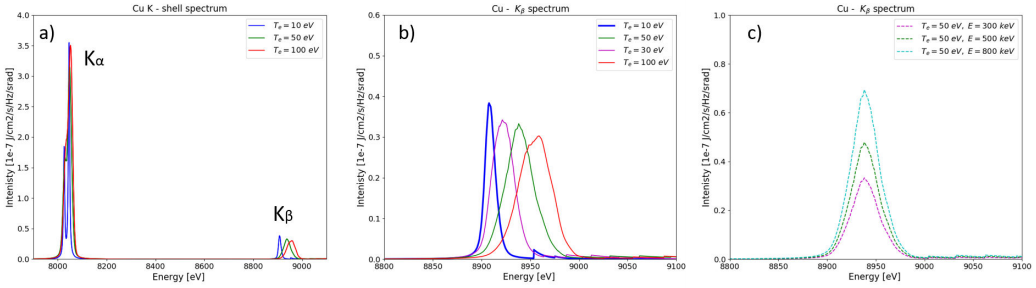

Fig. 3.6 K_α and K_β spectrum of copper when it is crossed by fast electron beam with mean energy of 300 keV simulated with the FLYCHK code for different plasma temperatures (a,b). We observe the decay of the K_β line as the temperature increases.

Bremsstrahlung emission

Bremsstrahlung radiation of fast electrons when deflected by collision gives essential information about the fast electron beam. Two notable differences exist with the emission lines indicated above. First, as it is a braking radiation and not an atomic transition, the bremsstrahlung does not have emission lines, but a continuous spectrum and decreasing in energy. Its intensity is much lower and therefore more difficult to detect that K_α radiation. Then, as it comes from the movement of the electron, it will have a privileged direction, close to that of the electron beam. For relativistic electronsthe Bremsstrahlung spectrum is usually calculated numerically and then tabulated [170, 196]. It is also more marked for the fastest electrons (> 1 MeV) emits more energetic photons. The knowledge of the bremsstrahlung spectrum allows one, in principle, to estimate the energy distribution of the incident electrons. The angular distribution [190] has a maximum emission for a given energy. This characteristic angle is of the order of 1° for very fast electrons (> 10 MeV), and is approaching 20 ° for less fast electrons (> 1 MeV). We see that the bremsstrahlung is directed mainly in the direction of the electron beam. More specifically, the average emission angle of a bremsstrahlung photon, relative to the initial direction of the electron, is proportional to $1/\gamma$.

Bragg crystal

All the instruments of X-ray diagnostics presented in this section are based on the principle of the Bragg's diffraction law. This law was found by M. Bragg, father and son, in the beginning of the 20th century, and stating that X-rays with a certain wavelength λ are reflected by the crystals for a given grazing angle θ (Fig. 3.7) . These are the angles of incidence for which waves reflected at each crystalline layer interfere constructively. The law is written by noting θ, the crystalline planes distant from each other d and the diffracted wavelength λ is given by:

$$n\lambda = 2dsin\theta \tag{3.11}$$

where n is an order of diffraction.

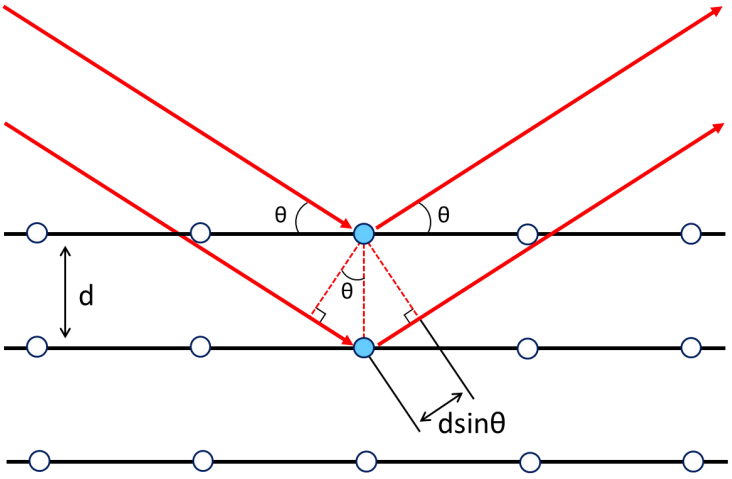

Fig. 3.7 Demonstration of work principle of Bragg's law for the incident photon at the grazing angle θ.

Basically , knowing the photon wavelength λ we can find a crystal and appropriate angle θ. However , even though theoretically it is possible to detect any photon with energy $E = hc/\lambda$, one should take into account that by reducing the incidence angle we decrease the signal intensity. Therefore we prefer to use θ greater than 10° in general. In addition, high reflection orders decrease significantly the accuracy of the X-ray diagnostics reflectivity and it is best to use n = 1 or 2. By considering the restrictions on θ and n the working range of energy within range of each crystal can be found. Most of the crystals we use scan a range of energy from 1 keV to 30 keV.

X-ray spectroscopy

We are interested in the K_α emission lines that are generated by the fast energetic electrons. Other transitions require even more energy than for the K_α lines, but they are not very intense in the case of a cold or warm solid. The aforementioned cross section shell ionization factor for copper, described in Sec. 3.1.1, has a large value above 20 keV. It means the electrons with energies > 20 eV can be detected. In our experiment we are focused in the detection of the Copper K_α emission. In this section several Bragg crystal spectrometer used in various geometries are described. They are almost all used regularly by different teams for the laser - plasma interaction experiments throughout in the world. In our experiment the Cu K_α spectrometer was used in cylindrical geometry and imaging spectrometer in spherical geometry.

Flat crystal spectrometer

This is the easiest form to use a Bragg crystal for a point source of x-rays such as laser produced plasma. In this configuration the crystalline planes are parallel to its surface, making it similar to a mirror. A given point of the crystal receives at the same time many X-rays of different energies. Following the Bragg's law (Eq. 3.11), an indent photon with an energy of $E = hc/\lambda$ should have a specific angle of incidence θ in order to be reflected by the crystal. Therefore a given point of the crystal receives at the same time many X-rays of different energies that will be reflected depending on its wavelength with only one wavelength reflected at high efficiency due to Bragg diffraction. We are thus able to spatially separate the different wavelengths, hence obtaining an X-ray spectrum.

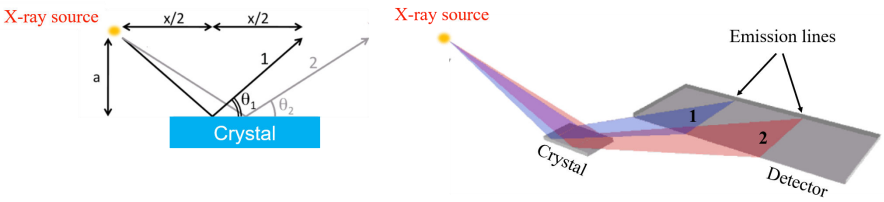

Fig. 3.8 Flat crystal geometry for two incident photons at different energies.

The sources used are much smaller than the size of the spectrometer, so they can to be considered as a points like. Using the notations in Figure 3.8 and the Bragg's law Eq.[3.11], the grazing incidence θ for the X-ray 1 an be expressed as :

$$sin\theta = \frac{a}{\sqrt{a^2 + x^2/4}} = \frac{nhc}{2dE} \tag{3.12}$$

Therefore the dispersion function of the flat crystal is found by :

$$E = \frac{nhc}{2da}\sqrt{a^2 + x^2/4} \tag{3.13}$$

The dispersion function is approximately linear for this type of spectrometer $x \gg a$. Each wavelength is reflected on an area of the crystal that has the shape of a line. We observe finally, on the detector, several lines corresponding to each wavelength present in the spectrum of the source X. In reality these lines are arcs of circle but the size of the spectrometers is often too small to observe the curvature of these arches. They are therefore fitted to straight lines.

In reality the X-ray source is an extended one. However taking into account the crystal geometry it is possible to understand directly that an extended source widens the lines spectrally which reduces the resolution.Let's consider the monochromatic source of size δx in the x - axis parallel to the crystal plane. As this crystal is flat , the spectral line will have the same size δx. Let's obtain the crystal spectral resolution relation. By differentiating the relation $x/(2a) = 1/\tan\theta$, we obtain:

$$d\theta = -\sin^2\theta \frac{dx}{2a} \tag{3.14}$$

And from another side by replacing the $\lambda = hc/E$ in the Eq. 3.11 and differentiating it we get:

$$d\theta = -\tan\theta \frac{dE}{E} \tag{3.15}$$

Combining both equations we get the dispersion relation valid for the small movements $dE/E = \frac{cos\theta \sin\theta}{2}\frac{dx}{a}$, where dx corresponds to the size of the spectral line, equal to the size of the source δ_x, and the dE is basically ΔE_x - a widening of the source according to x. Then it can be rewritten as:

$$\frac{\Delta E_x}{E} = \cos\theta \sin\theta \frac{\delta_x}{a} \tag{3.16}$$

Therefore if one now assumes a spherical source with a size δz in the z direction, perpendicular to the crystal, the broadening of the line is expressed as separate x, z broadening and we get the spectral resolution relation:

$$\frac{\Delta E_z}{E} = \cos^2\theta \frac{\delta_z}{2a} \tag{3.17}$$

Basically, if the spectral resolution is important for the measurements one should take into account the size and the position of the source and estimate the limits for this crystal configuration .

Cylindrical spectrometer

In the laser-plasma interaction experiments, intense radiation, especially due to bremsstrahlung in the target or the fluorescence induced by the particles escaping from the target, cause a quite large background noise signal. One of the main problems is then to be able to measure a very weak signal among this noise. To increase the signal-to-noise ratio we can focus the emission lines on the detector thus substantially increasing the brightness of signal. Spectra are then focused in the direction perpendicular to that of the dispersion. The easiest way to converge X-rays is to use a crystal which is concavely curved with a radius of curvature R_C The easiest way is to bend the crystal cylindrically because it preserves the surface density, and facilitates the manufacturing. By placing the X-ray source on the axis of the cylinder, the symmetry imposes that the radii all converge on this axis as shown in Figure 3.9 (left). This configuration in called a Von Hamos configuration [93]. An example of an experimental data obtained with such spectrometer configuration is shown in 3.9 (right). Here Cu - K_{α_1} and Cu - K_{α_2} emission lines are focused onto detector plane.

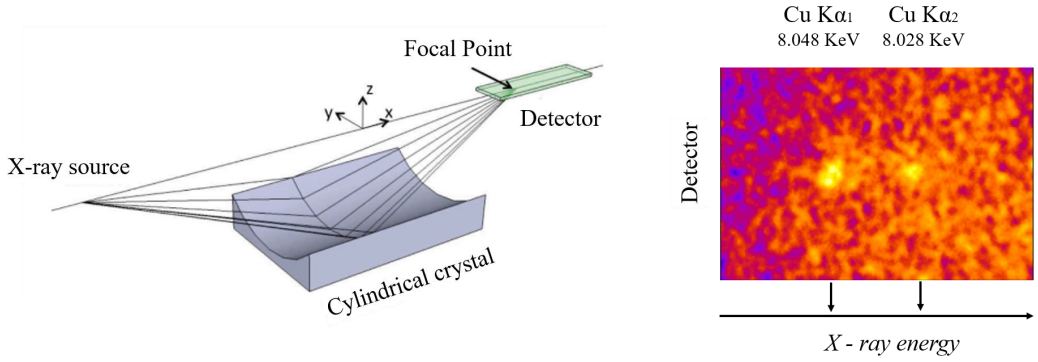

Fig. 3.9 Cylindrical crystal geometry in Von Hamos configuration. Graph taken from [163] (left). The example of the experimental data (right).

The scheme is very similar to the flat spectrometer . Therefore we have the same dispersion and the same spectral resolution as a flat crystal. However, in the y direction, the curvature of the crystal must be taken into account. The details of the curved crystal spectrometer used in this experiment are given in the Table 3.1. The achieved spectral resolution allows one to fully separate Cu - K_{α_1} and Cu - K_{α_2} [163, 209].

Table 3.1 Characteristics of the cylindrical crystal used in experiment

Crystal type	Crystal	$2d$	R_c	Dimensions	Spectral lines
Von Hamos	Quartz 2243	2.024 A	250 mm	$6 \times 5\ cm^2$	Cu - K_{α_1}, Cu - K_{α_2}

Besides two different spectrometers presented here the other geometries are also commonly used in laser- plasma experiments such as conical [91], spherical and toroidal [96] spectrometers. Each one has advantages or defects that you need to know when preparing an experiment. The required spectral resolution depends on the Bragg angle, the distance to the source, and the shape of this source and the crystal parameters. It is therefore necessary to adapt the configuration at to achieve the required resolution.

X-ray imaging

One of the possible fast electron beam characterizations that can be performed experimentally is the imaging of the x-ray emission generated by fast electrons propagating into the target. This X-ray imaging system [4, 116] can be used to estimate the spatial size of fast electron beam or its divergence depending on the tracer layer configuration. Obviously, we are interested in selection of K_α emission for viewing. It is therefore necessary to use a monochromator crystal such as a Bragg crystal described in the previous section. Different kinds of X-ray imagers are widely used in laser-plasma experiments. Here we describe one type of K_α imager used in our experiment.

Spherically bent crystal

Bragg crystals play the same role as mirrors in classical optics. So the analog of the spherical mirror is therefore the spherical crystal. Used in the same way as in conventional optics, it allows the formation of an X-ray image. The general scheme is shown in Figure3.10. As for a spherical mirror, for a crystal with a radius of curvature - R_C, the relation between the distance a between X-ray source and the crystal and the distance b between the crystal and the image is given by:

$$\frac{1}{a}+\frac{1}{b}=\frac{2}{R_c} \tag{3.18}$$

However this relation works only when considering objects close to the mirror axis and for a near normal incidence X-rays to the mirror surface (paraxial approximation). More generally, if we consider the appearance of two image planes (sagittal and tangential) during a non paraxial use, we same relation can be written as next:

Table 3.2 Characteristics of the spherical crystal used in experiment

Crystal type	Crystal	$2d$	R_c	M	Spectral lines
Spherical	Quartz 2243	2.024 A	250 mm	8.96	Cu - K_α, 8047.78 $\pm$ 5 eV

$$\frac{1}{a}+\frac{1}{b_t}=\frac{2}{R_t \sin\theta_B} \qquad \frac{1}{a}+\frac{1}{b_s}=\frac{2\sin\theta_B}{R_s} \tag{3.19}$$

where R_t and R_s correspond to tangential and sagittal image planes respectively and θ_B is a Bragg angle at the center of the mirror. The object must be located inside the Rowland circle at a distance a satisfying $2f_t > a > f_t$, where $f_t = R_t \sin\theta_B/2$ is a focal length of the tangential plane of incidence. The rays contained in the tangential plane usually focus first, leading to a distortion of the final image due to the astigmatism of the focusing crystal.

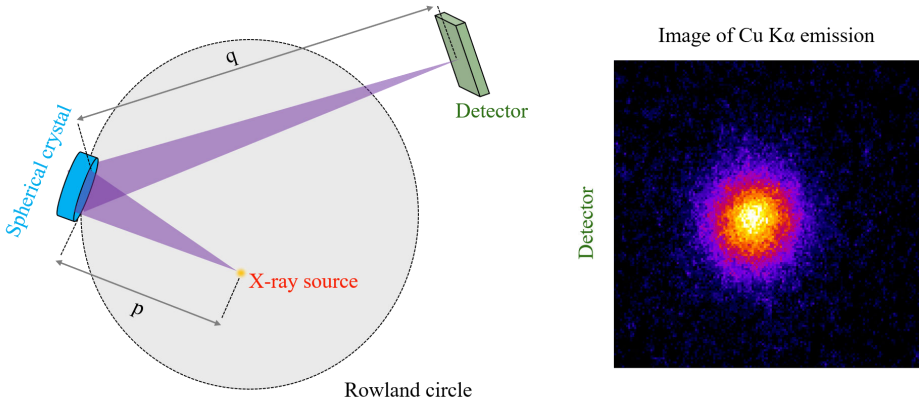

Fig. 3.10 The geometrical scheme of a Bragg imager using a spherical crystal (left). Example of Cu - K_α image obtained in experiment (right)

Knowing this one can choose the geometrical parameters, such as the radius of curvature of the crystal R_c and the a and b distances to achieve the required magnification and resolution. The magnification in fully stigmatic conditions can be estimated as $M = a/b$. For our experiments, the good spatial resolution required paraxial geometry ($\theta_0 \sim 90$) and a magnification b / a of the order of 10. We used a spherical Bragg crystal designed to detect the Cu K_α emission with characteristics presented in Table 3.2.

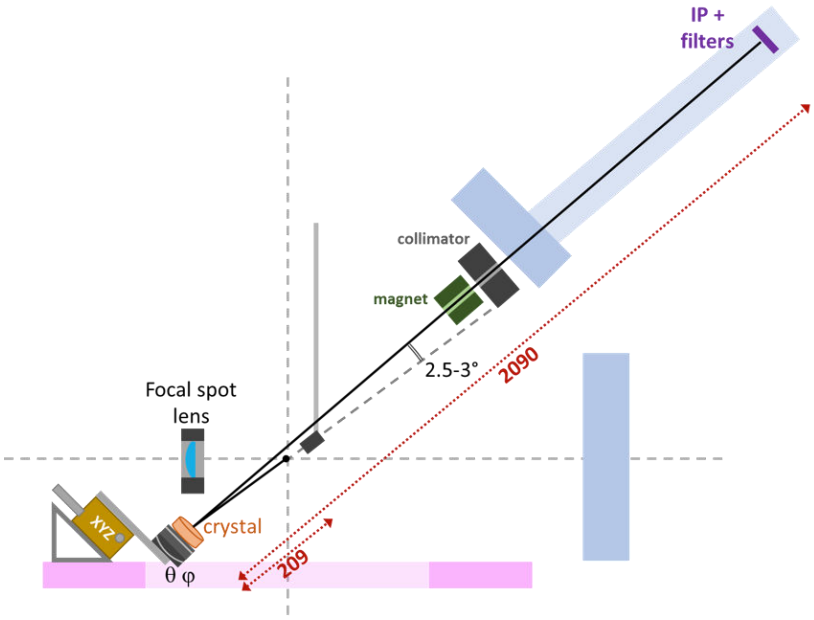

Fig. 3.11 Bragg imager setup. The distances are given in mm. The magnet and collimator that consist of lead shielding and aperture of 1 cm is employed to deflect electrons from the axis of the X - ray propagation. The Bragg imager was mounted in the special holder equipped with X-Y-Z manual translation stages in order to adjust the crystal position with respect to TCC.

The Figure 3.11 presents our experimental setup of Cu K_α imager looking at the target rear surface with the viewing angle of 37.5° and imaging the CuK_α spot onto Image Plate (IP). One could use an X - ray CCD camera instead of IPs.

The magnification and resolution of Cu K_α imager was estimated by focusing both laser pulses 300 μm × 300 μm away from the corners of a 12.5 mum thick Cu foil. Such position of the laser focusing allowed to highlight the edges of target by the cold K_α emission that surrounds the Cu K_α spot. By taking the line out of the target edge obtained with imager and comparing it to the sharp edge we estimate the final resolution of 15 μm.

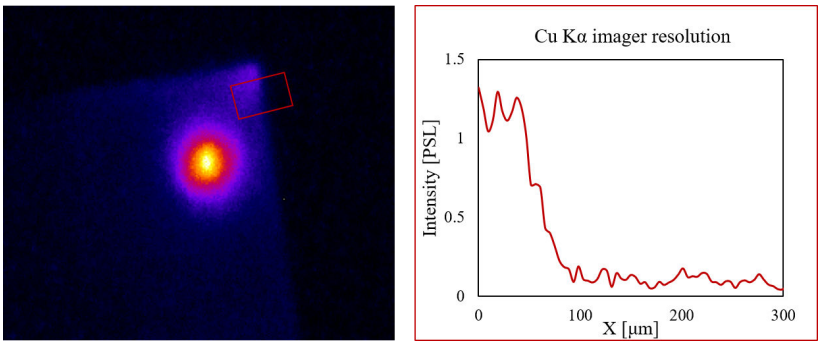

Fig. 3.12 The experimental IP image obtained with Cu K_α imager for the estimation of magnification and resolution (left). The line-out of the target edge indicated as the red square in the IP image (right).

The reflectivity of Bragg's crystal directly depends on the plasma temperature [163]. Indeed, the energy bandwidth accessible with such crystals is close to 10 eV. Line emissions are consequently shifted out of this bandwidth when the temperature increases significantly. This important effect has to be taken into account when setting up a spherical crystal during an experiment. In order to get a good enough signal-to-noise ratio one has to work on the suppression of the direct irradiation of the detector by the unwanted emissions. The intense X-ray noise can be mostly suppressed by inserting a thick enough lead block between the source and the detector. Some alignment precautions must however be taken in order to avoid any hiding of the reflected signal of interest. Since angles between incident rays of interest on the crystal and the reflected signal are quite small, the set-up of such a lead block is not so trivial. Another important source of noise emission may come from fast electrons interacting with the detector which is minimized using a deflection magnet.

3.1.2 Coherent Transition Radiation (CTR)

A Coherent Transition Radiation(CTR) is emitted by the REB crossing radiating interfaces and carries important information about the electron beam time duration, energy and electron

beam shape. The diagnostics for the CTR detection should look at the prompt self-emission from the rear target surface produced mostly by CTR at $2\omega_0$ with very good temporal (in order of fs - ps) and spectral resolution [169, 186]. Here we summarize the theoretical aspects of the CTR produced by an electron bunch and explain the diagnostics setup used in our experiment at the LULI - ELFIE laser facility.

Theoretical aspects of CTR

The transition radiation (TR) can be described by classical electrodynamics and corresponds to the passage of an electron through an interface that separates two media with different dielectric responses. The Maxwell's equations of the problem reduce to:

$$\begin{aligned} \nabla \times \mathbf{H} &= \frac{\partial \mathbf{D}}{\partial t} + e\mathbf{v}\delta(\mathbf{r} - \mathbf{v}t) \\ \nabla \times \mathbf{E} &= -\frac{\partial \mathbf{B}}{\partial t} \\ \nabla \mathbf{B} &= 0 \\ \nabla \mathbf{D} &= e\delta(\mathbf{r} - \mathbf{v}t) \end{aligned} \tag{3.20}$$

where δ is the Dirac distribution and $\mathbf{r} = \mathbf{v}t$ is determining the electron's trajectory. The solution of the system of equation is obtained for the case of a semi-infinite plasma ([22, 193, 227, 226]). The energy W emitted per unit angular frequency and solid angle in the forward direction, for a particle traversing normal to an interface separating plasma and vacuum is:

$$\frac{d^2W}{d\omega d\Omega_{coll}} = \frac{e^2}{\pi^2 c} \frac{\beta^2 \sin^2\theta}{(1 - \beta^2 \cos^2\theta)^2} \tag{3.21}$$

where the transition radiation field is radially polarized for a particle normally incident to the interface (due to the radial symmetry of the dipole response of the material) and θ is the angle between the direction of the particle and the direction of the observation. This equation shows that the radiation has its peak at angle $\theta = 1/\gamma$ and has zero of emission along the axis. Then radiation is emitted in a cone of $\theta_{1/2} \approx 1/\gamma$. The total radiation is roughly proportional to the particle's energy.

Bellei et. al [22] has deduced the total emitted TR per unit of angular frequency and unit solid angle solving the problem using geometric parameters shown in the Fig. 3.13.

By introducing the particle momentum vector $\mathbf{p} = |p|(\sin\psi\cos\phi, \sin\psi\sin\phi, \cos\psi)$ and the observation vector $\mathbf{k} = \omega/c(\sin\theta\cos\alpha, \sin\theta\sin\alpha, \cos\theta)$ the total emitted TR can be

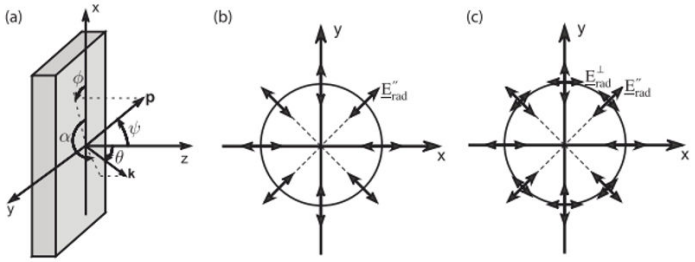

Fig. 3.13 Geometrical parameters involved in the calculation of TR (a). **p** is the particle's direction, **k** is the wave (observation) vector and z is the normal to the target rear surface(b). For a charge crossing normal to the interface, the radiation is radially polarized. The magnetic field (not shown) is azimuthal. In general, there is a component of the electric field parallel and normal to the radiation plane, with the magnitude dependent on the angle of observation (this figure is relevant to an electron moving in the x z plane)(c). Graph and legend are taken from [22].

written as:

$$\begin{aligned}\frac{d^2W}{d\omega d\Omega} =& \frac{e^2N}{\pi^2 c}\left[\int d^3\mathbf{p}(\varepsilon_{\parallel}^2+\varepsilon_{\perp}^2)+\right.\\ &\left.(N-1)\left(\left|\int d^3\mathbf{p}g(\mathbf{p})\varepsilon_{\parallel}F\right|^2+\left|\int d^3\mathbf{p}g(\mathbf{p})\varepsilon_{\perp}F\right|^2\right)\right.\end{aligned} \tag{3.22}$$

where $g(\mathbf{p})$ is the momentum distribution function, $\varepsilon_{\parallel}$ and $\varepsilon_{\perp}$ are the Fourier-transforms of the electric fields in the plane parallel and perpendicular to the radiation plane as a function of ω and F is a coherence function that takes into account the exact time and position at which electrons reach the interface:

$$F = \frac{1}{(\mathbf{p})}\int d^2\mathbf{r}_{\perp}e^{-i\mathbf{k}_{\perp}\mathbf{r}_{\perp}}\int_{-\inf}^{+\inf} dz e^{-iz(\omega t-\mathbf{k}_{\perp}\mathbf{v}_{\perp})/v_z}h(\mathbf{r},\mathbf{p}) \tag{3.23}$$

where $h(\mathbf{r},\mathbf{p})$ is the six-dimensional electron beam distribution and the phase term is given by:

$$\Phi = \mathbf{k}_{\perp}\mathbf{r}_{\perp} - \omega t \tag{3.24}$$

The coherent component of the radiation is given by the second term in Eq. 3.22. The phase term is the sum of a spatial term Φ_s and a temporal term Φ_t. To obtain the expressions for both of the terms one should have a look at the geometry and parameters shown in the Fig. 3.14 taken from the aforementioned paper [22].

Then the $|\mathbf{k}_{\perp}| = \omega/c\sin\theta$ is the component of the wave vector in the plane xy and the space shift associated to the planes waves emitted at positions A_1 and A_2 reaching the

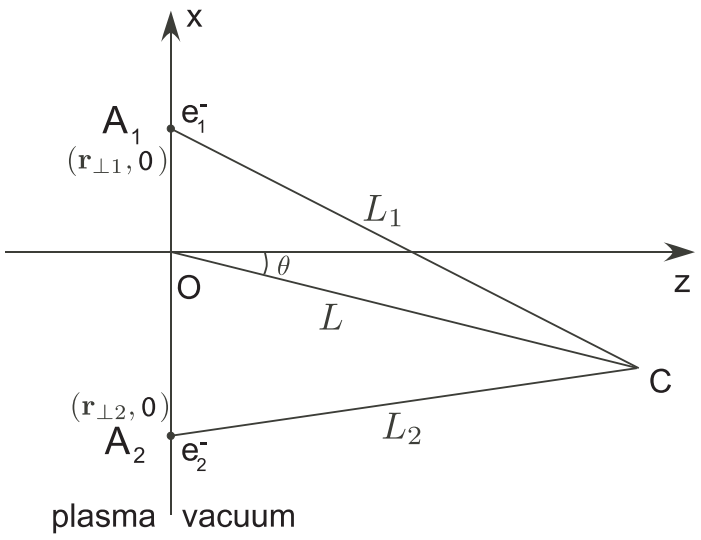

Fig. 3.14 Parameters used for the evaluation of the phase term for a single electron [22].

observer after having respectively travelled a distance L_1 and L_2. Then one can write the spatial component of the phase term as:

$$\Delta\Phi_s = 2\pi\frac{(L_1 - L_2)}{\lambda} = \mathbf{k}_\perp(\mathbf{r}_{\perp\mathbf{2}} - \mathbf{r}_{\perp\mathbf{1}}) \tag{3.25}$$

And the temporal component can be written as:

$$\Delta\Phi_t = \omega(t_2 - t_1) \tag{3.26}$$

Then the Eq. 3.21 can be expressed in discrete form:

$$I_{TR} \approx \sum_i |\mathbf{E_i}|^2 + \sum_i \sum_{i,i\neq j} |\mathbf{E_i}||\mathbf{E_j}| e^{i(\Phi_j - \Phi_i)} \tag{3.27}$$

where the electric is expressed as $\mathbf{E} = \mathbf{E}_\parallel + \mathbf{E}_\perp$ and the phase term is $e^{i(\Phi_j - \Phi_i)}$. Here the first term of the equation is defined as incoherent term and the second term is the coherent.

In the relativistic laser-plasma interactions, where a large amount of fast electrons is produced, coherent radiation can be emitted for wavelengths $\lambda = c\tau_b$, where τ_b is the duration of the fast electron population crossing the radiating interface. These wavelengths can be much bigger than the usually observed visible spectrum.

CTR imaging technique

In the past decade a large amount of experiments were focused on the coherent transition radiation CTR emitted from the target rear side using spectral, time - resolved and imaging technique. The performed experiments report the experimental evidence that part of the fast-electron population is microbunched in time [18, 226] as well as the importance of the various mechanisms resonant absorption, vacuum heating, ponderomotive acceleration, etc. in the generation of those microbunched fast electrons observed by the spectral analysis of CTR [169]. It was discovered that this diagnostic is only sensitive to high-energy electron energies larger than 1 MeV. Estimates have shown that the energy in those relativistic bunches is a modest fraction less than 1% of the laser energy. That means the CTR diagnostic gives no information on the lower energy part of the fast-electron spectrum. The rear surface thermal and CTR imaging performed by J. Santos *et al.* [188, 186] had shown that the $2\omega_0$ signals have both thermal and CTR contributions for foil thickness $\leq 50\mu$ m, associated, respectively, with the bulk and the relativistic tail of the fast-electron energy distribution. Meanwhile the $2\omega_0$ emission is dominated by the CTR for thicker targets. Besides that, the half-angle divergence of the bulk electrons was evaluated to $\Theta = 35 \pm 5$ and the fast electron source estimated to be about just the size of the laser focal spot.

In the experimental campaign described in this thesis, the CTR imager is a complementary diagnostics to Cu K_α imager that provides information about the electron population with energies above 8.5 keV while the CTR imager is a tracer for REB with energies $\geq$ MeV. The CTR emission from 50 μm thick Al foil at $2\omega_0$ (the laser wavelength λ_0 = 1057 nm) was collected by its imaging onto a Gated Optical Imager (GOI) using a one lens imaging system with the total magnification of 5. The setup is presented in the Fig. 3.15.

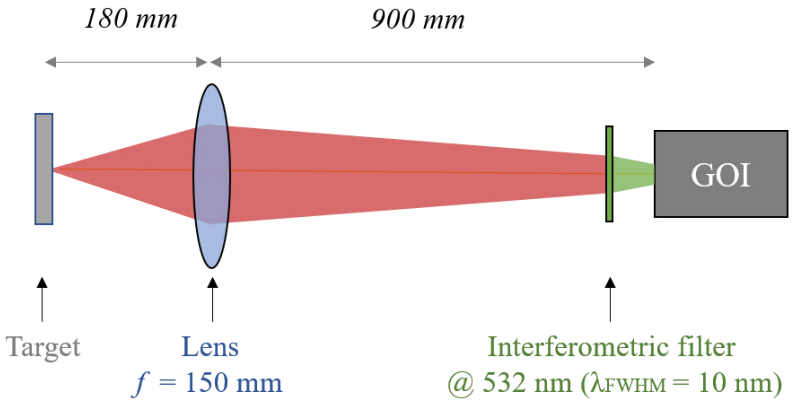

Fig. 3.15 The experimental setup of target's rear side emission imaging at $2\omega_0$

The interferometric filter with a central wavelength λ = 532 nm $\pm$ 10 nm was used to select the wavelength of interest. The GOI is a CCD with the adjustable gate that allows to gate the image in time and collect the signal over the calibrated time starting from 200 ps up to 5 ns. The main difference of GOI from the streak camera is the signal integration over selected time without the signal streaking. Our observed CTR emission spot is a time - integrated signal over 200 ps. It is worth noting, that a streak camera, S20, was also employed to measure time and spatially resolved CTR emission but the results were not reliable enough to present and describe them in this thesis.

3.2 Enhanced relativistic-electron beam collimation using two consecutive laser pulses

The experiment described in this sections was performed on the LULI-ELFIE laser facility (LULI). The experimental campaign was prepared and performed in collaboration with Laboratoire pour l'Utilisation des Lasers Intenses (France), University of Bordeaux, Centre Lasers Intenses et Applications (CELIA) (France), Laboratori Nazionali di Frascati (INFN) (Italy), Institut fur Kernphysik, Technische Universitat Darmstadt, Schlossgartenstrasse (Germany), ETSI Aeronáuticos, Universidad Politécnica de Madrid (Spain), Institute of Plasma Physics and Laser Microfusion,(Poland) and Institute of Laser Engineering, Osaka University (Japan).

3.2.1 LULI-ELFIE laser facility

ELFIE is a highly versatile and manageable facility coupling a fully-equipped experimental room with a Ti:Sa laser system based on the chirped pulse amplification (CPA) technique. Two ultra-intense laser beams (compressed under vacuum – up to 20 J in roughly 0.35 ps at 1.057 μm (ω - 2ω available) are optically synchronized to an uncompressed chirped laser beam with an energy of $\sim$ 50 J in 0,6 ns and to a probe beam (100 mJ in 0.35 ps at 2ω and 3ω available). The repetition rate is 1 shot every 20 minutes, at full energy. An adaptive-optics closed-loop system allows optimizing the focal spot quality. A set of beam splitters and optical delay lines allows fine tuning of the beams (115 mm of diameter).

3.2.2 Experimental design

Setup

We used a dual beam configuration, with two $\lambda = 1.06\,\mu$m, τ = 470 fs full-width-at-half-maximum (FWHM) pulses, containing 13 ± 2 J of energy each and focused symmetrically at $\pm$ 28.5° incidences with respect to the target normal (Fig.3.16). The use of two different off-axis parabolic mirrors, one for each beam, allowed to vary the focal spot size of the first pulse, generating the seed magnetic field, from $\varphi_1 = 20\,\mu$m to 30 μm FWHM while keeping constant the focal spot of the second pulse ($\varphi_2 = 8\,\mu$m FWHM). These yielded intensities of $\sim 10^{18}$ W/cm^2 and 1×10^{19} W/cm^2, respectively. The 3×3 mm^2 planar double-layer targets were composed of Al[50 μm] - Cu[5 μm], with the Al layer facing the two laser pulses. The two pulses, originating from the same oscillator, were temporally synchronized using interferometry techniques. The delay Δt between the laser pulses was varied between 0 ps and 5 ps, with a precision of 100 fs.

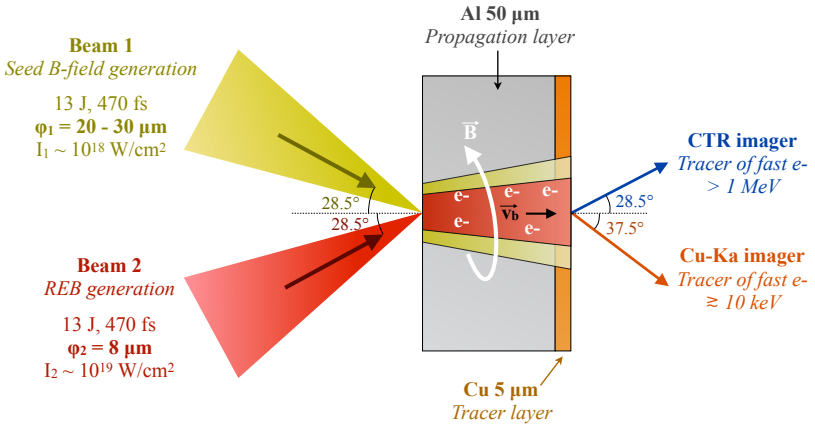

Fig. 3.16 Experimental setup.

Cu-K$_\alpha$ x-ray emission ($\hbar\omega \approx 8$ keV) produced by electrons passing through the copper tracer was imaged onto a FUJI image plate using a spherically bent quartz 22-43 [**?**] crystal described previously , with a radius of curvature of 25 mm, looking at 37.5° with respect to the target normal. Coherent transition radiation at twice the laser frequency [186] produced by relativistic electrons of energies $\gtrsim 1$ MeV was recorded using a Gated Optical Imager (GOI) looking at the target rear surface at 28.5^0 with respect to the target normal and with an acquisition time of 200 ps, limiting the contribution to the signal of delayed Planckian thermal radiation. The layout of diagnostics is presenented on Fig. 3.17.

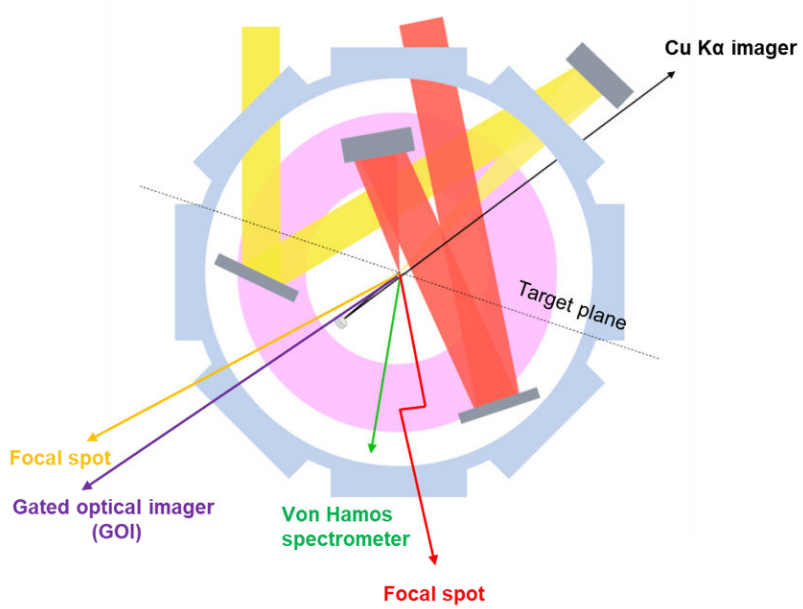

Fig. 3.17 The layout of LULI - ELFIE chamber for the double - pulse experiment.

Targetry

The target for this experiment consist of two layers: the so - called propagation layer of 50 μm Al and tracer layer of 5 μm Cu at the rear side for X - ray diagnostics with the total area of $3 \times 3\,\mathrm{mm}^2$. The targets were glued to the glass needles in the flag configuration like as shown in the Fig. 3.18 (left). 5 μm thick iron wire was attached to the top of foil for the alignment purposes. The targets were aligned firstly at the target alignment stage equipped with four image systems absolutely referenced with the image systems for TCC by using thick 10μm tip. To align the target and set the target angle in four image systems we used the target holder with the X-Y-Z manual translation and goniometer as shown in Fig. 3.18 (right).

Laser alignment

The experiment required accurate focusing and time synchronization of the two laser pulse in at TCC. That's why precise alignment of laser pulses was a task of primary importance. In the diagram of the setup shown in the Fig. 3.17 the main laser pulse is indicated as a red beam that is focused by an F/5 off-axis parabolic mirror onto a target with the optimum focal spot of $\varphi_2 = 8\mu$m. This focal spot was optimized to this value for all experimental runs. The seed laser pulse indicated as yellow beam was initially optimized onto the minimum focal spot of $\varphi_1 = 18\mu$m by an F/13 parabola, which is almost twice bigger than the optimized

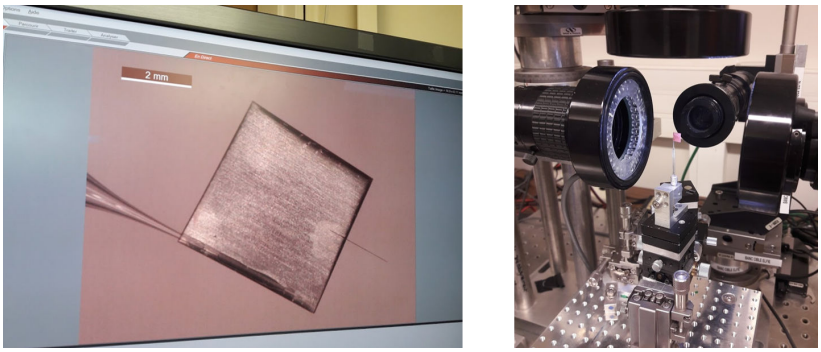

Fig. 3.18 The magnified image of the target used in experiment (left). The target on the external alignment bench (right).

focal spot of the main laser. Two separate imaging systems were used for laser alignment to TCC and focal spot imaging (shown as red and yellow arrows respectively). The different settings of the seed laser pulse were obtained by progressively moving away from best focus of parabola. This variation was however small enough to avoid any modification of the performance, which is particularly true for the central part of this seed beam that is overlapped with the smaller focal spot of the main beam. However, we were not satisfied by the focal spot quality of the seed laser beam at its minimum. After a series of adjustments, we achieved a homogeneous focal spot characterized by a 22.5 μm diameter, corresponding to the run $\varphi_1/\varphi_2 = 2.5$. A special care was taken to monitor the evolution of the focal spot profile in order to avoid any clear degradation of it. The maximum focal spot ratio of this experiment, $\varphi_1/\varphi_2 = 3$, was also achieved for a still not degraded seed beam profile. One of the crucial requirements for this experimental campaign was the necessary overlapping of the laser focal spots. We performed a series of tests to measure the laser pointing stability, achieving a value of few μm. Increasing the focal spot of the seed laser pulse guarantees a better spatial overlapping of the two laser focal spots. A focal spot ratio smaller than 2 would have decreased the probability of precisely overlapping the focal spots from one shot to another. This is the reason why the run with $\varphi_1/\varphi_2 = 2$ should be considered as a test one, presenting fairly extended error bars on experimental measurements with respect to the other runs, which were caused by the unstable laser conditions.

The second crucial requirement for this experiment is the laser pulse synchronization within a few hundreds of fs. To perform the laser synchronization with such resolution one should use an interferometric technique. A thin 480 μm piece of glass (a microscope slide cover) at TCC to reflect the red beam (the main laser pulse) in the path of the yellow beam (the seed laser pulse) as it shown in the Fig. 3.19. This latter was consequently going through

the glass. Then the images were captured with image system for yellow beam while varying the length of the delay line of one of the pulses.

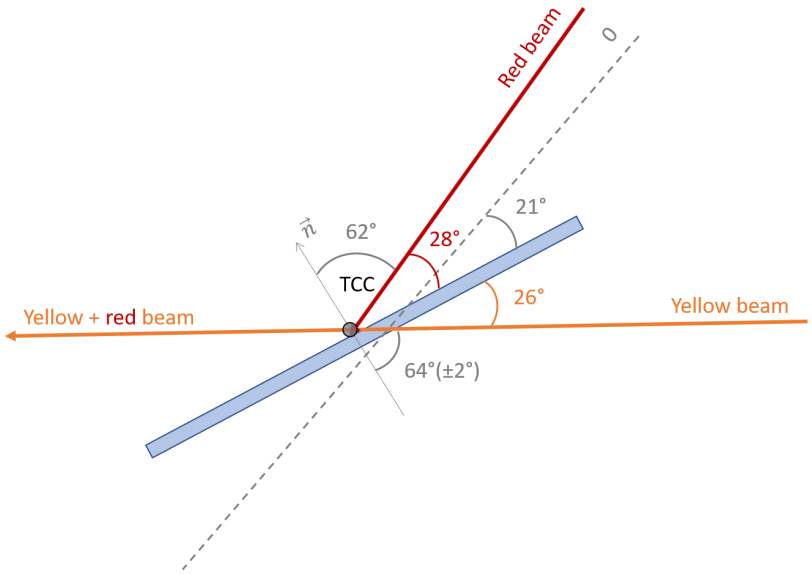

Fig. 3.19 The scheme of the setup for two laser pulses synchronization.

When the beams are totally unsynchronized one should see just a uniform spot on the image system. Then with the movement of the delay line and getting closer from the point of perfect synchronization t_0, one should see interference fringes. The contrast of the image increases as closer one gets to the t_0 - the dark fringes get darker while the bright fringes get brighter. After getting this 0 we have to take to account that the yellow beam travelled more than the red beam by crossing the microscope slide cover. The extra distance m travelled by the yellow beam through the glass with the incidence angle respect to the glass normal of θ_0 can be calculated as:

$$m = \frac{d}{\cos[\arcsin(\frac{n_0}{n_g \sin\theta_0})]} \tag{3.28}$$

where d is a glass thickness , n_0 is a vacuum refractive index , n_g is a glass refractive index. Then the time travelled by the yellow beam is:

$$\Delta t_g = t_g - t_0 = \frac{m}{c_g} - \frac{m'}{c_0} = d(n_g - 1)\frac{1}{\cos[\arcsin(\frac{n_0}{n_g \sin\theta_0})]} \tag{3.29}$$

where m' is a distance travelled by yellow beam if there was no glass obstacle. Then Δt_g is equal 0.54×10^{-12} and corresponds to the time yellow beam arrives later to TCC. This is the

time we should compensate with the delay line of the yellow beam to be synchronized with the red beam.

It is worth to note, that the interferometric technique works if the laser pulses are not that far away from the optimum. Normally before this technique one needs to use a photodiode and determine the the delay between two signals with the oscilloscope. However, at LULI ELFIE we skipped this step because the beams were previously synchronized within a few hundreds of ps.

3.2.3 Experimental results

Cu-K_α imager and CTR imager

Figure 3.20(a) presents the evolution of the Cu-K$_\alpha$ spot size as a function of delay time between the two laser pulses for different ratios φ_1/φ_2. An optimum delay, corresponding to a maximum collimation of the fast electron beams, was measured for each focal spot ratio. Both Cu-K$_\alpha$ and CTR diagnostics confirm that the collimation of the main electron beam occurs at delays $\Delta t = 3, 2.5, 2$ ps respectively for the run with focal spot ratios $\varphi_1/\varphi_2 = 2.5, 2.8, 3$ (Fig.3.20 (b)). The higher the ratio φ_1/φ_2, the shorter is the delay at which an optimum collimation occurred.

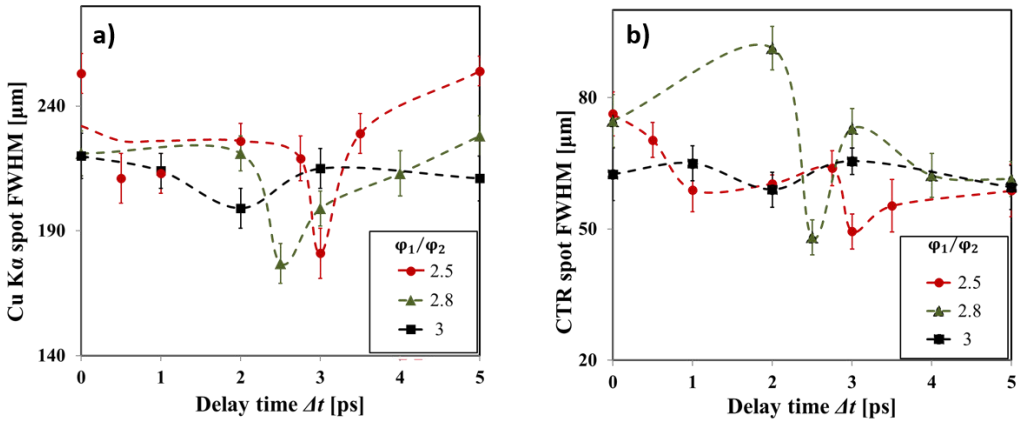

Fig. 3.20 Evolution of the diameter of the emission area on target rear side of **(a)** Cu-K$_\alpha$ fluorescence and **(b)** CTR, as a function of the delay between the two laser pulses for different focal spot ratios: $\varphi_1/\varphi_2 = 2.5$ (red circles), $\varphi_1/\varphi_2 = 2.8$ (green triangles), $\varphi_1/\varphi_2 = 3$ (black squares). The dashed curves are guides for the eyes.

Examples of experimental images are shown in figure 3.21(a) for $\varphi_1/\varphi_2 = 2.5$, while figure 3.21(b) reports the size as measured by the two diagnostics on the same graph (same data as Figure 3.21(a)).Similar images are shown in the Figure 3.22 and Figure 3.23 for

$\varphi_1/\varphi_2 = 2.8$ and $\varphi_1/\varphi_2 = 3$ respectively. Compared to the K_α signals the absolute smaller size of CTR signal confirms that this emission is due to the high energy component of electron beam, which has a smaller angular spread. Efficient Electron beam collimation can be represented by introducing the compression parameter C defined as the ratio between the Cu-K_α peak intensity and the Cu-K_α spot FWHM [217]. A compression of the beam is indeed achieved when a reduction of the electron beam size is accompanied by an increase of the peak intensity of the signal: a larger value of C corresponds to a more collimated electron beam. For $\varphi_1/\varphi_2 = 2.5$ the maximum compression corresponds to the maximum value of Cu-K_α emission at the delay time of 3 ps where the electron beam area is decreased by a factor of 0.5 and the Cu-K_α intensity is increased by a factor of 1.37 (Fig. 3.24). This suggests that more than 70% of hot electrons are collimated in the process. The CTR signal shows also a reduction of the beam size by a fairly comparable factor ~ 0.6 although there is not a clear increase of the detected signal yield. This seems to suggest a lower effect of the magnetic field on the high energy electron beam component which results both because of the larger difference between the radial extent of the magnetic field and the spatial size of the high energy component in the beam, and the smaller deviation of higher energy electrons.

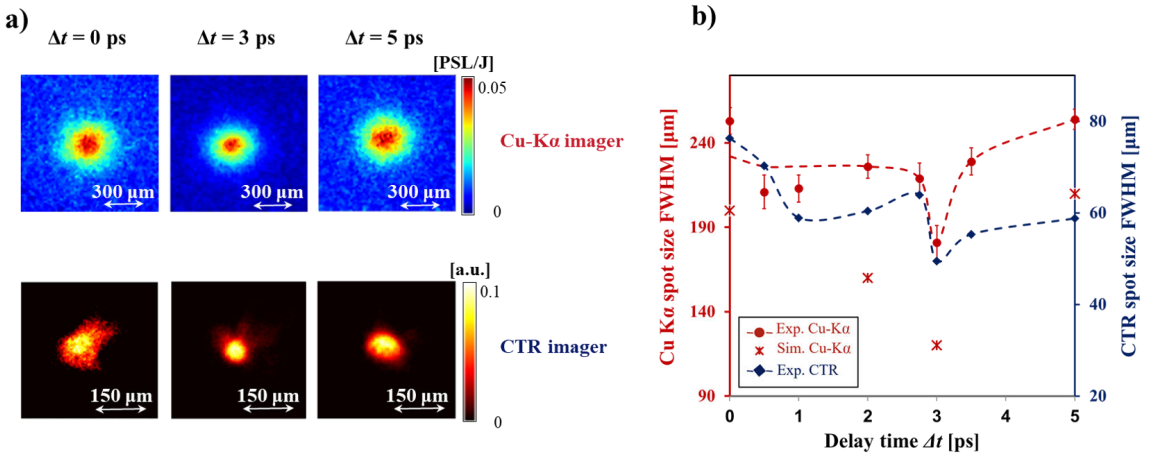

Fig. 3.21 Data obtained for a focal spot ratio $\varphi_1/\varphi_2 = 2.5$. **(a)** Set of typical Cu-K_α (top) and CTR (bottom) images obtained at different delays $\Delta t = 0$ ps (left), 3 ps (middle) and 5 ps (right). **(b)** Comparison of Cu-K_α (red circles) and of CTR (blue circles) emission spot sizes. The red crosses show the results of the simulated Cu-K_α emission, reproducing the delay at which optimal collimation occurs.

Two main effects were observed when varying the laser focal spot ratio of the laser pulses: a variation of the maximum compression coefficient and a shift of the optimum delay time. Such tendencies are explained by the dynamics of the self-generated magnetic fields governed by the diffusion equation which combines the generalized Ohm′s law with

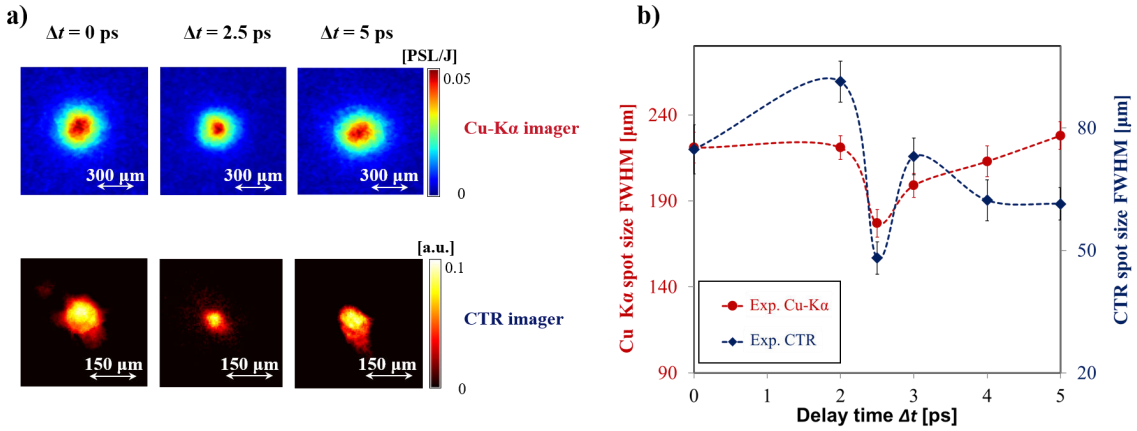

Fig. 3.22 Data obtained for a focal spot ratio $\varphi_1/\varphi_2 = 2.8$. **(a)** Set of typical Cu-K$_\alpha$ (top) and CTR (bottom) images obtained at different delays $\Delta t = 0$ ps (left), 3 ps (middle) and 5 ps (right). **(b)** Comparison of Cu-K$_\alpha$ (red circles) and of CTR (blue circles) emission spot sizes.

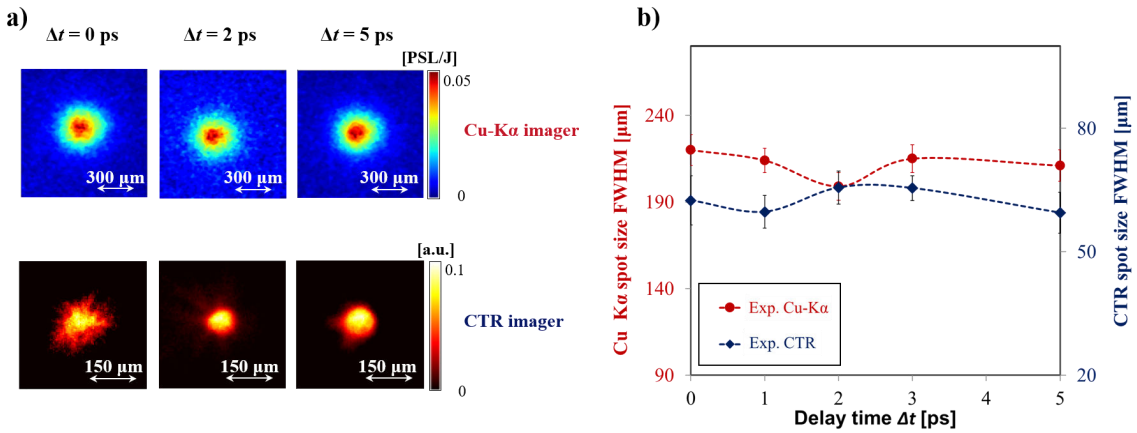

Fig. 3.23 Data obtained for a focal spot ratio $\varphi_1/\varphi_2 = 3$. **(a)** Set of typical Cu-K$_\alpha$ (top) and CTR (bottom) images obtained at different delays $\Delta t = 0$ ps (left), 3 ps (middle) and 5 ps (right). **(b)** Comparison of Cu-K$_\alpha$ (red circles) and of CTR (blue circles) emission spot sizes.

Maxwell-Faraday′s law:

$$\frac{\partial \vec{B}}{\partial t} = \eta \vec{\nabla} \times \vec{j_b} + \vec{\nabla}(\eta) \times \vec{j_b} + \frac{\eta}{\mu_0} \vec{\nabla}^2 \vec{B} - \frac{1}{\mu_0} \vec{\nabla}(\eta) \times \vec{B} \tag{3.30}$$

with the plasma resistivity η, the magnetic field B and the fast electron current density j_b. The terms in the right-hand-side of Eq. 3.30 are responsible for the magnetic field generation and evolution. The maximum amplitude B_{max}, the rise and diffusion times are mainly dependent on the laser pulse duration, intensity and focal spot size via the target resistivity evolution and the fast electron beam current density. Applying this equation to our case, we can explain the magnetic field dynamics and its influence on the observed electron beam collimation. An increase of the focal spot size of the first laser pulse causes (see Fig. 3.20):

1. A reduction of the optimum delay time
2. An increase of the time window for second electron beam injection
3. A mitigation of the REB collimation.

The later effect (3), estimated by the compression ratio, is caused by the natural reduction of the maximum amplitude of the magnetic field B_{max} because a larger spot implies a reduced laser intensity on target: the Δt scan with $\varphi_1/\varphi_2 = 3$ is the least efficient.

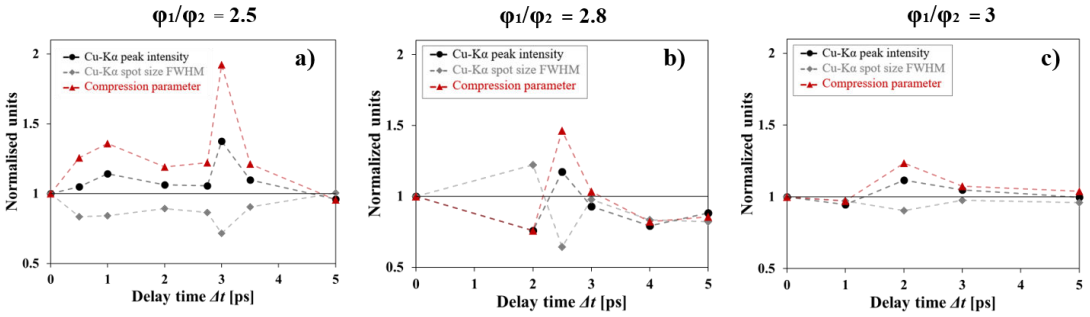

Fig. 3.24 Evolution of the Cu-K$_\alpha$ peak intensity (black circles), Cu-K$_\alpha$ emission spot size (grey circles) and compression factor C (red triangles), normalized to the values at $\Delta t = 0$ ps for the run with the focal spot ratio $\varphi_1/\varphi_2 = 2.5$.

The reduction of the optimum delay time between the two laser pulses when the focal spot ratio increases (1) is due to the change in target resistivity following the evolution of the target temperature. With the increase of laser focal spot φ_1, the injected energy density reduces, therefore the target electron temperature T_e decreases and the resistivity η becomes larger implying a decrease of the B-field rise time $\xi \sim \frac{1}{\eta}$. As a consequence the magnetic

field reaches B_{max} faster, when the REB collimation is observed. As for the optimum time window (2) for the injection of the second electron beam, this appears because the collimation of the REB is caused by a resistive magnetic field presenting a sufficiently long lifetime, the later being directly related to the magnetic field diffusion time, scaling as $\tau_{\text{diff}} \propto \frac{R^2}{\eta}$. As a consequence, the bigger the radial size of the first electron beam, the longer the seed magnetic field lasts, extending the optimum time window for the injection of the main electron population. The existence of the optimum focal spot ratio, when the compression reaches its maximum, is a trade-off between the maximum amplitude of the magnetic field B_{max} and its diffusion time. Taking to account the observed effects as well as requirement to precise overlapping the focal spots, one can suggest that the laser focal spot ratio should lie between $2 - 2.8$, the most evident collimation effect having been observed for a focal spot ratio of 2.5.

K_α spectroscopy results

The Von Hamos spectrometer in cylindrical configuration was used to detect Cu - K_{α_1} and K_{α_2} lines emitted by the propagation of electron beam through the 5 μm Cu - tracer layer. As was discussed in Section 3.1.1, this type of spectrometer is employed to estimate the target electron temperature based on the detected shift and visible modification of the spectrum in agreement with atomic simulation presented on Fig. 3.5. Here we present the results of spectroscopy with the analysis details and possible interpretation of results. The reference spectra were taken by focusing the main laser pulse with intensity of $\approx 10^{19}\text{W}/\text{cm}^2$) focused within a focal spot 9 μm onto a Cu foil of 12.5 μm thickness with a transversal size of 3×3 mm. Using the Copper target would increase the Cu - K_α yield and that allows to calibrate image plate in terms of eV/μm. The Figure 3.25 shows the raw image of IP for the reference Shot 034 with a scale of 100 μm (top). The conversion of X - axis in μm to energies in eV can be done by estimating a distance between two visible peaks of K_{α_1} (8046 eV) and K_{α_2} (8027 eV) that gives us a final resolution of 0.074 eV/μm. The obtained spectrum is quite clean with very bright intensities in both lines and supported by Flychk simulation of cold Cu - spectrum with density of 8.9 g/cm^3 crossed by fast electron beam of 300 keV mean energy.

For the experimental runs with the target of 50 μ m Al propagation layer and Cu 5 μm tracer layer the Von Hamos spectrometer spectra are rather noisy and complicated to analyse. However here we aim to compare the obtained Copper spectra for each of the runs with three different focal spot ratio (2.5, 2.8 and 3) showing the two cases - the 0 delay time between pulses and the case of optimum delay for each run (3, 2.5, 2 ps).

As can be seen on the Fig. 3.26 the obtained image on IP has higher noise level in comparison with reference shot Fig. 3.25 and moreover it is not homogeneous. That is

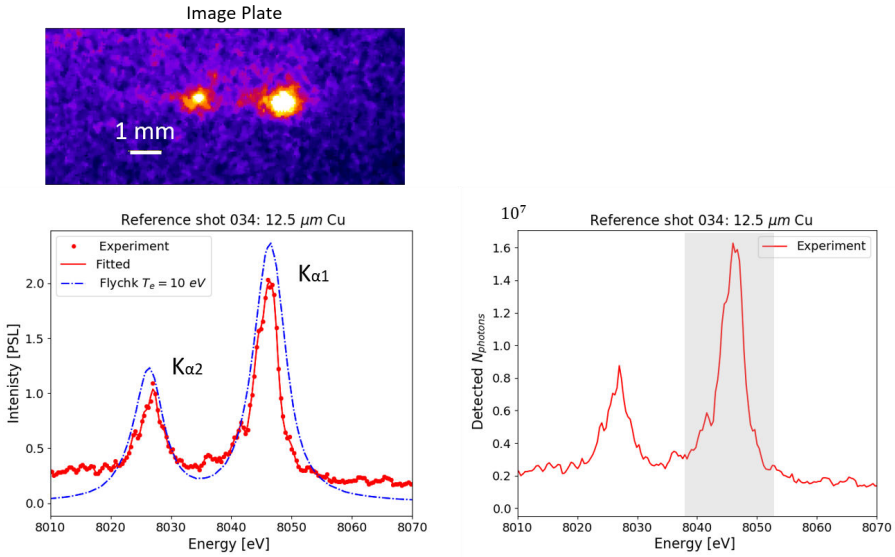

Fig. 3.25 The example of raw IP experimental image (up) and raw spectrum in units of PSL as a function of energy previously converted by the calibration ratio (red dashed curve). The Number of detected photos as a function of energy.

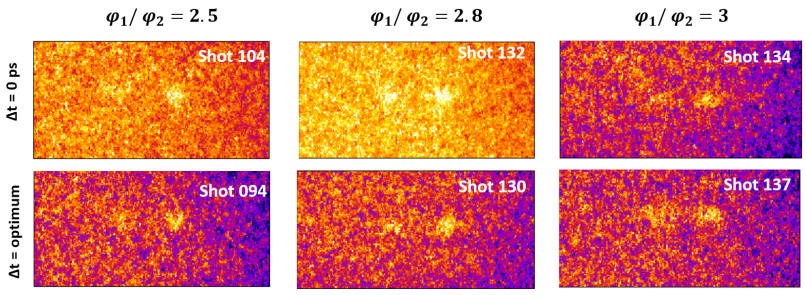

Fig. 3.26 The raw data of Von Hamos spectrometer diagnostics for each of three runs and two important delay times between laser pulses $\Delta t = 0$ and Δt= optimum.

partially related to the double increased energy on target during the interaction (double pulse) and technical issues with shielding.

To analyse such kind of data one should get a fit to the background for the each shot and then subtract it from the signal of interest like it is shown here:

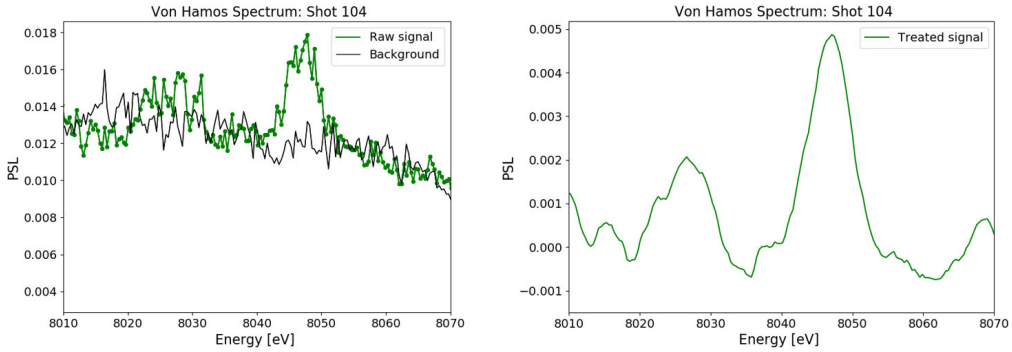

Fig. 3.27 Example of the raw data treatment. The profiles are taken with the line width of 20 pixels. The signal smoothed with Savitskyi Goolay filter (right)

Applying such technique to the raw data of Fig. 3.26 we get the following spectra for each run Fig. 3.28. For all of the experimental run we observe that the Cu - K_α signal is more intense for the case of 0 delay time. Simultaneously with the increase of seed laser focal spot the Cu - K_α signal gets weaker as can be seen by intensity difference between the experimental runs.

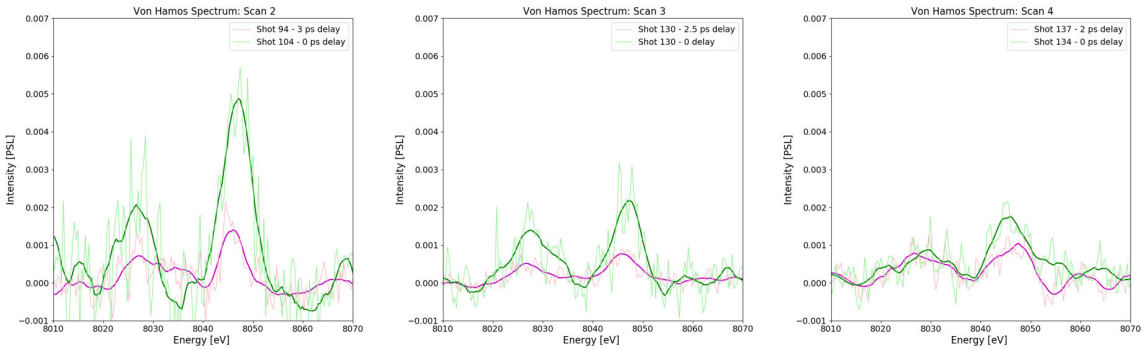

Fig. 3.28 The experimental results of Von Hamos spectrometer after signal treatment for each experimental scan (φ_1/φ_2 = 2.5, 2.8 and 3 from left to right respectively) and two chosen delay times between the laser pulses.

The main purpose of this diagnostic is to estimate the target electron temperature as was discussed in Sec. 3.1.1. However experimentally there are several challenges that can affect this type of measurements. The Fig. 3.29 shows results of the one of experimental run with

two delay time between laser pulses - 0 and 3 ps (dashed green and violet curve respectively) as well as the reference curve obtained with 12.5 μm Cu target normalized to the maximum intensities. The two Flychk simulations represent the case of electron temperature 10 and 30 eV (blue and yellow solid lines). As can be seen, we don't observe any broadening or shift of K_{α_1} and K_{α_2} lines that is expected for higher target electron temperatures. Our explanation is based on the target planar geometry issue. The Von Hamos spectrometer is collecting the emitted photons from the all target rear surface that has dimensions of 3×3 mm. The efficient target heating is normally follows REB propagation axis. The results of the K_α imager estimated the electron beam size of approximately 200 μm. But we are getting not only the K_α emitted from this axis but also the cold K_α contribution, emitted over the larger area than the heated area of target. Consequently, in order to measure the electron temperature on the axis one should reduce lateral size of the target by reducing the dimensions to 300×300 μm.

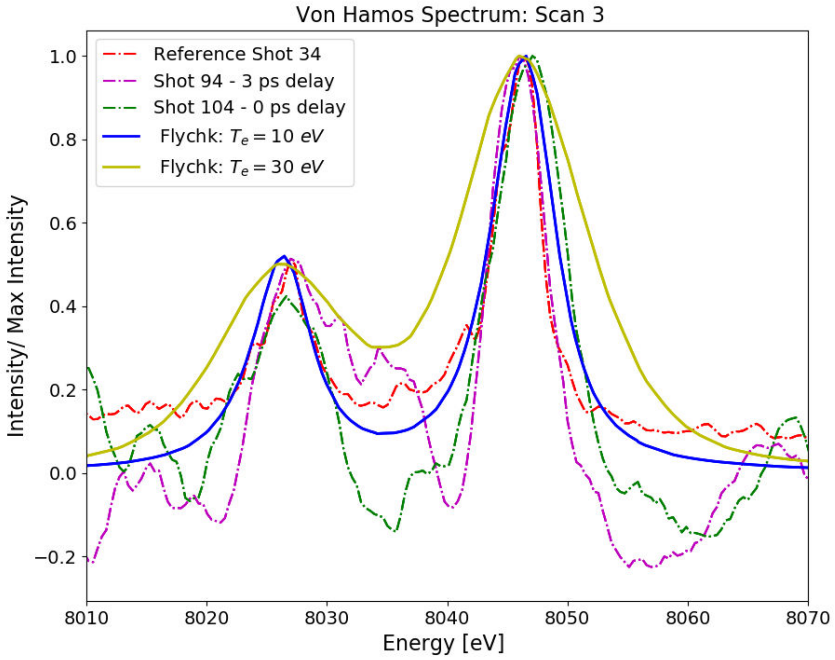

Fig. 3.29 The experimental results of Von Hamos Spectrometer for the experimental run of the focal spot ratio $\phi_1/\phi_2 = 2.8$. The spectrum are normalized to the maximum intensity in order to estimate possible broadening effects.

K_α photon number

To calculate the total number of K_α photons one should take into account the IP Response to the 8.09 keV energy η_{PSL} per cm^{2}and spectrometer specification such as detector area A in cm^2 and crystal reflectivity R:

$$N_{Cu-K_\alpha} = \frac{\eta_{PSL} I_{PSL} RA}{x^2} \tag{3.31}$$

where I_{PSL} is an experimental intensity value of the line in PSL and x is a scanner resolution. In our case $x = 50\mu$m. The IP response for 8.09 keV is 3mPSL per incident photon estimated by using the calibration curve obtained in [3] shown in Fig.3.30. The

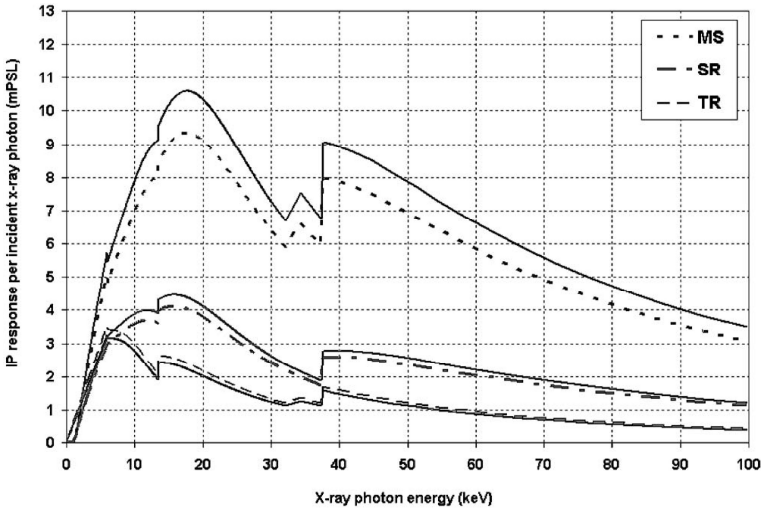

Fig. 3.30 Absolute x-ray sensitivities of the Fuji BAS IPs from 0 to 100 keV using the Fuji FLA7000 scanner dashed line and the Fuji FLA3000 scanner solid line [3]

cylindrical crystal Quartz 2141 used for this spectrometer has dimensions of 60 $\times$ 50 mm and x-ray rocking curve reflectivity R = 2×10^{-4} srad. To estimate the number of K_{α_1} photons it is necessary to integrate the area of the measured K_α peak and it yields in 2.6×10^8 emitted photons. The Figure 3.25 (right) shows the spectrum in number of K_α photons for the reference shot with target of 12.5 μm Cu. The results of the experimental runs with different focal spot ratios in terms of the number of K_α photons are shown in Fig. 3.31. The number of emitted K_α photons is directly related to the total electron energy E and electron beam radius R - varied parameters between experimental runs. The bigger the focal spot, the less is the intensity on target and less energy converted into electrons. We observe twice less K_α photons emitted for the experimental run with the largest focal spot ($\phi_1 = 30$ μm) in

comparison to a smaller focal spot ($\phi_1 = 22.5\ \mu$m) run. Let's have a look at the change in photon number for the cases with two delay times between laser pulses - 0 time delay and optimum time delay for each experimental run discussed in previous section. It's worth to note all three experimental scans had shown the same tendency - the number of K_α photons reduces with the increase of the delay time between pulses. Such behaviour can be explained by taking to account the different condition of laser - target interaction at the moment of the second laser pulse arrival.When the first laser pulse arrives prior to the second pulse by couple of ps the target has more pre- plasma part then for the case when two pulses arrive simultaneously with 0 delay time. The aforementioned pre-plasma can change the laser absorption mechanism described in the Introduction and therefore change the electron source parameters such as electron number and electron energy leading to the change in the K_α photon number

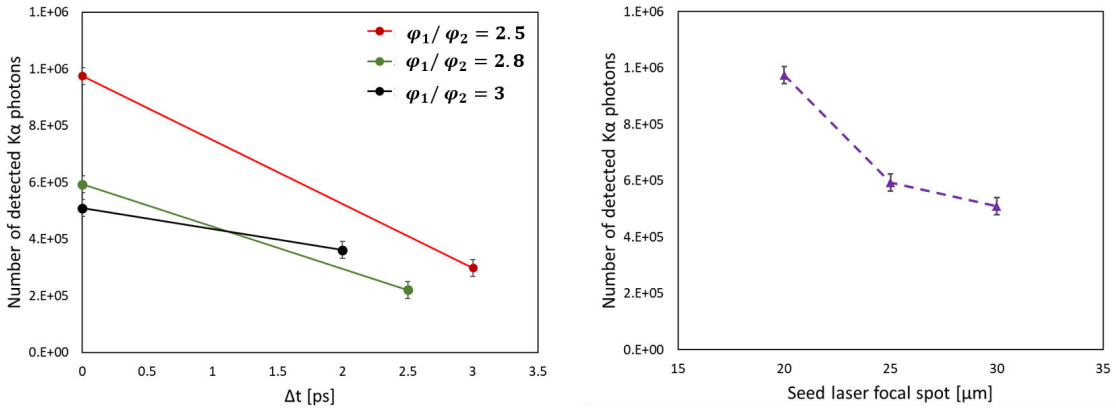

Fig. 3.31 The total K_{α_1} photon number as a function of delay time for each of the scan (left). The total K_{α_1} photon number as a function of seed laser focal spot for 0 delay time between laser pulses (right)

Experimental REB divergence estimation

The experimental REB divergence was determined by the method explained in the 2.2.2 section using K_α imager. The Cu - K_α spot size was measured for the aluminium targets of 30 μm and 50 μm thickness with 5 μm Copper tracer. The two laser pulses with 0 delay time were focused onto the target with their optimum focuses of $\phi_1 = 19\ \mu$m and $\phi_2 = 9\ \mu$ m yielding in intensities $10^{18} - 10^{19}$W/cm^2. Obviously the contribution of the REB beam generated by the second, most intense pulse is higher than the REB beam generated by the first, less intense pulse.

The full spot divergence half angle is estimated to be $\theta_{1/2} = 64^\circ$ that is slightly higher than predicted by Green et al. [88] .

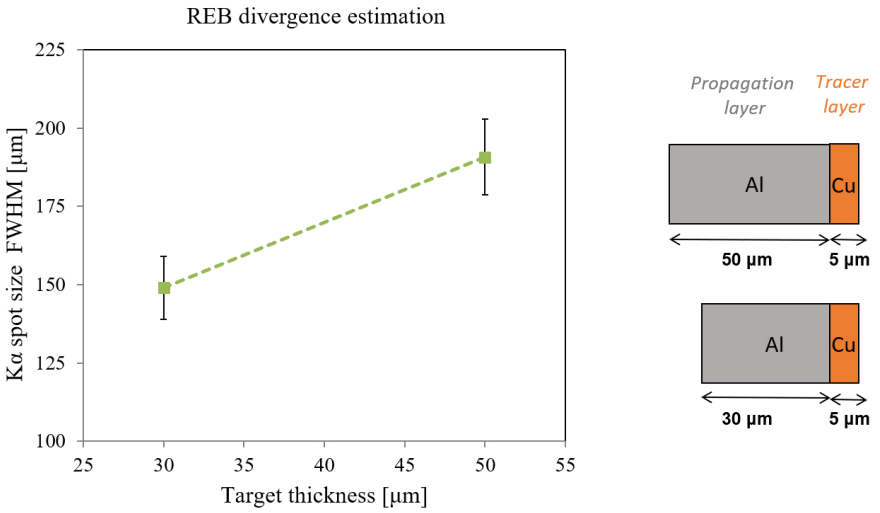

Fig. 3.32 Cu - K_α spot radii against target depth (right). Target configuration (left)

3.3 Theoretical modelling

In order to support our physical interpretation of the experimental results of fast electron collimation, we performed multi - step numerical simulations covering all the involved time scales. The plasma expansion at the target front surface was estimated using the 1D hydro code MULTI-fs [172] while the laser-driven electron source was characterized using the 2D Particle-in-Cell (PIC) code SMILEI [55]. And the transport of fast electrons through the target was simulated using a 3D hybrid-PIC code [104, 103]

3.3.1 Hydrodynamic simulations of preplasma

In our experiment, the interaction laser pulse had an amplified spontaneous emission (ASE) low-intensity pedestal with a contrast in energy of 10^{-4} arriving 1.5 ns before the short part. From simulations performed with the hydrocode MULTI-fs [172], the propagation of the ASE-induced shock wave is expected to take 4.5 ns to cross 17 mm of Al (the thinner target used), and should not consequently interfere with the fast-electron transport.

3.3.2 PIC simulations of laser driven electron source

The 2D PIC simulations were performed in collaboration with Frederic Perez (LULI) using 2D PIC code Smilei [55]. The main purpose of PIC simulations is to characterize the fast electron source generated by main laser pulse in terms of energy and angular distribution. Then, the output result of the PIC simulation was used as input data for the electron beam in

the 3D Hybrid PIC Code that was used to study the fast electron beam transport in the target. As was discussed in introduction the fasts electron beam generation strongly depends on the length and density of the pre plasma formed before the laser peak arrival. We characterized the laser driven electron source in terms of energy and angular distribution for four different pre - plasma profiles:

1. $n_e \propto e^{x/3.2\mu m}$
2. $n_e \propto e^{x/1.6\mu m}$
3. $n_e \propto e^{x/0.8\mu m}$

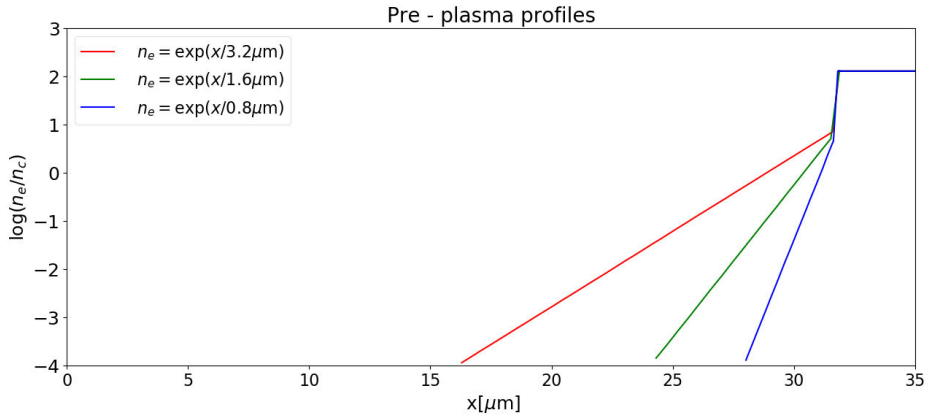

Fig. 3.33 The pre plasma profiles inserted in PIC simulation at t = 0 simulation time.

The final pre - plasma type was selected to be the closed to the hydrodynamic simulations performed with MULTI-fs.

Simulation setup The simulation box in dimensions of c/ω_0 with ω_0 given by the laser frequency is shown in the Fig. 3.34.

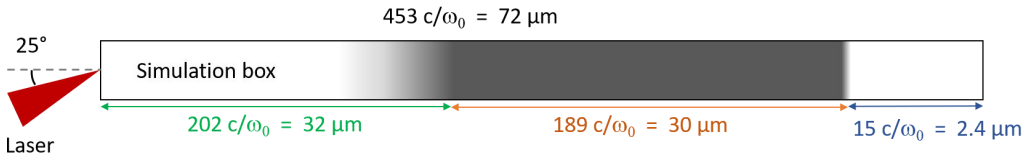

Fig. 3.34 The scheme of the simulation box for the performed PIC simulations.

The laser pulse of intensity $I \sim 10^{19}\mathrm{W/cm^2}$ and pulse duration of $\tau_L = 470$ fs with incidence angle $\theta_0 = 25^\circ$ interacts with the plasma of density $\rho_{Al} \times 1/4$ (solid density) ionized

10 times with initial temperature $T_e = 200$ eV. The pre - plasma type is varied corresponding to the aforementioned values. The cell size is chosen as $1.7 \times 10^{-2} c/\omega_0 = 2.7 \times 10^{-3} \mu m$ and it is not able to resolve the Debye length in the dense and low-temperature region of the given plasma. The total number of cells per simulation is $\sim 2 \times 10^7$ and yields to the total number of particles $\sim 5 \times 10^8$ The total time of the simulation duration is 1 ps with the time step of $10^{-2} \omega_0^{-1} = 6 \times 10^{-3}$ fs.

Simulation results As was mentioned before, the main goal of PIC simulations for this experiment is to characterize the electron source generated by the main laser in order to use its initial characteristic for its transport in Hybrid PIC code. The main information obtained with PIC simulations are electron distribution, laser to electron conversion efficiency and angular distribution. The Fig. 3.35 shows the typical results of PIC simulation extracting the 2D electron density profiles at different simulation times. We can see the laser interaction with the solid matter, and acceleration of electrons outwards and inwards inside the target. We are interested in post processing PIC simulation data in order to acquire the electron conversion efficiency, energy spectrum and angular distribution.

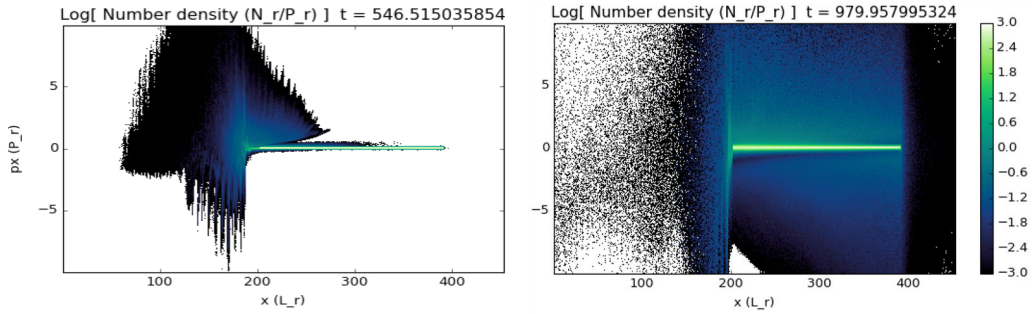

Fig. 3.35 Example of PIC simulation results extracted at 546 fs and 1000 fs simulation time

First of all, let's have a look at the obtained conversion efficiency as a function of time for the first pre - plasma type. The conversion efficiency is evaluating how much laser intensity was converted into electrons. In this case we don't take to account the conversion efficiency to lower electron energies because the experimental diagnostics look at the electron energies > 10 keV. As far as we are interested in generation of high energy electrons here and in the following discussion we will consider the electrons with energies >13 keV The Gaussian fit was used to fit the experimental data - $f(\eta_L) = \alpha \times \eta_{L_{th}} \exp(-0.5(t - t_1/\sigma_1)^2)$, where $\alpha = 110$, $\eta_{L_{th}} = 0.55$ the theoretical conversion efficiency obtained by Eq. 2.52, $t_1 = 590$ fs and $\sigma_1 = 0.8\sigma_{laser}$ with standard deviation of the laser σ_{laser}. We find a conversion efficiency of about 65 % that is in the margin of predicted values of 50 - 65 % shown in the Fig. 2.3.

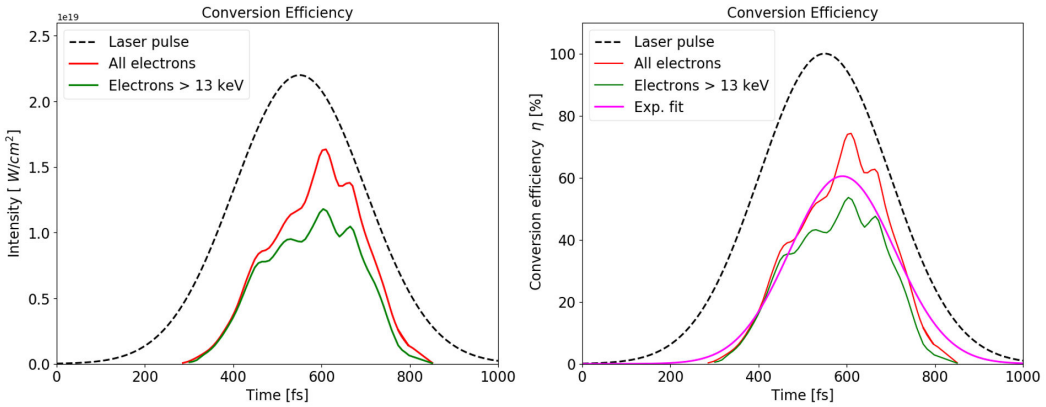

Fig. 3.36 Intensity in $\mathrm{W/cm^2}$ as a function of time of laser pulse (black dashed line), all accelerated electrons(red solid line) and fraction of electrons with energies > 13 keV (green solid line) extracted at 1 ps simulation time (right). The conversion efficiency from the total laser intensity to the electron intensity in %.(left)

For the other pre - plasma profiles we observe a decrease of the conversion efficiency for the more steep density gradients as shown in the Fig. 3.37. This effect is directly related to the absorption mechanism and critical density in the corona. In the case of the less steep pre - plasma profile, the plasma density is rises slower that allows the laser to propagate inside transferring energy, conversely the closer we are to the solid the more laser light is just reflected. Since the laser can not propagate below critical density n_c, it can accelerate the electrons below it. Therefore the electron acceleration becomes more efficient with the pre - plasma formed at the front - surface (normally generated by the rising edge of the laser pulse). Comparing the simulations with the larger pre - plasma density gradient (red curve) and the smaller one (blue curve) one can estimate the gain in efficiency of almost three times. At the same time another effect can be observed - the acceleration of electrons occurs more to the end of the total laser pulse duration.

The electron spectra integrated over 1 ps simulation time was used to obtain the energy distribution function. The mean electron kinetic energy is estimated as $< E >= 917keV$ for the type 1 preplasma.

The electron distribution function in the Hybrid PIC code is shown in Fig.3.38 and can be presented as:

$$f(E) = \exp\left(-\frac{E}{T_b}\right) + \exp\left(\frac{T_c}{E}\right) \times \left[\frac{(\gamma_0 - 1)\, m_e c^2}{E}\right]^a \exp\left(-\frac{E}{T_{sh}}\right) \tag{3.32}$$

It consist of two exponential fits:

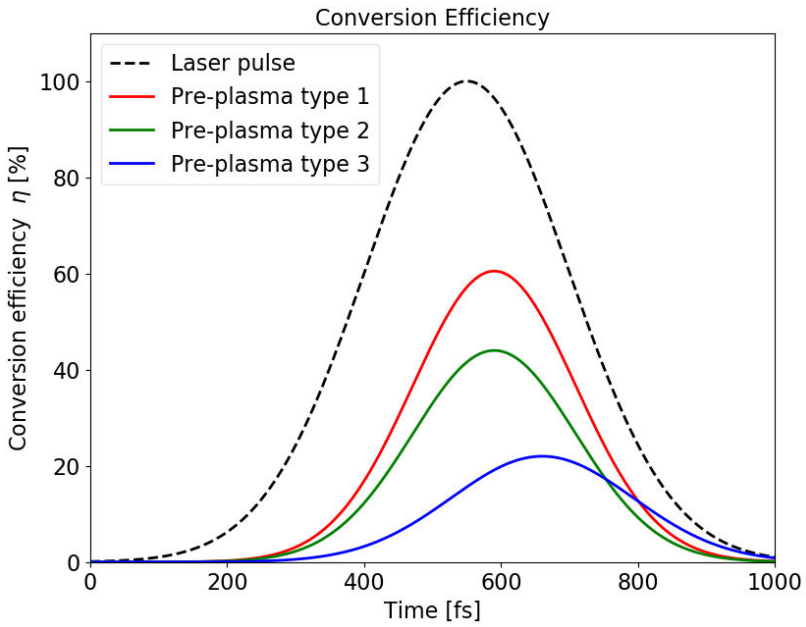

Fig. 3.37 The laser to electron conversion efficiency as a function of time obtained for different pre - plasma profiles of $n_e \propto e^{x/3.2\mu m}$ (red curve), $n_e \propto e^{x/1.6\mu m}$(green curve), $n_e \propto e^{x/0.8\mu m}$ (blue curve) at 1 ps simulation time. The Gaussian fits are shown in this plots with the following fitting parameters: $\alpha_2 = 80$, $t_2 = 590$ fs (pre plasma type 2) and $\alpha_3 = 40$, $t_3 = 520$ fs (pre plasma type 3)

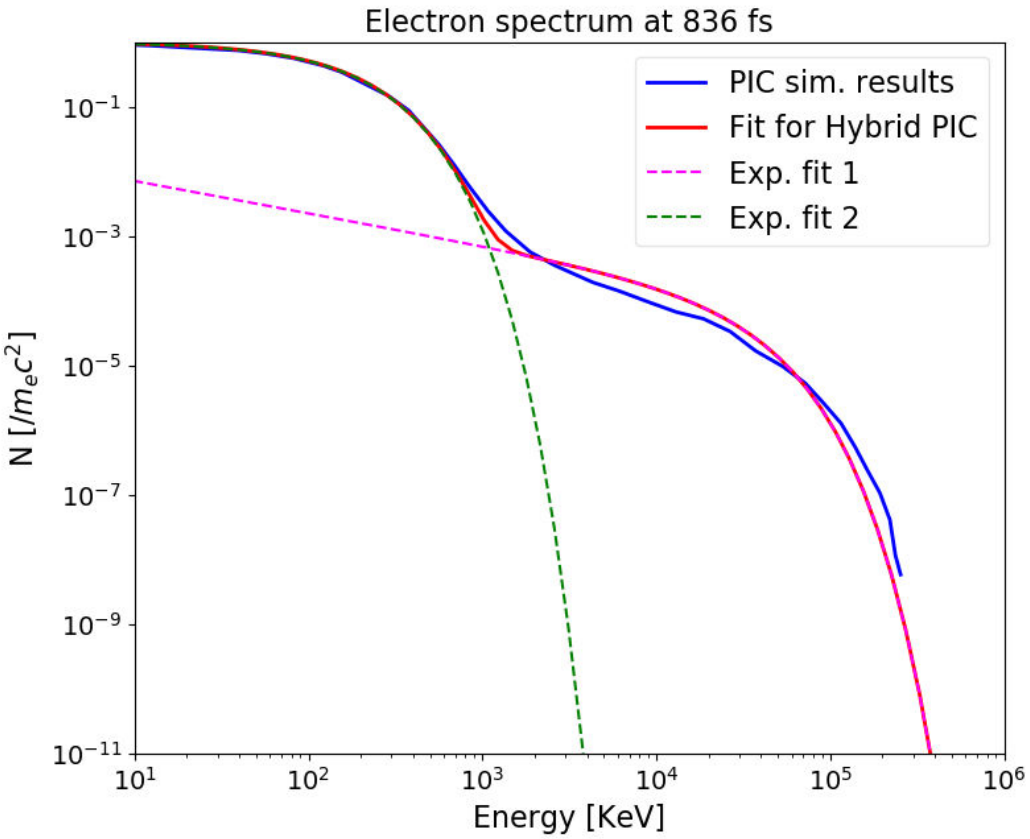

Fig. 3.38 Electron spectrum obtained by PIC simulations with pre - plasma type 1 (blue curve), the experimental fit $f(E)$ for the Hybrid PIC simulation input (red curve), exponential fit $f_1(E)$ with high cut off(pink dashed curve) and exponential fit $f_2(E)$ with the lower cut - off (green dashed curve)

$$f_1(E) = \exp\left(\frac{T_c}{E}\right) \times \left[\frac{(\gamma_0 - 1)\, m_e c^2}{E}\right]^a \exp\left(-\frac{E}{T_{sh}}\right) \tag{3.33}$$

$$f_2(E) = \exp\left(-\frac{E}{T_b}\right) \tag{3.34}$$

The fitting parameters: $T_b = 1.5 \times 10^2$ keV, $T_c = 5 \times 10^{-3}$ keV, $\gamma_0 = 1.000001$, $a = 0.5$, $T_{sh} = 2.5 \times 10^4$ keV.

The hot electron temperature $T_{hot} = T_b = 1500$ keV that is in good agreement with the pondemorotive scaling. Using the scaling laws shown in the Fig. 2.4 one can predict the hot electron temperature of the electron beam generated with the ELFIE main laser pulse peak intensity $I \sim 2.6 \times 10^{19} W/cm^2$ as $T_{hot}^{Beg} = 636$ keV , $T_{hot}^{Wilks} = 1773$ keV ,$T_{hot}^{Tanimoto} = 1100$ keV and following experimental results of Chen et al. [42] $T_{hot}^{Chen} = 1400$ keV. The Beg's law is underestimating hot electron temperature for the laser intensities $> 10^{19} W/cm^2$ while the pondemorotive scaling is consistent with the experimental data obtained in the last decade.

The electron source angular distributions at different simulation times are shown in Fig. 3.39 and are used to estimate the initial half divergence angle of $\theta_{1/2} \approx 50^\circ$. It is quite a bit higher than the divergence angle predicted by Green *et al.* [88] which was $\approx 35^\circ$ for the given intensity. This can be explained by the different pre - plasma conditions. However Robinson et al. [176] refer to the higher half angle divergence for the laser intensities of $10^{19} W/cm^2$ equal to $\approx 55^\circ$. This also is in agreement with the divergence estimation performed in this experiment featuring half angle of $\approx 60^\circ$ discussed in the previous section. We also observe the variation of the angular distribution in time that is directly related to the electron beam scattering and straggling in the target.

3.3.3 Hybrid PIC Simulations of fast electron transport

The next step of the modelling is the transport of main fast electron beam with the parameters simulated by the 2D PIC code using axially symmetric 3D Hybrid PIC code. It is worth to note that coupling the results of the PIC code to the initialization of the electron beam in the Hybrid PIC requires some approximations. We want to take the initial electron beam generated by laser plasma interaction from LPI (laser plasma interaction) and neglect any transport effects simulated by the PIC code. The 3D PIC simulation is used to simulate the transport of fast electron beam and self - induced resistive magnetic fields. One of the main effects of the observation is the collimation of fast electron beam by self - induced magnetic fields. First of all, we are going to study the pre - generated magnetic field dynamics by the first electron beam produced by the seed laser pulse. This electron beam is generated

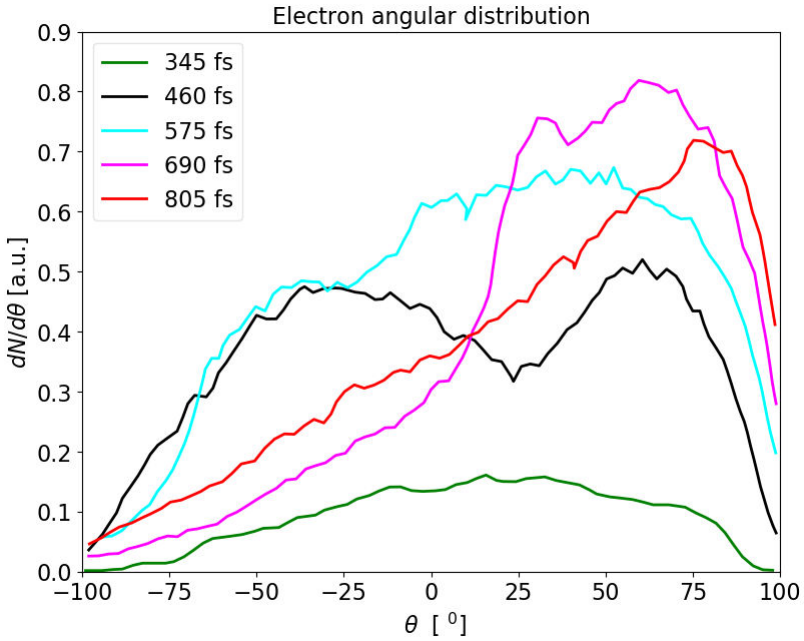

Fig. 3.39 Electron angular distribution obtained by PIC simulations with pre - plasma type 1 extracted at different simulation times.

by the laser intensity of $\approx 10^{18} W/cm^2$ and is used to produce the magnetic field inside the target before the main electron beam arrives. Secondly, we are going to simulate the main fast electron beam transport without pre - generated field and after that compare it with the double pulse simulations with the pre - generated field of different radius and evolution time generated by the first electron beam.

Simulation setup As was discussed in the introduction the Hybrid PIC code is used to simulate fast electron beam propagation in the matter by solving the Vlasov Poisson system of equations coupled with Maxwell equations for macro particles and fields while treating the background plasma as fluid. Then the input for this code is basically electron beam initial parameters such as energy distribution, angular distribution and spatial electron beam size. Such parameters were obtained for the electron beam generated by main laser pulse by 2D PIC Smilei simulations. For the seed electron beam , the hot electron temperature was estimated using the Beg's law and energy distribution function was automatically fit with this temperature in the code, the divergence angle was selected accordingly to the Green et al. [88]. It is worth to note that the divergence angle is not a directly accessible parameter in this code due to the complicated angular distribution function Eq. 2.63. The real input parameters are propagation and dispersion angles. A separate fast electron divergence study was performed to be able to achieve the required electron beam divergence that will be

Table 3.3 The Hybrid PIC input deck

Laser	I_L $[W/cm^2]$	ϕ [μm]	T_{hot}	$f(E)$	η	θ
Main	$\approx 10^{19}$	8	1500 keV (PIC)	from PIC	0.6 (PIC)	50° (PIC)
Seed	$\approx 10^{18}$	22 - 30	400 keV (Beg's law)	Fit	0.3	30° (Green)

discussed in the following section. The electron beam size was set twice as at twice the size of the laser focal spot. The summary of the input parameters is presented in the table 3.3.

Simulation of divergent electron beam

First of all, the 2D angular description of the accelerated electron source from the PIC code has to be extracted locally at 1 μm behind the laser interaction region, just after the zone where the Weibel instability is excited in order not to include the transport affected results. Then the angular distribution of the electrons is then called local angular distribution.

Angular distribution function The local angular distribution of fast electrons generated by the laser interaction at normal incidence is presented by the Gaussian function:

$$f_l(\theta) = \frac{A}{\lambda_L} \exp\left[-\frac{r^2}{r_0^2} - \left(\frac{\theta - \theta_0(r)}{\Delta\theta_0}\right)^2\right] \tag{3.35}$$

where A is a constant , r_0 is the the transverse Gaussian laser radius at $1/e$,$\theta_0(r)$ is the mean propagation angle of electrons at the radial distance r and $\Delta\theta_0$ is the mean dispersion angle around the direction defined by $\theta_0(r)$. The mean propagation angle is defined by the deviation of electrons from its main propagation axis due to the pondemorotive force that is found by the integration of the fast electron density in the transverse direction. It is related to the fast electron transverse velocity while the dispersion angle is related to the electron transverse temperature. The additional contribution to the beam divergence is coming from the electron scattering in small scale magnetic fields generated near the critical density n_c due to the Weibel instability. The propagation angle is expressed as:

$$\theta_0(r) = \arctan\left[\frac{p_x}{p_z}\right] \sim \arctan\left[\frac{\lambda_L r}{R_0^2}\right] \tag{3.36}$$

where p_x and p_z are the transverse and longitudinal electron momentum normalized to $m_e c$. We can also write it with use of the angular representation of $\tan\xi = A/R_0$. The behaviour of the propagation angle respect to the electron beam radius is shown in the Fig.

3.40 (left).

$$\theta_0(r) =\sim \arctan\left[\frac{\tan(\xi)r}{R_0}\right] \tag{3.37}$$

The case that correspond to our PIC simulations provides the mean $<\theta_0(r)>\sim 10^\circ$ 3.40 (left) (green line). The corresponding distribution function is shown in the the Fig. 3.40 (right) with the dispersion angle is of order of $\Delta\theta_0 = 60^\circ$. In 2D planar geometry the average angular electron distribution function is presented as:

$$f_p(\theta) = \int_{-\infty}^{-\infty} f_l(\theta, r)dr \tag{3.38}$$

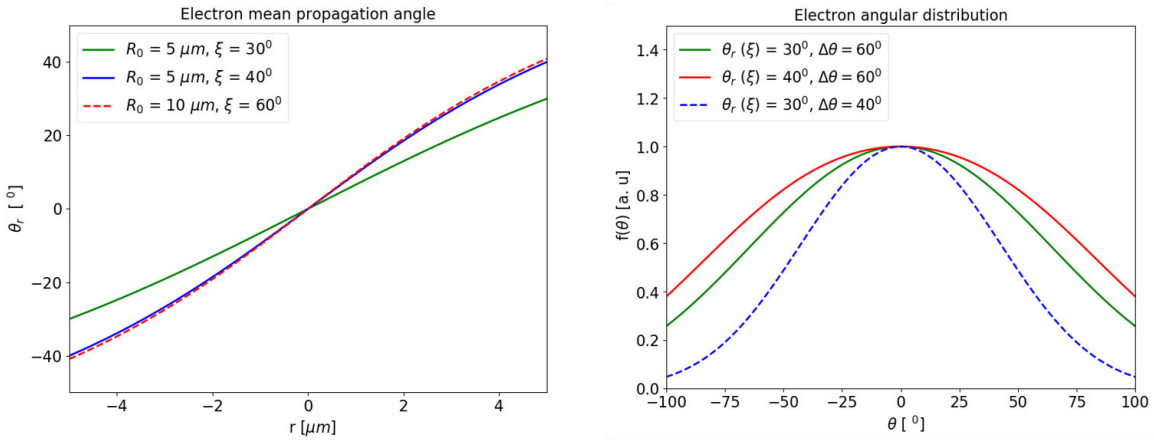

Fig. 3.40 The mean electron propagation angle θ_0 as a function of a radial distance r (left) and the electron angular distribution function(right) in planar geometry.

However in order to apply the results of 2D PIC simulations of electron acceleration as a source for 3D axially symmetric electron transport calculations, we have to define the average electron angular distribution function f_c in 3D cylindrically symmetric geometry that conserves information about the beam transverse velocity:

$$f_c(\theta) = \int_{-\infty}^{0} f_l(-\theta, r)dr + \int_{0}^{\infty} f_l(\theta, r)dr \tag{3.39}$$

Such definition allows all electrons propagating outwards from the laser axis have a positive angle $\theta > 0$.

Then the local angular distribution of a radially propagating electron beam in the injection surface is written as:

$$f_l(\theta) = f(\gamma)\exp\left[-\frac{r^2}{r_0^2} - \left(\frac{\theta-\theta_0(r)}{\Delta\theta_0}\right)^2\right] \tag{3.40}$$

where $f(\gamma)$ - the electron beam spectrum.

The cylindrical angular distribution function was used to fit the PIC simulation results (Fig. 3.41) with the following parameters as $R_0 = 5\mu m$ - radius of the electron beam, $\Delta\theta_0 = 60^\circ$ - dispersion angle and propagation angle $\theta_0(r)$ with $\xi = 30^\circ$.

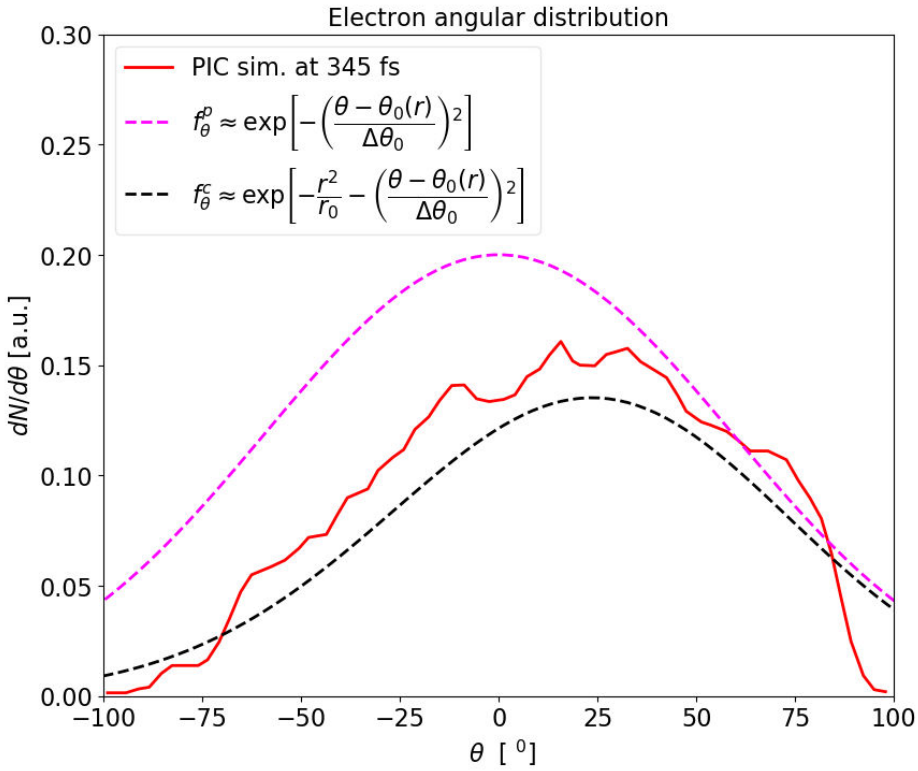

Fig. 3.41 2D full electron angular distribution function defined according to Eq. 3.35 (green dashed curve). “Cylindrical" full electron angular distribution function defined by Eq. 3.40 (black dashed curve). The red solid line represent the PIC simulation results of electron angular distribution extracted at 345 fs simulation time.

It’s worth noting, that the existence of preplasma with a larger scale length can drastically affect the electron beam divergence. This is because electrons are accelerated in a larger volume around the critical density, the critical layer is pushed forward by the laser longitudinal ponderomotive force and by the relativistically induced transparency. Therefore the laser plasma interaction region can’t be any more considered as planar. This effect “ballistically”

increases the electron transverse velocity behind interaction region, and therefore its propagation angle. At the same time, the energy of generated electrons is higher, which increases magnitude of the magnetic fields generated by the Weibel instability and therefore enhance the fast electron scattering. Then we should add a correction to the total mean propagation angle in with order to include the effect of pre - plasma length, which can be approximately given by:

$$\theta_{bal}(r) \sim \frac{rL}{2R_0^2}\Delta\theta_0^2 \tag{3.41}$$

where L is a pre - plasma length over which the electron scattering occurs. In our case $L \sim 3-4\mu m$. That adds another 10° to the average value of the mean propagation angle $< \theta_0(r) > + < \theta_{bal}(r) >= 30^0$.

In conclusion, to simulate the main electron divergence with the angular distribution provided by 2D PIC simulations we have to use the equivalent cylindrical full angular distribution function assuming the electron beam is initially propagating normally to the target.

Estimating the simulated beam divergence In order to validate the introduced fast electron angular distribution function, the used divergence of the electron beam as an output of the 3D Hybrid PIC code has to be estimated. One of the methods of the beam divergence measurement used in the experiments [127, 88, 188] is the dependence of the K_α spot sizes as a function of the target thickness. We performed a series of main electron beam transport simulations with the two different Al target thickness 50 μm and 30 μm with the Cu tracer layer of 5 μm to estimate the beam divergence using this experimental method. The initial parameters of the electron beam are taken from PIC simulations. The post - processed Cu - K_α signal from rear - target side integrated over 3 ps simulation is shown in the Fig. 3.42. The FWHM of Cu - K_α spot was compared between the two target thickness. The half angle of divergence is then defined by the slope of the line $\theta_{1/2} = \tan(a)$ Fig. 3.42 (right).

Simulations using different propagation and dispersion angular width are shown in Figure 3.43. The estimate divergence angle for the first case ($\theta_r = 20^\circ$,$\Delta\theta_0 = -40^\circ$) is 32° while for the second case ($\theta_r = 25^\circ$,$\Delta\theta_0 = -35^\circ$) it was found 80°.

We can see that the small change of the propagation angle triggers the increase of the electron beam angular spread. From the PIC simulations we know that the mean propagation angle has to be about 20°.

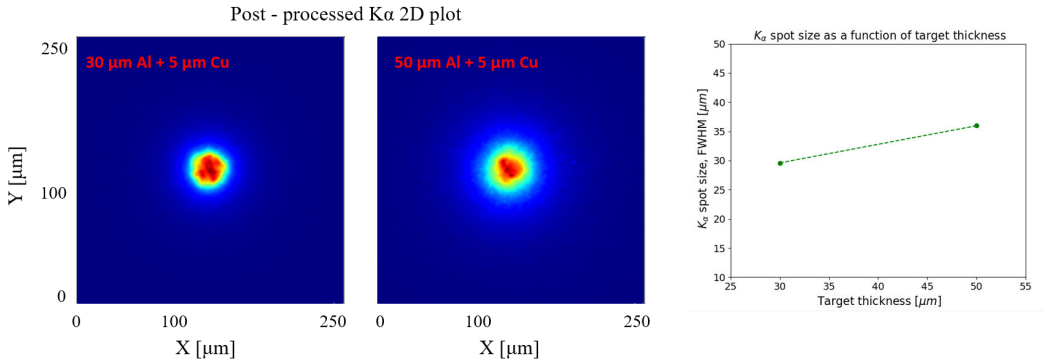

Fig. 3.42 The post - processed Cu - K_α signal at the target rear surface emitted by the fast electron beam crossing the Cu tracer layer for Al targets of 30 μm and 50 μm thickness (left). The FWHM of Cu - K_α spot size as a function of a target thickness (right).

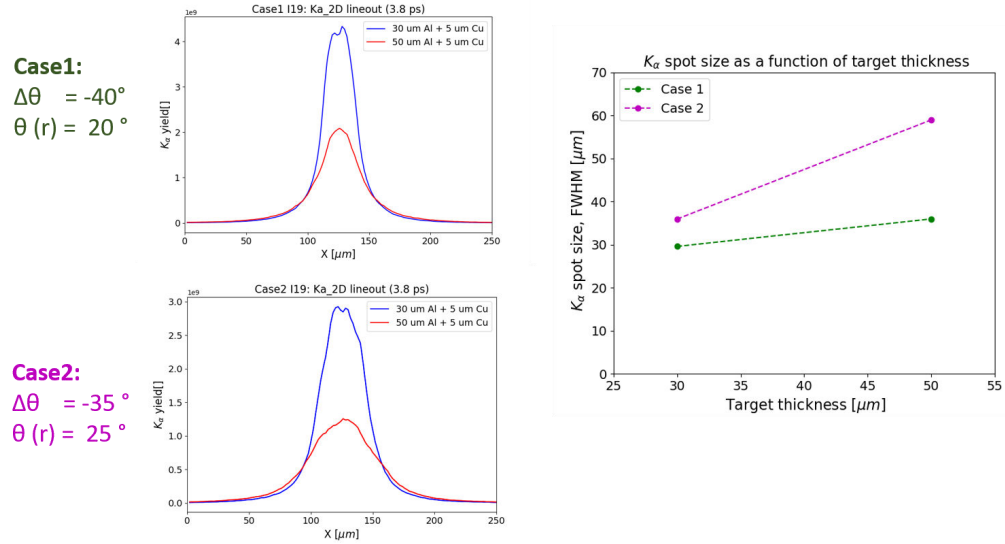

Fig. 3.43 The FWHM of Cu - K_α spot size as a function of a target thickness for two different simulation cases. Case 1 : The mean propagation angle $\theta_r = 20°$ and the dispersion angle $\Delta\theta_0 = -40°$ yielding to the total input angle of 30°. Case 2 : $\theta_r = 25°$ and the dispersion angle $\Delta\theta_0 = -35°$ yielding to the total input angle of 30°.

Seed magnetic field

The seed magnetic field defines the efficiency of collimation of the main electron beam. Experimentally, it was observed the importance of the radius of magnetic field , its intensity and time of the main electron beam insertion. A series of simulations were performed to optimize the parameters of the generator electron beam. The Fig. 3.45 and Fig. 3.46 show the 2D plots of the Y - component of azimuthal magnetic field and fast electron density extracted at different simulation times.

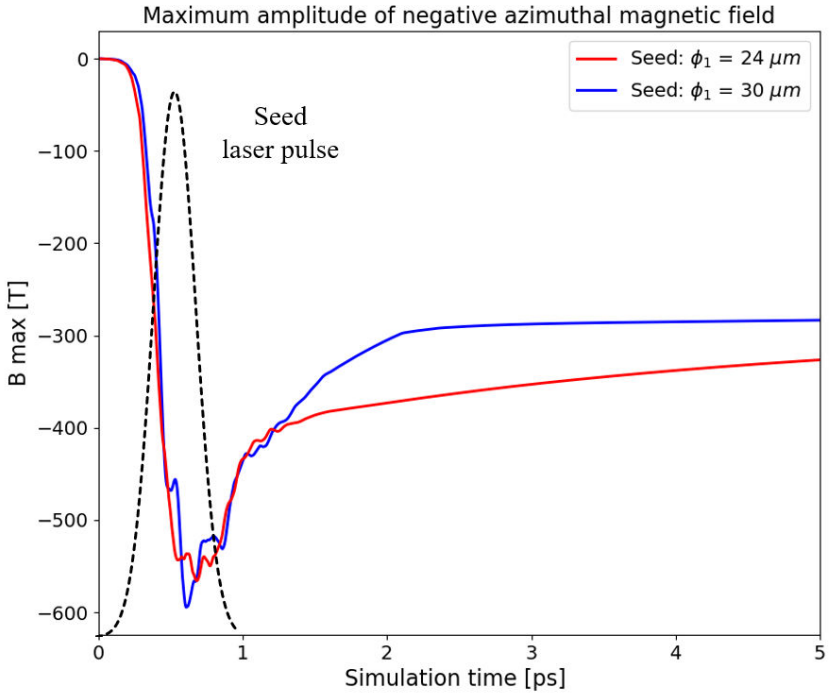

Fig. 3.44 The evolution of the maximum amplitude of negative azimuthal seed magnetic field.

The variation of the focal spot of the seed laser pulse affects the spatial extension of the magnetic field and its evolution in time. Here we consider the maximum amplitude of the negative azimuthal magnetic field for the simulation cases with the laser focal spots of $\phi_1 = 24$ μm (red line) and $\phi_1 = 30$ μm (blue line) shown in the Fig. 3.44 that correspond to the focal spot ratios of $\phi_1/\phi_2 = 2.5$ and $\phi_1/\phi_2 = 3$ investigated experimentally. The magnetic filed reaches its maximum at around 800 fs, about the end of the laser pulse. We can see that the slight variation of the electron beam R does not change the time of reaching the maximum amplitude of the magnetic field but it changes the magnetic field diffusion time

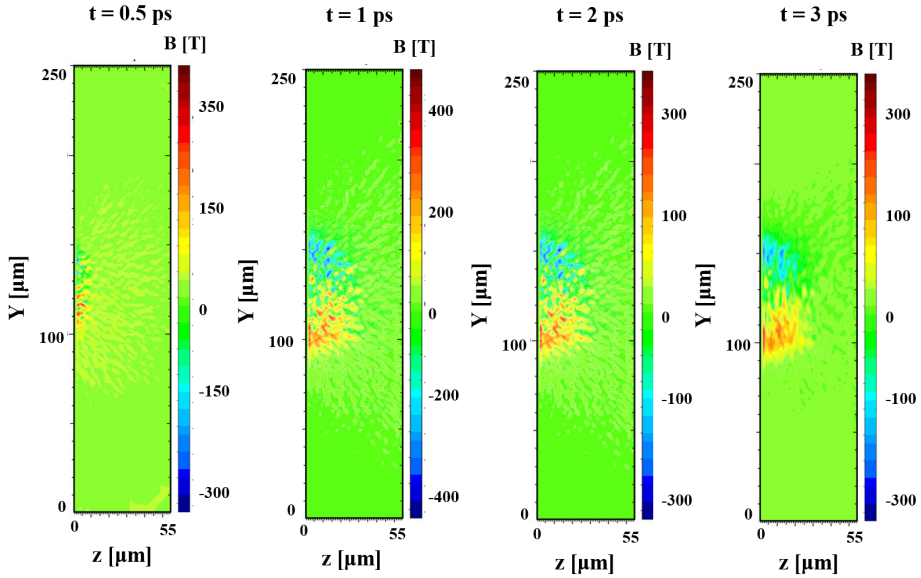

Fig. 3.45 Y - component of azimuthal magnetic field in [T] generated by the seed laser pulse of intensity $I = 3 \times 10^{18} W/cm^2$ and the focal spot of $\phi_1 = 24 \mu m$. The results extracted at simulation times of 0.5, 1, 2 and 3 ps.

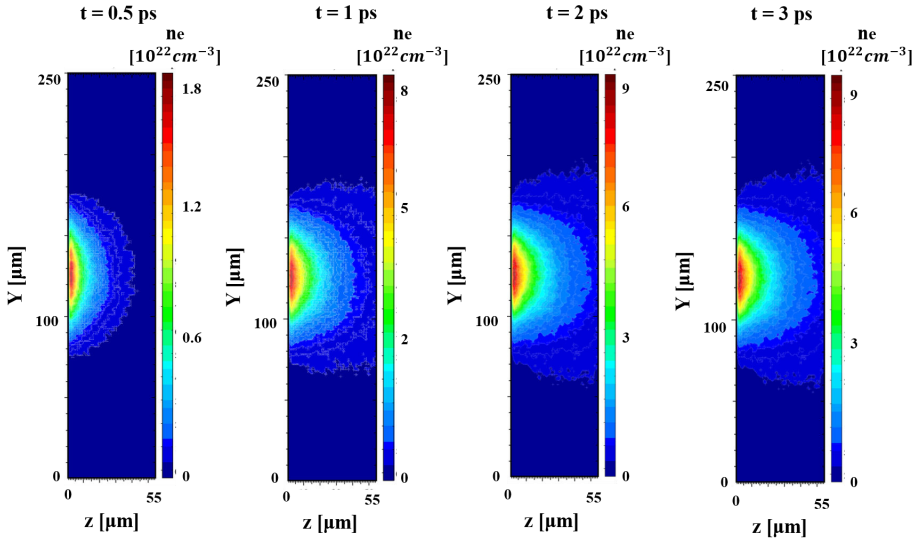

Fig. 3.46 Fast electron beam density generated by the seed laser pulse of intensity $I = 3 \times 10^{18} W/cm^2$ and the focal spot of $\phi_1 = 24 \mu m$. The results extracted at simulation times of 0.5, 1, 2 and 3 ps.

and its amplitude in the tail of the diffusion by the definition:

$$\tau_{\text{diff}} \propto \frac{R^2}{\eta} \tag{3.42}$$

The experimentally observedcollimation efficiency for the case with the seed laser pulse focal spot $\phi_1 = 30\ \mu$m (blue line) is very low in comparison with the case of $\phi_1 = 24\ \mu$m (red line) which can explained by the intensity of the collimating magnetic field. At the moment of injection of the main electron beam, where the collimation occurred (optimum delay time) the pre - generated magnetic filed reaches 300 T for the first case (at 2 ps injection time) and 400 T for the second case (at 3 ps injection time).

However the experimental optimum delay time was found to be not in the moment of the magnetic field reaching its maximum as was theoretically predicted by [217], but by the time magnetic field is already formed and starts to diffuse. The injection of the beam with 1 ps delay time, when the seed magnetic field reached its maximum didn't show any collimation observed. For the experimental run with the seed laser pulse with focal spot of $\phi_1 = 25\mu m$ the optimum time of the main electron beam injection was 3 ps and 2 ps for the $\phi_1 = 30\mu m$. According to the simulations of the seed magnetic field, there is no difference when to inject the second electron beam, after 1 ps of its evolution. Therefore the collimation effect can be explained only partially in terms of the seed magnetic field maximum amplitude evolution in time. One of the possible interpretation of the existence such optimum delay time is the seed magnetic field formation as a guiding field by itself. The example of the 2D magnetic field evolution in time is presented in the Fig. 3.45. The magnetic field starts to have guiding structure for at around 3 ps simulation time, while at 1 ps , when the magnetic field has a maximum amplitude overall guiding the magnetic field is still not formed. The importance of the form of the seed magnetic field is related to the process of the reconnection of the seed field with the magnetic field generated by the main electron beam that has a higher maximum amplitude by itself.

Double pulse simulation

The integrated simulation with two pulses was performed to study numerically the double pulse scheme and the importance of the pre generated field in the collimation of the main fast electron beam. It was found that the collimation to be caused primarily by the seed pre - generated magnetic field, however the significant role is also played by the collimating magnetic field generated by main electron beam that sustains the collimation deeper in the target. The simulation was performed with parameters of the main electron beam provided by 2D PIC simulation and the seed electron beam parameters that were optimized in the previous

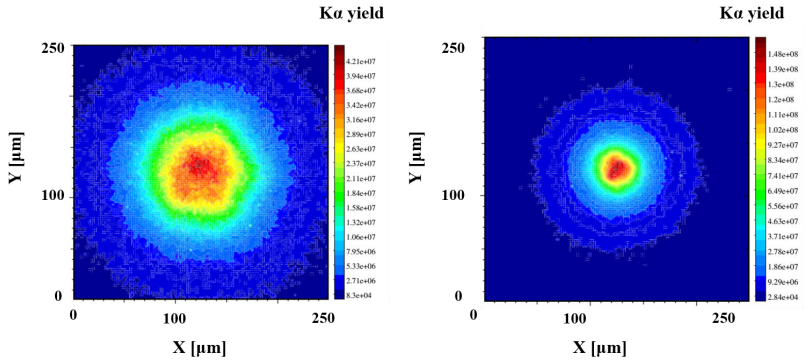

Fig. 3.47 The comparison of simulated post - processed Cu - K_α spot for the case with main pulse only (left) and with two consecutive laser pulses (right). The results are integrated over the simulation time of 5 ps.

section. The divergence was artificially increased by 5^0 in order to observe the collimation effect caused by the pre-generated magnetic field and not by the self - collimation of the main beam by itself, that is occurring numerically if the input electron beam divergence is small. The second main electron beam was injected at $\Delta t = 3$ ps delay time after the seed laser pulse injection to the target. The Fig. 3.48 shows the results of the simulations extracted at the peak of the main laser pulse arrival - 3.5 ps. The studied variables are the fast electron density, magnetic field , resistivity and post - processed Cu - K_α spot , generated by the fast electron beam crossing the Cu tracer layer. It can be seen that the collimating field which guides the electrons in the target has been produced with the pre - generated seed magnetic field by the first electron beam. It is seen that the post processed integrated Cu - K_α spot is also reduced twice the size in the comparison with the run with only main divergent beam 3.47. While the simulated spot sizes are smaller than those experimentally observed the reduction of size is of the same order as the experiment and the simulations elucidate much of the detailed physics leading to the guiding effect.

3.4 Conclusion

We extensively studied the double pulse approach to the collimating of relativistic electron beams produced in high-intensity laser-plasma interactions. By changing the ratio between the focal spots of the two lasers ϕ_1/ϕ_2 and the injection time Δt, we observed a clear signature of collimation, validating the theory [176, 175]. Two complementary diagnostic techniques have been implemented, which mainly show the respective behaviour of very fast vs. less fast hot electrons. The results are essentially in agreement. In particular, both from experimental results and from simulations, we have shown that for each value of ϕ_1/ϕ_2 there is an optimal

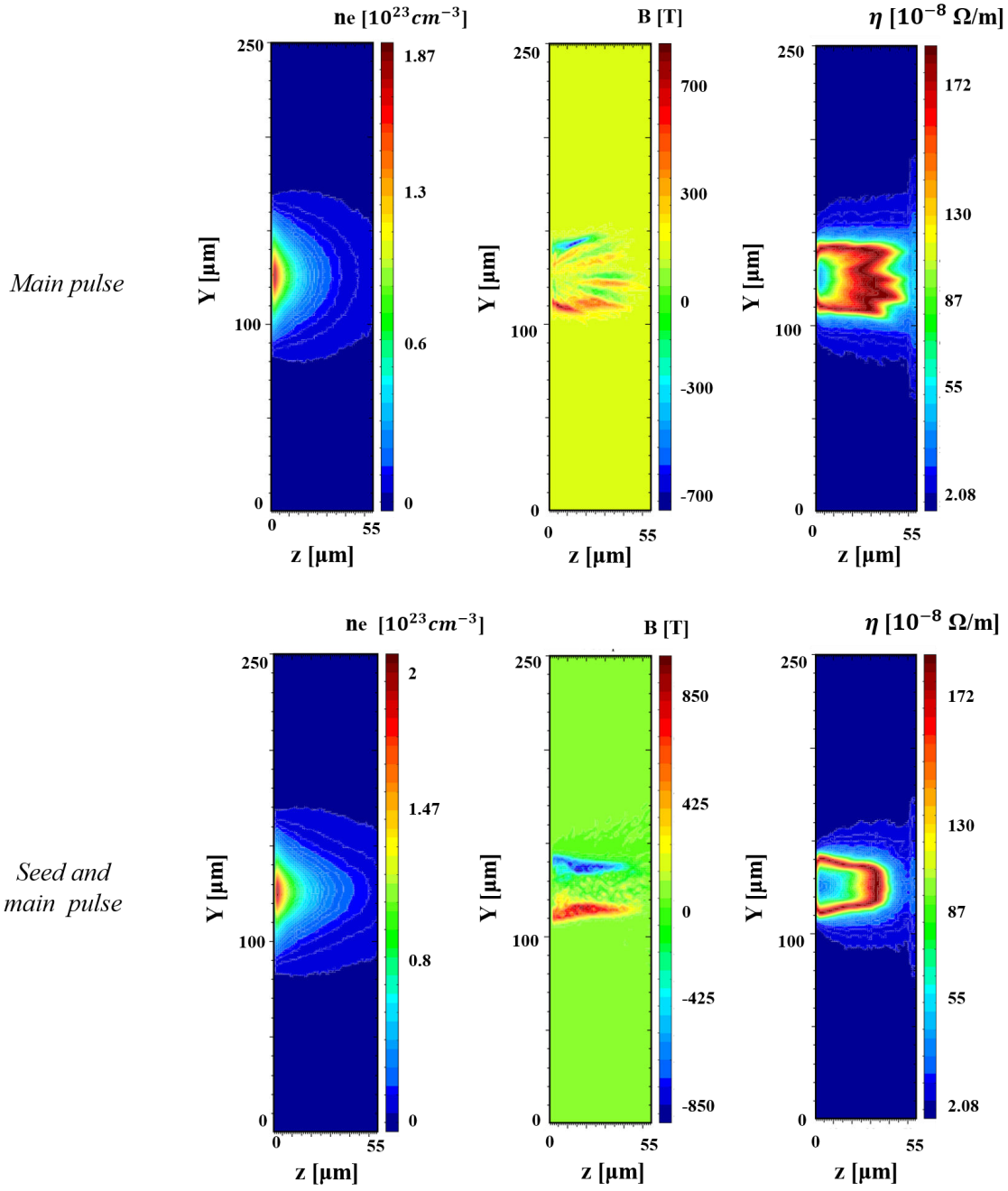

Fig. 3.48 The comparison of the simulated fast electron, Y-component of the azimuthal magnetic field and the resistivity for the case with the main laser pulse only (top) and with two consecutive laser pulses (bottom).The simulation plotted at the peak of the main laser pulse arrival.

injection time Dt, which, in agreement with expectations, increases when ϕ_1/ϕ_2 is decreased. We also found that about 70 % of hot electrons can be collimated by this mechanism. In conclusion, the double pulse technique appears to be an easy and controllable way to limit the divergence of fast electrons and improve energy transport deep into the target. This result opens interesting perspectives for a large variety of applications including the fast ignition approach to inertial confinement fusion and the optimisation of laser-driven particle sources.

Experimental results report that the optimum delay time is a function of the focal spot ratio, that comes from the time evolution of the magnetic field. According to the numerical simulations the magnetic field reaches its maximum in the end of the laser pulse interaction with solid target $\tau_L \approx 0.5$ ps. The collimation occurs with delay time between laser pulse of Δt = 3 ps, corresponding to $6 \times \tau_L$ for the minimum focal spot ratio of $\phi_1/\phi_2 = 2.5$ and Δt = 2 ps, corresponding to $4 \times \tau_L$ for the maximum focal spot ratio of $\phi_1/\phi_2 = 3$. It seems to be in good agreement with previous experiment, in which laser pulse duration was τ_L= 1 ps and collimation occurred between 4 - 6 ps of delay time of the laser pulses, that also correspond to the 4 - 6 $\times \tau_L$. Taking to account, that intensity range of referred experiment was $10^{18} - 10^{19}$ W/cm^2, one can clearly indicate that the optimum delay time is not a function of the laser intensity.

The more detailed numerical study of the scheme is ongoing in order to explore the magnetic field dynamics occurring in the target and the parameters that play important role in the efficient collimation of the fast electron beam.

Chapter 4

Proton stopping power at low velocities in warm dense matter

The main objective of the proposed experimental campaign is to measure ion stopping power of proton beam in a moderately coupled and degenerate plasma target close to the Bragg peak region where the ratio between proton velocity and electron thermal velocity approaches unity. Experimentally, investigating the regime $v_p \sim v_{th}$ is challenging, especially due to a strong stopping power dependence with temperature and density, requiring a precise characterization of the target conditions. For this reason we propose a two steps approach: i) in the first part of the experiment we propose to characterise the proton probe created by using a 1.2 T magnetic selector field and select 0.3 - 0.5 MeV proton beam projectiles with an energy spread below 50 keV. ii) after characterizing the proton beam we will study stopping power in 1 μm cold carbon target and later in carbon plasma at given temperature and density conditions. The high repetition rate provided by CLPU VEGA II system can guarantee a sufficient number of shots to statistically samples plasma conditions and be confident in obtaining a sufficient number of shots that reproduce the same plasma medium condition.

4.1 Theoretical modelling

Theoretical modelling was performed for this experimental campaign aimed at clarifying the range of ion beam and plasma conditions that could be accessed using the laser parameters of CLPU VEGA - II laser facility and at optimizing conditions in order to achieve the ion beam - plasma interaction at low velocity projectile ratio. The main constrain for high quality stopping power beam are reproducibility of the target conditions and stability of the ion beam source due to the laser fluctuation in energy and pulse duration. To provide a good estimation

of the predicted ion beam energy loss in warm dense matter, the simulations were performed in the following steps:

1. The warm dense matter generation by a fs laser (heater) is simulated by the 1D hydrodynamic code MULTI-fs [173] and 2D hydrodynamic code RALEF2D [206] providing the characterization of target electron temperature T_e and density n_e when the target still remains at solid and near solid density. The simulations are performed in first 100 ps before significant hydrodynamic expansion occurs.

2. The ionization state Z of the generated plasma conditions for each expansion time of interest with different parameters of T_e and n_e is calculated with FLYCHK atomic code in non LTE [45].

3. The stopping power is estimated for proton projectile energies of 0.3, 0.5 and 0.8 MeV for each expansion time taking the ionization state Z, n_e T_e using the different stopping power analytical models Bethe, unified stopping power models Li - Petrasso [130], T - Matrix [66] , ad - hoc bound + free stopping power model by Zimmermann [229] and Casas [35].

4.1.1 Warm dense matter simulation

The simulations of the plasma generation and its expansion in space and time are very important for the high quality ion stopping power measurements. Besides achieving target temperature of several eV with densities ≈ 1 g/cm^3, transversal and longitudinal homogeneity with respect to the ion beam propagation is required. Transversal uniformity of the plasma is needed to ensure that all the ions in the beam interacted with the plasma with same condition at a probing time. The heated region has to be twice as big as the incident proton beam in order to provide a good overlapping. On another hand, good longitudinal uniformity has to be achieved for constant ionization degree of the matter along the axis of the ion beam propagation. Indeed, such high requirements are hard to fullfill experimentally due to the inhomogeneity of the fs-laser - target interaction, laser focal spot inhomogeneity and fluctuations and target impurities. The Figure 4.1 shows the tentative geometrical scheme of the laser - target and ion beam - target interaction. The 1D hydrodynamic simulations provide good estimation of the target temperature and density evolution along the ion propagation axis. Then the ionization of the target according to the predicted hydrodynamic values is estimated. In addition, the 2D hydrodynamic simulations provide more complete information on the target expansion longitudinally and transversally with respect to the ion beam

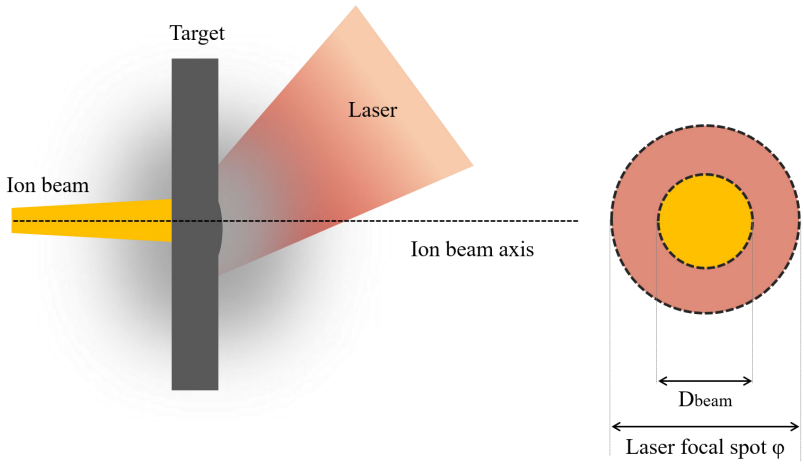

Fig. 4.1 The geometry of the interaction between the ion beam with diameter D_{beam} and warm dense matter target generated by laser pulse with focal spot diameter ϕ.

propagation axis. It allows more precise prediction of the time when plasma condition tend to be more homogenous to satisfy both mentioned requirements.

General simulation setup For the warm dense matter generation a p-polarized laser pulse with wavelength $\lambda_L = 800$ nm, pulse duration $\tau_L = 100$ fs and energy of 0.2 J is focused on 1 μm thick Carbon foil with the density of ρ = 1.3 g/cm^3 with the incidence angle of 35° and the focal spot of 100 μm diameter yielding in an intensity of $I \approx 10^{16}$ W/cm^2. The relatively large focal spot was chosen in order to heat more homogeneously the larger area of the target and as well taking to consideration the experimental constrains explained in the experimental section. It is worth noting, that the pre - heated area should be larger than the proton beam size that interacts with the matter. For both 1D and 2D hydrodynamic simulations, the same laser and target parameters were used to a certain extent. Indeed, in the 1D simulation the parameters of the focal spot are not used.

1D - Hydrodynamic simulation

The 1D hydrodynamic simulations were performed with Langrangian MULTI-fs code [172] based on the MULTI radiation-hydrodynamic code [171] developed by R. Ramis *et al.*. The hydrodynamic motion is solved together with laser energy deposition and transport by the thermal conductivity and radiation in a one dimensional geometry using fractional step scheme and takes to account the difference in interaction between ns-laser pulses with solid, where normally hydrodynamic codes are applied, and fs - laser pulse with solid, when a more steep plasma gradient is generated with the $L_H \leq \lambda_L$. This is achieved by solving Maxwell's

equations in anexplicit way to obtain the light field. A Two - temperature fluid model (See Laser-Plasma Modelling subsection) is used to describe the material from solid state to hot plasma conditions.

Simulation input The material properties of Carbon are evaluated with SESAME EOS. The electron collision frequency (Eq. 2.93) is calculated by a modified Drude - Sommerfeld model that takes into account the electron degeneracy in warm dense matter and modifications in Coulomb scattering which apply to slow electrons having velocities $Ze^2/\hbar v \geq 1$ [208]. The laser temporal profile was assumed to be Gaussian. For each time step of simulation the hydrodynamic values are evaluated in each layer of the target as shown in the Figure 4.2. The target was separated by three zones with different layer thicknesses starting from very thin layered region needed for resolving the features of the direct laser pulse - matter interaction on the front side to the medium and larger layered regions where just radiation transport coefficients have to be evaluated. As an output of the code one gets $T_e(x_i)$ and $\rho(x_i)$ for each i layer.

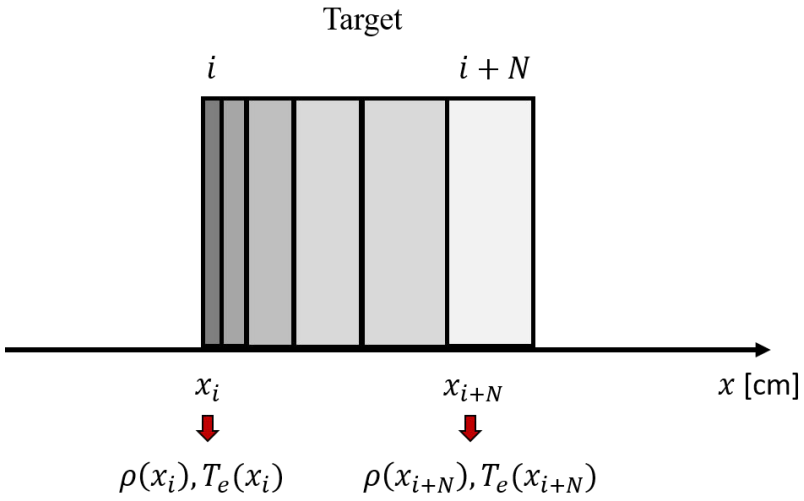

Fig. 4.2 The scheme of the fraction step scheme used in the MULTI-fs simulations with total number of layers $N = 160$. The laser arrives from left to right.

Results The simulation results of target density ρ and electron temperature T_e are shown in the Figure 4.3 for the wide range of the expansion times starting from very early 10 ps and finishing at 120 ps when the target tends to hydrodynamically expand to below solid densities. The target is heated very quickly during the first 10 ps and after starts to cool down slowly and tends to have a more stable and uniform temperature profile through it areal density. It's worth noting, that the laser angle of incidence was adjusted in order to

reach higher laser absorption. Taking into account, that with the increased incidence angle, enhanced absorption is expected, one can adjust the incidence angle to the maximum value allowed by experimental conditions. For the 35° laser incidence on target, an absorption of 22 % was achieved.

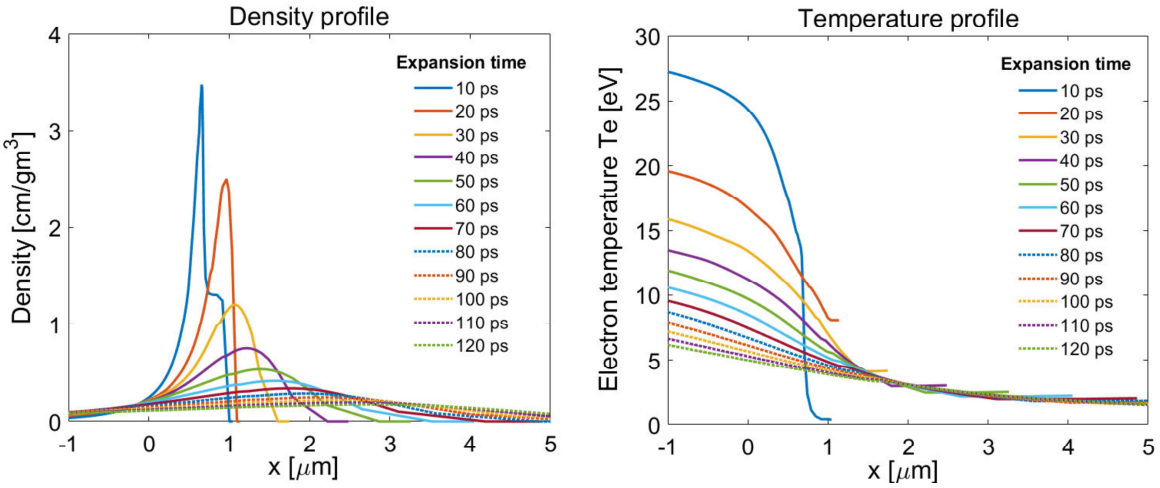

Fig. 4.3 Density profiles simulated with 1D hydrodynamic code MULTI-fs for different expansion times from 10 - 120 ps (left). Corresponding temperature profiles for the expansion times from 10 -120 ps (right). The laser pulse arrives from left to right.

According to the simulated profiles the target achieves conditions of interest between 20 to 45 ps of expansion time, when the $\rho \approx 1$ g/cm^3 and $T_e = 15 - 20$ eV that corresponds to the Warm Dense Matter regime shown in the Figure 4.4 giving a more detailed evolution of the hydrodynamic profiles for each 5 ps of expansion time. For the following calculations it is convenient to use the units of the target areal density $\rho R = \rho \times \Delta x_i$ instead of the units of distance.

For the matter ionization calculation, it is assumed that the plasma is in not local thermal equilibrium (non LTE). The collisional - radiative atomic code FlYCHK is use to estimate an ionization degree caused by electron exchange dynamics. In order to calculate the ionization state dynamic for each plasma condition at certain plasma expansion time, the hydrodynamic

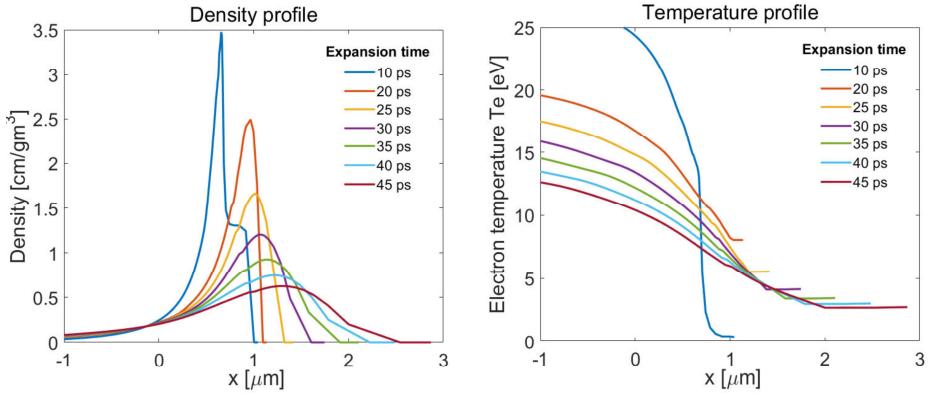

Fig. 4.4 Density profiles simulated with 1D hydrodynamic code MULTI-fs for different expansion times from 10 - 45 ps (left). Corresponding temperature profiles for the expansion times from 10 - 45 ps (right). The laser pulse arrives from left to right.

profiles $T_e(x_i)$ and $\rho(x_i)$ were introduced into the atomic code and the ionization calculated as a function of time for each Lagrangian layer. Figure 4.5 represents the simulated ionization Z_{ion} as a function of target areal density ρR for 10, 20, 20 and 40 ps of plasma expansion time. Figure 4.6 shows that the plasma ionization varies from Z = 4 to 1 within the target areal density being partially ionized. At early expansion times the ionization is very unstable caused by the high matter inhomogeneity in terms of temperature and density as shown in Figure 4.4, however at 20 - 30 ps it reaches more constant ionization degree behaviour with mean value of $< Z >= 2.5$ that corresponds to the 40 % of full ionization of the carbon matter.

According to the 1D hydrodynamic simulations of plasma generated by the fs laser heater, the acceptable homogenous target conditions are achieved with an expansion time between 20 to 40 ps featuring the warm dense matter of $T_e =$ 10-20 eV at solid density with partial material ionization. It is worth noting, that the choice of the low Z material for target such as Carbon with $Z = 6$ was due to the heating / ionization degree obtainable by the fs - laser pulse with the parameters at the VEGA II laser facility. Indeed, by using low Z, low solid density material $\rho \approx 1.3\text{g/cm}^3$ ensures heating up to high enough ionization states as required for the regime where the ion stopping power has to be measured.

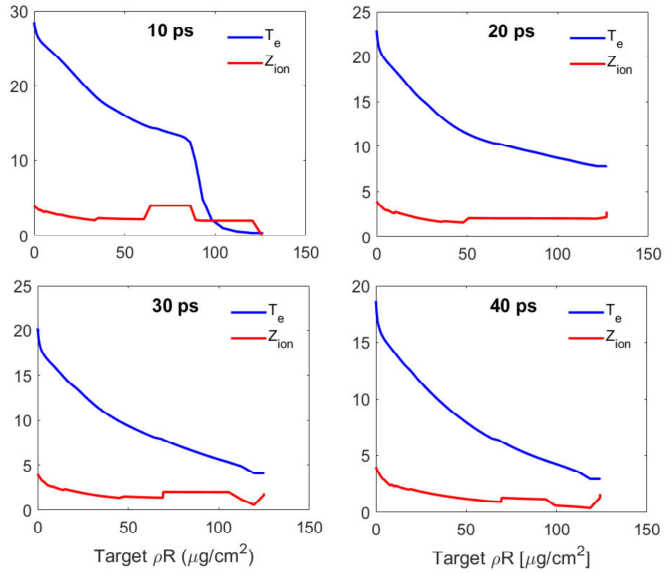

Fig. 4.5 The ionization state of the plasma as a function of the target areal density (red solid line) estimated using FLYCHK and corresponding temperature T_e as a function of target areal density used for the calculation (blue solid line) for the different plasma expansion times - 10, 20, 30 and 40 ps.

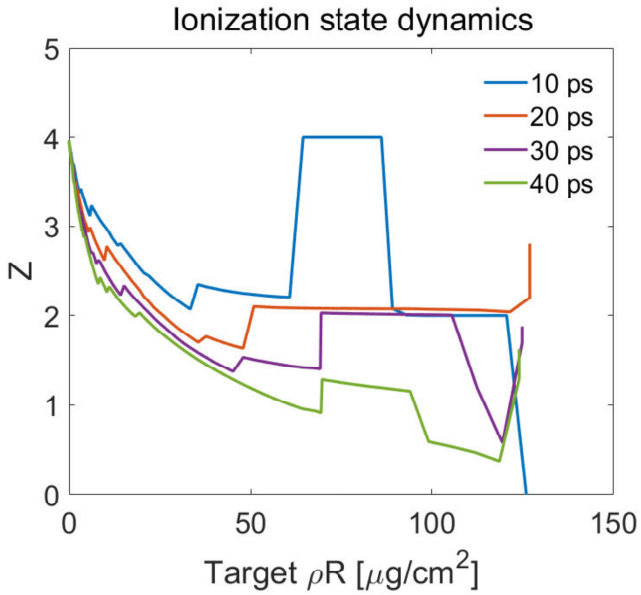

Fig. 4.6 The plasma ionization state as a function of the target areal density (red solid line) estimated using FLYCHK for the different plasma expansion times - 10, 20, 30 and 40 ps.

2D Hydrodynamic simulations

The 2D hydrodynamic simulations were performed in collaboration with Ana Tauschwitz (GSI, Fermany) using RALEF2D (Radiation Arbitrary Lagrangian-Eulerian Fluid dynamics) code [206]. This code was very well benchmarked with experiments performed at the GSI PHELIX laser facility [32, 75, 38]. The code based on a one- fluid and one-temperature hydrodynamic model solving heat and radiative transport by solving of frequency-dependent radiative transport equation in its quasi-static approximation in two- dimensional geometry.

Simulation setup The material properties of Carbon are evaluated with SESAME EOS. The reflectivity of the Carbon surface is taken as 10 %. The heater irradiated the Carbon foil with the focal spot $\phi = 100$ μm (FWHM). The laser pulse spatial and temporal profiles are assumed to the Gaussian. The target surface is divided by the 31 transversal Rays with 5 μm separation between each other. For each step hydrodynamic profiles are evaluated along all the rays starting from Ray 1 that correspond to the ion beam transversal axis - central axis.

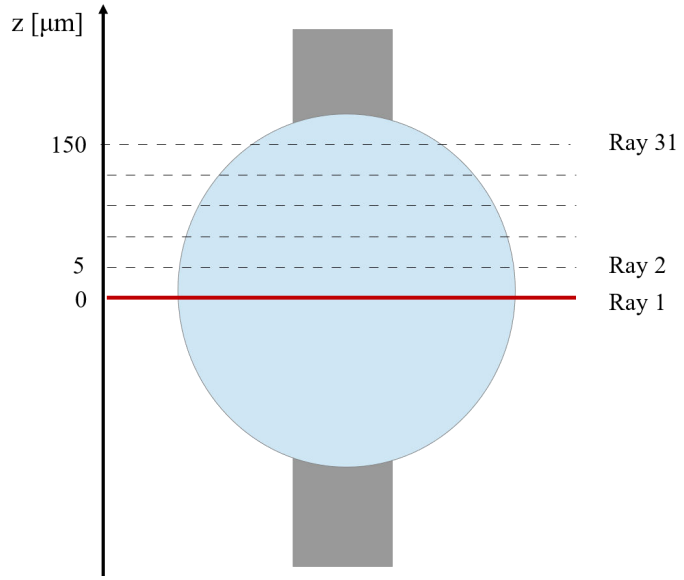

Fig. 4.7 The scheme of the Rays used in RALEF2D simulations. The simulation covers 150 μm of the transverse distance treated by 31 Rays. The simulation is axisymmetric. The red line corresponds to the ion axis

The simulations were performed for expansion times up to 100 ps with output steps of 5 ps. The expansion times correspond to the ones simulated with MULTI - fs in order to to compare the hydrodynamic data.

Results First of all, let's consider the plasma areal density spatial variation in time. The Figure 4.8 shows the plasma density profile as a function of the transversal radius with respect to the ion axis for all the expansion times. Initially the target expands very quickly and after 30 ps slowly expands with velocity of 0.03 μm/ps on the central axis. At 100 ps the target density is still close to solid with $\rho \approx 0.27$ g/cm^3. The most important feature of this simulation is to estimate the radius of areal density homogeneity on the central axis. The areal density is more stable in transverse direction at early expansion time, when the heating 2D effects still do not affect the profiles significantly. Assuming the ion beam size of 50 μm, that corresponds to the $\pm$ 25 μm from the ion axis, one can estimate the variation of 117.2 $\pm$ 0.5 μg/cm^3 for the 10 ps profile, 112.2 $\pm$ 0.5 μg/cm^3 for 20 ps, 108.2 and 105.1 $\pm$ 1.1 μg/cm^3 for 30 and for 40 ps of expansion time respectively. This variation is very small and will allow the sufficient precision of the measurement. One can mitigate any fluctuation by increasing the focal spot size of the laser beam, thus heating a larger area, or by decreasing the ion beam size.

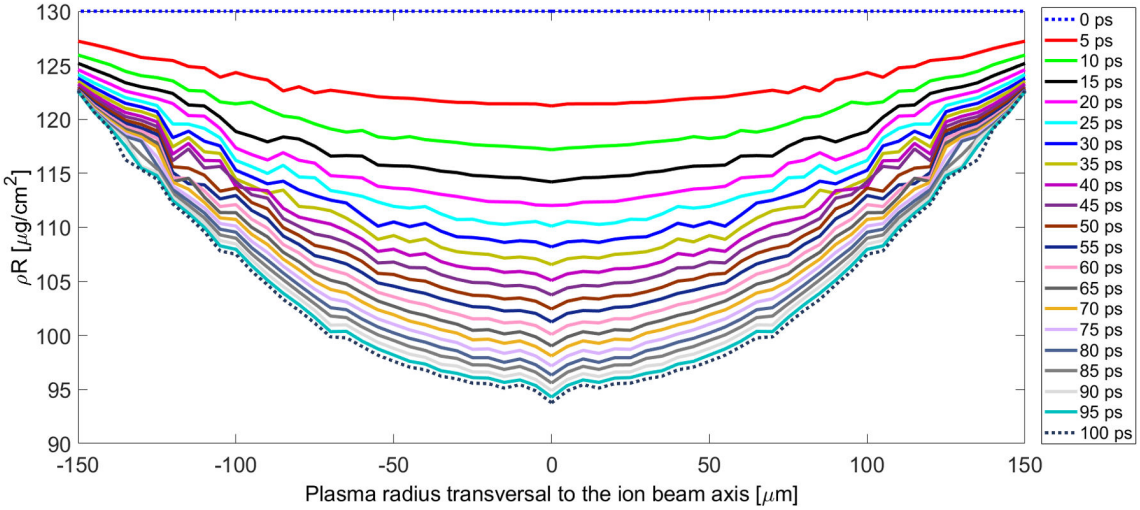

Fig. 4.8 The areal density as a function of the radial size to the ion beam axis for 0 - 100 ps expansion times simulated with RALEF2D

The 2D effect of the heating can be seen on the Figure 4.9, where the areal density is calculated along the target longitudinal at different position respect to the central axis. The most dynamic expansion is observed at the distances up to +75 μm from the central axis, that corresponds to the focal spot size. The areal densities at the central axis and +25 μm do not have any major difference up to 35 ps expansion time, then a small variation can be seen at later time of expansion on the order of 2 μg/cm^2. Thus, it can be concluded that the 100 μm focal spot size of the heater can be used for the ion stopping power measurements with a maximum ion beam diameter of 50 μm.

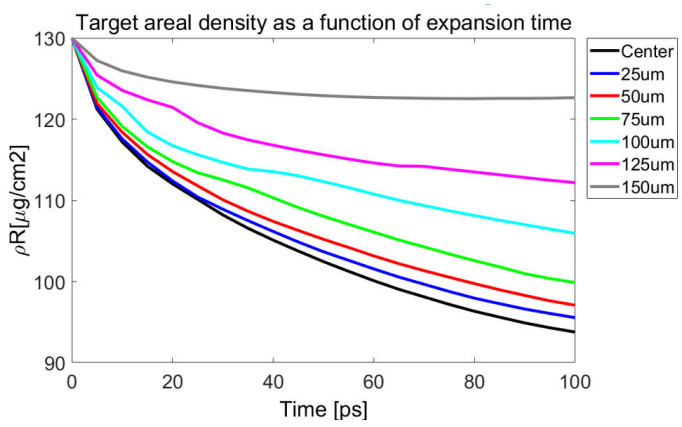

Fig. 4.9 The areal density as a function of expansion time calculated along the Rays starting at central ion axis (black) to +150 μm from the central ion axis with the step of 25 μm.

The hydrodynamic profiles of the target temperature T_e and density ρ for the expansion times of 10 to 50 ps simulated at the ion axis are presented on the Fig. 4.10. The results are quite in good agreement with MULTI-fs and features the optimum target conditions at 20-40 ps of expansion time. It seems , that the MULTI - fs provides higher temperature by 3-4 eV for the profiles of interest, most probably caused by not taking into account 2D effects related to the finite focal spot of the laser.

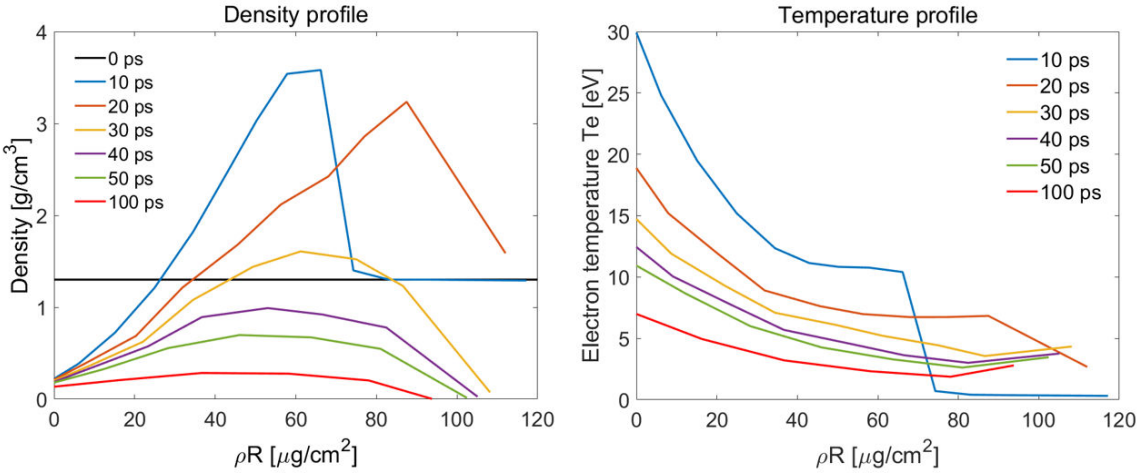

Fig. 4.10 Density profiles as function of areal density simulated with 2D hydrodynamic code RALEF2D for different expansion times from 10 - 50 ps (left). Corresponding temperature profiles for the expansion times from 10 - 50 ps (right).

The mean ionization degree calculated in LTE mode inside the RALEF2D code is shown in the Fig. 4.11. It is important to note, that in order to calculate the plasma charge state the hydrodynamic profiles should be post-processed in an atomic physics code in non LTE mode.

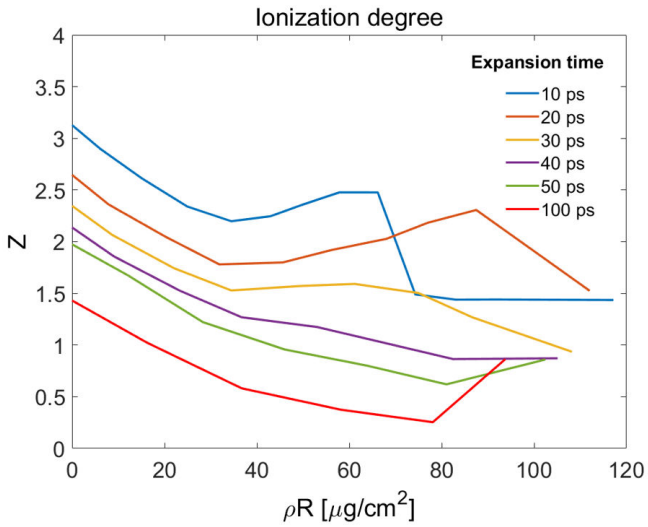

Fig. 4.11 The calculated plasma ionization for the given hydrodynamic profiles at 10, 20, 30, 40 ps.

4.1.2 Theoretical predictions on ion stopping power

The ion stopping power calculations were performed using the target conditions simulated with MULTI-fs primarily for the 500 keV ion projectile. To define better the warm dense matter conditions the plasma degeneracy Θ and plasma coupling Γ are calculated for each of the expansion time Fig. 4.12 as well as the velocity projectile ratio v_p/v_{th}. For the given parameters, the ratio of $v_p/v_{th} \approx 3-3.5$ can be achieved. By varying projectile velocity to 0.2 - 0.3 MeV results to quite same ratio, while increasing the energy of projectile to 0.8 MeV increases the ratio to $v_p/v_{th} \approx 4-5$. As mentioned in the introduction the modelling of this regime of ion beam - warm dense matter interaction for low velocity projectiles is quite challenging and requires special approaches in calculation taking into account degeneracy effects and bound electron contributions to stopping power.

Many models are not even valid for this regime of interaction as discussed previously, such as BPS [33] , RPA [11] and T- Matrix [121]. Therefore the most appropriate analytic models that were proposed to treat the exotic interaction were considered.

Results In order to estimate predicted energy loss of the E_p = 500 KeV projectile with charge state Z_p = 1 (proton beam) at $v_p/v_{th} \approx 3$ in the warm dense matter three different models were employed:

- Li - Petrasso stopping power model including degeneracy effects [130] indicated as **LIP deg**

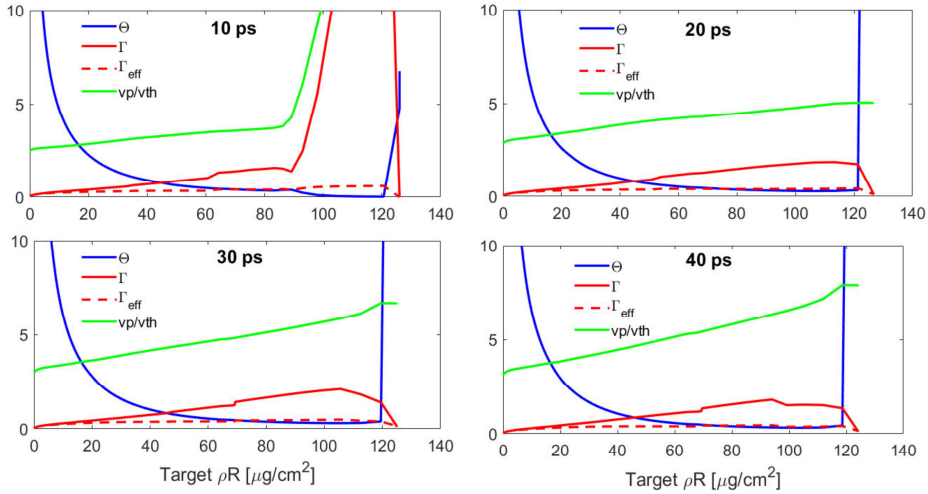

Fig. 4.12 The calculated plasma degeneracy and plasma coupling parameters for the given simulated hydrodynamic profiles with MULTI-fs as well as velocity projectile ratio v_p/v_{th} at 10-40 ps of expansion time.

- Zimmerman parametrization [229] taking both bound- and free-electron components of the Maynard-Deutsch stopping power model [141] shown as **ZIM**
- T-Matrix with dynamic screening length λ_D' [66] shown as **TM**

The stopping power was calculated for each of the expansion times taking the MULTI-fs hydrodynamic profiles of electron temperature T_e and mass density ρ and ionization charge state of plasma Z_{ion} provided by FLYCHK simulations and shown in the Fig. 4.13 for the 10 and 20 ps times and in the Fig. 4.14 for 30 and 40 ps times of expansion time. The stopping power calculated by SRIM code [228] is added for the reference of the solid cold carbon target.

The simulations show that the proton stopping power is highly uniform at 10 ps of the expansion time , when target conditions are varying a lot along its areal density. For the target conditions starting from 20 ps expansion time the proton stopping power is more homogeneous through all target. Thus, expansion times of 20-40 ps are more suitable for the experimental measurements. The energy loss was calculated by integrating the stopping power over the target areal density along the proton projectile trajectory. The initial projectile energy is calculated integrating to its stopping power along the trajectory by using Runge - Kutta scheme of first order to obtain the energy loss for each spatial step dx in plasma. The

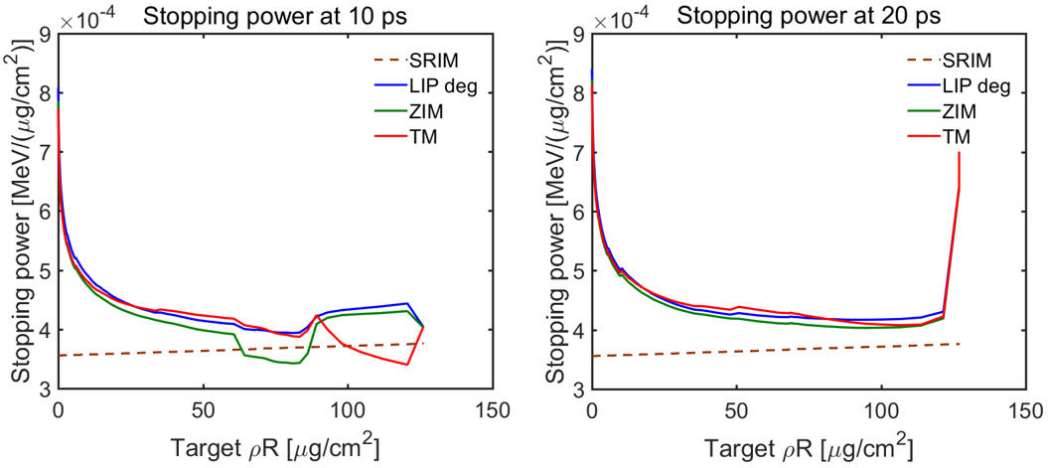

Fig. 4.13 Stopping power of 0.5 MeV proton beam projectile as a function of target areal density calculated with SRIM [228](dashed brown line), Li - Petrasso with degeneracy [130] (blue solid line) and T-Matrix with λ_D' [66] (red solid line) at 10 ps (left) and 20 ps expansion time (right).

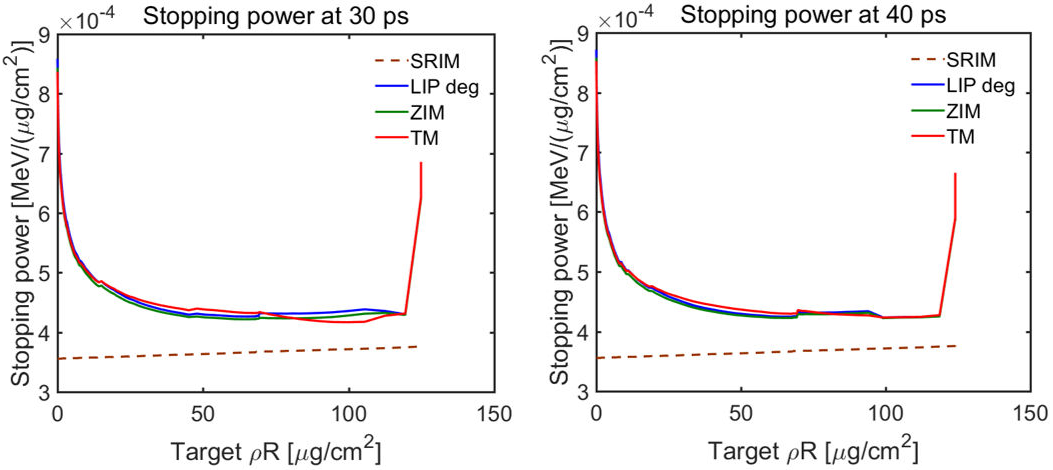

Fig. 4.14 Stopping power of 0.5 MeV proton beam projectile as a function of target areal density calculated with SRIM [228](dashed brown line), Li - Petrasso with degeneracy [130] (blue solid line) and T-Matrix with λ_D' [66] (red solid line) at 30 ps (left) and 40 ps expansion time (right).

step dx is defined from the MULTI-fs spatial step of the simulations. The energy loss as a function of time is presented in the Fig. 4.15 estimated with the aforementioned models. It was precisely calculated for the time range between 20 to 30 ps with a time step of 2 ps with the previously simulated hydrodynamic profiles and ionization states. Here it is assumed that the proton projectile does not have a time duration,which does not correctly correspond to the experimental conditions, where the proton beam has the energy bandwidth and spread in time (See Section of Energy Selector). The minimum estimated time spread for the 0.5 MeV projectile is $\approx$ 15 ps. Therefore, the proton beam would probe the plasma conditions integrated over 15 ps of expansion time.

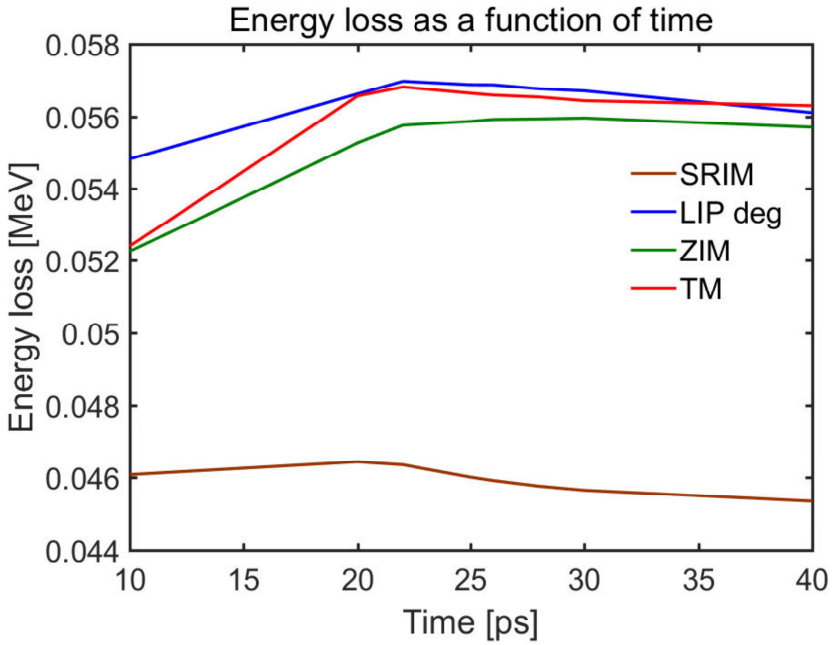

Fig. 4.15 The energy loss of 0.5 MeV proton beam as a function of plasma expansion time calculated with different stopping power models : SRIM(solid brown line), Li - Petrasso with degeneracy (blue solid line) and T-Matrix with λ_D' [66]

The projectile energy loss in the solid was calculated with the SRIM code for the 500 keV projectile interacting with a 130 μg/cm^2 Carbon foil and is equal to 0.046 MeV. The energy loss in the plasma conditions is compared to the solid target case, to observe the enhancement of the energy loss .

At 10 ps expansion time the Zimmerman and T-Matrix with λ_D' predict an additional 13 % energy loss with respect to the solid target case simulated with SRIM while LIP deg predicts additional 17 % loss. At 20 ps expansion time LIP deg and TM converge on 22 % energy loss while Zimmerman predicts a lower loss of 19 % . At 30 ps of expansion LIP deg and Zimmerman predict the 24.2 and 23.6 % energy loss respectively while Zimmerman still

predicts a smaller additional energy loss of 22.6 %. At 40 ps of expansion the energy loss is similar to the one at 30 ps. The period of 30 to 40 ps gives a relatively constant period for probing the plasma. Additionally, the energy loss was calculated for the E_p = 0.5 MeV and 0.8 MeV proton projectiles for the same target conditions and are shown in the Figure 4.16 (left) and (right) respectively.

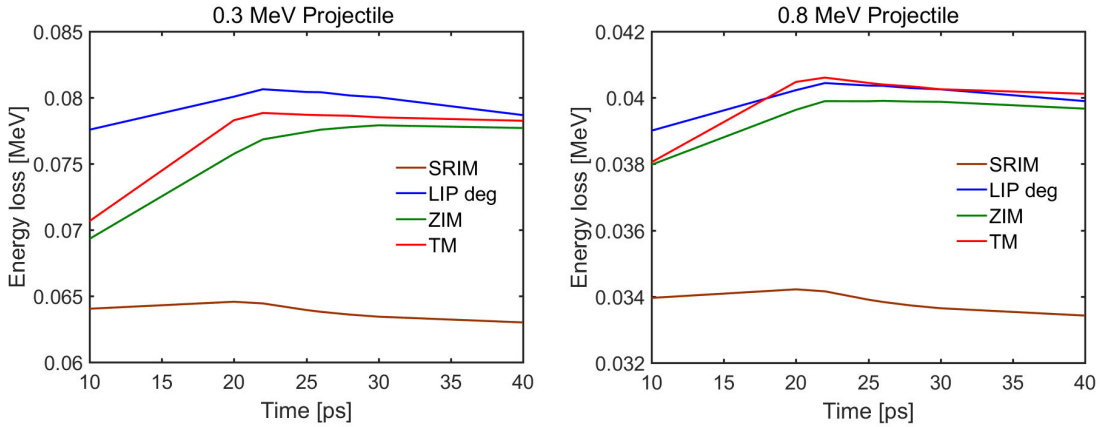

Fig. 4.16 The energy loss of 0.3 MeV (left) and 0.8 MeV (right) protons as a function of plasma expansion time calculated with different stopping power models : SRIM(solid brown line), Li - Petrasso with degeneracy (blue solid line) and T-Matrix with λ'_D [66]

As expected, the largest discrepancies between models are seen for the case of the lowest velocity protons with an energy of 0.3 MeV. Here, at 10 ps of expansion time, Zimmerman model predicts 8.2 % , T-Matrix - 10.2 % and LIP deg - 21.1 % additional energy loss respect to the solid target case (SRIM) where it is equal to 0.064 MeV. Such large discrepancies most probably coming from the fact the LIP deg does not treat the bound electrons that start to play a bigger role in case of low velocity projectiles. At 20 ps expansion time the energy loss is enhanced to 17.3 % according to Zimmerman, 21.3 % to TM and LIP deg predicts the maximum value of 24 %. As noted before and observed in simulations the Li-Petrasso model even with included degeneracy tends to give a larger energy loss with decrease of velocity projectile. The other models still also have discrepancies between each other that can be resolved with the diagnostics. On another hand, the energy bandwidth of the 0.3 MeV beam is slightly bigger than for the 0.5 MeV resulting to increased time spread of almost 20 ps, and the variation of target condition variation over the probing time has to be taken into account

4.1.3 Summary on modelling

A full set of the simulations was performed in order to characterize the generated warm dense matter conditions by the fs-laser pulse and to predict the energy loss of 0.3, 0.5 and 0.8

MeV proton beam projectiles in the predicted target conditions with use of the Li-Petrasso model with degeneracy effects, the ad-hoc Zimmerman model and the T-Matrix with dynamic screening length λ_D'

The target simulation performed with 1D and 2D hydrodynamic codes concluded that using the fs - laser pulse focused with large focal spot on the target guarantees the transversal homogeneity of plasma conditions within a radius of ≤ 50 μm with respect to the proton propagation axis and relatively uniform heating and ionization over the target areal density at 20 - 40 ps of expansion time. This leads to a target temperature of $T_e \approx 15$ - 20 eV and target density of $\rho \approx 1$ g/cm^3 with plasma degeneracy of $\Theta \sim 2$ and coupling parameter $\Gamma \sim 0.2$ that corresponds to WDM regime.

The stopping power simulations using the 1D hydrodynamic profiles showed the discrepancies between models of up to 5 % in energy loss estimation for 0.5 MeV ion projectile. However, the largest discrepancies between stopping power models up to 12 % occur for the lowest velocity projectile case of E_p= 0.3 MeV. To make more precise stopping power predictions, the 2D hydrodynamic profiles should be incorporated in simulations.

Three different models were presented, while the calculation with other stopping models such as DT-OF-DFT [58] and ad-hoc stopping model of D. Casas *et al.* [35] are still in progress in collaboration with University of Rochester (USA) and University of Castilla y La Mancha (Spain). Simultaneously more detailed calculation of the ionization state dynamic of the plasma by the ABAKO collisional - radiative atomic code with included degeneracy effects [74] are being carried out with University of Gran Canaria (Spain).

4.2 Experimental approach for ion stopping power measurements

This section describes the experimental campaign which focused on studying proton stopping power close to the Bragg peak for velocity ratios v_p/v_{th} close to unity, The preliminary results of the successful technique for proton energy selection are shown and discussed. The experiment was designed for and performed at the VEGA II system at CLPU in January 2020. CLPU VEGA II system has all the necessary requirements for conducting such an experiment: i) VEGA II offers pump and probe experimental conditions, ii) the two beams can be easily synchronised and the required time window (tens of ps) for the measurement can be easily obtained, iii) the same experimental set up can be used both to measure plasma conditions and for stopping power measurement, iv) The high repetition rate working mode achievable with VEGA II permits the accumulation of many shots and reduce the statistical

error in the results. It is important to note that plasma characterization and stopping power measurement can be done in different steps thanks to the high repetition mode of working that can give us access to statistical sampling of the results. On the contrary kilojoule facilities working in single shot mode are forced to do these two phases simultaneously. The experiment described in this sections was prepared and performed in collaboration with CEA DAM (France), University of Alberta (Canada), University of Bordeaux, Centre Lasers Intenses et Applications (CELIA) (France), ETSI Aeronáuticos, Universidad Politécnica de Madrid (Spain), University of California San Diego (USA) and Universidad de Castilla La Mancha (Spain).

4.2.1 CLPU VEGA - II laser facility

The CLPU has been founded by Spanish Ministry of Economy, Junta de Castilla y Leon and the University of Salamanca and its main system VEGA consists in a 30 fs pulse delivered in three different arms of 20 TW (VEGA I), 200 TW (VEGA II) and 1 PW (VEGA III). CLPU has recently started operation phase, the first user access period on the VEGA II already started at the beginning of 2018 and a commissioning experiment on VEGA III was carried out in 2019. VEGA II has been previously tested in different configurations depending on the focusing optics and targets used [216]. One configuration is designed for underdense laser–matter interaction where VEGA 2 is focused with a long focal length off axis parabola $F = 130\ cm$, $\phi_L = 20\ \mu m$, $Z_r = 260\ \mu m$, where F is the focal length, ϕ_L is the diameter of the laser focal spot and Z_r is the Rayleigh length onto a low density gas-jet generating via the wakefield mechanism electron beams with maximum energy up to 500 MeV and an X-ray betatron source with 10 keV characteristic critical energy. The second configuration is designed for over critical density laser–matter interaction where VEGA 2 is focused with a short focal length off axis parabola $F = 40\ cm$, $\phi_L = 7\ \mu m$, $Z_r = 25\ \mu m$) onto a 5 μm Al target generating (via target normal sheath acceleration (TNSA) mechanism) a proton beam with a maximum energy of 10 MeV and average temperature of 2.5 MeV. For the proposed experiment the proton energies of interest are significantly lower tan the TNSA spectrum produced by the second VEGA -II configuration by using the short focal parabola. Therefore, the first focusing configuration of VEGA - II was used in order to generate TNSA proton beams with the cut-off energy of 4 MeV with peak energies of 0.8 - 1 MeV. The generated proton spectrum was carefully characterized and results presented in the following sections.

4.2.2 Experimental design

The proposed experiment consist of two important parts - the proton source generation and warm dense matter generation, that divides the experimental scheme in two interaction zones. The outline of the experiment layout is shown in the Figure 4.17.

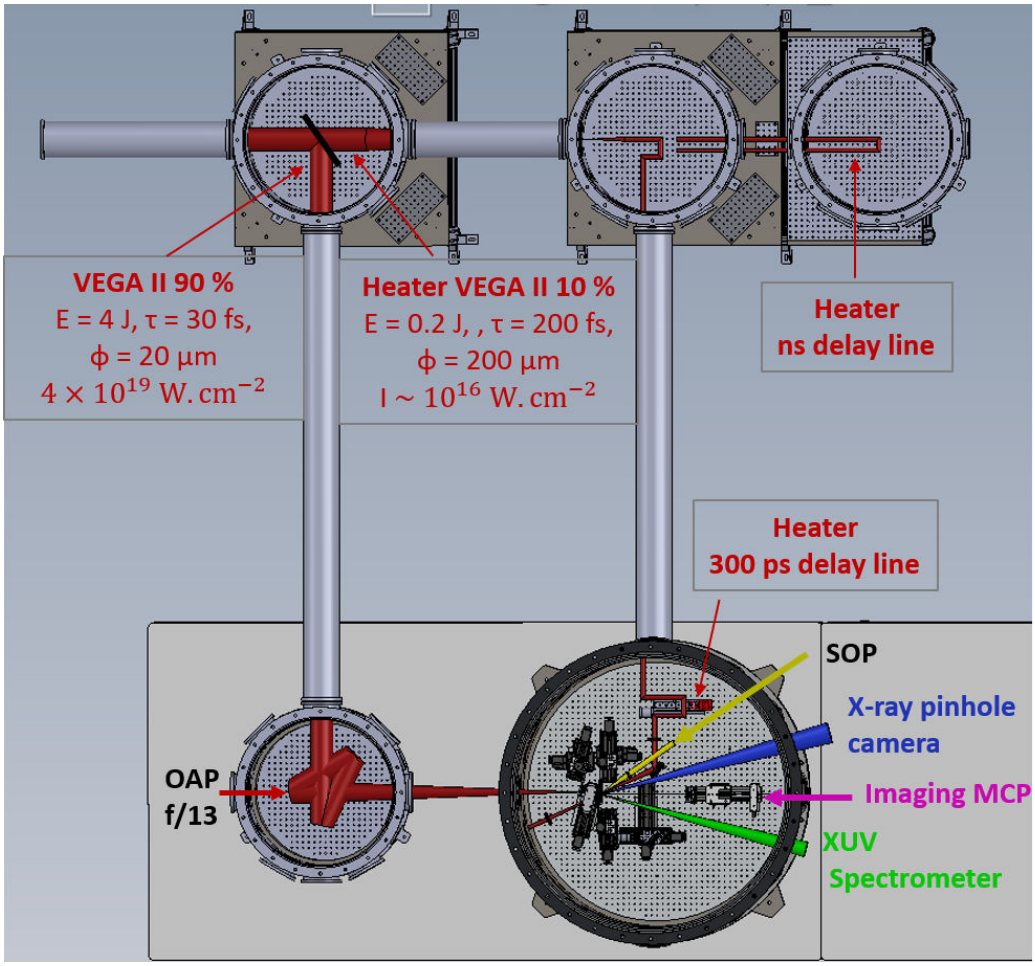

Fig. 4.17 2D layout of the experimental campaign at CLPU VEGA 2 laser facility and outline of the diagnostics.

The current VEGA II laser system splits in two arms with a 90 % reflecting mirror placed in the first beam-transport chamber. The 90 % reflected beam (main pulse) is transported and focused by an $F/13$ (F = 130 cm) gold coated parabolic mirror onto 3 μm thick Aluminium foil within a 20 μm focal spot yielding an intensity of $\sim 10^{19} W/cm^2$ in order to accelerate protons via TNSA mechanism up to 2 MeV. Then, for selection of the "quasi monoenergetic" proton beam with a projectile velocity of interest a so - called proton energy selector system was designed. It is based on the spatial dispersion of the initial proton beam by a 1.2 T permanent magnet. The particle tracking simulations with the use of measured

3D magnetic field distributions predict the projectiles trajectories that defines the position of the slit in order to select the given energy of interest with an energy band < 10 KeV and uncertainty less than 5 KeV. The measurement of the proton energy after the interaction is carried out by energy spectrometer that consist of a magnet of 0.2 T coupled with imaging multichannel plate (MCP) discussed in the diagnostics section 4.2.2. Figure 4.18 represents the conceptual outline of the energy selection principle for the protons centred at 0.5 MeV, that corresponds to $\approx 14^\circ$ deflection from the initial proton beam axis. The energy bandwidth of a projectile is controlled by the exit slit width. For the experimental goal , the lowest energy bandwidth possible that corresponds to the lowest possible time spread is required for the needed measurements resolution. The Figure 4.19 shows photos of the experimental setup in the interaction chamber (R = 6 cm). The proton energy selector detailed design and characterization is discussed in the following subsection 4.2.2. Simultaneously the transmitted 10 % beam (heater beam) is firstly reduced using a telescope down to 30 mm diameter and then focused with a lens (F = 40 cm) on the investigated sample of 1 μm carbon foil within a 100 - 150 μm diameter focal spot yielding an intensity of $\sim 10^{16}\mathrm{W/cm^2}$ in order to heat the sample to WDM state. The carbon target is located on the axis of the selected proton beam. The heater - proton beam time delay is controlled by a delay line accounting for proton time of flight to the WDM sample (4.2.2). In order to perform the statistical measurements of the downshifted proton spectrum passed through the WDM sample, the experimental setup was designed for multi-shot repetition working mode by motorizing the energy selector parts and developing target holders suitable for more than 100 shots. (4.2.2). From the diagnostics point of view, several different techniques are used to characterize the generated WDM. Particularly, Streak Optical Pyrometry and X - ray spectroscopy in the XUV spectral range are employed to estimate electron temperature.

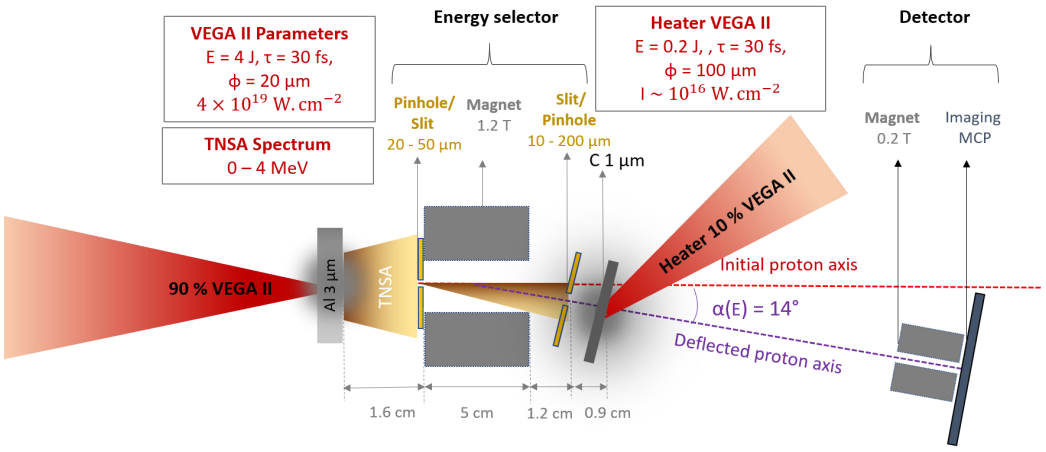

Fig. 4.18 Visual scheme of the selection of the 0.5 MeV projectile

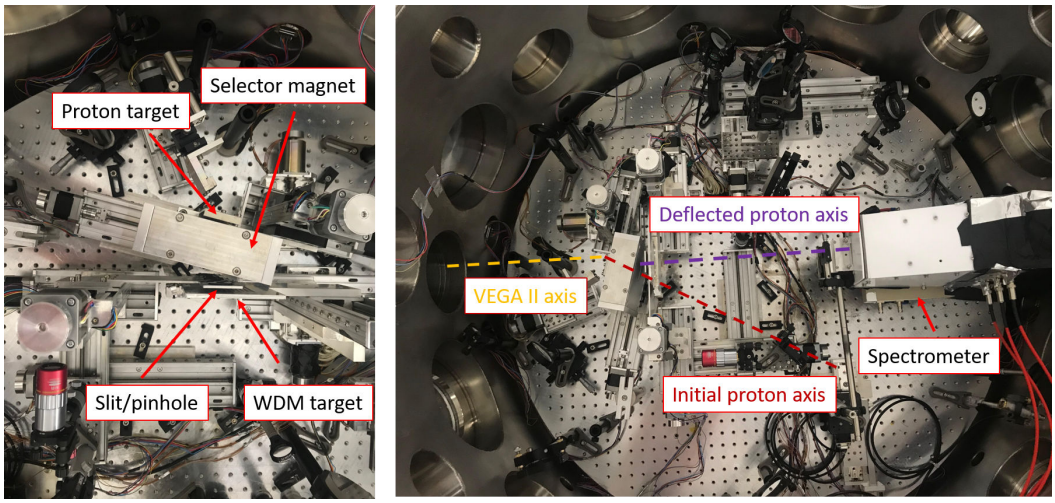

Fig. 4.19 The photos of the experimental setup with the indication of the energy selector elements, proton spectrometer and drawn lines of the initial and deflected proton axes. The photo of the proton energy selector (left) and whole view of the interaction chamber (right).

Targetry

One of the advantages of the high repetition rate (HRR) laser systems is the possibility to acquire a lot of data for the statistical study without interrupting the vacuum of the interaction chamber. In most high energy laser single shot systems the target is changed between the shots. In contrast, HHR system require a different type of targetry that allows fielding a large number of targets inside one target holder. In order to bring the targets to TCC one can move the X-Y-Z motors of the target holder. Therefore the target holder is motorized in height, lateral and focal directions with respect to the laser focus position - TCC. In this experiment the tagetry consists of two target types:

- Target A: Target for proton generation via well established TNSA mechanism by focusing VEGA 2 onto 3 μm thick Aluminium foil. The foil of size 20 $\times$ 20 mm is placed between two plates with the 800 μ m apertures for targets located 3 mm between each other(Figure 4.21). This design was successfully tested in the series of internal and external experimental campaigns at CLPU.

- Target B: Target for warm dense matter generation by focusing the heater beam onto 1 μm thick Carbon foil. The target holder has an apertures of 800 μm in the front plate (proton beam interaction side) and 1.2 mm aperture in the back side (heater laser side) located 5 mm away from each other (Figure 4.21). The bigger apertures in the back plate is required for the free heater interaction with the target at an incidence angle of 35°. The 1 μm C foil is very fragile and can't be located free standing in its holder. In

a previous experiment, the interaction of the heater beam with a free standing foil was found to damage a large area of the foil. A special design of the back plate matching the Carbon holder was used to provide strong compression of the foil between the front and back plates while also separating the interaction areas by 5 mm and securing the stability of the foil inside.

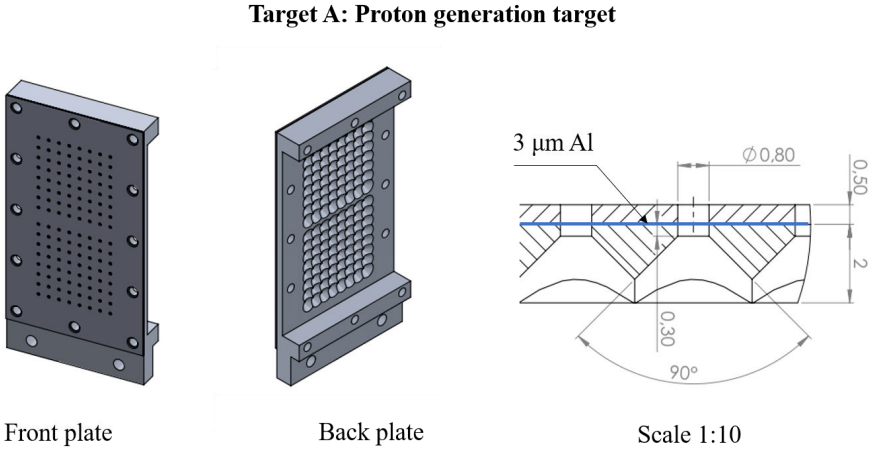

Fig. 4.20 3D design of the target holder for 3 μm thick Al foil for the TNSA proton generation.

Both target holders are designed for 100 shots per run.

Proton energy selector

Setup The adjustable platform for the proton energy selection was designed and developed for this experiment. It allows the energy selection from the TNSA - like proton sources in the wide range of energies starting from 0.2 MeV and up to the cut - off energies of the proton spectrum. For the purpose of this experiment, the energy selector was adjusted for the selection of 0.5 MeV proton beam with the minimum observed bandwidth of 0.025 MeV. The scheme of the energy selector is shown in the Figure 4.22. It is based on the use of a vertical magnetic field of 1.2 T to deflect the proton beam in the horizontal plane. Firstly, the TNSA proton beam with the opening half-angle of 22° is generated by the laser pulse - target interaction. The exchangeable pinhole attached in front of the entrance of the magnet selects a narrow pencil - like proton beam from the cone. This is a primary definition of the bandwidth of proton beam. It directly depends on the pinhole size (10 - 50 μm) and the distance from the proton source to the pinhole. After the magnet, the protons are deflected accordingly to their energy. By making trajectory calculations with the 3D map of the magnetic field, it was estimated that the 0.5 MeV projectile is deflected by 14° from

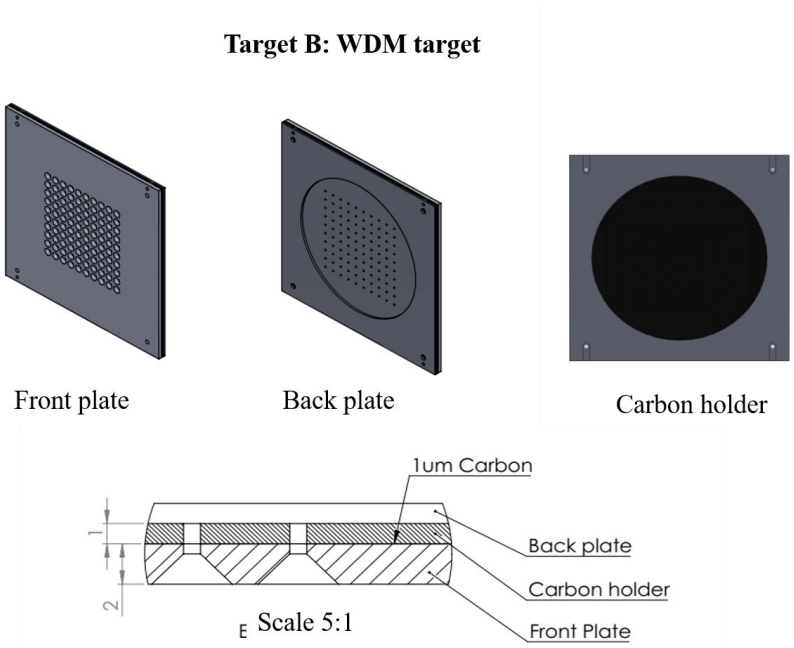

Fig. 4.21 3D design of the target holder for 1 μm thick Carbon foil for the Warm Dense Matter generation.

the initial propagation axis that is normal to the target as is shown in Figure 4.18. However, for the convenience of setup, the proton target and the magnet were tilted by 14° in order to guide the deflected proton axis co-linear with the laser axis, which simplifies the alignment of the adjustable slits, the WDM target, and the detection spectrometer.

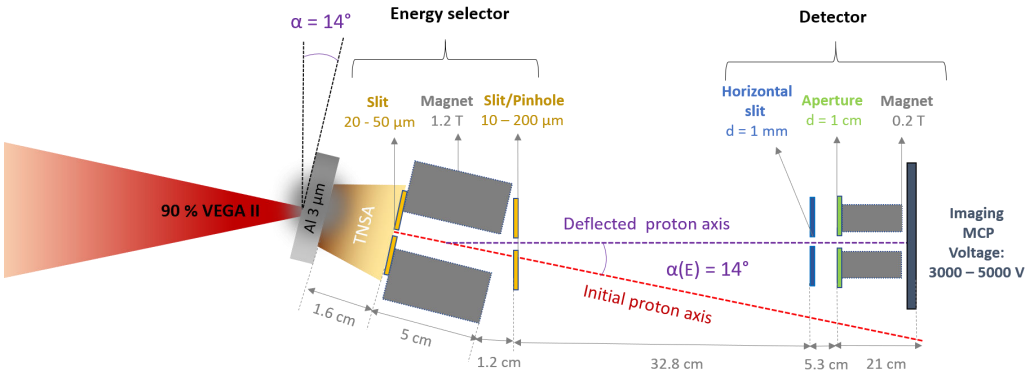

Fig. 4.22 The tentative scheme of the energy selector.

The containment of the magnetic field inside the magnet is crucial for the scheme. The design of the proton selector dipole magnet is presented on the Figure 4.23. It consists of two sets of 1 inch permanent magnets placed with 5 mm aperture between each other in

order to provide a constant 1.2 T magnetic field in 25.4 mm × 5 mm area along the proton propagation axis. A special yoke is employed to contain the magnetic field inside the magnet. This is required due to the fact, that protons can be easily deflected by the magnetic field leaking outside the dipole, before entering the pinhole, and therefore change their axis of propagation. Thus one needs a yoke to protect the protons from the unwanted deflection by any magnetic field outside of magnet. An Iron-Cobalt-Vanadium alloy consisting of 49 % Cobalt, 49% Iron, and 2% Vanadium (Hiperco 50) was used for the yoke material. It has a high magnetic saturation of 24.2 kGauss and good mechanical strength. The magnets were glued to the yoke with use of epoxy glue.

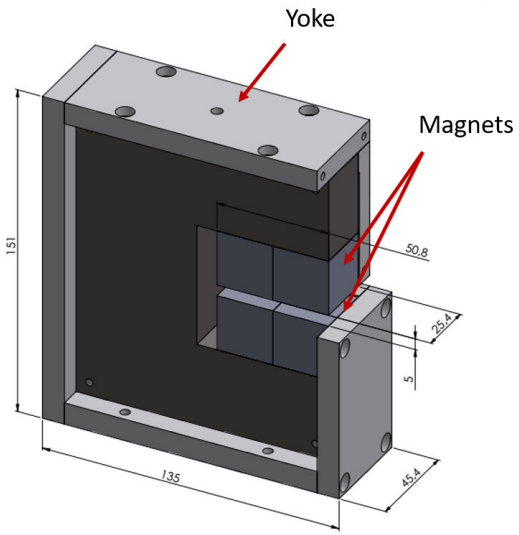

Fig. 4.23 3D design of the 1.2 T dipole proton selector magnet. The distances are given in cm.

In order to characterize and create a map for the magnetic field, a gaussmeter probe (Lakeshore) with 1.02 mm active area motorized in three axes was used. It allowed a measurement of magnetic field in a range of 55 mm with step of 1 mm along the proton propagation axis, 1 mm in the transverse direction and 1 mm in height providing a 3D magnetic field map 4.24, that was used for the trajectory calculation. The measurement was started 20 mm before the aperture of the magnet and finished 10 mm behind covering 55 mm distance along the initial propagation axis.

The magnet is motorized in the transverse direction with respect to the proton axis allowing to move it out for the acquisition of reference TNSA proton spectrum and move it in for the proton energy selection as well as adjust its position with the minimum step of 1 μm. The height of magnet can be adjusted manually by the vertical translation stage. This is very important since the attached pinhole in front of the aperture of magnet has to be centred

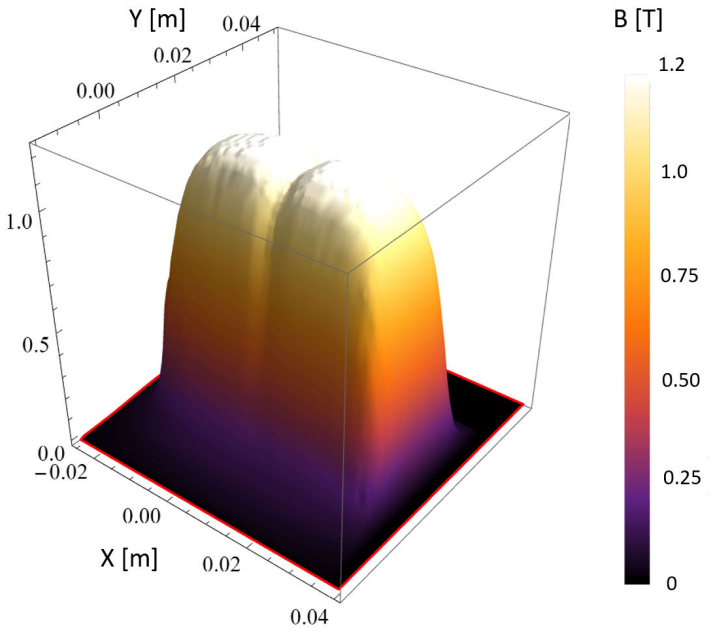

Fig. 4.24 3D magnetic map of the B - field in T of the proton energy selector dipole magnet measured with the step of 1 mm in the longitudinal direction, 1 mm in the height direction and 1 mm in the transverse direction.

in height with respect to the proton beam, that is normally at the height of the laser - target interaction at TCC. This means the precision of alignment has to be on the order of several microns, in order for the proton beam to pass through the 10 - 50 μm pinhole, and propagate precisely in the horizontal plane. This is not easily achievable just by manual adjustment. An easy solution to mitigate the problem of matching the height of the pinhole to the height of the generated proton beams to replace the pinhole by a slit of the same width but 3 mm long in height.

The second element of the proton energy selector is the motorized slit or pinhole located at the predicted axis of the deflected proton beam. The slit is located 9 mm away from the magnet and can be also moved in and out, as well as in height. When it is out, the reference spectrum of the protons deflected by the magnet in the field of view of the spectrometer is acquired. In fact, the slit holder can have up to 5 different slits or pinholes located 30 mm away from each other in height. This allows uninterruptible shot runs with changing of the pinholes (10- 20 μm) during the run. This slit or pinhole defines the final energy bandwidth of the selected proton beam. The energy bandwidth is related to the pinhole or slit width (slit size), the smaller it is, the smaller the bandwidth one obtains. However, reducing the second slit or pinhole size also decreases the number of protons in the selected proton beam. It is important to have an optimum balance between the number of protons required to

achieve the measurement of interest and the energy bandwidth required for the precision of the measurement. Thus, the quality of selected proton beam has to be characterized in terms of:

1. **Energy bandwidth**. To select the energy of interest with the slit or pinhole of the certain size one should adjust its lateral position with respect to the deflected protons. In this experiment, 20 μm and 50 μm slits in front of the magnet were used to characterize the energy selection with 4 different second slit or pinhole sizes - 200 and 20 μm slits, 20 and 10 μm pinholes providing a wide range of accessible bandwidths. For example, the 0.5 MeV projectile bandwidth was gradually decreasing from 0.090 MeV to 0.025 MeV by reducing the pinhole or slit size.

2. **Time spread**. It is crucial for determining the range of plasma conditions probed. It directly depends on the energy bandwidth and can be optimized only by reducing it.

3. **Proton beam size**. When the proton projectile of the energy of interest is selected and characterized in terms of mentioned parameters, the target sample is located as close as possible to the second slit or pinhole in order to guarantee a small enough proton beam size interacting with the target. As discussed in the previous section, one needs a proton beam size of 50 μm size to probe the uniform plasma conditions. One should take into account, the existence of spatial proton beam divergence affected by the space charge effects.

4. **Time of flight**. Another important parameter of the energy selector is the time of flight of the proton beam to the target sample - WDM target. It depends on the total projectile travel distance and its velocity. The minimum distance between the proton source and the target sample accessible in this experiment is 83 mm, given by the constraint of the selector dimensions, corresponding to 10 ns time of flight for the 0.5 MeV projectile. The TOF is a key variable required for the synchronization between the heater and when proton beam is arriving at the target.

In order to design the experimental setup of the proton energy selector and estimate parameters of the selected proton beam in experimental conditions, a full set of numerical simulations for the proton trajectories has been performed.

Numerical trajectory simulations The full characterization of the proton energy selector has been performed using the proton trajectory numerical simulations. The goal of the simulations is to provide the following data for a certain setup geometry:

- Selected proton energy bandwidth
- Selected proton time of flight and time spread at the WDM target
- Estimations of proton beam divergence before the WDM target

Equations of motion have been numerically solved using a standard Verlet finite difference method [213] carried out in second order. Knowing two initial consecutive positions $r(t)$ and $r(t-dt)$ and the acceleration $a(t)$, the trajectory can be computed recursively in the following way:

$$r(t+dt) = 2r(t) - r(t-dt) + (dt^2 a(t)) \tag{4.1}$$

where dt is a time step. For proton energies of 0.5 MeV the magnetic field energy was conserved within an error of 0.0016% using a computational step of time dt = 0.5 ps. The magnetic field 4.24 has been numerically interpolated in 1st order while carrying out the Verlet integration. Two spatial filters were used, one before the magnet (divergence control) and the other after it (energy selection). Pinholes and slits were used in those positions depending on the experimental run goals. The first filter had defined the maximum divergence (only trajectories passing through it were computed). The second filter was treated asa "hard edge" trajectory filter, evaluating pass/no-pass event in all the steps and cutting or continuing the trajectory accordingly. In order to ensure proper bandwidth estimations for the selector, spectra of 10 times the bandwidth (square form) were used, i.e. if observed bandwidth of selected proton beam is 10 keV FWHM, an initial spectrum of 100 keV is used. The proton source was considered to be point-like. As explained in the previous paragraph the source divergence was totally defined by the clear aperture of the first spatial filter (pinhole or slit). Thus, only trajectories going through the first filter were computed.

First of all, the optimum distance between proton source and the first pinhole was estimated. The figure 4.25 (left) presents the simulated energy bandwidth and corresponding time spread as a function of the distance between the proton source and the pinhole for the fixed proton energy selector parameters. It seems, that locating the pinhole more far from the source guarantees conservation of the minimum energy bandwidth while approaching the source increases the bandwidth drastically. One can explain this effect by the acceptance of more random proton trajectories arriving with different angles from the source to the pinhole. However, the increasing the distance affects the time of flight and therefore time spread of the beam. Then, the optimum distance between the proton source and the pinhole can be found to reasonably satisfy both requirements. It is between 1.5 - 2.5 cm. This behaviour is repeatable for all the sets of parameters of the energy selector. The Figure 4.25 (right) shows the simulations performed with fixed optimum distance from source to the

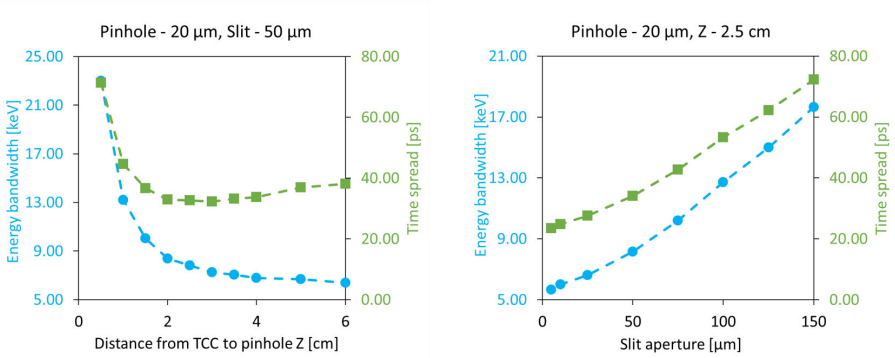

Fig. 4.25 The energy bandwidth and time spread as a function of distance between proton source to the pinhole for the fixed proton energy selector parameters: 20 μm pinhole with 50 μm slit (left) . The energy bandwidth and time spread as a function second slit size for the fixed distance from proton source to the pinhole and 20 μm pinhole (right)

Table 4.1 Numerically estimated energy bandwidth and time spread for o.5 MeV projectile

Pinhole [μm]	Slit [μm]	Energy bandwidth [MeV]	Time spread [ps]
50	20	0.0130	92.371
50	10	0.0078	80.04
20	20	0.0032	35.14
20	10	0.0027	29.76
10	50	0.0061	25.91
10	20	0.0035	14.88

pinhole and pinhole size for the various slit sizes in order to estimate the minimum energy bandwidth. The estimations of the energy bandwidth and time spread for 0.5 MeV projectile using different parameters of the selected is presented in the Table 4.1.

Proton energy spectrometer

The ion spectrometer is composed by a 0.2 T permanent magnet coupled with an MCP screen and an imaging system to let the measurement work at HRR (0.1 Hz). The MCP detector (Hamamatsu) provides a minimum spatial resolution of 20 microns (channel size). The MCP screen has 7.5 cm length in the vertical direction - the proton deflection axis as shown in the Figure 4.26 (left). The height of the MCP screen respect to the magnet was adjusted in order to allow the maximum length along the proton deflection axis. The bright spot on the MCP screen indicated the initial proton beam height on axis assuming it corresponds to the

laser height axis. The numerical particle tracking simulations with use of 3D map of the magnetic field were performed to obtain the calibration energy/position curve and energy resolution in proton energy spectrometer and is presented in the Figure 4.26 (right). The 0 of the calibration curves corresponds to the initial height of the proton beam before entering the magnet. The energy resolution of the spectrometer is below 5 keV and satisfies the high precision requirements for the experimental campaign. The use of the MCP fluorescence screen instead of any other detector screen is due to the possibility to enhance the proton signal level by applying external voltages up to 5000 V. The Multi channel plate (MCP) uses voltages to amplify the electron cascade of the electrons hitting the walls of the channels caused by the proton interaction. Then, even small number of protons can be detected by the increasing the sensitivity by increasing the voltage. The thin foil of 2 μm Mylar with 100 nm layer of aluminium was used to cover the MCP fluorescence screen on the front side in order to protect it from the laser light. It is worth noting, that the viewing acceptance angle of the spectrometer is limited by the 1 cm aperture of in front of the entrance to the spectrometer.

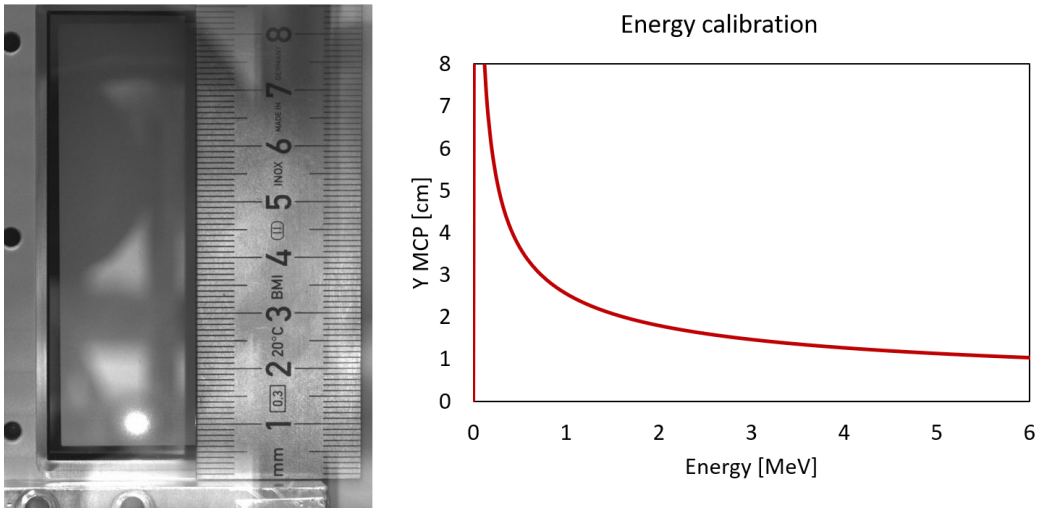

Fig. 4.26 The MCP screen size measurement (left). Energy calibration curve of the magnet-based spectrometer obtained by the proton trajectory numerical simulations with the 3D map of the magnetic field (right).

Heater proton beam synchronization techniques

One of the most challenging aspects of this experiment is the synchronization between the selected proton projectiles and the heater used to generated the warm dense matter. To define the time of the proton beam probing the plasma, it is firstly planned to observe the larger energy loss difference between the solid target case, when the proton beam arrived before

the heater, and expanding plasma, when the proton beam arrives much later after the heater. Then, one can move the delay line of the heater in smaller steps of 10 ps to find the fine 0. Taking to account the TOF of the 0.5 MeV projectile to the WDM $\approx$ 10 ns, the heater beam has to arrive to the WDM target 10 ns after the main pulse - target interaction that generates TNSA protons. The heater and main beam have been synchronized with 10 ns delay that corresponds to the central position on the 2 ns range motorized delay line for the heater beam, giving a rough 0 delay between the heater and proton bean. Using the long range delay line, allows heater to arrive 0.7 ns before the predicted proton beam arrival and 0.8 ns after the proton beam arrival to the WDM target. This technique has been tried in the experiment and the data analysis in ongoing to estimate the success of this approach.

4.3 Experimental results

Proton energy selector

The preliminary experimental results of the proposed design of the proton energy selected are presented in this section. Six different configurations of the energy selector, combining different sizes of slits and pinholes, were used during the experiment providing a qualitative parametric study of the proton energy bandwidth for the selected projectile of $\approx$ 0.5 MeV.

First element of the selector First of all, the energy selector is optimized by using the first element of the selector - the size of the slit in front of the magnet and its position respect to the source, that defines the window of proton energies that can be detected by the spectrometer. The spectrometer was placed on the predicted proton axis with quite large viewing angle allowing observation of part of the deflected proton beam line. By moving the magnet with attached slit transversally, one changes the deflection of the protons in the horizontal direction that leads to the energy window detected on the spectrometer. The position of the magnet was optimized to deflect the proton energies of the window of energy centred on $\approx$ 0.5 MeV in the axis of the spectrometer,therefore the initially pre - aligned axis of the proton beam. In order to simplify the mentioned alignment between magnet and the proton source height, the slits of 20 μm and 50 μm width were used in current experiment in place of pinholes. The example of the raw data acquired with the the proton spectrometer is shown in the Figure 4.27. The first image (left) corresponds to the reference TNSA proton spectrum with a cut-off energy of 4 MeV detected at 14° with respect to its propagation axis. When the magnet with 50 μm slit is used, the deflected proton beam between 0.475 MeV and 0.53 MeV is detected (middle) while using the slit width of 20 μm the energies between 0.49 MeV and 0.532 MeV

were detected with optimized magnet positions with respect to source to obtain the needed energy window.

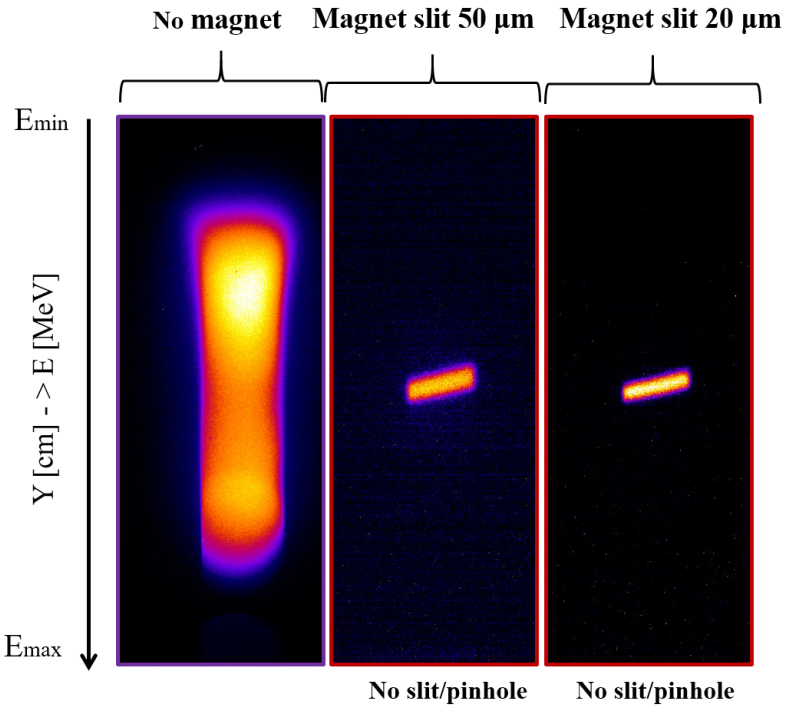

Fig. 4.27 The examples of the raw experimental images of the MCP fluorescence screen obtained with the magnet spectrometer. The vertical axis of the image corresponds to the proton energy from low to high energies - from up to bottom. The reference TNSA proton spectrum obtained by the moving out the dipole magnet of the proton energy selector and acquired with the 3000 V applied on MCP (left). The data obtained with the dipole magnet of proton energy selector moved in with 50 μm slit (middle) and 20 μm slit (right) in front of the magnet aperture and without second element of the selector. Acquired with 4000 V.

Second element of the selector The fine selection of the proton energy beam is made by inserting the second element of the selector as close as possible $\approx$ 1.7 cm from the exit of the proton energy selector dipole magnet. The raw experimental data with use of various second elements are shown in Figure 4.28 for a fixed 50 μm slit and in Figure 4.29 for a 20 μm slit in front of the magnet. The position of the second element was carefully adjusted in order to select $\approx$ 0.5 MeV $\pm$ ΔE_p proton projectile, where ΔE_p is an observed energy bandwidth. To ensure the correct energy detection with the magnet spectrometer, additional horizontal slit with a width of 1 mm has been inserted at the laser axis height in front the 1 cm aperture of the spectrometer. Then, the proton beam height can be optimized by adjusting the second element height in order to enter the aperture. The second element (slit or pinhole) was moved

Table 4.2 Experimental characterization of proton energy selector

First element	Second element	Center energy [MeV]	Energy bandwidth [MeV]
50 μm slit	200 μm slit	0.494	0.091
50 μm slit	20 μm slit	0.451	0.068
50 μm slit	20 μm pinhole	0.498	0.059
50 μm slit	10 μm pinhole	0.502	0.05
20 μm slit	20 μm pinhole	0.498	0.052
20 μm slit	10 μm pinhole	0.504	0.025

in height with step of 100 μm both ways up and down until the signal totally disappears when cut by the edges of the horizontal slit. Then the displacement in height which was found is applied as a correction the proton axis height origin position for the calibration curve. This procedure has been performed for all the second elements. As can be seen, by reducing the size of the second element the proton signal level significantly drops even with the highest applied MCP voltage of 5000 V. In this way, the lowest signal is obtained in the configuration of 20 μm magnet slit and 10 μm pinhole. As mentioned before, the number of protons passing through such small apertures can be very low.

The Table 4.2 presents the observed proton central energy and energy bandwidth obtained by optimization of the energy selector with various configurations. It is worth noting, that the given values of the central energy and the bandwidth are estimated statistically with tens of the acquired spectrum for each of the configurations showing very stable selected central energy with a precision of less than 3 keV (0.003 MeV). The corresponding proton spectra obtained for the both magnet slit configuration with the second elements is shown in the Figure 4.30 (left) for the 50 μm magnet slit and Figure 4.30 (right) for the 20 μm magnet slit.

Simultaneously the proton beam size after the selection by the second proton energy selector element at distance 0.85 cm from it has been measured by placing Radiochromic Film (RCF). This position corresponds to the position, where the target sample has to be aligned. The proton beam size after selection by 20 μm slit is estimated to be 50 μm $\pm$ 5 μm. At the same time the observed spatial size of the beam in the MCP screen of the proton signal is about 500 μm.

These promising results indicate the repetitive and very well defined selected proton projectile of $\approx$ 0.5 MeV with use the wide range of proton energy selector parameters starting from a 200 μm slit to the smallest 10 μm pinhole leading to gradually decreasing observed

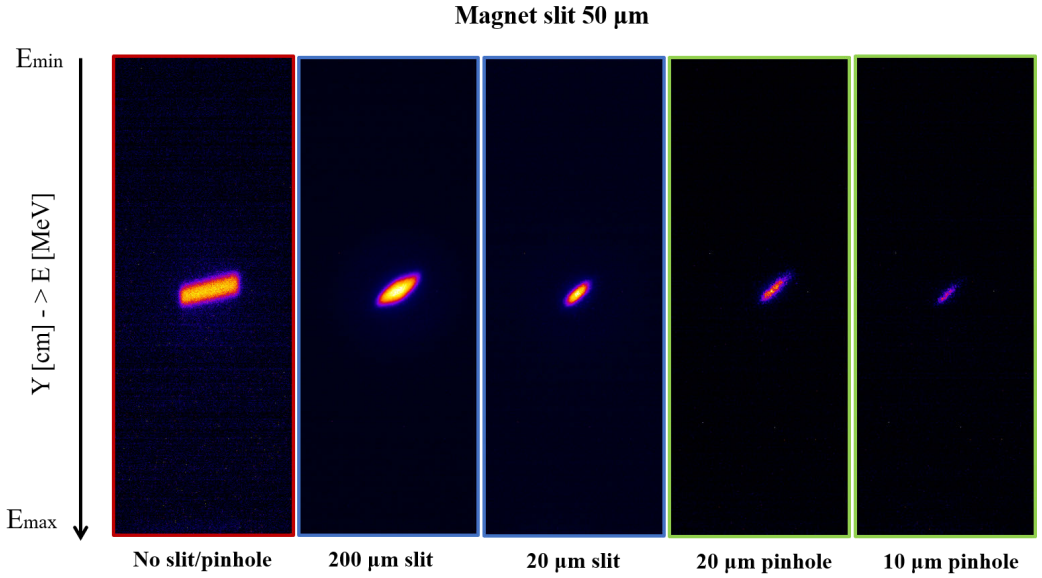

Fig. 4.28 Examples of the raw experimental images of the MCP fluorescence screen obtained with the fixed magnet spectrometer with the 50 μm slit in front of the magnet aperture (right) and various slit/pinholes sizes of the second element of the selector (from left to right) - 200 μm slit acquired with 4000 V on the MCP and 20 μm slit, 20 μm and 10 μm pinhole acquired with 5000 V MCP voltage. The colour scale is fixed for all the images.

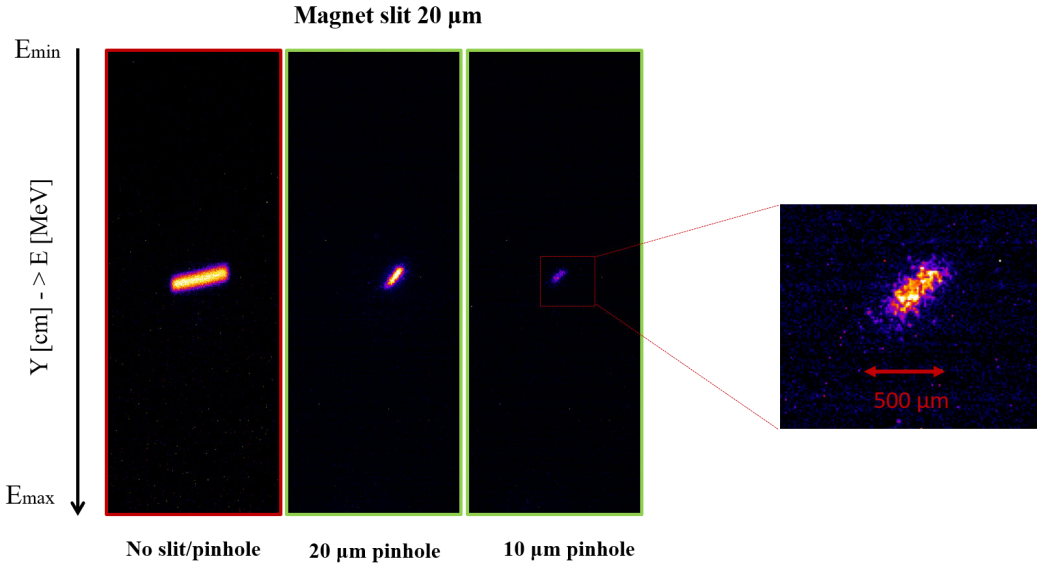

Fig. 4.29 Examples of the raw experimental images of the MCP fluorescence screen obtained with the fixed magnet spectrometer with the 20 μm slit in front of the magnet aperture (right) and various slit/pinholes sizes of the second element of the selector (from left to right) - 20 μm and 10 μm pinhole acquired with 5000 V MCP voltage. The colour scale is fixed for all the images.

energy bandwidth from 0.091 MeV to 0.025 MeV respectively. One can notice a discrepancy between numerically estimated bandwidths with proton energy selector parameters shown in the Table 4.1 and the measured ones. The ongoing post-processing of the data and numerical simulations are aimed at finding the reason. However, one of the possible reasons can be the divergence of the proton beam from the second slit to the detector that affects the measurement in bandwidth. For the more precise data analysis the Mote - Carlo simulation will be employed in order to estimate the contribution of the proton divergence to the measured bandwidth in order to de-convolve the real energy bandwidth of the proton beam in the plane, where the warm dense matter sample will be placed - 0.9 mm from the second slit.

It is worth noting, that the selected proton energy does not depend on the the shot to shot variation of the laser parameters for the TNSA proton generation. Still this variation does affects the intensity of the proton signal on the detector therefore varying the number of the selected protons from shot to shot.

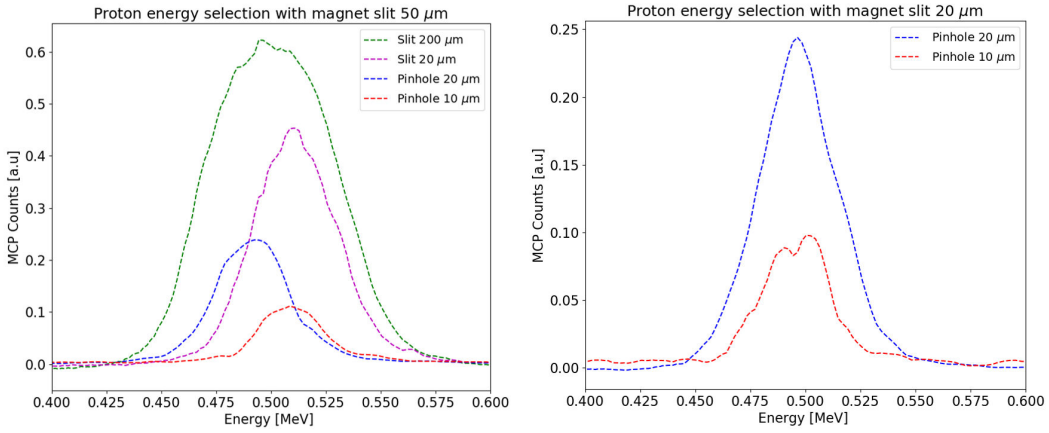

Fig. 4.30 The proton energy spectrum selected with use of a fixed 50 μm magnet slit and second element as 200 μm slit (green dashed line), 20 μm slit (magenta dashed line), 20 μm pinhole (blue dashed line), 10 μm pinhole (red dashed line) (left) and with use of a fixed 20 μm magnet slit with 20 μm pinhole (blue dashed line), 10 μm pinhole (red dashed line) (right).

Measurements of the proton energy loss in solid target

The feasibility of the developed proton energy selector for the proton stopping power measurements in matter has been confirmed by the measuring the energy loss of the selector proton projectile in cold solid targets of different thicknesses. Particularly, the energy loss in solid 1 μm C has been a primary interest, as far as it is a cold solid target reference for the proton stopping power in warm dense carbon. Three different configurations of the proton

energy selector were used featuring the two projectiles with central energy of 0.510 MeV selected with a 50 μm slit and 20 μm slit and 0.498 MeV selected with a 50 μm slit and 20 μm pinhole and a 20 μm slit and 20 μm pinhole. Cold solid samples of 1 μm C, 2 μm C with ρ - 1.3 g/cm^3 and 2 μm Mylar with 100 nm Al layer has been placed in the WDM target holder located on the proton axis 0.9 cm away from the second energy selector element. In order to align the aperture of the WDM target holder shown in Figure 4.21 with respect to the selected proton axis, the free aperture without target has been moved in both lateral and height direction with steps of 100 μm to center the proton beam inside 800 μm aperture. When the beam was aligned in the center of the target hole, the target holder was moved to the aperture with the target sample inside. The raw experimental data for the 0.510 MeV projectile is shown in the Figure 4.31. The data was acquired with the horizontal slit placed in front of the spectrometer. However, this slit cuts the real beam shape that can be observed on the detector. It can be clearly seen in the Figure 4.32 that presents the data obtained with 50 μm slit and 20 μm pinhole (left) and 20 μm slit and 20 μm pinhole (right) proton energy selector parameters to select the projectile of 0.498 keV. The proton beam observed on the detector after passing through the cold sample has been modified in terms of its size, number of protons and indeed its energy. One of the explanations of such change of the proton beam shape is an effect of the proton beam straggling and scattering in the matter. In order to estimate precisely the energy loss the line over the area of the proton peak signal of the reference shot has been taken in the position of the reference shot where the central energy is located.

The measured energy loss of the 0.510 MeV proton in cold target samples is shown in the Figure 4.33. SRIM predicts the energy loss of 0.0454 MeV in 1 μm C, 0.0908 MeV in 2 μm C and 0.11 MeV in 2 μm Mylar with 100 nm Al layer for 0.51 MeV energy of the projectile. The measured energy loss is 0.046 $\pm$ 0.004 MeV, 0.009 $\pm$ 0.005 MeV and 0.115 $\pm$ 0.005 MeV. The error bar is given by the data points acquired with 4 shots per the solid target condition. The results of the energy loss is very repetitive and in good agreement with the theoretical predictions.

On the other hand, the energy loss of 0.498 MeV proton selected with use of 20 μm magnet slit and 20 μm second slit slightly overestimating the predicted energy loss value of 0.0462 MeV featuring 0.054 $\pm$ 0.003 MeV as shown in the Figure 4.34. To understand all the features of the measured energy loss in solid matter, a more detailed analysis is in process.

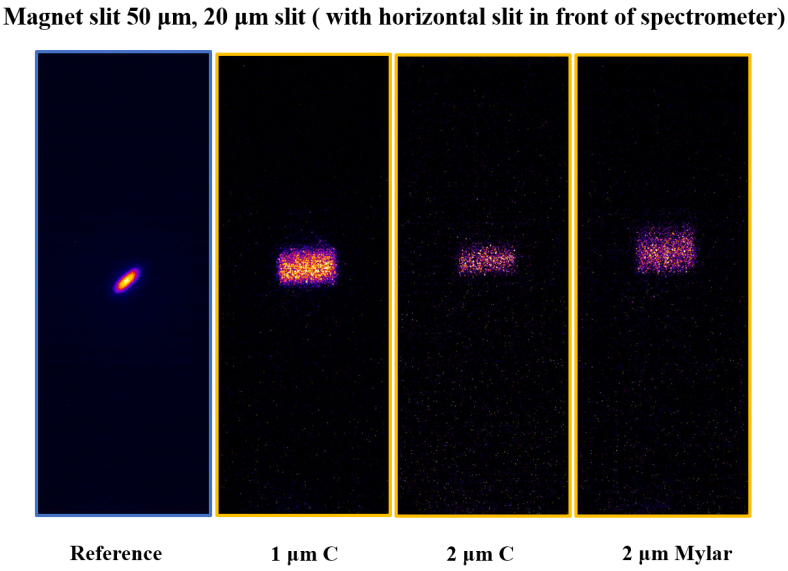

Fig. 4.31 The examples of the raw experimental images of the MCP fluorescence screen obtained with the fixed magnet spectrometer with the 50 μm slit in front of the magnet aperture and 20 μm slit after proton beam passing through the cold matter samples of 1 μm C, 2 μm C and 2 μm Mylar with 100 nm Al. The data is acquired with the 1 mm horizontal slit in front of the spectrometer with MCP voltage - 5000 V. The colour scale is fixed for all the images.

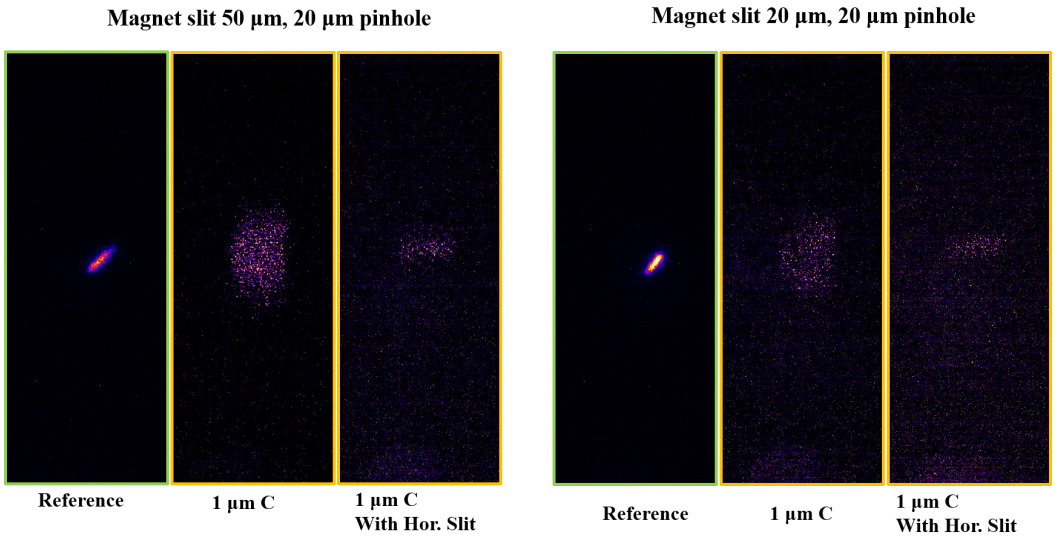

Fig. 4.32 The examples of the raw experimental images of the MCP fluorescence screen obtained with the fixed magnet spectrometer with the 50 μm slit in front of the magnet aperture and 20 μm slit after passing through the cold matter samples of 1 μm C with and without horizontal slit in front of spectrometer (left). The same set of data was acquired for the configuration of the proton energy selector with the 20 μm magnet slit and 20μm pinhole (right) with MCP voltage - 5000 V. The colour scale is fixed for all the images.

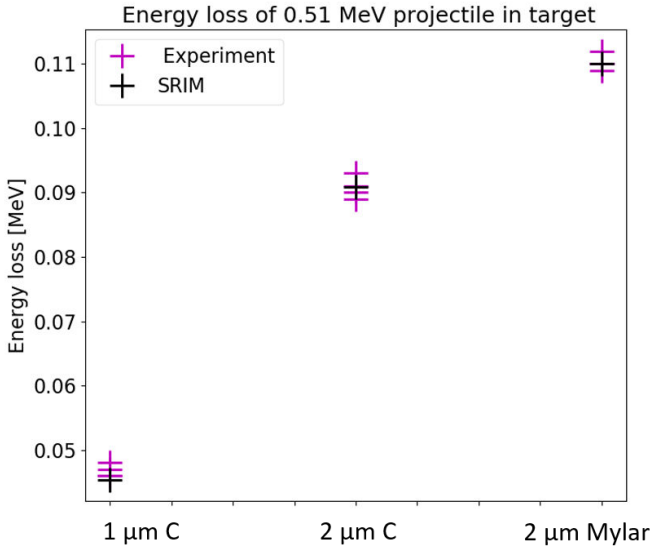

Fig. 4.33 The measured energy loss of the 0.51 MeV protons selected with use of 50 μm magnet slit and 20 μm second slit in cold 1 μm Carbon, 2 μm Carbon and 2 μm Mylar with 100 nm Al layer (magenta crosses) and predicted energy loss by SRIM (black crosses). The corresponding raw is data shown in the Figure 4.31.

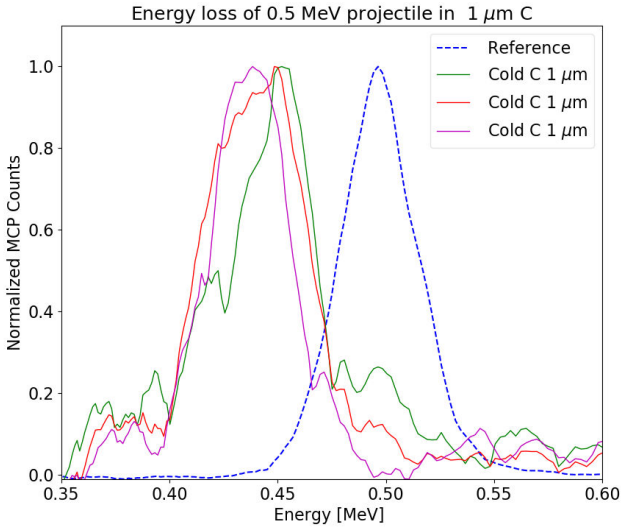

Fig. 4.34 The proton spectra of the protons of 0.498 MeV selected with 20 μm magnet slit and 20 μm second slit and passed through the 1 μm C cold target sample acquired with three consecutive shots. The corresponding raw data shown in the Figure 4.32(right).

4.4 Conclusions

An experimental approach to measure proton stopping power in warm dense matter has been proposed and the experimental campaign designed and performed at CLPU VEGA - II laser facility in January 2020. The preliminary results features the success of the developed platform for proton energy selection from laser driven TNSA proton beam-independent of the laser stability over a wide range of energies restricted only by the cut - off energy of the generated proton spectrum. Particularly, the proton energy selector has been optimized to select protons of 0.5 MeV with the minimum energy bandwidth 0.025 MeV. A more precise energy bandwidth estimation taking into account the observed projectile divergence angle is under the process. The selected proton projectiles were also successfully used for energy loss measurements in solid target samples justifying the use of such a scheme for the proton energy loss measurement in the warm dense matter. The measured energy loss was in good agreement with SRIM data base with the very impressive experimental error bar up to 0.005 MeV achieved statistically. Based on the obtained results, different ideas of further proton energy selector optimization are under development and are mostly focused on the mitigating the effect of the proton projectile divergence using proton focusing optics as well as general improvement of the energy bandwidth and time spread. The proton stopping power for 0.5 MeV protons in the warm dense matter also has been performed and currently is under the analysis together with the analysis of diagnostics for the target temperature measurements - SOP and X-ray pinhole grating camera employed to define the target conditions where the proton energy loss has been measured.

Chapter 5

Conclusions and perspectives

The work performed for this thesis is dedicated to the study of laser driven charged particle transport in plasmas and warm dense matter. In particular, it is focused on the experimental investigation of relativistic electron beam collimation technique for the laser intensities $10^{18} - 10^{19}$ W/cm^2 and to the study of the ion stopping power in warm dense matter at low velocities $v_p/v_{th} \approx 3$, numerically and experimentally.

5.1 Double pulse REB collimation scheme

The experimental results of the LULI-ELFIE experiment, focused on the parametric study of the relativistic electron beam guiding by using two consecutive laser pulses, featured a clear signature of collimation of 70 % of hot electrons with reduced beam size by a factor of ≈ 2 and guiding them over 50 μm in plasma obtained by tuning certain parameters between laser pulses. By using two independent diagnostic techniques (K_α imaging and CTR imaging) it was observed that by modifying the laser intensity ratio I_1/I_2, focal spot ratio ϕ_1/ϕ_2 and time delay Δt between two laser pulses, one can control the collimation scheme efficiency. Both from experimental results and from numerical simulations, performed in order to support the scheme, it was shown that for each value of ϕ_1/ϕ_2 there is an optimal injection time is δt, which, in agreement with expectations, increases when ϕ_1/ϕ_2 reduced. This study validates the theoretical studies of A. Robinson [176, 175] and extends the understanding of the first experimental validation of the double pulse scheme by R. Scott [194], where the scheme was studied only in terms of the time delay between laser pulses.

Experimental results show that the optimum delay time is a function of the focal spot ratio, which results from the time evolution of the magnetic field. According to the numerical simulations the magnetic field reaches its maximum at the end of the laser pulse interaction with solid target $\tau_L \approx 0.5$ ps.

It seems to be in good agreement with the previous experiment, in which the laser pulse duration was τ_L= 1 ps and collimation occurred between 4 - 6 ps of delay time of the laser pulses, which also correspond to the 4 - 6 $\times$ τ_L. Taking to account, that intensity range of referred experiment was $10^{18} - 10^{19}$ W/cm^2, one can conclude that the optimum delay time is not a function of the laser intensity.

The numerical and experimental study given in this thesis pushes forward the understanding of the double pulse scheme in terms of the various parameters that affect the magnetic field evolution in plasma.

One of the potential applications of this electron collimation technique is the integrated scheme for fast ignition approach for inertial confinement fusion, where the laser driven relativistic electron beam has to be guided through 50 - 100 μm of hot dense plasma in order to deliver enough energy into a hot spot enough high for ignition ($\geq$ 18 kJ). However, this electron beam has intrinsically high divergence and does not arrive to the hot core with the required energy for the ignition. One can use the first laser pulse of the intensity of $I \approx 10^{19}$ W/cm^2 to generate the azimuthal magnetic field in order to control the divergence and guide the main electron beam generated by laser pulse of $I \approx 10^{20}$ W/cm^2. However, one would need detailed numerical studies to understand quantitatively how well the collimation observed in current experiments would translate to the laser and target conditions in a fast ignition scenario.

From another side, the double pulse scheme can be used for the optimisation of laser-driven particle x -ray radiation and proton sources, for applications that demand the compact size and high brilliance of the referred source.

5.2 The adjustable platform for proton energy selection

The novel design of the proton energy selector system that allows to select the "mono-energetic" proton beams from the laser - driven TNSA spectrum generated by laser intensity of $I \approx 10^{19}$ W/cm^2 has been performed in the framework of this thesis. The study was motivated by the requirement of a mono-energetic proton beam for the investigation of the proton stopping power at low velocities in Warm Dense Matter, where the high precision experimental proton energy loss measurements in the fast evolving conditions of matter require a stable proton beam with small energy bandwidth (1 %) and time spread, small spatial size < 50 μm and low energy < 0.5 MeV and that can be used at high repetition rate in order to average over many shots and reduce statistical error. The very first demonstration of the selection of such proton beam with the required quality has been shown in this thesis.

The TNSA proton sources, generated by high - intensity short pulse lasers with intensities of $I = 10^{19} - 10^{21}$ W/cm^2, typically have broad spectrum with cut - off energy of order of tens of MeV with corresponding time spread. Therefore, in order the select the proton beam energy of interest the concept of magnet - based energy selector system has been presented in this thesis. The featured proton energy selector is based on the use of 1.2 T dipole magnet with two steps of selection, before and after the proton deflection by the magnet, is very compact, with longitudinal dimension of 8 cm, and can be placed close as needed to the proton source.

The preliminary experimental results of the energy selector optimization, performed on VEGA-II laser facility, show the selection of the proton projectiles of 0.5 MeV energy with the minimum measured **energy bandwidth of 0.025 MeV** with a reasonable signal level using a 20 μm slit and 20 μm pinhole as proton energy selectors. Different configurations of the proton energy selector have been experimentally characterized in terms of the proton signal intensity and energy bandwidth, which was gradually reducing from 0.09 MeV to 0.025 MeV with the use of the pinholes of smaller sizes from 200 μm to 10 μm. The experimental study shows the statistical precise repetitive selection of the proton energy, and a small variation in intensity of the signal, that directly connected to the number of protons. It demonstrates that the energy selector platform is insensitive to the laser - target interaction variations due to laser stability, that is usually common for high intensity laser systems, and target imperfections. Another possibilities for future improvement is to add a tunable magnetic field in order to optimize the energy selector in terms of the energy selected without changing the lateral position of the magnet. In future one could also add quadrupole focussing magnets to re collimate the energy selected point source of protons onto the application samples and detectors. The presented theoretical and experimental study of designed proton energy selector is very promising and has many use in different fields of science particularly for the stopping power measurements and in medical and biological applications. The energy selector also features easy use and allows manipulation possibilities with the motorization of the all elements of the selector, that allows the change of the selected proton energies without experiment interruption, that makes it perfectly suitable for HRR experiments.

5.3 Proton stopping power in WDM at low velocity projectile ratio

A novel experimental approach for the proton stopping power measurements in the warm dense matter conditions at low velocity projectile ratio has been proposed in this thesis. Until now, there no experimental data to benchmark the exiting ion stopping power models for this regime and parameter domain, mainly because of the difficulties to generate the low energy projectile velocities that would give the velocity projectile ratio $v_p/v_{th} \approx 1$ for the warm dense matter, that is typically characterized by solid densities $\rho \sim 1$ and electron temperature of $T_e \sim$ 1-100 eV. The proposed experimental approach to be able to achieve this regime of ion beam - plasma interaction has been based on the use of the proton energy selector to select a low energy proton beam with small bandwidth and time spread from laser driven TNSA spectrum and on the use of a fs laser to generate WDM with electron temperature of $\mathbf{T_e \approx 15 - 20\ eV}$ to be probed by the proton beam. The theoretical modelling and experimental studies performed towards understanding the physics of this regime has been presented in the framework of this thesis. The theoretical predictions with the use of the various ion stopping power models, that take into account the numerous processes occurring, which are still not well understood in the WDM state, have been compared between each other for the different velocity protons of 0.2 - 0.8 MeV energy in the simulated conditions of WDM with 1D and 2D hydrodynamic code.

The highest discrepancies between models of 30 % is predicted for the proton projectile of 0.2 MeV. However a first approach for the current experimental study of the stopping power has been performed with projectile energies of 0.5 MeV, for which the models predict the energy loss with discrepancies of 10 %. At the same time, there are no measurements in this regime and it has to be studied at least to validate predicted energy loss before starting to differ the models from one another.

In order to validate the quality of energy loss measurement of the proton beam selected by the featured proton energy selector, the proton stopping power was firstly measured in solid matter. The preliminary experimental results totally justify use of such an experimental approach for the proton energy loss measurement in the warm dense matter. The measured energy loss of 0.5 MeV proton projectile in different solid targets of 1 μm C, 2μm C and 2 μm Mylar are in good agreement with SRIM data base with the very small experimental error of the order of **0.005 MeV** achieved statistically.

The performed measurements of the proton energy loss of 0.5 MeV proton projectiles in the femtosecond laser heated warm dense matter featuring the velocity projectile ratio of $\mathbf{v_p/v_{th} \approx 3}$ are currently under analysis together with target temperature data analysis

provided by X-ray pinhole grating camera and Streak Optical Pyrometry that would clarify the conditions which correspond to the proton probing time.

The final measurement of interest to be performed are for the 0.2 MeV proton projectile in WDM conditions, that would have the largest discrepancies between theories. The performed experimental study confirms the feasibility of such measurements by using the designed proton energy selector and such studies are planned in the near future.

One of the outcome of this work is related to better understanding not the physics of WDM, that it turn would help in the further improving knowledge about implosion physics of Inertial Confinement Fusion and astrophysics. Another area of impact is related to detailed understanding of alpha particle heating in Inertial Confinement Fusion.

Chapter 6

Resumen y conclusiones

El trabajo realizado para esta tesis está dedicado al estudio del transporte de partículas cargadas por láser en plasmas y materia densa y caliente. En particular, se centra en la investigación experimental de la técnica de colimación de haz de electrones relativista para las intensidades láser $10^{18} - 10^{19}$ W / cm^2 y el estudio de el poder de detención de iones en materia cálida y densa a bajas velocidades $v_p/v_{th} \approx 3$, numérica y experimentalmente.

6.1 Esquema de colimación REB de doble pulso

Los resultados experimentales del experimento LULI-ELFIE, centrados en el estudio paramétrico de la guía del haz de electrones relativista mediante el uso de dos pulsos láser consecutivos, presentaron una clara firma de colimación del 70 % de electrones calientes con un tamaño de haz reducido por un factor de ≈ 2 y guiándolos a más de 50 μm en plasma obtenido ajustando ciertos parámetros entre pulsos láser. Mediante el uso de dos técnicas de diagnóstico independientes (K_α de imágenes y CTR) se observó que al modificar la relación de intensidad del láser I_1/I_2, relación de punto focal ϕ_1/ϕ_2 y el tiempo de retraso Δt entre dos pulsos láser, uno puede controlar la eficiencia del esquema de colimación. Tanto a partir de resultados experimentales como de simulaciones numéricas, realizadas para apoyar el esquema, se demostró que para cada valor de ϕ_1/ϕ_2 hay un tiempo de inyección óptimo es Δt , que, de acuerdo con las expectativas, aumenta cuando ϕ_1/ϕ_2 se reduce. Este estudio valida los estudios teóricos de A. Robinson [176, 175] y amplía la comprensión de la primera validación experimental del esquema de doble pulso por R. Scott [194], donde el esquema se estudió solo en términos de El tiempo de retraso entre pulsos láser.

Los resultados experimentales muestran que el tiempo de retraso óptimo es una función de la relación de punto focal, que resulta de la evolución temporal del campo magnético.

Según las simulaciones numéricas, el campo magnético alcanza su máximo al final de la interacción del pulso láser con el objetivo sólido $\tau_L \approx 0.5$ ps.

Parece estar de acuerdo con el experimento anterior, en el que la duración del pulso del láser fue $\tau_L = 1$ ps y la colimación se produjo entre 4 y 6 ps del tiempo de retraso de los pulsos del láser, que también corresponden al 4 - 6 $\times$ τ_L. Teniendo en cuenta que el rango de intensidad del experimento referido fue $10^{18} - 10^{19}$ W / cm^2, se puede concluir que el tiempo de retraso óptimo no es una función de La intensidad del láser.

El estudio numérico y experimental realizado en esta tesis impulsa la comprensión del esquema de doble pulso en términos de los diversos parámetros que afectan la evolución del campo magnético en plasma.

Una de las aplicaciones potenciales de esta técnica de colimación electrónica es el esquema integrado para el enfoque de encendido rápido para la fusión por confinamiento inercial, donde el haz de electrones relativista impulsado por láser debe guiarse a través de 50 - 100 μm de plasma denso caliente para entregar suficiente energía en un punto caliente lo suficientemente alto para el encendido ($\geq$ 18 kJ). Sin embargo, este haz de electrones tiene una divergencia intrínsecamente alta y no llega al núcleo caliente con la energía requerida para el encendido. Se puede usar el primer pulso láser de la intensidad de $I \approx 10^{19}$ W/cm^2 para generar el campo magnético acimutal para controlar la divergencia y guiar el haz de electrones principal generado por pulso láser de $I \approx 10^{20}$ W/cm^2. Sin embargo, uno necesitaría estudios numéricos detallados para comprender cuantitativamente qué tan bien la colimación observada en los experimentos actuales se traduciría en las condiciones del láser y del objetivo en un escenario de encendido rápido.

Desde otro lado, el esquema de doble pulso puede usarse para la optimización de la radiación de rayos X de partículas impulsada por láser y las fuentes de protones, para aplicaciones que exigen el tamaño compacto y el alto brillo de la fuente referida.

6.2 La plataforma ajustable para la selección de energía de protones

El novedoso diseño del sistema selector de energía de protones que permite seleccionar los haces de protones "monoenergéticos" del espectro TNSA impulsado por láser generado por una intensidad láser de $I \approx 10^{19}$ W/cm^2 se ha realizado en el marco de esta tesis. El estudio fue motivado por el requerimiento de un haz de protones monoenergético para la investigación de la potencia de detención de protones a bajas velocidades en la materia densa cálida, donde las mediciones experimentales de pérdida de energía de protones de alta

precisión en las condiciones de la materia en rápida evolución requieren un protón estable. haz con un ancho de banda de energía pequeño (1 %) y tiempo extendido, tamaño espacial pequeño <50 μm my baja energía <0.5 MeV y que puede usarse a una alta tasa de repetición para promediar muchas tomas y reducir estadísticas error. La primera demostración de la selección de dicho haz de protones con la calidad requerida se ha demostrado en esta tesis.

Las fuentes de protones TNSA, generadas por láser de pulso corto de alta intensidad con intensidades de $I = 10^{19} - 10^{21}$ W/cm^2, generalmente tienen un amplio espectro con energía de corte del orden de decenas de MeV con la distribución de tiempo correspondiente. Por lo tanto, para seleccionar la energía de haz de protones de interés, en esta tesis se ha presentado el concepto de sistema selector de energía basado en imanes. El selector de energía de protones presentado se basa en el uso del imán dipolo de 1.2 T con dos pasos de selección, antes y después de la desviación del protón por el imán, es muy compacto, con una dimensión longitudinal de 8 cm, y puede colocarse cerca según sea necesario para La fuente de protones.

Los resultados experimentales preliminares de la optimización del selector de energía, realizada en la instalación láser VEGA-II, muestran la selección de los proyectiles de protones de 0.5 MeV de energía con el mínimo textbf ancho de banda de energía medido de 0.025 MeV con un nivel de señal razonable usando un 20 μm hendidura y 20 μm pinhole como selectores de energía de protones. Las diferentes configuraciones del selector de energía de protones se han caracterizado experimentalmente en términos de intensidad de señal de protones y ancho de banda de energía, que se redujo gradualmente de 0.09 MeV a 0.025 MeV con el uso de agujeros pequeños de 200 μm - 10 μm. El estudio experimental muestra la selección estadística precisa y repetitiva de la energía del protón, y una pequeña variación en la intensidad de la señal, que se conecta directamente con el número de protones. Demuestra que la plataforma del selector de energía es insensible a las variaciones de interacción láser-objetivo debido a la estabilidad del láser, que generalmente es común para sistemas láser de alta intensidad e imperfecciones objetivo. Otra posibilidad para mejoras futuras es agregar un campo magnético sintonizable para optimizar el selector de energía en términos de la energía seleccionada sin cambiar la posición lateral del imán. En el futuro, también se podrían agregar imanes de enfoque cuadrupolo para volver a colimar la fuente de protones de energía seleccionada en las muestras y detectores de la aplicación. El estudio teórico y experimental presentado del selector de energía de protones diseñado es muy prometedor y tiene muchos usos en diferentes campos de la ciencia, particularmente para las mediciones de potencia de frenado y en aplicaciones médicas y biológicas. El selector de energía también presenta un uso fácil y permite posibilidades de manipulación con la motorización de todos los elementos del selector, lo que permite el cambio de las energías de protones seleccionadas

sin interrupción del experimento, lo que lo hace perfectamente adecuado para experimentos de HRR.

6.3 Potencia de frenado de protones en WDM a una relación de proyectil de baja velocidad

En esta tesis se ha propuesto un enfoque experimental novedoso para las mediciones de potencia de detención de protones en condiciones de materia cálida y densa a una relación de proyectil de baja velocidad. Hasta ahora, no había datos experimentales para comparar los modelos de potencia de parada de iones existentes para este régimen y dominio de parámetros, principalmente debido a las dificultades para generar las velocidades de proyectil de baja energía que darían la relación de proyectil de velocidad $v_p/v_{th} \approx 1$ para la materia densa cálida, que se caracteriza típicamente por densidades sólidas $\rho \sim 1$ y temperatura de electrones de $T_e \sim$ 1-100 eV. El enfoque experimental propuesto para poder lograr este régimen de interacción entre el haz de iones y el plasma se ha basado en el uso del selector de energía de protones para seleccionar un haz de protones de baja energía con un ancho de banda pequeño y un tiempo extendido desde el espectro TNSA accionado por láser y el uso de un láser fs para generar WDM con una temperatura de electrones de $\mathbf{T_e \approx 15 - 20}$ textbf eV para ser sondeado por el protón haz. El modelado teórico y los estudios experimentales realizados para comprender la física de este régimen se han presentado en el marco de esta tesis. Las predicciones teóricas con el uso de varios modelos de potencia de parada de iones, que tienen en cuenta los numerosos procesos que ocurren, que todavía no se comprenden bien en el estado WDM, se han comparado entre sí para los diferentes protones de velocidad de 0.2 - 0.8 MeV energía en las condiciones simuladas de WDM con código hidrodinámico 1D y 2D.

Las mayores discrepancias entre los modelos de 30 % se predicen para el proyectil de protones de 0.2 MeV. Sin embargo, un primer enfoque para el estudio experimental actual de la potencia de frenado se ha realizado con energías de proyectil de 0,5 MeV, para lo cual los modelos predicen la pérdida de energía con discrepancias del 10 %. Al mismo tiempo, no hay mediciones en este régimen y debe estudiarse al menos para validar la pérdida de energía prevista antes de comenzar a diferenciar los modelos entre sí.

Para validar la calidad de la medición de pérdida de energía del haz de protones seleccionado por el selector de energía de protones presentado, la potencia de detención de protones se midió en primer lugar en materia sólida. Los resultados experimentales preliminares justifican totalmente el uso de este enfoque experimental para la medición de la

pérdida de energía de protones en la materia densa cálida. La pérdida de energía medida del proyectil de protones de 0,5 MeV en diferentes objetivos sólidos de 1 μ m C, 2 μm C y 2 μm Mylar está en buen acuerdo con la base de datos SRIM con el muy pequeño experimental error del orden de textbf 0.005 MeV logrado estadísticamente.

Las mediciones realizadas de la pérdida de energía de protones de los proyectiles de protones de 0,5 MeV en la materia densa calentada con láser de femtosegundo que presenta la relación de proyectil de velocidad de $\mathbf{v_p/v_{th}} \approx \mathbf{3}$ están actualmente bajo análisis junto con análisis de datos de temperatura objetivo proporcionados por la cámara de rayos X con cámara estenopeica y la pirometría óptica Streak que aclararían las condiciones que corresponden al tiempo de sondeo de protones.

La medición final de interés a realizar es para el proyectil de protón de 0.2 MeV en condiciones WDM, que tendría las mayores discrepancias entre las teorías. El estudio experimental realizado confirma la viabilidad de tales mediciones mediante el uso del selector de energía de protones diseñado y dichos estudios se planifican en un futuro próximo.

Uno de los resultados de este trabajo está relacionado con una mejor comprensión, no con la física de WDM, que a su vez ayudaría a mejorar aún más el conocimiento sobre la física de implosión de la fusión por confinamiento inercial y la astrofísica. Otra área de impacto está relacionada con la comprensión detallada del calentamiento de partículas alfa en la fusión por confinamiento inercial.

List of publications and communications

Publications

- S. Malko, X. Vaisseau, F. Perez, A. Curcio, M. Ehret, J. Santos, D. Batani, K. Jakubowska, J. Honrubia, A. Morace and L. Volpe: "*Enhanced relativistic electron beam collimation using two consecutive laser pulses*", Scientific Reports **9**(1) (2019)

- L. Volpe, R. Fedosejevs, G. Gatti, J. A. Pérez-Hernández, C. Méndez, J. Apiñaniz, X. Vaisseau, C. Salgado, M. Huault, S. Malko, G. Zeraouli, V. Ospina, A. Longman, D. De Luis, K. Li, O. Varela, E. García, I. Hernández, J. D. Pisonero, J. García Ajates, J. M. Alvarez, C. García, M. Rico, D. Arana, J. Hernández-Toro, L. Roso: "*Generation of high energy laser-driven electrons and proton sources with the 200 TW system VEGA 2 at the CLPU*", High Power Laser Science and Engineering **7** (2019)

- G. Cristoforetti, L. Antonelli, D. Mancelli, S. Atzeni, F. Baffigi, F. Barbato, D. Batani, G. Boutoux, F. D'Amato, J. Dostal, R. Dudzak, L. Juha, O. Klimo,M. Krus, S. Malko, Ph. Nicolai, V. Ospina, O. Renner, J. Santos, V. T. Tikhonchuk, J. Trela, S. Viciani, L. Volpe, S. Weber and L. A. Gizzi: "*Time evolution of Stimulated Raman Scattering and Two Plasmon Decay at laser intensities relevant for Shock Ignition in a hot plasma*", High Power Laser Science and Engineering **7** (2019)

- S. Malko, S. Pavlov, K. Tretiak: "*Fast computation of complex error function of the real argument*", Problems of atomic science and technology, **107** - 1, pp.76 -79 (2017)

Oral communications

- S. Malko, W. Cayzac, V. Ospina, X. Vaisseau, J. Apinaniz, D. Batani, M. Barriga-Carrasco, R. Fedosejevs, M. Huault, P. Neumayer, J.A. Perez-Hernandez, G. Prestopino, R. Ramis, C. Verona and L. Volpe: "*Ion stopping power measurements in a coupled and degenerate plasma*", 61st Annual Meeting of the American Physical Society Division

of Plasma Physics (APS DPP),Fort Lauderdale, Florida, USA (2019) **(Dissertation talk)**

- S. Malko, W. Cayzac, V. Ospina, X. Vaisseau, J. Apinaniz, D. Batani, M. Barriga-Carrasco, R. Fedosejevs, M. Huault, P. Neumayer, J.A. Perez-Hernandez, G. Prestopino, R. Ramis, C. Verona and L. Volpe: "*Ion stopping power measurements at low velocity projectile*", International Conference on High Energy Density (ICHED), Oxford, United Kingdom (2019)

- S. Malko, X. Vaisseau, F. Perez, A. Curcio, M. Ehret, J. Santos, D. Batani, K. Jakubowska, J. Honrubia, A. Morace and L. Volpe: "*Enhanced relativistic electron beam collimation using two consecutive laser pulses*", 45th EPS Conference on Plasma Physics, Prague, Czech Republic (2018)

- S. Malko, X. Vaisseau, F. Perez, A. Curcio, M. Ehret, J. Santos, D. Batani, K. Jakubowska, J. Honrubia, A. Morace and L. Volpe: "*Relativistic electron beam collimation in warm-dense aluminium using two consecutive laser pulses*", 10th International Conference on Inertial Fusion Sciences and Applications (IFSA), Saint-Malo, France (2017) **(INVITED)**

- S. Malko, X. Vaisseau, F. Perez, A. Curcio, M. Ehret, J. Santos, D. Batani, A. Morace, L. Volpe: "*Parametric study of fast electron beam guiding using two consecutive laser pulses*", 12th Direct Drive and Fast Ignition Workshop, Bordeaux, France (2015) **(INVITED)**

Contributions to poster sessions

- S. Malko, C. Salgado, G. Gatti , R. Fedosejevs, J. A. Perez-Hernandez and L. Volpe: "*Characterization of the pre-plasma formation for high intensity laser-solid target experiment*", 3rd European Conference on Plasma Diagnostics (EPCD), Lisbon, Portugal (2019)

- S. Malko, W. Cayzac, X. Vaissesau, P. Neumayer, L. Antonelli, B. Canaut, F. Philippe, M. Temporal, B. Vauzour, I. Lantuéjoul , W. Garbet, C. Spindloe , D. Batani and L. Volpe: "*Ion stopping power measurements in plasma targets*", First LMJ-PETAL User Meeting , Le Barp, France (2018)

- M. Ehret, J. Alpiñaniz, V. Bagnoud, M. Bailly-Grandvaux, C. Brabetz, E. d'Humières, Ph. Korneev, S. Malko, C. Matveevskii, A. Morace, L. Volpe, M. Roth, G. Schaumann ,

V. T. Tikhonchuk and J. J. Santos: "*Transient Electromagnetic Fields for High Energy-Density Beam Tailoring Driven by ps-Laser Pulses*", 45th EPS Conference on Plasma Physics, Prague, Czech Republic (2018)

- S. Malko, X. Vaisseau, F. Perez, A. Curcio, M. Ehret, J. Santos, D. Batani, A. Morace, L. Volpe: "*Relativistic electron beam transport in warm dense matter*", Laser -Plasma Interaction Forum, Ile d'Oleron, France (2018)

- S. Malko, X. Vaisseau, F. Perez, A. Curcio, M. Ehret, J. Santos, D. Batani, L. Volpe: "*Parametric study of fast electron beam collimation using two consecutive pulses*", 9th Omega Laser Facility User Group Workshop, University of Rochester, Laboratory of Laser Energetics, USA (2017)

- S. Malko, A. Longman, C. Salgado, J. Ajates, J. Apiñaniz, G. Gatti, I. Hernandez, L. Roso, J. Perez Hernandez, J. Pisonero, X. Vaisseau, L. Volpe, G. Zeraouli, R. Fedosejevs: "*Study of ionization states dynamics of warm dense aluminium*", 13th Direct Drive and Fast Ignition Workshop, Salamanca, Spain (2017)

- C. Salgado, A. Longman, S. Malko, G. Zeraouli, M. Huault, J. Pérez-Hernández, X. Vaisseau, J. Apiñaniz, E. Garcia, O. Varela, C. Méndez, T. Hernandez, G. Gatti, L. Volpe, L. Roso, R. Fedosejevs: "*Laser driven electrons and X-ray Betatron radiation generation at VEGA*", 13th Direct Drive and Fast Ignition Workshop, Salamanca, Spain (2017)

- S. Malko, X. Vaisseau, F. Perez, A. Curcio, M. Ehret, J. Santos, D. Batani, L. Volpe: "*Relativistic electron beam guiding by using two consecutive laser pulses*", 2nd EMP Meeting, IPPLM, Warsaw, Poland (2017)

- S. Malko, X. Vaisseau, F. Perez, A. Curcio, M. Ehret, J. Santos, D. Batani, L. Volpe: "*Fast electron transport in dense plasmas*", International Conference-School on Plasma Physics and controlled Fusion 2016, Kharkiv, Ukraine (2016)

- J.J. Santos, M. Bailly-Grandvaux, D. Batani, C. Bellei, M. Ehret, J. Feugeas, L. Giuffrida, S. Hulin, E. D'Humières, Ph. Nicolaï, A. Poye, V. Tikhonchuk, Ph. Korneev, M. Roth, G. Schaumann, S. Fujioka, K. F .F Law, A. Morace, J. I. Apiñaniz, C. Brabetz: "*Strong magnetic fields produced by laser-plasma interactions-an all-optical platform for magnetized high-energy-density physics*", 18th International Congress on Plasma Physics, Kaohsiung, Taiwan, (2016)

- M. Bailly-Grandvaux, J. Santos, J.I. Apiñaniz, V. Bagnoud, C. Brabetz, J. Dubois, M. Ehret, S. Hulin, S. Malko, A. Morace, J. Ribolzi, M. Roth, G. Schaumann, V. Tikhonchuk, L. Volpe: "*Time-resolved highdischarge current in coil-shaped targets irradiated by ps intense laser pulses applied to proton-beam tailoring*", 43rd EPS Conference on Plasma Physics, Belfast, Ireland (2016)

Bibliography

[Pst]

[2] (2010). Basic research needs for high energy density laboratory physics. *DOE Office of Science and NNSA*.

[3] A. L. Meadowcroft, C. D. B. and Stott, E. N. (2008). Evaluation of the sensitivity and fading characteristics of an image plate system for x-ray diagnostics. *Rev. Sci. Instrum*, 79(113102).

[4] Aglitskiy, Y. and Lehecka, T. e. a. (1998). High-resolution monochromatic x-ray imaging system based on spherically bent crystals. *Appl. Opt.*, 37(5253).

[5] Albert, F. e. a. (2008). Betatron oscillations of electrons accelerated in laser wakefields characterized by spectral x-ray analysis. *Physical Review E*, 77:056402–1.

[6] Albert, F. e. a. (2016). Applications of laser wakefield accelerator-based light sources. *Plasma Physics and Controlled Fusion*, 58:103001–1–35.

[7] Alexiou, S. (2009). Overview of plasma line broadening. *High Energy Density Phys.*, 5(225).

[8] Alfvén, H. (1939). On the motion of cosmic rays in interstellar space. *Physical Review*, 55(425).

[9] Bailly-Grandvaux, M. (2017). *Laser-driven strong magnetic fields and high discharge currents : measurements and applications to charged particle transport*. PhD thesis, University of Bordeaux.

[10] Bailly-Grandvaux, M., Santos, J. J., and Bellei, C. e. a. (2018). Guiding of relativistic electron beams in dense matter by laser-driven magnetostatic fields. *Nature Communications*, 9(102).

[11] Balescu, R. (1960). Irreversible processes in ionized gases. *Physics of Fluids*, 3:52–63.

[12] Balescu, R. (1975). *Equilibrium and nonequilibrium statistical mechanics*. Wiley.

[13] Bambynek, W. (20984). X-ray and inner-shell processes in atoms, molecules and solids. *A. Meisel and J. Finster, Leipzig,Karl-Marx-Universität*, 5.

[14] Barkas, H., Dyer, J. N., and Heckman, H. H. (1963). Resolution of the -mass anomaly. *Physical Review Letters*, 11:26–28.

[15] Barriga-Carrasco, M. D., Casas, D., and Morales, R. (2016). Calculations on charge state and energy loss of argon ions in partially and fully ionized carbon plasmas. *Physical Review E*, 93:033204.

[16] Batani, D., Antonicci, A., and Pisani, F. e. a. (2002). Inhibition in the propagation of fast electrons in plastic foams by resistive electric fields. *Physical Review E*, 65:066409.

[17] Batani, D., Davies, J. R., and et al., B. (2000). Explanations for the observed increase in fast electron penetration in laser shock compressed materials. *Physical Review E*, 61:5725–5733.

[18] Baton, S. D., Santos, J. J., and Amiranoff, F. e. a. (2003). *Physical Review Letters*, 91(105001).

[19] Beg, F. N., Bell, A. R., and Dangor, A. E. e. a. (1997). A study of picosecond laser–solid interactions up to 1019 wcm2. *Physics of Plasmas*, 4(2):447–457.

[20] Bell, A. R. and Kingham, R. J. (2003). Resistive collimation of electron beams in laser-produced plasmas. *Physical Review Letters*, 91(4):035003.

[21] Bell, A. R. e. a. (1997). *Plasma Phys. Control. Fusion*, 39:653.

[22] Bellei, C., Davies, J. R., and Chauhan, P. K. e. a. (2012). Coherent transition radiation in relativistic laser-solid interactions. *Plasma Physics and Controlled Fusion*, 54(035011).

[23] Bethe, H. (1930). Zur theorie des durchgangs schneller korpuskularstrahlen durch materie. *Annalen der Physik*, 397:325–400.

[24] Bethe, H. (1932). Bremsformel für elektronen relativistischer geschwindigkeit. zeitschrift fur physik. *Zeitschrift fur Physik*, 76:293–299.

[25] Bethe, H. (1933). *Handbuch für physik (Julius Springer)*. Julius Springer.

[26] Bethe, H. (1953). Molière's theory of multiple scattering. *Physical Review*, 89(1256).

[27] Betz, H. D. (1983). Heavy ion charge states. *In S. Datz, editor, Applied Atomic Collision Physics*, 4(4).

[28] Böhlen, T. T., Cerutti, F., and Chin, M. P. W. e. a. (2014). "the fluka code: Developments and challenges for high energy and medical applications". *Nuclear Data Sheets*, 120:211–214.

[29] Bloch, F. (1933). Zur bremsung rasch bewegter teilchen beim durchgang durch materie. *Annalen der Physik*, 408:285–320.

[30] Bohr, N. (1913). On the theory of the decrease of velocity of moving electric field particles on passing through matter. *Phil. Mag*, 25(6):10–31.

[31] Borghesi, M. e. a. (2006). Fast ion generation by high-intensity laser irradiation of solid targets and applications. *Fusion Sci. Technol.*, 49:412.

[32] Borner, M. e. a. (2012). Development of a nomarski-type multi-frame interferometer as a time and space resolving diagnostics for the free electron density of laser-generated plasma. *Review of Scientific Instruments*, 83(4):043501.

[33] Brown, L., B.L, P., and J., S. (2005). Charged particle motion in a highly ionized plasma. *Physics Reports*, 410(4):237–333.

[34] Brunel, F. (1987). Not-so-resonant, resonant absorption. *Physical Review Letters*, 59(52).

[35] Casas, D. (2016). Stopping power of a heterogeneous warm dense matter. *Laser and Particle Beams*, 34:306–314.

[36] Casas, D., Barriga-Carrasco, M. D., and Rubio, J. (2013). Evaluation of slowing down of proton and deuteron beams in ch_2, lih, and al partially ionized plasmas. *Physical Review E*, 88:033102.

[37] Casnati, E. e. a. (1982). An empirical approach to k-shell ionisation cross section by electrons. *Journal of Physics B*, 15(155).

[38] Cayzac, W. (2013). *Ion energy loss at maximum stopping power in a laser-generated plasma*. PhD thesis, University of Bordeaux.

[39] Cayzac, W. e. a. (2015). Predictions for the energy loss of light ions in laser-generated plasmas at low and medium velocities. *Physical Review E*, 92(053109).

[40] Cayzac, W. e. a. (2017). Experimental discrimination of ion stopping models near the bragg peak in highly ionized matter. *Nat. Commun.*, 8(15693).

[41] Chandrasekhar, S. (1943). Stochastic problems in physics and astronomy. *Reviews of Modern Physics*, 15(1):89.

[42] Chen, C. D., Patel, P. K., and Hey, D. S. e. a. (2009a). Bremsstrahlung and k fluorescence measurements for inferring conversion efficiencies into fast ignition relevant hot electrons. *Physics of Plasmas*, 16(8):082705.

[43] Chen, H., Wilks, S. C., Kruer, W. L., Patel, P. K., and Shepherd, R. (2009b). Hot electron energy distributions from ultraintense laser solid interactions. *Physics of Plasmas*, 16(2):020705.

[44] Chimier, B., Tikhonchuk, V. T., and Hallo, L. (2008). Effect of pressure relaxation during the laser heating and electron ion relaxation stages. *Applied Physics A: Materials Science Processing*, 92(843).

[45] Chung, H. e. a. (2005). Generalized population kinetics and spectral model for rapid spectroscopic analysis for all elements. *High Energy Density Phys.*, 1(3).

[46] Cowan, T. E., Fuchs, J., and Ruhl, H. e. a. (2004). Ultralow emittance, multi-mev proton beams from a laser virtual-cathode plasma accelerator. *Physical Review Letters*, 92(20):204801.

[47] Danson, C. e. a. (2015). *High Power Laser Science and Engineering*, 3:14.

[48] David, F. and Pellat, R. (1980). Resonant absorption by a magnetic plasma at a rippled critical surface. *The Physics of Fluids*, 23(1682).

[49] Davies, J. R. (2002). *Physical Review E*, 65:026407.

[50] Davies, J. R. (2003). Electric and magnetic field generation and target heating by laser generated fast electrons. *Physical Review E*, 68(056404).

[51] Davies, J. R. (2008). Laser absorption by overdense plasmas in the relativistic regime. *Plasma Physics and Controlled Fusion*, 51(1):014006.

[52] Davies, J. R., Bell, A. R., and Haines, M. G. e. a. (1997). Short-pulse high-intensity laser-generated fast electron transport into thick solid targets. *Physical Review E*, 56(7193).

[53] Debayle, A., Gremillet, L., Honrubia, J. J., and d'Humières, E. (2013). Reduction of the fast electron angular dispersion by means of varying-resistivity structured targets. *Physics of Plasmas*, 20(1):013109.

[54] Debayle, A., Honrubia, J. J., d'Humières, E., and Tikhonchuk, V. T. (2010). Divergence of laserdriven relativistic electron beams. *Physical Review E*, 82:036405.

[55] Derouillat, J., e. a. (2018). Smilei : A collaborative, open-source, multi-purpose particle-in-cell code for plasma simulation. *Comput. Phys. Commun.*, 222:351 – 373.

[56] Deutsch, C. e. a. (2014). *NIMPA*, 733:39–44.

[57] Dietrich, K. G. e. a. (1990). Energy loss of heavy ions in a dense hydrogen plasma. *Zeitschrift fur Physik D Atoms Molecules Clusters*, 16:229–230.

[58] Ding, Y. H., White, A. J., Hu, S. X., Certik, O., and Collins, L. A. (2018). Ab initio studies on the stopping power of warm dense matter with time-dependent orbital-free density functional theory. *Physical Review Letters*, 121:145001.

[59] Drake, P. (2006). *High-Energy-Density Physics: Fundamentals, Intertial Fusion, and Experimental Astrophysics*. Springer.

[60] Dromey, B. and Kar, S.and Zepf, M. e. a. (2004). The plasma mirror – a subpicosecond optical switch for ultrahigh power lasers. *Rev. Sci. Instrum.*, 75:645.

[61] Edie, D. e. a. (2013). *EPJ Web of Conferences*, 59(5018).

[62] Eidmann, K., Meyer-ter Vehn, J., Schlegel, T., and Hüller, S. (2000). Hydrodynamic simulation of subpicosecond laser interaction with solid-density matter. *Physical Review E*, 62(1202).

[63] Estin, A. J. (1965). The propagation of electromagnetic waves in plasmas. v. l. ginzburg.translated from the russian edition (moscow, 1960) by j. b. sykes and r. j. tayler. pergamon, london; addison-wesley, reading, mass., 1964. *Science*, 147(1563).

[64] et al., D. G. (2002a). *Physical Review E*, 65(036406).

[65] et al., D. G. (2002b). Dense plasma temperature equilibration in the binary collision approximation. *Physical Review E*, 65(036418).

[66] et al., D. G. (2003). Energy deposition of heavy ions in the regime of strong beam-plasma correlations. *Physical Review E*, 65(037401).

[et al.] et al., Y. K.

[68] Faure, J. e. a. (2004). A laser-plasma accelerator producing monoenergetic electron beams. *Nature*, 431:5414.

[69] Faussurier, G., Blancard, C., Cossé, P., and Renaudin, P. (2010). Equation of state, transport coefficients, and stopping power of dense plasmas from the average-atom model self-consistent approach for astrophysical and laboratory plasmas. *Physics of Plasmas*, 17(5):052707.

[70] Fermi, E. (1940). The ionization loss of energy in gases and in condensed materials. *Physical Review*, 57(485).

[71] Ferrari, A., Sala, P., Fasso, A., and Ranft, J. (2005). "fluka: a multi-particle transport code". *CERN-2005-10*, INFN/TC$_0$5/11($SLAC-R-773$) : 211 − −214.

[72] Flacco, A., Sylla, F., and Veltcheva, M. e. a. (2010). Dependence on pulse duration and foil thickness in high-contrast-laser proton acceleration. *Physical Review E*, 81:036405.

[73] Flippo, K. A., d'Humières, E., and Gaillard, S. A. e. a. (2008). Increased efficiency of short-pulse laser-generated proton beams from novel flat-top cone targets. *Physics of Plasmas*, 15:056709.

[74] Florido, R., Rodríguez, R., and Gil, J. M. e. a. (2008). ABAKO: A new code for population kinetics and radiative properties of plasmas under NLTE conditions. *Journal of Physics: Conference Series*, 112(4):042008.

[75] Frank, A. (2011). *Energieverlust und Umladung von schweren Ionen in lasererzeugten Plasmen*. PhD thesis, Technische Universität Darmstadt.

[76] Frank, A. e. a. (2013). Energy loss and charge transfer of argon in a laser-generated carbon plasma. *Phys. Rev. Let.*, 110(115001).

[77] Frenje, J. A. e. a. (2015). Measurements of ion stopping around the bragg peak in high-energy-density plasmas. *Phys. Rev. Let.*, 115(205001).

[78] Frenje, J. A. e. a. (2019). Experimental validation of low-z ion-stopping formalisms around the bragg peak in high-energy-density plasmas. *Physical Review Letters*, 122:015002.

[79] Fuchs, J. (2006). Laser-driven proton scaling laws and new paths towards energy increase. *Nature Physics*, 2:48–54.

[80] Fuchs, J., Antici, P., and d'Humie'res, E. e. a. (2006). *J. Phys. IV (France)*, 133:1151.

[81] Gauthier, M., Blancard, C., and Chen, S. e. a. (2013). Stopping power modeling in warm and hot dense matter. *High Energy Density Physics*, 9(3):488 – 495.

[82] Geddes, C. G. R. e. a. (2004). High-quality electron beams from a laser wakefield accelerator using plasma-channel guiding. *Nature*, 431:53841.

[83] Gericke, D. O.and Schlanges, M. (1999). Beam-plasma coupling effects on the stopping power of dense plasmas. *Physical Review E*, 60:904–910.

[84] Gibbon, P. (1994). Efficient production of fast electrons from femtosecond laser interaction with solid targets. *Physical Review Letters*, 73:664–667.

[85] Gibbon, P. (2005). *Short pulse laser interactions with matter*. World Scientific Publishing Company.

[86] Gibbon, P. and Bell, A. R. (1992). Collisionless absorption in sharp-edged plasmas. *Physical Review Letters*, 68:1535–1538.

[87] Golubev, A. e. a. (1998). Dense plasma diagnostics by fast proton beams. *Physical Review E*, 57(3363).

[88] Green, J. S., Ovchinnikov, V. M., and et al., E. (2008). Effect of laser intensity on fast-electron-beam divergence in solid-density plasmas. *Physical Review Letters*, 100:015003.

[89] Gremillet, L. (2001). PhD thesis, Ecole Polytechnique.

[90] Gus'kov, S.Y., Z. N. I. D. e. a. (2009). "a method for calculating the effective charge of ions decelerated in a hot dense plasma". *Plasma Phys. Rep.*, 35:709–718.

[91] Hall, T. (1984). *Journal of Physics E: Scientific Instruments*, 17(110).

[92] Hammer, D. A. and Rostoker, N. (1970). Propagation of high current relativistic electron beams. *Physics of Fluids*, 13(1831).

[93] Hamos, L. V. (1939). Formation of true x-ray images by reflection on crystal mirrors. *Zeitschrift für Kristallographie*, 101(17).

[Hansen et al.] Hansen, S. B., Faenov, A. Y., and Pikuz, T. A. e. a.

[95] Hatchett, S. (2000). Electron, photon, and ion beams from the relativistic interaction of petawattlaser pulses with solid targets. *Physics of Plasmas*, 7:2076–2082.

[96] Hauer, A., Kilkenny, J., and Landen, O. (1985). *Rev. Sci. Inst.*, 56.

[97] Haun, J. e. a. (2015). *Physical Review E*, 65(046407).

[98] Hayes, A. e. a. (2015). Reaction-in-flight neutrons as a test of stopping power in degenerate plasmas. *Physics of Plasmas*, 22(082703).

[99] Hicks, D. G. e. a. (2000). Charged-particle acceleration and energy loss in laser-produced plasmas. *Physics of Plasmas*, 7(12):5106–5117.

[100] Hoffmann, D. e. a. (1990). Energy loss of heavy ions in a plasma target. *Phys. Rev. A*, 42:2313–2321.

[101] Hombourger, H. (1998). Journal of physics b: Atomic, molecular and optical physics an empirical expression for k-shell ionization cross section by electron impact. *Journal of Physics B: Atomic and Molecular Physics*, 31(3693).

[102] Honrubia, J., Antonicci, A., and Moreno, D. (2004). Hybrid simulations of fast electron transport in conducting media. *Laser Part. Beams*, 129.

[103] Honrubia, J. J. and Meyer-Ter-Vehn, J. (2009). Fast ignition of fusion targets by laser-driven electrons. *Plasma Phys. Control. Fusion*, 51(014008).

[104] Honrubia, J. J. e. a. (2006). Simulations of heating of solid targets by fast electrons. laser part. *Laser Part. Beams*, 24:217–222.

[105] Hooper, M. (1985). Plasma processes in non-ideal plasmas. *Proceedings of the 29th Scottish Universities Summer School in Physics, Laser plasma interaction 3*.

[106] Hurricane, O., C. D. C. D. e. a. (2016). Inertially confined fusion plasmas dominated by alpha-particle self-heating. *Nature Physics*, 12:800–806.

[107] Kahoul, A., Abassi, A., Deghfel, B., and Nekkab, M. (2011). Radiation physics and chemistry. *Zeitschrift fur Physik*, 80:369.

[108] Kalashnikov, M. P. e. a. (1994). ynamics of laser-plasma interaction at $10^18w/cm^2$. $PhysicalReviewLetters, 73(260)$.

[109] Kaluza, M., Schreiber, J., and Santala, M. I. K. e. a. (2004). Influence of the laser prepulse on proton acceleration in thin-foil experiments. *Physical Review Letters*, 93:045003.

[110] Kar, S., Robinson, A. P. L., and Carroll, D. C. e. a. (2009). Guiding of relativistic electron beams in solid targets by resistively controlled magnetic fields. *Physical Review Letters*, 102:055001.

[111] Key, M. (1998). Hot electron production and heating by hot electrons in fast ignitor research. *Physics of Plasmas*, 5:1966–1972.

[112] King, N., e. a. (1999). *Nucl. Instrum. Methods Phys. Res., Sect. A*, 424(84).

[113] Kluge, T., Cowan, T., and Debus, A. e. a. (2011). Electron temperature scaling in laser interaction with solids. *Physical Review Letters*, 107:205003.

[114] Kneip, S. e. a. (2010). Bright spatially coherent synchrotron x-rays from a table-top source. *Nature Physics*, 6:980–983.

[115] Knoll, G. F. (2010). *Radiation Detection and Measurement, 4th Edition*. Wiley, New York.

[116] Koch, H. W. and Motz, J. W. (1959). Bremsstrahlung cross-section formulas and related data. *Rev. Mod. Phys.*, 31(920).

[117] Kodama, R., Norreys, P. A., and Mima, K. e. a. (2001). Fast heating of ultrahigh-density plasma as a step towards laser fusion ignition. *Nature*, 412(798).

[118] Kodama, R. e. a. (2004). Fast plasma heating in a cone-attached geometry—towards fusion ignition. *Nuclear Fusion*, 44(12):S276–S283.

[119] Kojima, S., H. M. I. N. e. a. (2019). Electromagnetic field growth triggering superponderomotive electron acceleration during multi-picosecond laser-plasma interaction. *Commun Phys*, 2(99):020705.

[120] Krall, N. and Trivelpiece, A. (1986). *Principles of Plasma Physics*. San Francisco Press, San Francisco.

[121] Kremp, D., Schlanges, M., and Bornath, T. (1985). Nonequilibrium real time green's functions and the condition of weakening of initial correlation. journal of statistical physics. *Journal of Statistical Physics*, 41:661–670.

[122] Kruer, W. (1988). *The physics of laser plasma interactions*. Addison-Wesley Publishing Co.

[123] Kruer, W. (2003). *The Physics of Laser Plasma Interactions,Frontiers in physics*. ABC.

[124] Kruer, W. L. and Estabrook, K. (1985). J × b heating by very intense laser light. *Physics of Fluids*, 28(430).

[125] Krygier, A. G., Schumacher, D. W., and Freeman, R. R. (2014). On the origin of super-hot electrons from intense laser interactions with solid targets having moderate scale length preformed plasmas. *Physics of Plasmas*, 21(2):023112.

[126] L., G. (2002). Filamented transport of laser-generated relativistic electrons penetrating a solid target. *Phys. Plasmas*, 9.

[127] Lancaster, K. L. and Green, J. S. e. a. (2007). Measurements of energy transport patterns in solid density laser plasma interactions at intensities of 5x $10^20 w.cm2. Physical Review Letters, 98(125002)$.

[128] Leemans, W. P., Nagler, B., and Gonsalves, A. J. e. a. (2006). Gev electron beams from a centimetrescale accelerator. *Nature Physics*, 2(696).

[129] Lenard, A. (1960). On bogoliubov's kinetic equation for a spatially homogeneous plasma. *Annals of Physics*, 10:390–400.

[130] Li, C. (1993). *Conceptual Study of Moderately Coupled Plasmasand Experimental Comparison of Laboratory*. PhD thesis, MIT.

[131] Lindhard, J. (1954). *On the Properties of a Gas of Charged Particles*. E. Munksgaard.

[132] Lindhard, J. and Schar, M. (1961). Energy dissipation by ions in the kev region. *Physical Review*, 124:128–130.

[133] Lovelace, R. V. and Sudan, R. N. (1971). Plasma heating by high-current relativistic electron beams. *Physical Review Letters*, 27(1256).

[134] Macchi, A., Borghesi, M., and Passoni, M. (2013). Ion acceleration by superintense laser-plasma interaction. *Review Modern Physics*, 85:751–793.

[135] Macchi, A. e. a. (2005). Laser acceleration of ion bunches at the front surface of overdense plasmas. *Physical Review Letters*, 94(165003).

[136] Mackinnon, A. J., Patel, P. K., and Borghesi, M. e. a. (2006). Proton radiography of a laser-driven implosion. *Physical Review Letters*, 97(045001).

[137] Mackinnon, A. J., Sentoku, Y. P., and Patel, P. K. e. a. (2002). Enhancement of proton acceleration by hot-electron recirculation in thin foils irradiated by ultraintense laser pulses. *Physical Review Letters*, 88:215006.

[138] Maksimchuk, A. e. a. (2000). Forward ion acceleration in thin films driven by a high-intensity laser. *Physical Review Letters*, 84:4108.

[139] Malka, V. e. a. (2012). Laser plasma accelerators. *Physics of Plasmas*, 19:055501.

[140] Mangles, S. P. D. e. a. (2004). Monoenergetic beams of relativistic electrons from intense laser-plasma interactions. *Nature*, 431:5358.

[141] Maynard, G. and Deutsch, C. (1985). Born random phase approximation for ion stopping in an arbitrarily degenerate electron fluid. *J.Physique*, 46:1113–1122.

[142] Maynard, G. e. a. (2001). Diffusion-transport cross section and stopping power of swift heavy ions. *Physical Review A*, 63(5):052903.

[143] McKenna, P., Neely, D., Bingham, R., and Jaroszynski, D. (2013). *Laser-Plasma Interactions and Applications*. Springer.

[144] Micheau, S., Debayle, A., d'Humières, E., Honrubia, J. J., Qiao, B., Zepf, M., Borghesi, M., and Geissler, M. (2010). Generation and optimization of electron currents along the walls of a conical target for fast ignition. *Physics of Plasmas*, 17(12):122703.

[145] Mo, M. e. a. (2013). Laser wakefield generated x-ray probe for femtosecond time-resolved measurements of ionization states of warm dense aluminum. *Rev. of Scientific Instrum.*, 84:123106–1–11.

[146] Moliere, G. (1948). Theorie der streuung schneller geladener teilchen ii. mehrfach- und vielfachstreuung. *Zeitschrift Naturforschung Teil A*, 3a(78).

[147] Mora, P. (1982). Theoretical model of absorption of laser light by a plasma. *Physics of Fluids*, 25(1051).

[148] Mora, P. (2003). Plasma expansion into a vacuum. *Physical Review Letters*, 90(18):185002.

[149] Mora, P. (2005a). Collisionless expansion of a gaussian plasma into a vacuum. *Physics of Plasmas*, 12(11):112102.

[150] Mora, P. (2005b). Thin-foil expansion into a vacuum. *Physical Review E*, 72(5):056401.

[151] Morawetz, K. and Röpke, G. (1996). Stopping power in nonideal and strongly coupled plasmas. *Physical Review E*, 54:4134–4146.

[152] Moseley, H. (1913). The high-frequency spectra of the elements. *Philosophical Magazin*, 26(1024).

[153] Mulser, P. and Bauer, D. (2010). High power laser-matter interaction. *Springer Tracts in Modern Physics*, 238.

[154] Myatt, J., Theobald, W., and Delettrez, J. e. a. (2007). High-intensity laser interactions with mass-limited solid targets and implications for fast-ignition experiments on omega ep. *Physics of Plasmas*, 14(056301).

[155] Nicolaï, P. e. a. (2011). Effect of the plasma-generated magnetic field on relativistic electron transport. *Phys. Rev. E*, 84:016402.

[156] Nigam, B. P., Sundaresan, M. K., and Wu, T.-Y. (1959). Theory of multiple scattering: Second born approximation and corrections to molière's work. *Physical Review*, 115(491).

[157] Nilson, P. M., Theobald, W., and Myatt, J. e. a. (2008). High-intensity laser-plasma interactions in the refluxing limit. *Physics of Plasmas*, 15(5):056308.

[158] Nilson, P. M. e. a. (2010). Scaling hot-electron generation to high-power, kilojoule-class laser-solid interactions. *Physical Review Letters*, 105(235001).

[159] Nuter, R., Gremillet, L., and Combis, P. e. a. (2008). Influence of a preplasma on electron heating and proton acceleration in ultraintense laser-foil interaction. *Journal of Applied Physics*, 104(10):103307.

[160] P., S. and A., S. (2006). Shell correction in stopping theory. *Nuclear Instruments and Methods in Physics Research B*, 243:457–460.

[161] Patel, P. K., Mackinnon, A. J., and Key, M. H. e. a. (2003). Isochoric heating of solid-density matter with an ultrafast proton beam. *Physical Review Letters*, 91(12):125004.

[162] Pelka, A. e. a. (2010). Ultrafast melting of carbon induced by intense proton beams. *Physical Review Letters*, 105(26):265701.

[163] Perez, F. (2010). PhD thesis, Ecole Polytechnique.

[164] Pérez, F., Debayle, A., and Honrubia, J. e. a. (2011). Magnetically guided fast electrons in cylindrically compressed matter. *Physical Review Letters*, 107:065004.

[165] Pert, G. J. (1978). The analytic theory of linear resonant absorption. *Plasma Physics*, 20(175).

[166] Pines, D. and Bohm, D. (1952). A collective description of electron interactions: Ii. collective vs individual particle aspects of the interactions. *Phys. Rev.*, 85(338).

[167] Ping, Y., Shepherd, R., and Lasinski, B. F. e. a. (2008). Absorption of short laser pulses on solid targets in the ultrarelativistic regime. *Physical Review Letters*, 100:085004.

[168] Pisani, F., Bernardinello, A., and Batani, D. e. a. (2000). Experimental evidence of electric inhibition in fast electron penetration and of electric-field-limited fast electron transport in dense matter. *Physical Review E*, 62:R5927–R5930.

[169] Popescu, H. e. a. (2005). Subfemtosecond, coherent, relativistic, and ballistic electron bunches generated at 0 and 20 in high intensity laser-matter interaction. *Physics of Plasmas*, 12(063106).

[170] Pratt, R. H. e. a. (1997). *At. Data Nucl. Data Tables*, 20(175).

[171] Ramis, R., Schmalz, and Meyer-Ter-Vehn, J. (1988). Multi — a computer code for one-dimensional multigroup radiation hydrodynamics. *Comput. Phys. Commun.*, 49:475 – 505.

[172] Ramis, R. e. a. (2011). Multi-fs – a computer code for laser–plasma interaction in the femtosecond regime. *Computer Physics Communications*, 183.

[173] Ramis, R. e. a. (2014). Three-dimensional symmetry analysis of a direct-drive irradiation scheme for the laser megajoule facility. *Phys. Plasmas*, 21(082710).

[174] Ren, C., Tzoufras, M., and Tsung, F. S. e. a. (2004). Global simulation for laser-driven mev electrons in fast ignition. *Physical Review Letters*, 93:185004.

[175] Robinson, A. e. a. (2014). Theory of fast electron transport for fast ignition. *Nuclear Fusion*, 54(5):054003.

[176] Robinson, A. P. L., Sherlock, M., and Norreys, P. A. (2008). Artificial collimation of fast-electron beams with two laser pulses. *Physical Review Letters*, 100:025002.

[177] Robson, L., e. a. (2007). Scaling of proton acceleration driven by petawatt-laser-plasma interactions. *Nature Phys.*, 3:58.

[178] Rohrlich, F. and Carlson, B. (1954). Positron-electron differences in energy loss and multiple scattering. *Phys. Rev.*, 93(38).

[179] Roth, M., Blazevic, A., Geissel, M., and et al., S. (2002). Energetic ions generated by laser pulses: A detailed study on target properties. *Physical Review Accelerators and Beams*, 5:061301.

[180] Roth, M. and C. Stöckl, C. e. a. (2000). Energy loss of heavy ions in laser-produced plasmas. *Physical Review Letters*, 50:28–30.

[181] Roth, M., Cowan, T. E., and Key, M. H. e. a. (2001). Fast ignition by intense laser-accelerated proton beams. *Physical Review Letters*, 86.

[182] Ruhl, H. e. a. (2001). Computer simulation of the three-dimensional regime of proton acceleration in the interaction of laser radiation with a thin spherical target. *Plasma Phys. Rep.*, 27(5):361.

[183] Rygg, J. e. a. (2008). Proton radiography of inertial fusion implosions. *Science*, 319(1223).

[184] Santos, J., Bailly-Grandvaux, M., and Giuffrida, L. e. a. (2015). Laser-driven platform for generation and characterization of strong quasi-static magnetic fields. *New Journal of Physics*, 17(8):083051.

[185] Santos, J., Batani, D., and Baton, S. e. a. (2013a). Supra-thermal electron beam stopping power and guiding in dense plasmas. *Journal of Plasma Physics*, 79(4):429–435.

[186] Santos, J. J., Amiranoff, F., and Baton, S. D. e. a. (2002). Fast electron transport in ultraintense laser pulse interaction with solid targets by rear-side self-radiation diagnostics. *Physical Review Letters*, 89:025001.

[187] Santos, J. J., Batani, D., and Baton, S. e. a. (2013b). Supra-thermal electron beam stopping power and guiding in dense plasmas. *Journal of Plasma Physics*, 79(4):429–435.

[188] Santos, J. J., Debayle, A., and Nicolaï, P. a. (2007). Fast-electron transport and induced heating in aluminum foils. *Physics of Plasmas*, 14(10):103107.

[189] Santos, J. J., Vauzour, B., and Touati, M. e. a. (2017). Isochoric heating and strong blast wave formation driven by fast electrons in solid-density targets. *New Journal of Physics*, 19(10):103005.

[190] Schiff, L. I. (1951). Energy-angle distribution of thin target bremsstrahlung. *Phys. Rev.*, 83(252).

[191] Schmitz, H., Lloyd, R., and Evans, R. G. (2012). Collisional particle-in-cell modelling of the generation and control of relativistic electron beams produced by ultra-intense laser pulses. *Plasma Physics and Controlled Fusion*, 54(8):085016.

[192] Schreiber, J., Bell, F., and Grüner, U. e. a. (2006). Analytical model for ion acceleration by high-intensity laser pulses. *Physical Review Letters*, 97(4):045005.

[193] Schroeder, C. B. e. a. (2004). Theory of coherent transition radiation generated at a plasma-vacuum interface. *Physical Review E*, 69(016501).

[194] Scott, R. H. H., Beaucourt, C., and Schlenvoigt, H.-P. e. a. (2012). Controlling fast-electron-beam divergence using two laser pulses. *Physical Review Letters*, 109:015001.

[195] Seltzer, S. (1974). Transmission of electrons through foils, technical report com-74-11792. *National Bureau of Standards*.

[196] Seltzer, S. M. and Berger, M. J. (1986). *At. Data Nucl. Data Tables*, 35(345).

[197] Sengebusch, A. e. a. (2007). Shift of cl k and k lines in laser produced dense plasmas. *Contrib. Plasma Phys.*, 47(309).

[198] Snavely, R. A. e. a. (2000). Intense high-energy proton beams from petawatt-laser irradiation of solids. *Physical Review Letters*, 85:2945–2948.

[199] Spitzer, L. (1956). *Physics of Fully Ionized Gases*.

[200] Sternheimer, R. (1966). Density effect for the ionization loss of charged particles. *Physical Review*, 145(247).

[201] Sternheimer, R. M., Seltzer, S. M., and Berger, M. J. (1982). Density effect for the ionization loss of charged particles in various substances. *Phys. Rev. B*, 26(6067).

[202] Strickland, D. and Mourou, G. (1985). Compression of amplified chirped optical pulses. *Optics Communications*, 56(219).

[203] T., T. and J.M., D. (1979). Laser electron accelerator. *Physical Review Letters*, 43:267–270.

[204] Tabak, M. e. a. (1994). Ignition and high gain with ultrapowerful lasers. *Physics of Plasmas*, 1:1626–1634.

[Tanimoto et al.] Tanimoto, T., Habara, H., and Kodama, R. e. a.

[206] Tauschwitz, A. e. a. (2013). 2d radiation-hydrodynamics modeling of laser-plasma targets for ion stopping measurements. *High Energ. Density Phys.*, 9:158–166.

[207] Town, R., Chen, C., and Cottrill, L. e. a. (2005). Simulations of electron transport for fast ignition using lsp. *Nuclear Instruments and Methods in Physics Research Section A: Accelerators, Spectrometers, Detectors and Associated Equipment*, 544(1):61 – 66.

[208] Tronnier, A. (2006). PhD thesis, Technical University Munich.

[209] Vaisseau, X. (2014). *Experimental study of fast electron transport in dense plasmas*. PhD thesis, University of Bordeaux.

[210] Vaisseau, X., Debayle, A., and Honrubia, J. J. e. a. (2015). Enhanced relativistic-electron-beam energy loss in warm dense aluminum. *Physical Review Letters*, 114:095004.

[211] Vaisseau, X., Morace, A., and Touati, M. e. a. (2017). Collimated propagation of fast electron beams accelerated by high-contrast laser pulses in highly resistive shocked carbon. *Physical Review Letters*, 118:205001.

[212] Vauzour, B., Santos, J. J., and Debayle, A. e. a. (2012). Relativistic high-current electron-beam stopping-power characterization in solids and plasmas: Collisional versus resistive effects. *Physical Review Letters*, 109:255002.

[213] Verlet, L. (1967). Computer "experiments" on classical fluids. i. thermodynamical properties of lennard-jones molecules. *Physical Review*, 159:98–103.

[214] Volpe, L., Batani, D., and Birindelli, G. e. a. (2013a). Propagation of a short-pulse laser-driven electron beam in matter. *Physics of Plasmas*, 20(3):033105.

[215] Volpe, L., Batani, D., Morace, A., and Santos, J. J. (2013b). Collisional and collective effects in two dimensional model for fast-electron transport in refluxing regime. *Physics of Plasmas*, 20(1):013104.

[216] Volpe, L., Fedosejevs, R., and Gatti, e. a. (2019). Generation of high energy laser-driven electron and proton sources with the 200 tw system vega 2 at the centro de laseres pulsados. *High Power Laser Science and Engineering*, 7.

[217] Volpe, L., Feugeas, J.-L., and Nicolai, P. e. a. (2014). Controlling the fast electron divergence in a solid target with multiple laser pulses. *Physical Review E*, 90:063108.

[218] Volpe, L. e. a. (2011). Proton radiography of cylindrical laser-driven implosions. *Physics of Plasma*, 18(012704).

[219] Wharton, K., Hatchett, S. P., and Wilks, S. C. e. a. (1998). Experimental measurements of hot electrons generated by ultraintense (> 1019 w/cm2) laser-plasma interactions on solid-density targets. *Physical Review Letters*, 81:822.

[220] White, T. e. a. (2012). *Sci. Rep.*, 2(889).

[221] Wilks, S. C., Kruer, W. L., Tabak, M., and Langdon, A. B. (1992). Absorption of ultra-intense laser pulses. *Physical Review Letters*, 69:1383–1386.

[222] Wilks, S. e. a. (2001). Energetic proton generation in ultra-intense laser–solid interactions. *Physics of Plasmas*, 8(2):542–549.

[223] Yabuuchi, T., Adumi, K., Habara, H., and Kodama, R. e. a. (2007). On the behavior of ultraintense laser produced hot electrons in self-excited fields. *Physics of Plasmas*, 14(4):040706.

[224] Yakovlev, D. G. and Urpin, V. A. (1980). Thermal and electrical conductivity in white dwarfs and neutron stars. *Soviet Astronomy*, 24(303).

[225] Zeil, K., Kraft, S. D., and Bock, S. e. a. (2010). The scaling of proton energies in ultrashort pulse laser plasma acceleration. *New J. Phys.*, 12:045015.

[226] Zheng, J., Tanaka, K. A., and Miyakoshi, T. e. a. (2003). Theoretical study of transition radiation from hot electrons generated in the laser-solid interaction. *Physics of Plasmas*, 10(2994).

[227] Zheng, J. e. a. (2002). Spectrum of transition radiation from hot electrons generated in ultraintense laser plasma interaction. *Physics of Plasmas*, 9(3610).

[228] Ziegler, J., Biersack, J., and Ziegler, M. (2008). Stopping and range of ions in matter. *SRIM Co., Chester, MD*.

[229] Zimmerman, G. (1990). Report no. ucrl-jc-105616. *LLNL*.

[230] Zwicknagel, G. (1999). *Phys. Rep.*, 309(117).

[231] Zylstra, A. e. a. (2015). Measurement of charged-particle stopping in warm dense plasma. *Phys. Rev. Let*, 114(215002).